CORA Cork Open Research Archive
Cartlann Taighde Oscailte Chorcaí

Title	Design and nonlinear modelling of general flexure beams and compliant mechanisms
Authors	Zhu, Jiaxiang
Publication date	2024
Original Citation	Zhu, J. 2024. Design and nonlinear modelling of general flexure beams and compliant mechanisms. PhD Thesis, University College Cork.
Type of publication	Doctoral thesis
Rights	© 2024, Jiaxiang Zhu. - https://creativecommons.org/licenses/by/4.0/
Download date	2026-11-03 09:23:07
Item downloaded from	https://hdl.handle.net/10468/17421



UCC
University College Cork, Ireland
Coláiste na hOllscoile Corcaigh



UCC

University College Cork, Ireland
Coláiste na hOllscoile Corcaigh

Design and Nonlinear Modelling of General Flexure Beams and Compliant Mechanisms

Thesis presented by

Jiaxiang Zhu

for the degree of

Doctor of Philosophy

Supervisor: **Prof. Guangbo Hao**

Co-Supervisor: **Dr. Denis Kelliher**

University College Cork

School of Engineering and Architecture

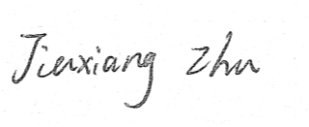
Head of School: **Prof. Jorge Oliveira**

March 2024

Dedicated to my family.

DECLARATION

I hereby certify that the work presented in this thesis is entirely my own and has not been submitted for any other degree at University College Cork or any other institution. All references to external sources and contributions from other individuals are acknowledged and appropriately cited within the text. I confirm that I have read and understood the University College Cork regulations regarding plagiarism and intellectual property, and I have complied with these standards throughout the preparation of this work.

Signature: 

Date:

PUBLICATIONS AND AWARDS

1) Publication arising from this thesis

Journal papers:

Zhu, J., Hao, G., Li, S., et al. (2025). "Nonlinear design of a general single-translation constraint and the resulting general spherical joint." *Journal of Mechanical Design*, 1-40. (**Related to Chapter 2 and Chapter 5**)

Zhu, J., & Hao, G. (2024). Modelling of a general lumped-compliance beam for compliant mechanisms. *International Journal of Mechanical Sciences*, *263*, 108779. (**Related to Chapter 2 and Chapter 5**)

Zhu, J., Hao, G., Liu, T. and Li, H., (2023). Design of an over-constraint based nearly-constant amplification ratio compliant mechanism. *Mechanism and Machine Theory*, *186*, p.105347. **(Related to Chapter 3**)

Zhu, J., Hao, G., Li, S. and Kong, X., (2022). A compact mirror-symmetrical XY compliant parallel manipulator for minimizing parasitic rotations. *Journal of Mechanical Design*, *144*(7), p.073303. **(Related to Chapter 4**)

Conference papers:

Zhu, J., Hao, G., Ye, S., (2024, June). Nonlinear modelling of a novel general single-translation constraint and centre drift analysis of the resulting spherical joint. In *MMT Symposium 2024.* Universidade do Minho.

Zhu, J., Hao, G., Liu, T., & Li, H. (2022, August). Design and Nonlinear Analysis of an Overconstraint Based Constant Amplification Ratio Compliant Mechanism. In *International Design Engineering Technical Conferences and Computers and Information in Engineering Conference* (Vol. 86281, p. V007T07A005).

Zhu, J., Hao, G., & Tang, H. (2022, August). Design and modelling of a generic compliant mechanism with bi-stability and static balancing. In *2022 IEEE International Conference on Manipulation, Manufacturing and Measurement on the Nanoscale (3M-NANO)* (pp. 172-177). IEEE.

Zhu, J., Hao, G., Li, S., Yu, S., & Kong, X. (2021, August). A mirror-symmetrical xy compliant parallel manipulator with improved performances without increasing the footprint. In *International Design Engineering Technical Conferences and Computers and Information in Engineering Conference* (Vol. 85444, p. V08AT08A012)

2) Other publications

Journal papers:

Zhu, J., & Hao, G. (2020). Design and test of a compact compliant gripper using the Scott–Russell mechanism. *Archives of Civil and Mechanical Engineering*, *20*, 1-12.

Hao, G., & **Zhu, J.** (2019). Design of a monolithic double-slider based compliant gripper with large displacement and anti-buckling ability. *Micromachines*, *10*(10), 665.

Liu, T., Hao, G., **Zhu, J.**, Kuresangsai, P., Abdelaziz, S., & Wehrle, E. (2024). Modeling compliant bistable mechanisms: An energy method based on the high-order smooth curvature model. *International Journal of Mechanical Sciences*, *275*, 109315.

Li, S., Hao, G., Chen, Y., **Zhu, J.**, & Berselli, G. (2022). Nonlinear analysis of a class of inversion-based compliant cross-spring pivots. *Journal of Mechanisms and Robotics*, *14*(3), 031007.

Li, K., He, X., Lv, L., **Zhu, J.**, Hao, G., Li, H., & Song, X. (2023). A single-fidelity surrogate modeling method based on nonlinearity integrated multi-fidelity surrogate. *Journal of Mechanical Design*, *145*(9).

Hao, G., He, X., **Zhu, J.**, & Li, H. (2024). Design and Analysis of Leaf Beam Single-Translation Constraint Compliant Modules and the Resulting Spherical Joints. *Journal of Mechanical Design*, *146*(8), 083301.

Mokhtari, M., Varedi-Koulaei, S. M., **Zhu, J.**, & Hao, G. (2022). Topology optimization of the compliant mechanisms considering curved beam elements using metaheuristic algorithms. *Proceedings of the Institution of Mechanical Engineers, Part C: Journal of Mechanical Engineering Science*, *236*(13), 7197-7208.

Conference papers:

Li, S., Hao, G., Chen, Y., **Zhu, J.**, & Berselli, G. (2021, August). Nonlinear Analysis of a Class of Inversion-Based Compliant Cross-Spring Pivots. In *International Design Engineering Technical Conferences and Computers and Information in Engineering Conference* (Vol. 85444, p. V08AT08A011).

Song, X., Li, K., Wang, S., Kan, Z., Li, H., **Zhu, J.**, & Hao, G. (2022, August). Framework design of a digital twin of an Xy compliant parallel manipulator based on non-negative matrix factorization. In *International Design Engineering Technical Conferences and Computers and Information in Engineering Conference* (Vol. 86212, p. V002T02A023).

3) Awards

2024 Shortlisted in the Student Mechanism & Robot Design Competition, *ASME-IDETC Conference*

2023 First Place in the Publication of the Year, *School of Engineering and Architecture, UCC*

2023 Winner of the Best Presentation Award, *2nd Forum for Chinese PhD Students in Ireland and Northern Ireland*

2023 Second Place in the Student Mechanism & Robot Design Competition, *ASME-IDETC Conference*

2022 Winner of the Compliant Mechanisms Award, *ASME Mechanisms and Robotics Committee*

2022 Second Place in the Student Mechanism & Robot Design Competition, *ASME-IDETC Conference*

2021 Second Place in the Best Research Image Competition, *School of Engineering and Architecture, UCC*

ABSTRACT

A compliant mechanism is a mechanical structure that achieves motion and force transmission through elastic deformation of its flexible components rather than relying on traditional rigid-body joints. Their ability to deliver smooth, repeatable motion with minimal backlash and wear has made them indispensable in practical and technological applications.

This research advances the field of compliant mechanisms by addressing critical challenges in nonlinear modeling and design. The primary modeling contributions include a 2D nonlinear general lumped-compliance beam model (GLBM) and a 3D model for general single-translation constraint (GSTC) leaf beams. These parameterized models incorporate a carefully selected set of geometric variables, striking a balance between computational efficiency and configurational versatility. By adjusting these parameters, the models can represent a wide range of compliant mechanism designs, enabling reconfigurable configurations, rapid nonlinear modeling, and efficient multi-objective optimization without unnecessary complexity.

On the design side, novel compliant mechanisms are proposed and modeled, including revolute joints, bistable mechanisms, spherical joints, an over-constraint-based nearly-constant amplification ratio compliant amplifier (OCARCM), and a mirror-symmetrical XY compliant parallel manipulator (XY CPM). The GLBM accurately predicts force-displacement behavior in 2D mechanisms, while the GSTC model enables versatile spherical joint design through parametric adjustments. Additionally, the nonlinear modeling of the OCARCM and XY CPM employs a closed-form beam constraint model (BCM), which can be derived from the 2D GLBM to facilitate efficient nonlinear analysis.

Comprehensive finite element analysis (FEA) and experimental validation demonstrate strong agreement with analytical models. The GLBM shows 2%–6% error for large deflections, and the GSTC beam remains within 10% error across typical motion ranges. The OCARCM achieves just 1% variability in amplification ratio, outperforming conventional designs. The XY CPM effectively reduces parasitic effects and enhances out-of-plane stiffness while maintaining precision and compactness.

TABLE OF CONTENTS

Declaration ..... **II**

Publications and Awards ..... **III**

Abstract ..... **VI**

Table of Contents ..... **VII**

Acknowledgment ..... **XI**

List of Figures ..... **XII**

List of Tables ..... **XXII**

Nomenclature ..... **XXIII**

Abbreviations ..... **XXV**

Chapter 1 Introduction **1**

1.1 Compliant mechanisms 1

1.2 The basic building block of compliant mechanisms 3

1.2.1 Basic types of flexure beams 3

1.2.2 Basic types of flexure hinges 5

1.3 The nonlinear modelling technics 8

1.3.1 The nonlinear deflection of a flexure beam 8

1.3.2 The state-of-the-art in 2D nonlinear modelling 10

1.3.3 The state-of-the-art in 3D nonlinear modeling 13

1.4 The design methodology of compliant mechanisms 15

1.5 Problem statement 17

1.6 Research objectives and thesis organization 19

1.6.1 Research objectives 19

1.6.2 Thesis organization 20

Chapter 2 Parameterized Nonlinear Models of General Flexure Beams 23

2.1 2D nonlinear modeling of a general lumped-compliance beam 24

2.1.1 The development of the general lumped-compliance beam model 24

2.1.2 FEA verification and parametric analysis 28

2.1.3 Discussions 36

2.2 3D nonlinear design of a general single-translation constraint 38

2.2.1 General single-translation constraint leaf beam design 39

2.2.2 FEA verification for four representative configurations 41

2.2.3 Further discussions 47

2.3 Summary 48

Chapter 3 Design and Nonlinear Analysis of Nearly-Constant Amplification Ratio Compliant Mechanisms 51

3.1 The prior art of compliant mechanism-based amplifier 52

3.2 Mechanism design 54

3.3 Nonlinear analytical modeling and analysis 56

3.3.1 Kinetostatic analysis of the amplifier 57

3.3.2 Characteristics analysis with FEA verification 60

3.4 Experiment tests 66

3.4.1 Fabrication of the OCARCM prototype 66

3.4.2 Experimental setup 67

3.4.3 Experimental results 68

3.5 Further discussions 71

3.5.1 Dynamic performance 71

3.5.2 Eliminating force-displacement nonlinearity 72

3.5.3 Reducing the footprint 74
3.6 Summary 74
Chapter 4 Design and Nonlinear Analysis of a Mirror-Symmetrical XY Parallel Manipulator 77
4.1 Prior art of the XY CPM 78
4.2 Mechanism design 81
4.2.1 The principle of minimising the parasitic rotation 81
4.2.2 Embodiment of the XY CPM 82
4.2.3 Nonlinear kinetostatic analytical modelling 83
4.3 FEA verifications 89
4.4 Experimental tests 94
4.4.1 Fabrication of the XY CPM 94
4.4.2 Low-cost apparatus setup for data acquisition 95
4.4.3 Experiment procedures 96
4.4.4 Experimental results 97
4.4.5 Further discussions 100
4.5 Summary 104
Chapter 5 Applications of the Parameterized Nonlinear Models in Designing Compliant Mechanisms 106
5.1 2D Design and nonlinear modelling of revolute joint and bistable mechanisms 107
5.1.1 Case I - revolute joint with two identical inverted beams 108
5.1.2 Case II - bistable mechanism using two types of GLBMs 111
5.1.3 Experimental validation of the revolute joint 114
5.1.4 Experimental validation of the bistable mechanism 116

5.2 3D Design and nonlinear modelling of the general spherical joint 118
5.2.1 Design of a general spherical joint based on the GSTC leaf beams.....118
5.2.2 Nonlinear modelling of the general spherical joint 119
5.2.3 FEA verification of the general spherical joint..... 122
5.2.4 Experiment 133
5.3 Summary..... 138
Chapter 6 Conclusions 140
6.1 Contributions 140
6.2 Conclusions 141
6.3 Future work 143
References..... 145
Appendix A Force-Displacement Characteristic of a Slender Flexure Beam 167
Appendix B The Nonlinear Spatial Beam Constraint Model of a Flexure Beam 168
Appendix C Force-Equilibrium Equations and Geometry Compatibility Conditions of the GSTC Leaf Beam 171
Appendix D Force-Displacement Characteristic of a Generic Flexure Beam 173

ACKNOWLEDGMENT

This dissertation marks the culmination of a journey made possible through the support, guidance, and encouragement of many people. I am deeply grateful to each of you for your invaluable contributions.

First and foremost, I extend my deepest gratitude to my supervisor, Prof. Guangbo Hao, with whom I have had the privilege of working for the past six years, both during my master's and PhD studies. Prof. Hao, your commitment to excellence and your unwavering support have been fundamental in shaping both this research and my development as a scholar. Your mentorship, with its emphasis on the principles of "Plan, Do, Check, Act," has instilled in me a disciplined and strategic approach to research and problem-solving. This invaluable framework will guide me well beyond my academic career. Thank you for your patience, your insightful feedback, and your steadfast belief in my potential. I could not have asked for a more inspiring mentor, and I am deeply honored to have had the opportunity to learn from you.

I would also like to express my sincere gratitude to my co-supervisor, Dr. Denis Kelliher, for his support and guidance throughout my research journey. Your willingness to provide assistance when needed is greatly appreciated.

To my wife, Yingying Song, your unwavering support and understanding have been my anchor, especially during the long hours and challenging times. To my newborn daughter, Aike Zhu, your arrival has filled my life with immense joy and motivation. This work is as much yours as it is mine. I would also like to thank my parents, Hongying Zhang and Xinsheng Zhu, for their lifelong encouragement, sacrifices, and belief in me. My two sisters, Xiaojuan Zhu and Lanying Huang, have been a constant source of support and inspiration, reminding me to strive for my goals.

A special acknowledgment to Mr. Timothy Power and Mr. Michael O'Shea, whose technical expertise and assistance were invaluable throughout the experimental phases of my research.

Moreover, I would like to express my appreciation to the University College Cork and China Scholarship Council for their financial support of my doctoral research.

LIST OF FIGURES

Figure 1.1 Compliant mechanisms in early human history: (a) the flexible hammer handle; (b) carrying pole; (c) bow. 1

Figure 1.2 Examples of compliant mechanisms used in modern engineering: (a) surgical grasper [1]; (b) complaint mechanical amplifier in MEMS application [2]; (c) nano-positioning stage [3]; (d) horological industry [4]; (e) aerospace application [5]; (f) energy harvesting device[6]. 2

Figure 1.3 Different forms of flexure beam: (a) cylindrical wire beam [21, 22]; (b) rectangular wire beam [23, 24]; (c) slender flexure beam [25, 7]; (d) folded beam [26, 27]; (e) tapered beam [28, 29]; (f) elliptical curved [30-32]; (g) circular curved (in-plane stiff) [33-35]; (h) circular curved (out-of-plane stiff) [36, 37]; (i) spline curved [38]. 5

Figure 1.4 Types of basic flexure hinge: (a) rectangular [39, 40]; (b) corner-filleted [43-45]; (c) elliptical [41, 42]; (d) circular [56, 57]; (e) V-shaped [58, 59]; (f) crossed [60, 61]; (g) split-tube [62, 63]; (h) topology optimized [46]; (i) multiple-axis elliptical [64, 65]; (j) two-axis corner-filleted [66, 67]; (k) spherical [68, 33]; (l) spiral [49, 50]; (m) asymmetric corner-filleted [51]; (n) single notch [52, 53]; (o) elliptical hyperbolic hybrid [54]; (p) crease-type [55]. 7

Figure 1.5 The DoF and DoC of a slender flexure beam with one end fixed. 8

Figure 1.6 Linear and nonlinear analyses of beam deflection 9

Figure 1.7 Summary of the methods for the design of compliant mechanisms 16

Figure 1.8 The flowchart of the thesis structure 21

Figure 2.1 Configuration of a general beam: (a) geometry parameters of the GLBM; (b) FBD of the general beam. 25

Figure 2.2 GLBM in different configurations: (a) straight/conventional lumped-compliance beam [95]; (b) distributed-compliance beam [99, 105]; (c) folded beam [26, 156]; (d) inverted beam [157-159]; (e) inclined beam [160, 161]; (g) half-inverted beam [162, 141]; (f) trapezoidal beam [163, 164] 27

Figure 2.3 Flowchart of the process of FEA simulation based on the software Comsol.30

Figure 2.4 FEA verification of the lumped-compliance beam: (a) displacement in X-direction versus the input force F_{in}; (b) displacement in Y-direction versus the input force F_{in}; (c) rotation about Z-axis versus the input force F_{in}..... 31

Figure 2.5 FEA verification of the distributed-compliance beam: (a) displacement in X-direction versus the input force F_{in}; (b) displacement in Y-direction versus the input force F_{in}; (c) rotation about Z-axis versus the input force F_{in}..... 31

Figure 2.6 FEA verification of the inverted beam: (a) displacement in X-direction versus the input force F_{in}; (b) displacement in Y-direction versus the input force F_{in}; (c) rotation about Z-axis versus the input force F_{in}. 32

Figure 2.7 FEA verification of the inclined beam: (a) displacement in X-direction versus the input force Fin; (b) displacement in Y-direction versus the input force Fin; (c) rotation about Z-axis versus the input force Fin. 32

Figure 2.8 FEA verification of the folded beam: (a) displacement in X-direction versus the input force F_{in}; (b) displacement in Y-direction versus the input force F_{in}; (c) rotation about Z-axis versus the input force F_{in}. 33

Figure 2.9 The stiffness in Y-direction with varying geometry parameters α and β: (a) instantons stiffness, the case of $Y_{in} = 0$ mm, $X_{in} = 0$ and $\theta_{in} = 0$; (b) under the case of $Y_{in} = 0.1$ mm, $X_{in} = 0$ and $\theta_{in} = 0$; (c) under the case of $Y_{in} = 0.2$ mm, $X_{in} = 0$ and $\theta_{in} = 0$; (d) and the general beam configurations for each peak. 35

Figure 2.10 The general process of using the GLBM to model compliant mechanisms.37

Figure 2.11 Wire beam and its equivalent: (a) a wire beam; (b) I-shape leaf beam; (c) GSTC leaf beam. 39

Figure 2.12 Four representative configurations in comparison: (a) I-shape leaf beam ($\beta_{xi} = \pi/2$; $\beta_{yi} = 0$; $\beta_{zi} = 0$); (b) SSTC leaf beam ($\beta_{xi} = \pi/2$; $\beta_{yi} = \pi/6$; $\beta_{zi} = \pi/6$); (c) L-shape leaf beam ($\beta_{xi} = \pi/2$; $\beta_{yi} = 0$; $\beta_{zi} = \pi/2$); (d) folded leaf beam ($\beta_{xi} = \pi/2$; $\beta_{yi} = \pi/2$; $\beta_{zi} = \pi/2$).42

Figure 2.13 (Colour lines) The displacement comparison between the FEA and analytical results for the SSTC leaf beam, subjected to incremental forces in the Y-direction, a

constant force in the X-direction and a constant moment along the X-direction: (a) the resultant displacement X_{si} ; (b) the resultant displacement Y_{si} ; (c) the resultant displacement Z_{si} ; (d) the resultant rotation θ_{xsi} ; (e) the resultant rotation θ_{ysi} ; (f) the resultant rotation θ_{zsi} ; 44

Figure 2.14 The displacement comparison between the FEA and analytical results for the I-shape leaf beam, subjected to incremental forces in the Y-direction, a constant force in the X-direction and a constant moment along the X-direction: (a) the resultant displacement X_{si} ; (b) the resultant displacement Y_{si} ; (c) the resultant displacement Z_{si} ; (d) the resultant rotation θ_{xsi} ; (e) the resultant rotation θ_{ysi} ; (f) the resultant rotation θ_{zsi} ; . 45

Figure 2.15 The displacement comparison between the FEA and analytical results for the L-shape leaf beam, subjected to incremental forces in the Y-direction, a constant force in the X-direction, and a constant moment along the X-direction: (a) the resultant displacement X_{si} ; (b) the resultant displacement Y_{si} ; (c) the resultant displacement Z_{si} ; (d) the resultant rotation θ_{xsi} ; (e) the resultant rotation θ_{ysi} ; (f) the resultant rotation θ_{zsi}... 45

Figure 2.16 The displacement comparison between the FEA and analytical results for the folded leaf beam, subjected to incremental forces in the Y-direction, a constant force in the X-direction and a constant moment along the X-direction: (a) the resultant displacement X_{si} ; (b) the resultant displacement Y_{si} ; (c) the resultant displacement Z_{si} ; (d) the resultant rotation θ_{xsi} ; (e) the resultant rotation θ_{ysi} ; (f) the resultant rotation θ_{zsi}... 46

Figure 2.17 Spherical joint with inverted single-translation constraint: (a) the sketch of the geometry; (b) the deformed configuration..... 47

Figure 2.18 Spherical joint with 45-degree I-shape leaf beams: (a) the sketch of the geometry; (b) the deformed configuration..... 47

Figure 3.1 A quarter of the bridge-type compliant amplifier with a nonconstant amplification ratio..... 52

Figure 3.2 Design from traditional rigid mechanism to compliant mechanism: (a) two rotationally symmetric double slider mechanisms; (b) its compliant equivalent; (c) the over-constraint compliant mechanism. 55

Figure 3.3 A schematic of OCARCM design with parameter labelling: (a) isometric view;

(b) the front view. 56

Figure 3.4 The static modelling of a quarter of the amplifier: (a) a quarter of the OCARCM; (b) the FBD of the OCARCM. 57

Figure 3.5 Displacement analysis: (a) the exaggerated view of the displacement plot of the OCARCM with the flexure beam slope of 30^0; (b) the deformation of the corresponding bridge-type amplifier. 61

Figure 3.6 Force-displacement characteristics without payload (F_L = 0): (a) lumped-compliance (A = 5 mm); (b) lumped-compliance (A = 10 mm); (c) distributed-compliance (A = 15 mm). 61

Figure 3.7 Comparison between bridge-type amplifier and OCARCM with the equal beam slope ($\alpha = \beta$): (a) lumped-compliance (A = 5 mm); (b) lumped-compliance (A = 10 mm); (c) distributed-compliance (A = 15 mm); (d) OCARCM compared with the bridge-type compliant amplifier with different compliance. 63

Figure 3.8 The amplification ratio under different payloads F_L: (a) the FEA results of the OCARCM compared with its analytical results; (b) the FEA results of the bridge-type compliant amplifier compared with its analytical results; (c) variation of the amplification ratio in response to the different payload F_L. 64

Figure 3.9 The comparison between the lumped-compliance and the distributed-compliance under different payloads F_L. 65

Figure 3.10 Amplification ratio of the lumped-compliance OCARCM with different beam slopes ($\alpha \neq \beta$). 65

Figure 3.11 Prototype and experiment setup of the OCARCM: (a) testing of loading spring; (b) monolithically fabricated; (c) assembly. 67

Figure 3.12 Force-displacement relationship: (a) without loading spring; (b) with loading spring 1; (c) with loading spring 2; (d) the error between experimental and analytical results; (e) integrated plots of experiment results; (f) integrated plots of analytical results. 69

Figure 3.13 Amplification ratio of the OCARCM with different loading springs: (a)

amplification ratio without payload; (b) amplification ratio with loading spring 1; (c) amplification ratio with loading spring 2; (d) Error between the experimental results and analytical results. 70

Figure 3.14 The first-four natural frequencies..... 71

Figure 3.15 (a) OCARCM with Z-shape beams; (b) its deformed configuration. 73

Figure 3.16 Nonlinear FEA results: (a) force-displacement plot; (b) amplification ratio comparison. 73

Figure 3.17 Three-layer design with reduced footprint: (a) geometry of the design; (b) deformed configuration. 74

Figure 4.1 Exactly-constrained 2-PP mechanism..... 78

Figure 4.2 Overconstrained 4-PP CPMs..... 80

Figure 4.3 Composition of the two-layer design. 81

Figure 4.4 Finalized design 82

Figure 4.5 The geometry parameter and loading condition of the DPF. 83

Figure 4.6 Rigid body free body diagrams..... 85

Figure 4.7 Motion range before yielding..... 90

Figure 4.8 Primary motion of the XY CPM. 91

Figure 4.9 Cross-axis coupling error in X-direction. 91

Figure 4.10 Lost motion along X-direction. 92

Figure 4.11 Actuator isolation index of the XY CPM. 92

Figure 4.12 Stage 1 rotation. 93

Figure 4.13 Motion stage rotation. 93

Figure 4.14 Fabricated XY CPM and its experimental setup..... 95

Figure 4.15 Stage rotation measurement..... 96

Figure 4.16 Load-displacement relationship and stiffness in Y-axis..... 98

Figure 4.17 Motion stage rotation and input stage 1 rotation..... 99

Figure 4.18 The first six modal shapes..... 100

Figure 4.19 Out-of-plane stiffness versus applied force F_Z under specific actuation forces 101

Figure 4.20 Three-layer design..... 102

Figure 5.1 Revolute joint with inverted beams: (a) geometry; (b) deformed configuration; (c) FBD of the joint 107

Figure 5.2 Translational joint derived from the revolute joint [65]: (a) geometric composition; (b) deformed configuration..... 108

Figure 5.3 FEA simulation in Comsol: (a) mesh type for the rigid bodies and flexure beams; (b) displacement plot of the revolute joint in Comsol.....110

Figure 5.4 FEA verification of the revolute joint with inverted beam: (a) displacement in X-direction versus the input force F_{in}; (b) displacement in Y-direction versus the input force F_{in}; (c) rotation about Z-axis versus the input force F_{in}. 111

Figure 5.5 Bistable mechanism with increased out-of-plane stiffness: (a) geometry parameters; (b) deformed configuration and the FBD of the shuttle.....112

Figure 5.6 Inflection points simulated in Comsol with one inflection point vanishing during snap-through: (a) bending with two inflection points; (b) the second bistable position with only one inflection point.....113

Figure 5.7 FEA verification of the behavior of the bistable mechanism.....113

Figure 5.8 Experimental setup and the prototype of the revolute joint: (a) Experimental setup; (b) 3D-printed positioning frame, motion stage, rigid link, and base; (c) its deformed configuration. 115

Figure 5.9 Tip force-displacement characteristics under different payload. 116

Figure 5.10 Experimental setup and the prototype of the bistable mechanism: (a) Experimental setup; (b) 3D-printed prototype; (c) Second stable position of the bistable mechanism. 117

Figure 5.11 Force-displacement characteristic of the bistable mechanism. 118

Figure 5.12 Spherical joints: (a) wire beam based spherical joint; (b) general spherical joint using SSTC leaf beams; (c) spherical joint using I-shape leaf beams; (d) spherical joint using folded leaf beams; (e) spherical joint using L-shape leaf beams. A video showcasing the design of the general spherical joint is available on YouTube: https://youtu.be/tWx_8c3q-Qw.....119

Figure 5.13 General spherical joint with GSTC leaf beams: (a) geometry labeling; (b) top view of the coordinate systems..... 120

Figure 5.14 The deformed spherical joints under combined forces and moments (all obtained from FEA): (a) spherical joint with SSTC leaf beams; (b) spherical joint with I-shape leaf beams; (c) spherical joint with L-shape leaf beams; (d) spherical joint with folded leaf beams..... 123

Figure 5.15 (Colour lines) The displacement comparison between the FEA and analytical results for the spherical joint with SSTC leaf beams, subjected to incremental moment along the Y-direction, a constant moment along the X-direction and a constant force in the Z-direction: (a) the resultant displacement X_t ; (b) the resultant displacement Y_t ; (c) the resultant displacement Z_t ; (d) the resultant rotation θ_{xt} ; (e) the resultant rotation θ_{yt} ; (f) the resultant rotation θ_{zt} ; 124

Figure 5.16 (Colour lines) The displacement comparison between the FEA and analytical results for the spherical joint with I-shape leaf beams, subjected to incremental moment along the Y-direction, a constant moment along the X-direction and a constant force in the X-direction: (a) the resultant displacement X_t ; (b) the resultant displacement Y_t ; (c) the resultant displacement Z_t ; (d) the resultant rotation θ_{xt} ; (e) the resultant rotation θ_{yt} ; (f) the resultant rotation θ_{zt} ; 124

Figure 5.17 (Colour lines) The displacement comparison between the FEA and analytical results for the spherical joint with L-shape leaf beams, subjected to incremental moment along the Y-direction, a constant moment along the X-direction and a constant force in the X-direction: (a) the resultant displacement X_t ; (b) the resultant displacement Y_t ; (c) the resultant displacement Z_t ; (d) the resultant rotation θ_{xt} ; (e) the resultant rotation θ_{yt} ;

(f) the resultant rotation θ_{zt} ; 125

Figure 5.18 (Colour lines) The displacement comparison between the FEA and analytical results for the spherical joint with folded leaf beams, subjected to incremental moment along the Y-direction, a constant moment along the X-direction and a constant force in the X-direction: (a) the resultant displacement X_t ; (b) the resultant displacement Y_t ; (c) the resultant displacement Z_t ; (d) the resultant rotation θ_{xt} ; (e) the resultant rotation θ_{yt} ; (f) the resultant rotation θ_{zt} ; 126

Figure 5.19 (Colour lines) The centre drift comparison between the FEA and analytical results for the spherical joint with SSTC leaf beams, subjected to incremental moment along the Y-direction, a constant moment along the X-direction and a constant force in the X-direction: (a) the resultant displacement D_{xc}; (b) the resultant displacement D_{yc}; (c) the resultant displacement D_{zc}; 127

Figure 5.20 (Colour lines) The centre drift comparison between the FEA and analytical results for the spherical joint with I-shape leaf beams, subjected to incremental moment along the Y-direction, a constant moment along the X-direction and a constant force in the X-direction: (a) the resultant displacement D_{xc}; (b) the resultant displacement D_{yc}; (c) the resultant displacement D_{zc}; 127

Figure 5.21 (Colour lines) The centre drift comparison between the FEA and analytical results for the spherical joint with L-shape leaf beams, subjected to incremental moment along the Y-direction, a constant moment along the X-direction and a constant force in the X-direction: (a) the resultant displacement D_{xc}; (b) the resultant displacement D_{yc}; (c) the resultant displacement D_{zc}; 128

Figure 5.22 (Colour lines) The centre drift comparison between the FEA and analytical results for the spherical joint with folded leaf beams, subjected to incremental moment along the Y-direction, a constant moment along the X-direction and a constant force in the X-direction: (a) the resultant displacement $D_{xc,}$ (b) the resultant displacement D_{yc}; (c) the resultant displacement D_{zc}. 128

Figure 5.23 (Colour lines) The influence of geometry parameters γ_0, β_0, and R_0 on the center drift of the spherical joint with SSTC leaf beams under constant motion stage

rotation (θ_{xt} = 0.2 rad, θ_{yt} = 0.3 rad and θ_{zt} = 0.5 rad): (a), (b), and (c) illustrate the incremental changes in γ_0 and β_0 with a constant R_0 value of 50 mm; (d), (e), and (f) showcase the incremental changes in γ_0 and R_0 with a constant β_0 value of π/4;..... 129

Figure 5.24 (Colour lines) The influence of geometry parameters γ_0, β_0, and R_0 on the center drift of the spherical joint with I-shape leaf beams under constant motion stage rotation (θ_{xt} = 0.2 rad, θ_{yt} = 0.3 rad and θ_{zt} = 0.5 rad): (a), (b), and (c) illustrate the incremental changes in γ_0 and β_0 with a constant R_0 value of 50 mm; (d), (e), and (f) showcase the incremental changes in γ_0 and R_0 with a constant β_0 value of π/4;..... 130

Figure 5.25 (Colour lines) The influence of geometry parameters γ_0, β_0, and R_0 on the center drift of the spherical joint with folded leaf beams under constant motion stage rotation (θ_{xt} = 0.2 rad, θ_{yt} = 0.3 rad and θ_{zt} = 0.5 rad): (a), (b), and (c) illustrate the incremental changes in γ_0 and β_0 with a constant R_0 value of 50 mm; (d), (e), and (f) showcase the incremental changes in γ_0 and R_0 with a constant β_0 value of π/4;..... 131

Figure 5.26 (Colour lines) The influence of geometry parameters γ_0, β_0, and R_0 on the center drift of the spherical joint with L-shape leaf beams under constant motion stage rotation (θ_{xt} = 0.2 rad, θ_{yt} = 0.3 rad and θ_{zt} = 0.5 rad): (a), (b), and (c) illustrate the incremental changes in γ_0 and β_0 with a constant R_0 value of 50 mm; (d), (e), and (f) showcase the incremental changes in γ_0 and R_0 with a constant β_0 value of π/4;..... 132

Figure 5.27 Experimental setup: (a) the spherical joint with L-shape leaf beams (pin tip is the remote centre P joint); (b) testing rig; (c) an overview of the experimental platform. 133

Figure 5.28 (Colour lines) Comparison of experimental, FEA, and analytical results: (a) force-displacement relationship of the motion stage; (b) centre drift analysis by comparing analytical and FEA results; (c) centre drift analysis by comparing analytical and experimental results. 136

Figure 5.29 Demonstration of the spherical joint (with L-shape leaf beams) in the application of minimally invasive surgery: (a) the configuration as fabricated; (b) rotation about one direction; (c) rotation about another direction. 137

Figure 5.30 Other fabricated prototypes: (a) the spherical joint with SSTC leaf beams; (b)

the spherical joint with L-shape leaf beams; (c) the spherical joint with folded leaf beams. 137

LIST OF TABLES

Table 2.1 Geometric parameters of the five configurations for the GLBM 28

Table 2.2 Geometry parameters of four representative configurations derived from the GSTC leaf beam 41

Table 3.1 Parameters for all the cases in this Section..... 60

Table 4.1 Displacements of each DPF unit..... 86

Table 4.2 Performance expressions of the XY CPM..... 88

Table 4.3 Geometry parameters..... 89

Table 4.4 First six resonant modes 100

Table 4.5 Performance characteristics compared with existing design (ANA= Analytical results; Exp = Experimental results; the comprehensive analysis for the proposed design 2 can be accessed in [233])..... 102

Table 5.1 The geometric parameters of the revolute joint..... 108

Table 5.2 The geometry parameters of the bistable mechanism.....111

Table 5.3 The geometric parameters of the fabricated revolute joint prototype.....114

Table 5.4 The geometry parameters of the fabricated bistable mechanism.....116

Table 5.5 Maximum centre drift comparison (γ_0 ranging from 0 to 2π and R_0 equals to 50 mm)..... 132

Table 5.6 The geometry parameters of the spherical joint with L-shape leaf beams ... 134

NOMENCLATURE

D_{T2}	Translation matrix for the free ends of GSTC leaf beams 2
D_{T1}	Translation matrix for the free ends of GSTC leaf beams 1
D_{T3}	Translation matrix for the free ends of GSTC leaf beams 3
F_i	Tip force on the flexure beam in the Y-direction
L_i	The length of i^{th} flexure beam
L_{i+1}	The length of $i+1^{th}$ flexure beam
M_i	Tip force on the flexure beam about Z-direction
P_i	Tip force on the flexure beam in the X-direction
R_{si}	The rotation matrix of the GSTC beam
R_t	The rotation matrix of the spherical joint
R_{ZT}	The 6×6 rotation matrix about the Z_T axis for the spherical joint
R_{XT}	The 6×6 rotation matrix about the X_T axis for the spherical joint
R_{YT}	The 6×6 rotation matrix about the Y_T axis for the spherical joint
R_{XS}	The 6×6 rotation matrix about the Xs axis GSTC leaf beam
R_{XC1}	The 6×6 rotation matrix of the GSTC leaf beam 2
R_{XC2}	The 6×6 rotation matrix of the GSTC leaf beam 3
X_i	Tip displacement on the flexure beam in the Y-direction
Y_i	Tip displacement on the flexure beam in the X-direction
θ_i	Tip rotation on the flexure beam along Z-direction
γ_i	The $(i+1)/2^{th}$ angle between i^{th} flexure beam and $i+1^{th}$ flexure beam
α_i	The $(i+1)/2^{th}$ angle of the i^{th} flexure beam with the X-axis
β_i	The $(i+1)/2^{th}$ angle of the $i+1^{th}$ flexure beam with the X-axis
F_{si}	Tip force on the general lumped-compliance beam in the Y-direction

P_{si}	Tip force on the general lumped-compliance beam in the X-direction
M_{si}	Tip moment on the general lumped-compliance beam about the Z-direction
Y_{si}	Tip displacement on the general lumped-compliance beam in the X-direction
X_{si}	Tip displacement on the general lumped-compliance beam in the Y-direction
θ_{si}	Tip rotation on the general lumped-compliance beam along Z-direction
I	Moment of inertia of the flexure beam
E	Elastic modulus of the flexure beam
F_X	Force applied in the X-direction
F_Y	Force applied in the Y-direction
y_γ	The normalised displacement in Y-direction of the γ^{th} DPF
x_γ	The normalised displacement in X-direction of the γ^{th} DPF
θ_γ	The normalised displacement along Z-direction of the γ^{th} DPF
f_x	The normalised input force in X-direction
f_y	The normalised input force in Y-direction
H_γ	Input force of the DPF in X-direction
M_γ	Input moment of the DPF along Z-direction
V_γ	Input force of the DPF in Y-direction
h_γ	The normalised input force of the DPF in X-direction
v_γ	The normalised input force of the DPF in Y-direction
m_γ	The normalised input moment of the DPF along Z-direction
x_s	The displacement of the motion stage in X-direction
y_s	The displacement of the motion stage in Y-direction
θ_s	The displacement of the motion stage along Z-direction

ABBREVIATIONS

BCM	Beam Constraint Model
CPM	Compliant Parallel Manipulator
DPF	Double Parallel Flexure
DoF	Degree of Freedom
DoC	Degree of Constraint
EIS	Elliptic Integral Solution
FBD	Free Body Diagram
FEA	Finite Element Analysis
GLBM	General Lumped-Compliance Beam Model
GSTC	General Single-Translation Constraint
MEMS	Micro-Electro-Mechanical Systems
OCARCM	Over-Constraint Based Nearly-Constant Amplification Ratio Compliant Mechanism
PLA	Polylactic Acid
PRBM	Pseudo-Rigid-Body Model
SBCM	Spatial Beam Constraint Model
SSTC	Single-Translation Constraint

CHAPTER 1

INTRODUCTION

1.1 Compliant mechanisms

The concept of compliant mechanisms is deeply rooted in human history, with early examples appearing in rudimentary machines and tools. These ancient tools demonstrated early insights into elasticity and flexibility, qualities that have informed the development of compliant mechanisms over millennia.

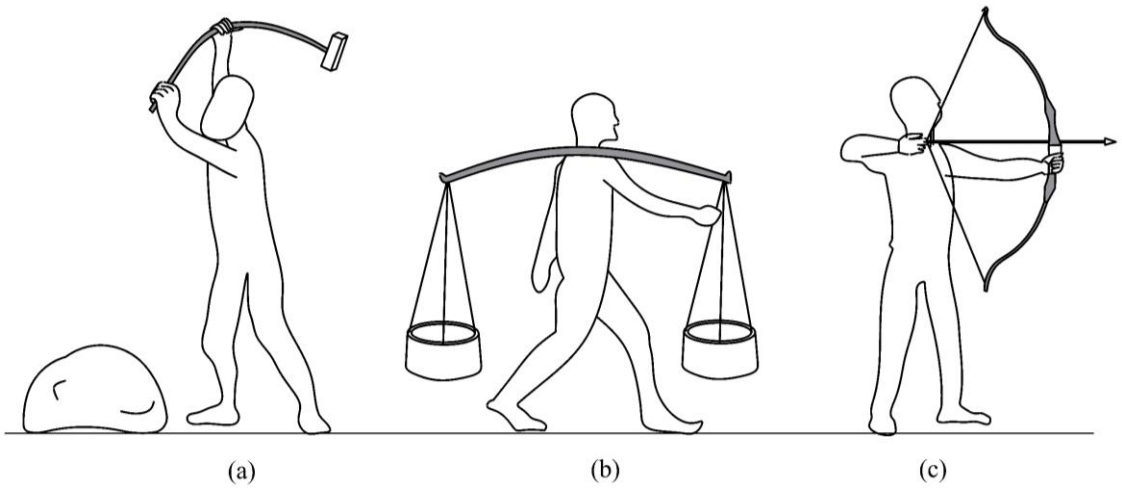


Figure 1.1 Compliant mechanisms in early human history: (a) the flexible hammer handle; (b) carrying pole; (c) bow.

In ancient times, the flexible hammer handle (Figure 1.1 (a)), used to absorb impact forces, minimized vibrations transmitted to the user's hand and arm, showcasing early insights into vibration damping through compliance. Similarly, the carrying pole (Figure 1.1(b)), widely used across many cultures, demonstrated an innate understanding of load distribution and stress relief. The elasticity of the pole allowed it to flex underweight, reducing the strain on the carrier and effectively dispersing forces across the pole's length.

Another example, the bow (Figure 1.1(c)) served as one of the most iconic compliant mechanisms, leveraging elastic deformation to store potential energy and release it in a controlled manner when needed. The bow's flexibility allowed it to convert stored energy into kinetic energy, providing the basis for early projectile weaponry.

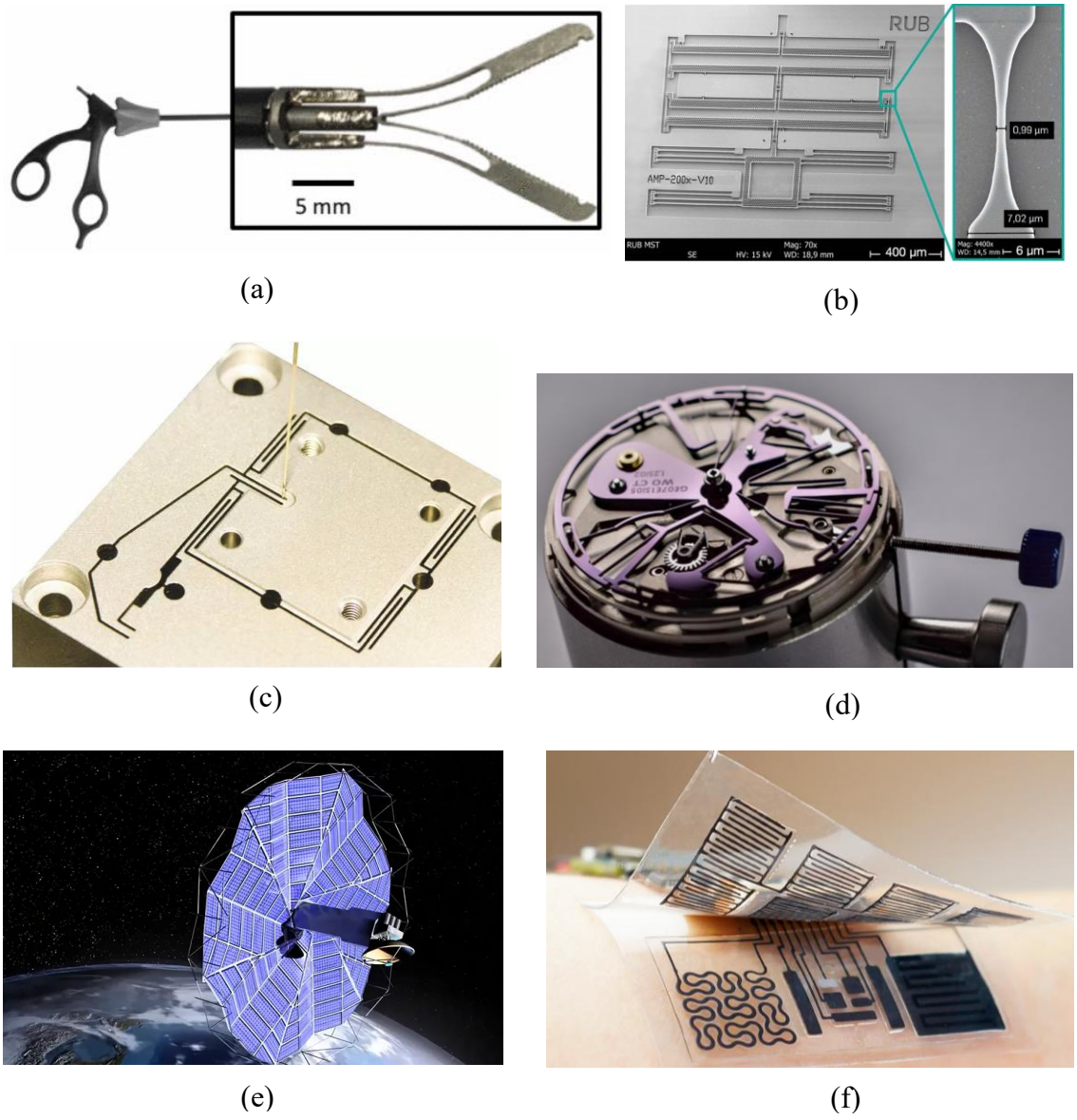


Figure 1.2 Examples of compliant mechanisms used in modern engineering: (a) surgical grasper [1]; (b) complaint mechanical amplifier in MEMS application [2]; (c) nano-positioning stage [3]; (d) horological industry [4]; (e) aerospace application [5]; (f) energy harvesting device[6].

In modern engineering, compliant mechanisms, have emerged as a promising solution for precision engineering applications due to their advantages, such as no backlash, smooth

motion, wear-free operation, and compactness [7-9]. These mechanisms are widely utilized in fields requiring high precision, such as medical devices [10-12, 1], MEMS (Micro-Electro-Mechanical Systems) [2, 10], micro- and nano-positioning systems [13-15, 3], watch-making [16, 17, 4], aerospace [18, 5] and energy harvesting devices [19, 6, 20]. In medical devices, for instance, compliant surgical graspers (Figure 1.2(a)) provide precision and gentle tissue handling through flexure-based actuation, enhancing control during minimally invasive surgeries. Compliant mechanisms in MEMS are widely used in micro-grippers for handling delicate objects, actuators for motion control, and sensors (Figure 1.2(b)) for force and displacement measurement. Their compact size, lightweight structure, and wear-free operation make them indispensable for achieving the high reliability and precision demanded by modern microdevices. Nano-positioning systems, as shown in Figure 1.2(c), employ compliant mechanisms to achieve precise movement control in microscopy and semiconductor fabrication, benefiting from their smooth, backlash-free motion. In horological industry, as depicted in Figure 1.2(d) flexure-based mechanisms replace traditional pivots to provide improved durability, compactness, and accuracy, enabling the design of high-performance, intricately crafted timepieces. Compliant mechanisms play a vital role in aerospace applications, including deployable structures (Figure 1.2(e)), vibration isolation, precision positioning systems, and morphing surfaces. Their monolithic design eliminates joints and fasteners, reducing stress concentrations, wear, and fatigue. This enhances reliability, minimizes failure points, and ensures durability in extreme environments like space, where traditional mechanisms may degrade due to thermal expansion, lubricant breakdown, or outgassing. In energy harvesting, they enable efficient conversion of mechanical vibrations, wind, or other ambient energy sources into electrical energy, with applications in self-powered sensors and wearable devices (Figure 1.2(f)), benefiting from their compactness and adaptability.

1.2 The basic building block of compliant mechanisms

1.2.1 Basic types of flexure beams

The basic building blocks of compliant mechanisms exhibit a wide variety of forms, each

tailored to specific engineering applications. Over recent years, advancements in design and material science have led to the development of more diverse types of flexure elements to meet the growing demands of precision engineering. These flexure elements form the foundation of compliant mechanisms, providing the desired flexibility and constraints for controlled motion.

A flexure beam is a slender structural element, characterized by a linear or curved geometry, typically designed with either a rectangular or custom cross-section to balance stiffness and flexibility along specific axes. Figure 1.3 illustrates key types of flexure beams widely employed in modern compliant mechanism designs, including wire beams, leaf beams, and curved beams. Their ability to control motion and compliance stems from the careful geometric configuration and strategic distribution of deformation, enabling precise mobility.

Wire beams are among the simplest and most versatile flexure elements, typically having one degree of freedom along its axial direction. Variations in cross-sectional geometry, such as cylindrical wire beams (Figure 1.3(a)) [21, 22] and rectangular wire beams (Figure 1.3(b)) [23, 24], enable engineers to customize mechanical properties. Cylindrical wire beams provide uniform stiffness in all transverse directions, making them ideal for isotropic load distribution, while rectangular wire beams offer anisotropic stiffness, allowing tailored compliance in specific directions to meet the demands of more specialized applications.

Leaf-type flexure beams (from Figure 1.3(c) to Figure 1.3(e)), which are flat and typically rectangular in cross-section, offer compliance primarily in one bending direction [25, 7]. Advanced designs, such as folded beams (Figure 1.3(d)) [26, 27] and tapered beams (Figure 1.3(e)) [28, 29], enhance performance by precisely controlling stiffness distribution. Folded beams, with their zigzag or serpentine geometries, mitigate axial stiffening effects and increase rotational stiffness along the axial direction, enabling compact designs with extended motion ranges. Tapered leaf beams, featuring gradually decreasing thickness or width, optimize stress distribution, reducing peak stresses and enhancing fatigue life. These design innovations allow leaf beams to perform effectively in high-precision, dynamic environments while maintaining robustness.

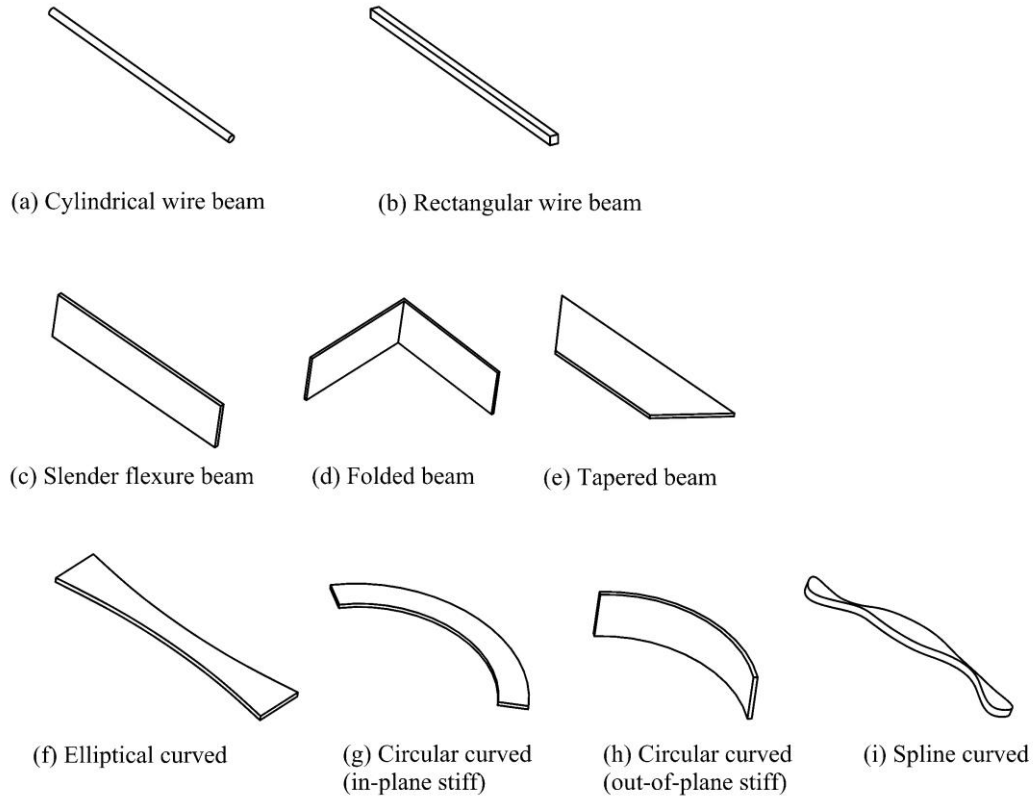


Figure 1.3 Different forms of flexure beam: (a) cylindrical wire beam [21, 22]; (b) rectangular wire beam [23, 24]; (c) slender flexure beam [25, 7]; (d) folded beam [26, 27]; (e) tapered beam [28, 29]; (f) elliptical curved [30-32]; (g) circular curved (in-plane stiff) [33-35]; (h) circular curved (out-of-plane stiff) [36, 37]; (i) spline curved [38].

Curved flexure beams (from Figure 1.3(f) to Figure 1.3(i)), including elliptical-curved [30-32], circular-curved [33-37], and spline-curved designs [38], introduce geometric advantages by leveraging their initial curvature to achieve tailored force-displacement characteristics. For example, the circular-curved beams efficiently store and release energy, enabling applications requiring elastic energy storage and bistable states. The pre-curved geometry helps minimize stress concentrations by distributing strain more evenly, preventing localized stress build-up that typically occurs in straight beams undergoing bending. This enhances stability during large deformations, improves fatigue resistance, and provides a smoother force-displacement response.

1.2.2 Basic types of flexure hinges

A flexure hinge enables relative rotational motion between two adjacent rigid members by utilizing the elastic bending of a flexible segment, typically about one or more specific

axes, while preserving high stiffness in other directions. The absence of moving parts results in seamless rotational or translational motion with extremely high repeatability and reliability. The range of motion, stiffness, and stress concentration at the hinge are determined by the geometry and material properties of the hinge.

Rectangular flexure hinges (Figure 1.4(a)) [39, 40], for instance, provide straightforward fabrication and predictable deformation but are limited in fatigue life due to stress concentrations. Elliptical flexure hinges (Figure 1.4(c)) [41, 42], on the other hand, enhance mobility by distributing stress more evenly, allowing greater angular deflection and improved durability under cyclic loads. Corner-filleted designs (Figure 1.4(b)) [43-45] further refine performance by alleviating stress concentrations and increasing fatigue resistance and range of motion. For advanced applications, topology-optimized flexure hinges (Figure 1.4(h)) [46, 47] balance stiffness and compliance through computationally enhanced designs, achieving superior performance in weight-sensitive and space-constrained systems [48]. This variety of hinge designs enables tailored solutions for specific applications, from compact instruments to large-scale precision mechanisms, ensuring smooth, controlled, and precise mobility across diverse engineering domains.

Flexure hinges continue to be an area of active research and development, with innovations focusing on enhancing their load-bearing capacity, reducing stress concentrations, and increasing their range of motion. Advanced manufacturing techniques, such as additive manufacturing, have opened new possibilities for creating complex flexure hinge geometries such as the spiral flexure hinge [49, 50] and topology-optimized flexure hinge [46, 47]. Additionally, the integration of flexure hinges with smart materials, such as shape-memory alloys or piezoelectric actuators, is paving the way for next-generation compliant mechanisms with adaptive or programmable behavior. Asymmetric flexure hinges, exemplified in Figure 1.4 (m) to 1.4(o), represent a significant category in compliant mechanism design. Notably, asymmetric corner-filleted hinges have been identified for their ability to minimize the stress-deflection ratio while enhancing rotational precision [51]. In comparison, single-notch flexure hinges are advantageous in applications requiring high sensitivity and compact structures [52, 53]. Comparative analyses indicate that hybrid flexure hinges, which integrate hyperbolic and elliptical

profiles, offer a balanced performance in terms of compliance, rotational accuracy, and stress distribution [54]. Additionally, crease-type hinges (Figures 1.4(p)) facilitate the rotation of adjacent panels about the crease, with the groove side forming an edge [55]. Unlike conventional joints, these equivalent joints exhibit variable stiffness, adapting to specific application requirements.

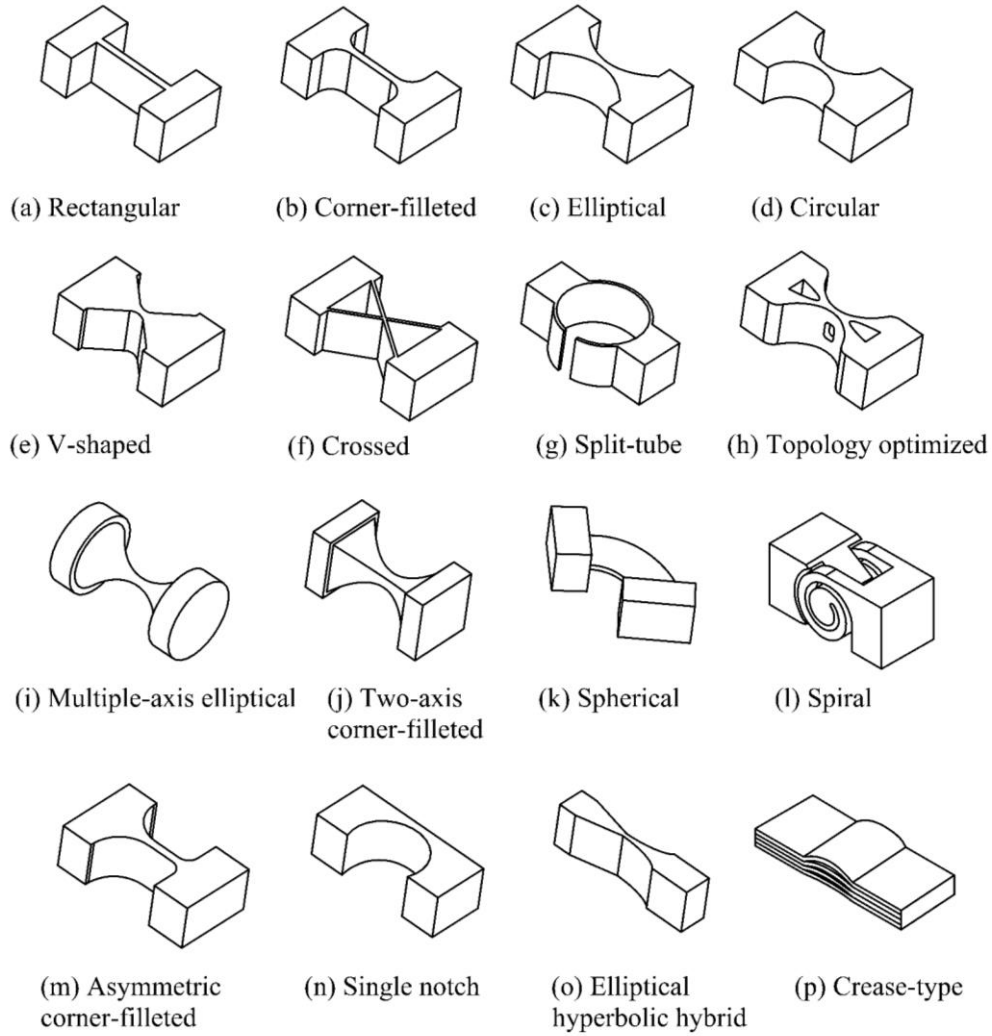


Figure 1.4 Types of basic flexure hinge: (a) rectangular [39, 40]; (b) corner-filleted [43-45]; (c) elliptical [41, 42]; (d) circular [56, 57]; (e) V-shaped [58, 59]; (f) crossed [60, 61]; (g) split-tube [62, 63]; (h) topology optimized [46]; (i) multiple-axis elliptical [64, 65]; (j) two-axis corner-filleted [66, 67]; (k) spherical [68, 33]; (l) spiral [49, 50]; (m) asymmetric corner-filleted [51]; (n) single notch [52, 53]; (o) elliptical hyperbolic hybrid [54]; (p) crease-type [55].

Choosing the appropriate flexure hinge is crucial for balancing flexibility, stiffness, and durability in compliant mechanisms. Stress distribution and fatigue resistance play a key role; while rectangular hinges are easy to fabricate, they concentrate stress and have

limited fatigue life. Elliptical and corner-filleted hinges offer better stress distribution, enhancing durability and motion range. For load-bearing capacity and precision, V-shaped and crossed flexure hinges provide high stiffness and accuracy, while topology-optimized and asymmetric designs optimize compliance and space efficiency. Range of motion is another factor—spiral and spherical hinges allow large angular deflections, while single-notch and hybrid designs balance flexibility and stress control. Manufacturing methods influence hinge selection. Traditional machining suits simple designs, whereas additive manufacturing enables complex, optimized geometries. Smart materials, like shape-memory alloys and piezoelectrics, allow adaptive behavior in advanced applications.

1.3 The nonlinear modelling technics

This section focuses on the introduction of the slender flexure beam, a critical component of our research. It highlights the beam's unique characteristics, including its mobility and nonlinear behavior, which are central to compliant mechanism design. Additionally, this section reviews existing nonlinear modeling techniques, encompassing both 2D and 3D approaches.

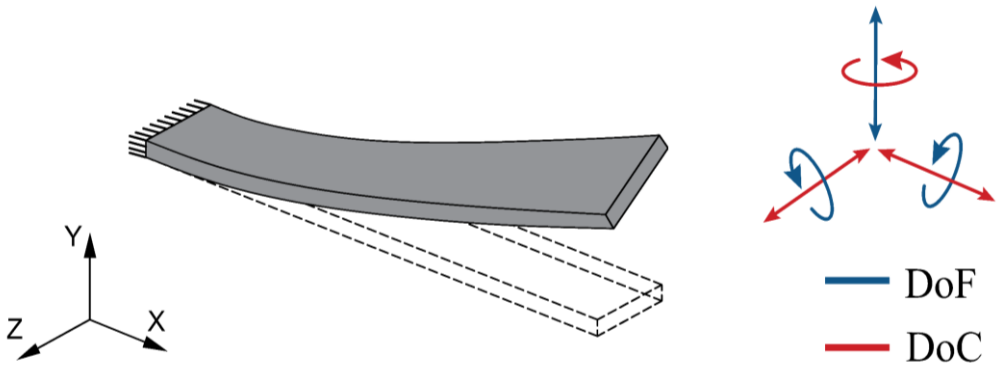


Figure 1.5 The DoF and DoC of a slender flexure beam with one end fixed.

1.3.1 The nonlinear deflection of a flexure beam

Flexure beams, which are compliant structural elements, serve as the foundational

building blocks of compliant mechanisms. These beams are typically characterized by their Degrees of Freedom (DoF) − the independent directions in which they can move or rotate and Degrees of Constraint (DoC) − the directions in which they are restricted. Unlike the rigid mechanisms, the direction of DoC is well constrained, the compliant mechanism however is not perfectly constrained in the DoC direction.

Figure 1.5 shows a slender flexure beam with one end fixed, which typically has 3 DoF and 3 DoC which are indicated by the green arrow and the red arrow, respectively. The small motion along the DoC direction is also always treated as parasitic motion (refer to some dependent motions that accompany with other independent motions) which is commonly not desired. However, it is not always a drawback. In [69], the authors introduce the parasitic motion principle-based piezoelectric actuators, which extend the motion displacement and improve the motion stability. Parasitic motion can also enhance precision positioning by enabling small, secondary adjustments in unintended directions. This is particularly valuable in applications requiring sub-micron accuracy, where controlled parasitic motions can correct misalignments or improve fine-tuning.

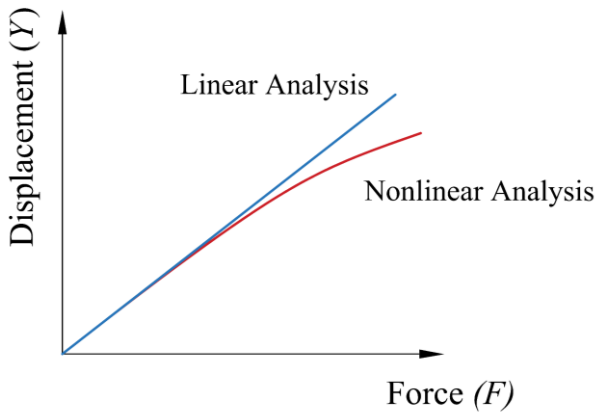


Figure 1.6 Linear and nonlinear analyses of beam deflection

The force-displacement relationship of flexure beams further demonstrates their complexity, as shown in Figure 1.6, which compares linear and nonlinear analyses of beam deflection. The nonlinear force-displacement curve illustrates deviations from linear predictions, highlighting the importance of accounting for nonlinearities in practical applications. These nonlinearities arise from three primary sources: material

constitutive properties, geometric compatibility, and force equilibrium [70-72]. Material constitutive properties introduce nonlinearity when materials surpass their elastic limits, leading to plastic deformation or nonlinear elasticity in polymers and rubber. Geometric compatibility adds complexity as large deflections alter the relationship between deformed and undeformed beam shapes, introducing nonlinear constraints that affect stiffness and displacements. Finally, force equilibrium conditions, such as load stiffening and elastokinematic effects, further complicate the beam's response. Axial forces generated during bending increase effective stiffness, while coupling between bending and axial stretching produces deflection-dependent stiffness variations. These nonlinear behaviors are crucial to understanding and optimizing the performance of compliant mechanisms in applications requiring both flexibility and precision.

To explore this evolving field in depth, the subsequent sections provide a detailed examination of state-of-the-art techniques for nonlinear modeling. These discussions will cover both 2D and 3D modeling approaches, illustrating how parameterized and advanced analytical frameworks can address critical challenges in design and optimization. By delving into the latest developments, this thesis aims to bridge the gap between theoretical modeling and practical applications, paving the way for more robust and versatile compliant mechanism designs.

1.3.2 The state-of-the-art in 2D nonlinear modelling

Selecting an appropriate nonlinear modeling method for compliant mechanisms depends on several key criteria, including computational efficiency, accuracy, applicability to different deformation ranges, and ease of implementation. 2D nonlinear modelling has become integral in analyzing compliant mechanisms, given its potential to balance analytical precision with computational efficiency. The FEA method is a popular and effective numerical approach for analyzing the kinetostatics and dynamics of compliant mechanisms, thanks to its ability to handle complex geometries and boundary conditions. However, it has inherent drawbacks. While users can refine models, accuracy is not always guaranteed. Discretization errors, arising from an insufficiently refined mesh, can lead to inaccurate deformation predictions. Stress singularities, which occur at sharp

edges or concentrated loads, may cause instability in numerical solutions. These issues become particularly problematic under compressive forces, where flexure beams are prone to buckling and large nonlinear deformations. As a result, FEA solvers may fail to converge on a stable solution, leading to unreliable or unrealistic shape predictions. The accuracy of FEA depends on factors such as mesh resolution, element type, and degrees of freedom, requiring careful consideration to ensure reliable results [73].

Apart from the FEA method, a considerable number of modeling methods have been developed for kinetostatic or dynamic modeling of compliant mechanisms. These methods include the PRBM, BCM [20], smooth curvature model (SCM) [74, 75], elliptic integral solution (EIS) and their derivatives like chained-BCM (CBCM) [37, 76], Timoshenko-BCM (TBCM) [77], dynamic BCM (DBCM) [78] the integral method based BCM (IMBCM) [79, 80], spatial-BCM (SBCM) [81, 82], chained-PRBM (CPRBM) [83-85], PRBM-based dynamic model [86], comprehensive-EIS (CEIS) [87], multiple-SCM (MSCM) [88].

The PRBM generally serves as an effective modeling method in the early-stage design of compliant mechanisms, where the nonlinear deflection of a flexure beam is approximated as a series of torsional springs or linear springs connected by rigid mechanisms [89, 90]. As a result of the limited degree of freedom, the 1R-PRBM has load dependent effect degrading the accuracy of the model. To improve the accuracy of 1R-PRBM, the 2R-PRBM [84], 3R-PRBM [85, 91], 5R-PRBM [92], and CPRBM [93, 94] were proposed. However, a higher amount of discretization of the PRBM model inevitably leads to higher dimensional mathematical models, which causes longer computational time. They are not capable of capturing the elasto-kinematic effect and large errors in response to arbitrary loads, which is another significant hinder in the application of compliant mechanism synthesize.

The BCM is based on the Euler-Bernoulli beam model and considers geometric nonlinearity and load-dependent effect associated with linearized beam curvature assumptions. It is simple, parametric, closed-form, and accurately predicts the behavior of flexure beams with intermediate deflections [95]. As aforementioned, BCM has been extended for different modeling scenarios of nonlinear deflections, including the SBCM

[96, 97], CBCM [37], IMBCM [79, 80], TBCM [77], dynamic BCM (DBCM) [78] and BCM with semi-rigid element [98]. The SBCM is capable of capturing the spatial motion of a wire beam. The CBCM discretizes a flexure beam into multiple segments to extend the range of the allowable axial load and the deflection. The CBCM with only two BCM elements, commonly known as Bi-BCM, is widely preferred and adopted due to its balance between accuracy and simplicity [99, 100]. The IMBCM is proposed to model nonlinear fillet leaf springs. The TBCM incorporates the sheer effect which can model stubby beams. The DBCM enables nonlinear kinetostatics and large-amplitude vibration analysis of compliant mechanisms with intermediate deformation. It incorporates P-Δ effects, uses a matrix-based method for efficient analysis, and avoids complex inner force and kinematics calculations. The BCM with a semi-rigid element is a method based on BCM to investigate the nonlinear static load-displacement relationships of beam-based flexure modules containing an intermediate semi-rigid element. An intermediate stiffening element is commonly treated as a perfect rigid element. The BCM with a semi-rigid element removes this untrue assumption, which is more accurate. The BCM modeling method is a versatile and easy-to-use tool that can be integrated into various modeling scenarios.

A classic method for solving large deflections (more than 0.15 of the beam's length [101]) of a compliant mechanism is the EIS, which is an exact solution to the Euler- Bernoulli beam equation. However, it is limited to the range of slope angles and has no inflection point [102, 101, 103]. To overcome the limitations of no inflection point, an EIS for a large beam deflection with an inflection point subject to arbitrary loading conditions was derived in [104]. In [87], a CEIS with multiple inflection points and subject to arbitrary loading was proposed. To eliminate the limitation of the range of slope angles, an alternative method was introduced in [101]. The original EIS has been improved in terms of the inflection point, end loads, and slope angles. However, it is not a preferred technique for intermediate displacement ranges due to its rather complex derivation and implementation. For instance, the derivation process may be sensitive to initial guesses of unknown parameters if the end slope and load parameters are not provided [105].

As opposed to many other modeling techniques that involve numerical integration or

discretization, the SCM [74] assumes that the curvature of a beam in bending is smooth and can therefore be approximated by low-order polynomials (e.g., Legendre polynomials). This approach enables the extraction of kinematic Jacobians and Hessians, as well as generalized stiffness matrices, which can be used to predict the deformation or stiffness of structures with multiple links. Additionally, it is capable of predicting the first several buckling modes, making it an attractive method for designing graspers. [106-108]. However, synthesizing more complex mechanisms using the smooth curvature mode has not been thoroughly studied.

Given these considerations, this thesis adopts the Beam Constraint Model (BCM) due to its balance between computational efficiency and accuracy. BCM, based on the Euler-Bernoulli beam theory, effectively captures geometric nonlinearities and load-dependent effects while maintaining a parametric, closed-form solution. It provides reliable predictions for intermediate deflections without requiring excessive discretization, making it well-suited for rapid nonlinear modeling and optimization of compliant mechanisms.

1.3.3 The state-of-the-art in 3D nonlinear modeling

Several spatial modeling techniques have emerged from 2D methodologies, including the BCM [109, 110], the pseudo-rigid-body model (PRBM) [90, 111, 85, 84], and the chained algorithm [112, 94, 113]. In particular, Sen et al. [97] introduced a Spatial Beam Constraint Model (SBCM) based on the planar BCM, which meticulously characterizes stiffness and error motions through nonlinear load-displacement relations, based on principles of virtual work. This method accurately represents nonlinear force-displacement characteristics within an intermediate translational and angular displacement range of 0.1 L and 0.1 rad, respectively. To enhance the versatility of the SBCM, this study extends its applicability to account for angular misalignments and variable cross-sections in spatial bisymmetric beams [81]. However, it's important to note that these models are exclusively applicable to beams with bisymmetric cross-sections, such as square and circular cross-sections, assuming identical moments of area for the cross-sections.

Several 3D-PRBMs have been developed based on the planar PRBM. In [114], this model provides deflection limits dependent on the beam's aspect ratio and has the potential to aid in designing spatial compliant mechanisms and analyzing planar mechanisms with large out-of-plane motions. Reference [115] introduces a chain algorithm element constructed from pseudo-rigid-body segments, enabling accurate prediction of the force-deflection relationship for beams undergoing large 3-D deflections, specifically lateral torsional buckling. However, both aforementioned models are only able to model the beam subject to end-force loads and yield relatively large errors for arbitrary loads. Reference [116] presents an enhanced version of the 3D PRBM, specifically tailored for straight cantilever beams with rectangular cross-sections and spatial motion under arbitrary loads. Nonetheless, this model is predicated on the assumption of no moment at the free end, imposing certain limitations, particularly in structures subjected to complex loading conditions.

Nijenhuis et al. [117] introduced an analytical model using a discretized version of a finite strain spatial flexure strip formulation to derive parametric expressions describing deformation and stiffness properties. However, this model is not a closed-form solution, making interpretation challenging. To address this limitation, Nijenhuis et al. [118] proposed an alternative approach that provides closed-form expressions in a mixed stiffness and compliance matrix format tailored for flexure mechanism analysis. This approach accurately considers bending, shear, elongation, torsion, and warping deformation. Nonetheless, the model neglects load-stiffening behavior along the width direction due to axial force, leading to significant errors in strips subjected to large axial forces [118, 119].

Based on the BCM, Bai et al. [120] initially introduced load-displacement relations as a parameterized tool for comprehending constraint behavior and designing compliant mechanisms with nonlinear kinetostatic behaviors, focusing primarily on rectangular cross-section beams. However, this model's applicability is limited to beams with small width-to-thickness ratios. In response, Bai et al. [119] subsequently devised a method to establish closed-form load-displacement relations tailored for strip flexures experiencing spatial deflections within an intermediate range. This resulting relation provides a

parameterized framework for comprehending constraint behavior and crafting compliant mechanism designs with nonlinear kinetostatic behaviors. To simplify this complex modeling task, Bai et al. proposed an energy-based approach that treats the compliant mechanism as a whole entity, eliminating the need to analyze load equilibriums between adjacent elements [121]. However, the theorem requires the calculation of partial derivatives of the strain energy concerning applied loads, which can be cumbersome and computationally expensive, especially for complex systems. Hao et al. [122] introduced a nonlinear spatial model utilizing the BCM under intermediate deflection and plane cross-section assumptions. These models are applicable only within the scope of intermediate deflections, typically when all normalized displacements are less than 0.1 and for structures with large slenderness ratios (usually length-to-diameter ratios exceeding 10 for slender beams, disregarding shear deformation).

1.4 The design methodology of compliant mechanisms

The synthesis methods for compliant mechanisms have significantly evolved over the years, offering diverse approaches to address varying design challenges. These methods are broadly classified into topology optimization, kinematics-based approaches, and building-block based methods. Each approach leverages unique principles and techniques to meet specific design objectives, whether for high-precision applications, compact configurations, or innovative functionalities.

One of the most prominent methods for compliant mechanism synthesis is topology optimization. This approach determines the optimal material distribution within a predefined design domain to minimize a cost function while satisfying constraints. Topology optimization has emerged as a robust tool for designing complex compliant systems due to its ability to consider intricate multi-objective requirements, such as stiffness and precision. Topology optimization methods are classified into discrete and continuum approaches [123, 124]. Discrete topology optimization [125-127], such as the ground structure approach, uses link or beam elements to discretize the design domain, enabling simultaneous consideration of flexibility and stiffness. The continuum topology optimization approach [124, 128-130], which utilizes continuum elements such as bilinear quadrilateral elements, has gained significant traction in recent years. Advanced

methods like evolutionary structural optimization [131, 132] and the level set method [133, 134] further enhance the capability of topology optimization to produce optimal designs with minimal assumptions. Despite its advantages, topology optimization can be computationally intensive and time-consuming, making it most suitable for high-complexity problems such as path-generating mechanisms or shape-morphing designs.

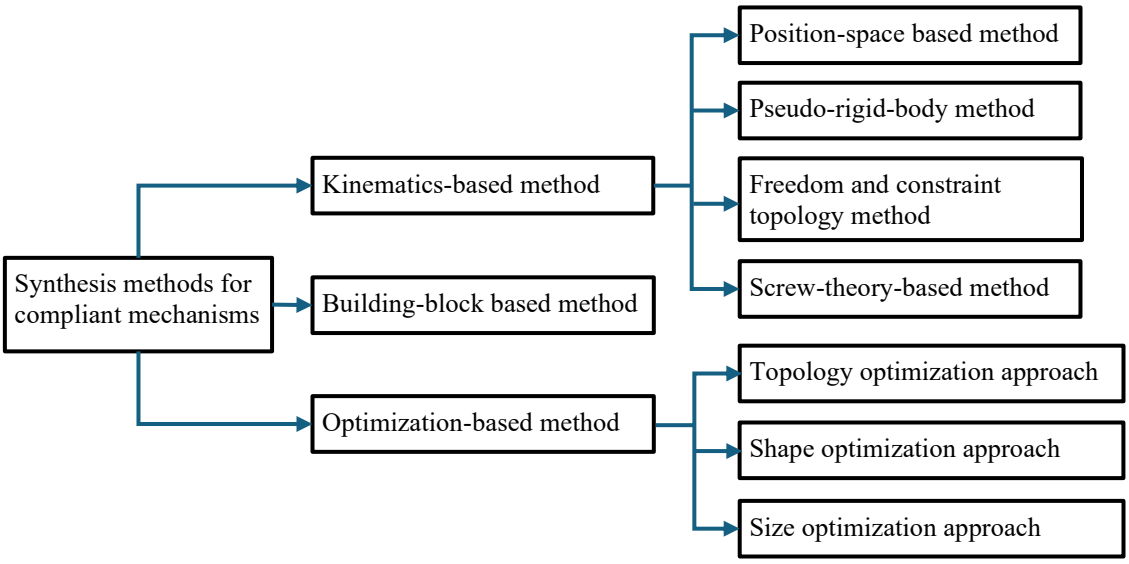


Figure 1.7 Summary of the methods for the design of compliant mechanisms

The kinematics-based approach draws heavily from the principles of rigid-body mechanism design, adapting them for compliant mechanisms. Among its most notable methods is the pseudo-rigid-body model (PRBM) [90, 135-138], which simplifies compliant systems by representing flexible elements with equivalent rigid-body components, such as torsional springs, pin joints, and rigid links. PRBM excels in designing compliant joints, chains, and lumped mechanisms where large deformations are required. However, its reliance on iterative design to ensure adequate constraints in series-connected mechanisms can be a limitation. Another kinematics-based method, freedom and constraint topology (FACT) [139, 140], applies screw theory to synthesize compliant mechanisms with well-defined constraints. FACT enables the visualization of constraints in three dimensions, making it ideal for designing complex 3D systems, such as metamaterials. However, FACT often requires complementary dimensional synthesis or optimization to complete the design process. The position-space-based method [141-143], a relatively new approach, focuses on the spatial configuration of compliant

modules within a system. It allows designers to optimize configurations for objectives such as compactness or reduced parasitic motion by considering the relative positions of compliant modules rather than treating them in isolation. The screw-theory-based method [144-146] is a sophisticated and mathematically rigorous approach to the design of compliant mechanisms. Rooted in screw theory, this method extends the principles originally developed for rigid-body mechanisms to the realm of compliant mechanism design. Screw theory provides a unified framework to describe both motions and constraints in terms of screw coordinates, offering a precise representation of the relationships between forces, moments, and displacements in 3D space. When applied to compliant mechanisms, this method enables designers to systematically analyze and synthesize configurations that satisfy specific motion and constraint requirements.

The building-block based method [147-151] emphasizes the construction of compliant mechanisms from predefined building blocks, offering scalability and adaptability. These building blocks, such as flexural pivots, beams, or trusses, are designed to perform specific motions or force-deflection responses. The design process begins with identifying the required motion or force transmission and then assembling the blocks in a systematic manner to achieve the desired functionality. Analytical models, FEA, or pre-defined databases are used to characterize the mechanical behavior of each block, ensuring precision and predictability in the overall design.

1.5 Problem statement

Compliant mechanisms, that derive motion from elastic deformation, have revolutionized precision engineering applications. Despite their advantages, the widespread adoption and optimal performance of these mechanisms are limited by persistent challenges in nonlinear modeling and design. These challenges stem from the inherent complexities of their behavior, particularly under large deformations, and the performance constraints of existing designs.

1) Limitations of Current Nonlinear Modeling Methods

Accurately modeling the nonlinear behavior of compliant mechanisms under large deflections remains a significant challenge. While techniques such as the Chained Beam

Constraint Model (CBCM) and Chained Pseudo-Rigid-Body Model (CPRBM) (previously discussed in Chapter 1.3) have significantly improved predictive accuracy, they require substantial computational resources and time due to their reliance on segmentation-based approaches. These methods approximate large deformations by discretizing flexure beams into multiple segments, each requiring iterative computations to satisfy geometric compatibility, force equilibrium, and nonlinear stiffness conditions. As the number of segments increases, the model's complexity grows exponentially, leading to higher computational costs and longer processing times, especially when applied to mechanisms with intricate geometries or a high density of compliant elements. This segmentation-based approach, while effective for capturing large deflection behaviors, becomes cumbersome and inefficient when dealing with complex designs, limiting its practicality for rapid design iterations and optimization tasks.

2) Need for Parameterized Nonlinear Modeling Frameworks

Parameterized nonlinear modeling offers significant potential to enhance force-displacement prediction accuracy under large deflection and streamline the design process. By incorporating essential parameterized variables into nonlinear models, designers can efficiently optimize compliant mechanisms to achieve desired performance characteristics, even in systems with intricate geometries or demanding constraints. However, the adoption and development of parameterized nonlinear modeling in the design of compliant mechanisms remain underexplored. This gap limits the field's ability to fully leverage its analytical power to address the complexities of modern engineering demands.

3) Design Challenges in Compliant Mechanisms

From a design perspective, widely used compliant mechanisms, such as compliant parallel manipulators (CPMs) and compliant amplifiers, face limitations. CPMs often experience issues such as parasitic motions, cross-axis coupling, and constrained motion ranges, which compromise their precision and reliability in high-accuracy applications. Similarly, compliant amplifiers struggle to maintain a consistent amplification ratio across varying displacements, resulting in performance instability in applications requiring consistent force or motion amplification. These challenges arise from the lack

of advanced modeling techniques that can predict and mitigate these effects during the design phase.

1.6 Research objectives and thesis organization

1.6.1 Research objectives

The primary objective of this research is to address the critical challenges in the nonlinear modeling and design of compliant mechanisms, enabling their enhanced performance and broader adoption in precision engineering applications. This involves developing parameterized nonlinear modeling frameworks and innovative compliant mechanisms. Specifically, this research aims to:

1) Develop parameterized nonlinear modeling frameworks:

Develop advanced parameterized nonlinear models to accurately predict the nonlinear force-displacement behavior of compliant mechanisms. By integrating parameterized variables, these models will extend traditional nonlinear modeling techniques, offering adaptable and efficient analytical solutions for mechanisms with complex geometries and diverse functional requirements. Furthermore, the frameworks will address challenges posed by large deformations, accounting for geometric nonlinearities, material properties, and load-stiffening effects. This objective aims to enable precise predictions and optimization for high-performance, precision-engineered systems.

2) Design of innovative compliant mechanisms:

Apply the parameterized nonlinear models to the design and optimization of innovative compliant mechanisms, such as compliant parallel manipulators (CPMs) and compliant amplifiers. These objective addresses key limitations of existing designs, including parasitic motions, cross-axis coupling, constrained motion ranges, and non-constant amplification ratios. The focus is on achieving enhanced precision, reliability, and consistency in performance, thereby expanding the functional capabilities of these mechanisms for diverse applications.

3) Integrate modeling and design for complex systems:

Employ the parameterized nonlinear modeling frameworks to design and analyze complex compliant mechanisms, focusing on their application to practical engineering challenges. This includes utilizing the developed 2D and 3D parameterized models to optimize mechanisms such as revolute joints, bistable mechanisms, and spherical joints. By bridging the gap between analytical modeling and real-world design, this objective aims to demonstrate the versatility and precision of the models in addressing diverse operational requirements, enabling efficient performance optimization and refinement of compliant systems across multiple applications.

4) Validate models and designs through experimental and computational analysis:

Validate the developed parameterized nonlinear models and proposed designs through a combination of comprehensive FEA and innovative, cost-effective experimental testing. This objective ensures the accuracy, reliability, and practical applicability of the methodologies in addressing real-world engineering challenges. The validation process will highlight the models' robustness and their effectiveness in guiding the design of compliant mechanisms with enhanced performance characteristics.

1.6.2 Thesis organization

This thesis is structured into six comprehensive chapters, each addressing specific aspects of the design and nonlinear modeling of general flexure beams and compliant mechanisms. The flow of the chapters is illustrated in the provided flowchart (Figure 1.8) and is outlined as follows:

The first chapter provides an overview of compliant mechanisms, emphasizing their significance and applications in precision engineering. It introduces the basic building blocks of compliant mechanisms, including flexure beams and flexure hinges, highlighting their fundamental roles in achieving compliance. This chapter also reviews the nonlinear deflection behavior of flexure beams and the various design methodologies employed for compliant mechanisms. The chapter concludes with a detailed statement of the research problem and objectives, setting the stage for the subsequent chapters.

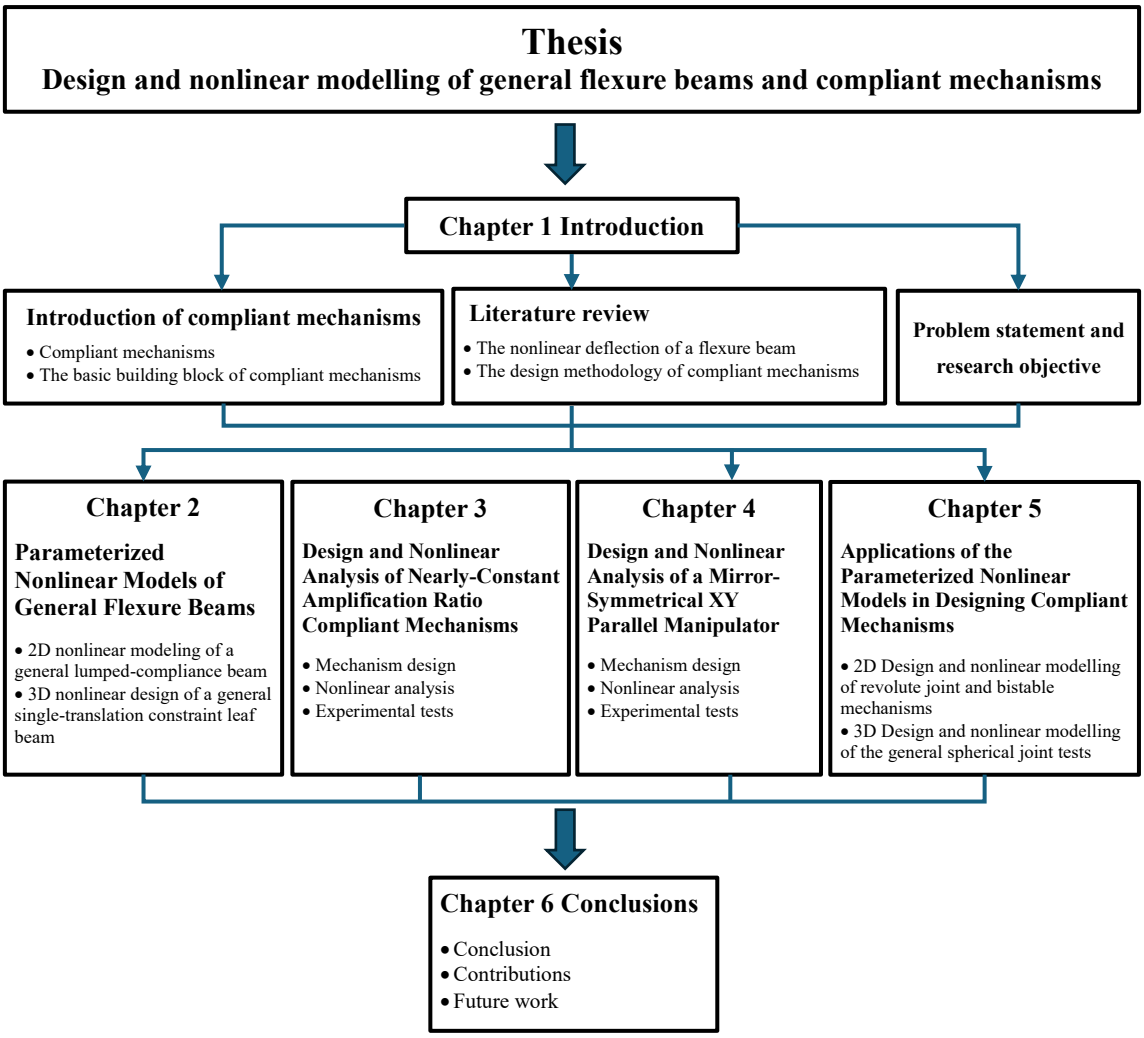


Figure 1.8 The flowchart of the thesis structure

Chapter 2 focuses on developing parameterized nonlinear models for general flexure beams. It begins with the 2D nonlinear modeling of a general lumped-compliance beam, discussing the prior art, model development, and its verification through FEA. The chapter extends into 3D nonlinear modeling, specifically for a general single-translation constraint leaf beam. The methodology, design process, and representative configurations are analyzed with FEA verifications. The chapter concludes with an in-depth discussion on the findings and contributions of these parameterized models.

Chapter 3 addresses the challenges of designing compliant mechanisms with nearly-constant amplification ratios. It reviews the state-of-the-art in compliant amplifiers and presents a novel mechanism design. The nonlinear analytical modeling and analysis of

the proposed mechanism are conducted, followed by validation through FEA and experimental testing. This chapter also explores the dynamic performance, force-displacement nonlinearity elimination, and footprint reduction, providing a detailed evaluation of the proposed compliant amplifier.

Chapter 4 focuses on the design and analysis of a novel mirror-symmetrical XY parallel manipulator (XY CPM). The chapter begins with a review of prior XY CPM designs and introduces the principles of minimizing parasitic motions and cross-axis coupling. The embodiment of the XY CPM is presented, followed by nonlinear kinetostatic modeling and FEA validation. Experimental tests are conducted to assess the design's performance under realistic conditions, and further discussions evaluate its contributions to precision positioning systems.

Chapter 5 applies the parameterized nonlinear models developed in Chapter 2 to real-world designs. It explores two distinct applications: the 2D modeling and design of revolute joints and bistable mechanisms, and the 3D modeling and design of a general spherical joint. Each case includes nonlinear modeling, FEA verification, and experimental validation to demonstrate the versatility and reliability of the parameterized models in optimizing compliant mechanisms for diverse operational requirements.

The final chapter summarizes the key contributions of this research. It highlights the development of advanced parameterized nonlinear models and the design of novel compliant mechanisms. These contributions are validated through extensive FEA and experimental testing. The chapter emphasizes the practical utility of these models and mechanisms in addressing challenges such as parasitic motions, amplification instability, and constrained motion ranges. Future directions for research and applications are also discussed, providing a roadmap for further advancements in the field of compliant mechanisms.

CHAPTER 2

PARAMETERIZED NONLINEAR MODELS OF GENERAL FLEXURE BEAMS

This chapter is organized to progressively introduce and develop two distinct parameterized nonlinear models tailored to general flexure beams: a 2D nonlinear model for general lumped-compliance beams (GLBM) and a 3D nonlinear model for general single-translation constraint (GSTC) leaf beams. The 2D model is formulated to incorporate essential geometric parameters, enabling an accurate characterization of lumped-compliance beams in planar applications. This approach effectively captures a broad spectrum of beam configurations, including distributed, inverted, and folded designs, to meet diverse compliance and motion requirements.

Building on the GLBM, the chapter introduces the 3D nonlinear model for the GSTC leaf beam, aimed at addressing the complexity of spatially constrained mechanisms. The single-translation constraint was chosen for parameterization because it is a fundamental compliant mechanism, serving as a building block for complex compliant systems. Unlike traditional single-translation constraint wire beams, which lack robustness against external loads and pose manufacturing challenges in CNC and additive fabrication, the GSTC leaf beam model offers an optimized, constraint-driven alternative. [152]. The GSTC leaf beam model overcomes these challenges by providing a versatile design framework that allows for customization through four key geometric parameters, enhancing its adaptability to various configurations. This 3D model enables precise control by constraining motion along one specified direction while allowing movement in the other five degrees of freedom. This characteristic is essential for applications such as compliant spherical joints where maintaining controlled motion within specific constraints is critical for achieving accurate, multi-directional flexibility.

2.1 2D nonlinear modeling of a general lumped-compliance beam

We introduce the GLBM, developed to overcome the limitations of existing nonlinear modelling methods by integrating a set of key geometric parameters. This model enables the accurate and efficient synthesis of force-displacement characteristics for various beam configurations, including inverted and folded beam designs, by employing an analytical approach that captures the nonlinear interactions within the beam structure.

To validate the accuracy and applicability of the GLBM, we perform a comprehensive FEA across various beam configurations, comparing analytical predictions with FEA results. Parametric analyses further illustrate the model's adaptability and reliability in different design scenarios, quantifying the impact of varying geometry and loading conditions.

The chapter concludes with a discussion of the GLBM's modeling method, summarizing its strengths in predicting nonlinear responses and identifying potential sources of error. This section provides a critical perspective on the model's applicability and limitations, offering insights into optimal usage conditions and areas for further refinement.

2.1.1 The development of the general lumped-compliance beam model

The objective of this section is to introduce the derivation of the GLBM. The section begins by presenting the BCM as a basis for the development of the model, which is documented in Appendix A. Subsequently, the derivation of the GLBM is elaborated step by step, providing detailed explanations of the process.

Figure 2.1 shows the parameterized lumped-compliance beam that features two flexure beams connected in serial. The GLBM is dominantly defined by six geometrical parameters, i.e., L_{i1}, L_{i2}, γ_i, α_i, β_i, and W_i, which are labeled in Figure 2.1(a). These six parameters provide a comprehensive set of variables that allow the model to represent various beam configurations while ensuring efficiency in nonlinear analysis. Other geometric properties, such as the width and thickness of each flexure beam, are not included as primary variables in this parameterization. These dimensions are predefined during the nonlinear analysis to maintain consistency across different configurations.

The symbol i corresponds to a general beam configuration. It is worth noting that the

length W is the distance between the two centre points of the two flexure beams. By manipulating these parameters, we can obtain any beam configurations that consist of any two flexure beams and one rigid stage in the middle (including only two flexure beams without a rigid stage as defined below).

$$W_i\cos(\gamma)=L_{i1}\cos(\alpha_i)/2+L_{i2}\cos(\beta_i)/2 \text{ and } W_i\sin(\gamma_i)=L_{i1}\sin(\alpha_i)/2+L_{i2}\sin(\beta_i)/2$$

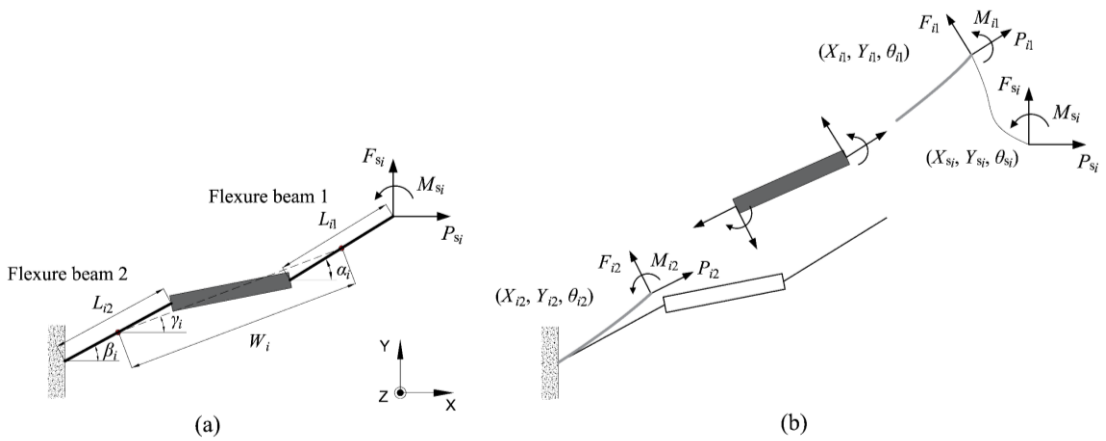


Figure 2.1 Configuration of a general beam: (a) geometry parameters of the GLBM; (b) FBD of the general beam.

To obtain the relationship between the tip input forces (F_{si}, P_{si}, M_{si}) and the tip output displacements (X_{si}, Y_{si}, θ_{si}) with respect to the coordinate frame X-Y-Z, we utilize the BCM in conjunction with the FBD method. This approach is what we commonly use in solving a typical mechanic problem which involves three components: constitutive equations, force equilibrium, and geometry compatibility [153-155]. The constitutive equation of each flexure beam is obtained from the BCM [95], which is explained in Appendix A.

The constitutive equations of flexure beam 1 can be expressed below.

$$\begin{bmatrix} F_{i1}L_{i1}^2/EI \\ M_{i1}L_{i1}^2/EI \end{bmatrix}=\begin{bmatrix} 12 & -6 \\ -6 & 4 \end{bmatrix}\begin{bmatrix} Y_{i1}/L_{i1} \\ \theta_{i1} \end{bmatrix}+P_{i1}L_{i1}^2/EI\begin{bmatrix} 1.2 & -0.1 \\ -0.1 & 2/15 \end{bmatrix}\begin{bmatrix} Y_{i1}/L_{i1} \\ \theta_{i1} \end{bmatrix}$$
$$\frac{X_{i1}}{L_{i1}}=((T_i/L_{i1}^2)^2/12)\cdot(P_{i1}L_{i1}^2/EI)+0.5\begin{bmatrix} Y_{i1}/L_{i1} & \theta_{i1} \end{bmatrix}\begin{bmatrix} 1.2 & -0.1 \\ -0.1 & 2/15 \end{bmatrix}\begin{bmatrix} Y_{i1}/L_{i1} \\ \theta_{i1} \end{bmatrix}$$
$$+(P_{i1}L_{i1}^2/EI)\begin{bmatrix} Y_{i1}/L_{i1} & \theta_{i1} \end{bmatrix}\begin{bmatrix} 1/700 & -1/1400 \\ -1/1400 & 11/6300 \end{bmatrix}\begin{bmatrix} Y_{i1}/L_{i1} \\ \theta_{i1} \end{bmatrix} \quad (2.1)$$

The constitutive equations of flexure beam 2 can be expressed below.

$$\begin{bmatrix} F_{i2}L_{i2}^2/EI \\ M_{i2}L_{i2}^2/EI \end{bmatrix} = \begin{bmatrix} 12 & -6 \\ -6 & 4 \end{bmatrix} \begin{bmatrix} Y_{i2}/L_{i2} \\ \theta_{i2} \end{bmatrix} + P_{i2}L_{i2}^2/EI \begin{bmatrix} 1.2 & -0.1 \\ -0.1 & 2/15 \end{bmatrix} \begin{bmatrix} Y_{i2}/L_{i2} \\ \theta_{i2} \end{bmatrix} \tag{2.2}$$

$$X_{i2}/L_{i2} = ((T_i/L_{i2}^2)^2/12)\cdot(P_{i2}L_{i2}^2/EI) + 0.5\begin{bmatrix} Y_{i2}/L_{i2} & \theta_{i2} \end{bmatrix} \begin{bmatrix} 1.2 & -0.1 \\ -0.1 & 2/15 \end{bmatrix} \begin{bmatrix} Y_{i2}/L_{i2} \\ \theta_{i2} \end{bmatrix}$$

$$+(P_{i2}L_{i2}^2/EI)\begin{bmatrix} Y_{i2}/L_{i2} & \theta_{i2} \end{bmatrix} \begin{bmatrix} 1/700 & -1/1400 \\ -1/1400 & 11/6300 \end{bmatrix} \begin{bmatrix} Y_{i2}/L_{i2} \\ \theta_{i2} \end{bmatrix}$$

The force balance equations are derived based on the deformed configuration as shown in Figure 2.1(b), which captures the contributions of the axial load to the bending moment.

$$\begin{bmatrix} P_{i1} \\ F_{i1} \end{bmatrix} = \begin{bmatrix} \cos(\alpha_i+\theta_{i2}) & \sin(\alpha_i+\theta_{i2}) \\ -\sin(\alpha_i+\theta_{i2}) & \cos(\alpha_i+\theta_{i2}) \end{bmatrix} \begin{bmatrix} P_{si} \\ F_{si} \end{bmatrix} \tag{2.3}$$

$$\begin{bmatrix} 0 \\ 0 \end{bmatrix} = \begin{bmatrix} \cos(\alpha_i+\theta_{i2}) & -\sin(\alpha_i+\theta_{i2}) \\ \sin(\alpha_i+\theta_{i2}) & \cos(\alpha_i+\theta_{i2}) \end{bmatrix} \begin{bmatrix} P_{i1} \\ F_{i1} \end{bmatrix} - \begin{bmatrix} \cos(\beta_i) & -\sin(\beta_i) \\ \sin(\beta_i) & \cos(\beta_i) \end{bmatrix} \begin{bmatrix} P_{i2} \\ F_{i2} \end{bmatrix}$$

$$M_{i1} - M_{si} = 0$$

$$M_{i1} + F_{i1}(X_{i1}+L_{i1}) - P_{i1}Y_{i1} - M_{i2} + \left(W_i\cdot\cos(\gamma_i+\theta_{i2}) - \cos(\beta_i+\theta_{i2})\cdot L_{i1}/2 - \cos(\alpha_i+\theta_{i2})\cdot L_{i1}/2\right)$$

$$\cdot\left(F_{i1}\cdot\cos\left(\alpha_i+\theta_{i2}\right) + P_{i1}\cdot\sin\left(\alpha_i+\theta_{i2}\right)\right)$$

$$+\left(W_i\cdot\sin(\gamma_i+\theta_{i2}) - \sin(\beta_i+\theta_{i2})\cdot L_{i1}/2 - \sin\left(\alpha_i+\theta_{i2}\right)\cdot L_{i1}/2\right)\cdot\left(F_{i1}\sin\left(\alpha_i+\theta_{i2}\right) - P_{i1}\cdot\cos\left(\alpha_i+\theta_{i2}\right)\right) = 0$$

In its deformed configuration, the tip displacement of the GLBM is generally the combination of the tip displacement of each beam in their local coordinates and the displacement caused by the rotation of the rigid stage in the global coordinates.

$$X_{i1}\cdot\cos(\alpha_i+\theta_{i2}) + X_{i2}\cdot\cos(\beta_i) - Y_{i1}\cdot\sin(\alpha_i+\theta_{i2}) - Y_{i2}\cdot\sin(\beta_i) \tag{2.4}$$

$$-2\cdot h_0\cdot\sin\left(\theta_{i2}/2\right)\cdot\cos\left(\pi/2 - \arcsin\left((W_i\cdot\sin(\gamma_i) - \sin\beta_i\cdot L_{i1}/2 + \sin\left(\alpha_i\right)\cdot L_{i1}/2)/h_0\right) - \theta_{i2}/2\right) - X_{si} = 0$$

$$Y_{i1}\cdot\cos(\alpha_i+\theta_{i2}) + Y_{i2}\cdot\cos(\beta_i) + X_{i1}\cdot\sin(\alpha_i+\theta_{i2}) + X_{i2}\cdot\sin(\beta_i)$$

$$+2\cdot h_0\cdot\sin\left(\theta_{i2}/2\right)\cdot\sin\left(\pi/2 - \arcsin\left((W_i\cdot\sin(\gamma_i) - \sin\beta_i\cdot L_{i1}/2 + \sin\left(\alpha_i\right)\cdot L_{i1}/2)/h_0\right) - \theta_{i2}/2\right) - Y_{si} = 0$$

$$\theta_{si} = \theta_i + \theta_{i2}$$

where

$$h_0 = \sqrt{\left(W_i\cdot\cos(\gamma_i) - \cos(\beta_i)\cdot L_{i1}/2 + \cos(\alpha_i)\cdot L_{i1}/2\right)^2 + \left(W_i\cdot\sin(\gamma_i) - \sin(\beta_i)\cdot L_{i1}/2 + \sin(\alpha_i)\cdot L_{i1}/2\right)^2}$$

The derivation of the force-displacement characteristic of the GLBM is based on the six constitutive equations (three each of the flexure beams), six force balance equations, and three geometry compatibility equations. When solving the system of equations, one can obtain the displacements (X_{si}, Y_{si}, θ_{si}) by giving the input force (F_{si}, P_{si}, M_{si}), and vice versa.

The input of the GLBM can consist of either external loads or geometric parameters, depending on the specific application. In one scenario, the input includes applied external forces along with the geometric parameters that serve as inputs while the output consists of the resulting tip displacements. Alternatively, in a geometry optimization context, the input can be a set of desired displacements and forces, and the output will be the optimized geometric parameters required to achieve the desired response.

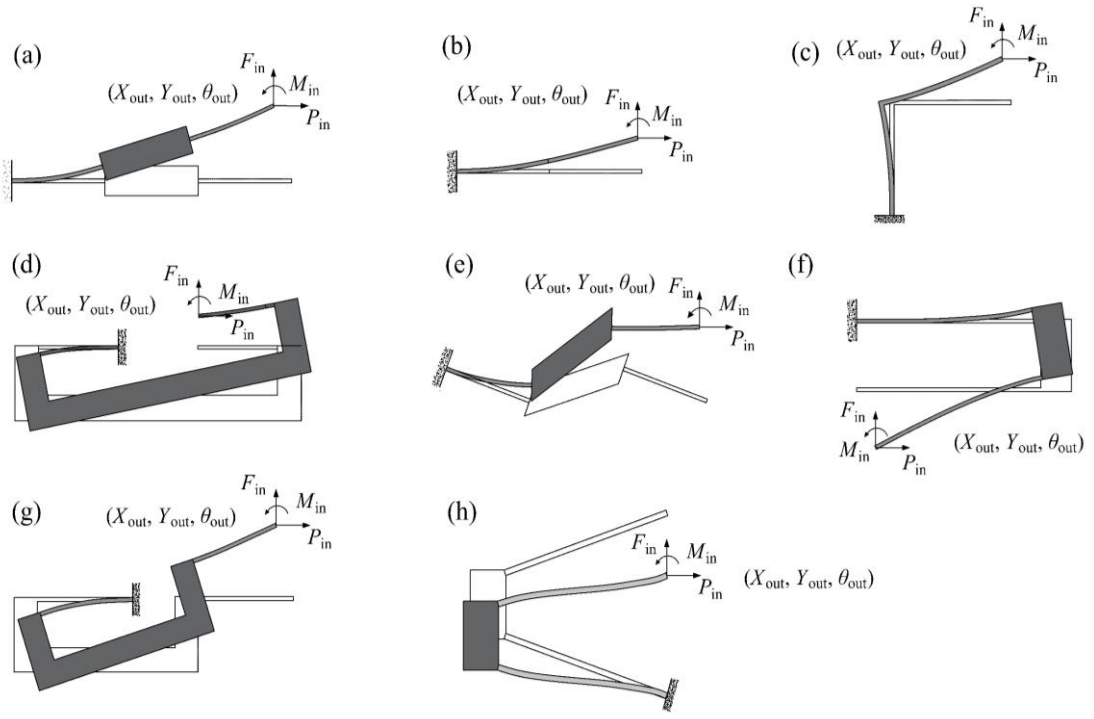


Figure 2.2 GLBM in different configurations: (a) straight/conventional lumped-compliance beam [95]; (b) distributed-compliance beam [99, 105]; (c) folded beam [26, 156]; (d) inverted beam [157-159]; (e) inclined beam [160, 161]; (g) half-inverted beam [162, 141]; (f) trapezoidal beam [163, 164]

Each GLBM contains 15 equations that govern the force-displacement characteristics. Using the GLBM to synthesize a complex structure that contains multiple general beams, the corresponding equations will be bulky. However, this issue can easily be solved in most existing mathematical software, i.e., Maple, MATLAB, and Mathematica by simply adding a loop function to repeat the force-displacement equations multiple times. In MATLAB, for instance, the system of equations can be solved symbolically or numerically using functions like *fsolve* for nonlinear numerical solutions. For structures with multiple beams, a loop function (e.g., a *for* loop) can be implemented to iteratively compute force-displacement relationships for each beam element.

2.1.2 FEA verification and parametric analysis

The GLBM offers a versatile approach to effectively model a general beam that incorporates any two flexure beams connected in series for various configurations. These general beam configurations are widely favoured in the design of compliant mechanisms, owing to their widespread popularity and numerous advantages. We have compiled a list of some existing specific configurations as shown in Figure 2.2.

In this section, we focus on showcasing five representative configurations (Figure 2.2(a) to Figure 2.2 (e)) using the GLBM. To ensure the credibility of our findings, we conducted a thorough verification process by comparing the analytical results with those obtained from the nonlinear FEA tool. Subsequently, a parametric analysis investigates how the primary geometric parameters impact the nonlinear behavior of the GLBM, emphasizing its flexibility in modeling diverse flexure beam configurations.

Table 2.1 Geometric parameters of the five configurations for the GLBM

Cases	α_i (deg)	β_i (deg)	γ_i (deg)	W_i (mm)	L_{i1} (mm)	L_{i2} (mm)	T_i (mm)	U_i (mm)
(a)	0	0	0	10	10	4	0.4	20
(b)	0	0	0	10	10	4	0.4	10
(c)	0	90	33.70	20	30	4	0.4	18.03
(d)	180	−180	0	10	10	4	0.4	20
(e)	−20	−20	0	10	10	4	0.4	20

These configurations, displayed in Figure 2.2, were chosen based on their prevalence in compliant mechanism applications and their distinct mechanical characteristics. The straight beam serves as a baseline reference, while the folded, inverted, inclined, and trapezoidal beams are frequently employed in practical designs due to their unique deformation properties. For instance, the inverted beam and the inclined beam, shown in Figure 2.2(d) and Figure 2.2(e), respectively, are frequently employed in the design of bistable mechanisms [157, 165, 161, 166, 160, 167] and translational joints [168, 159], whereas the folded beam, presented in Figure 2.2(c) is commonly used in the design of flexure joints [29, 169]. The trapezoidal beam (Figure 2.2(h)) is commonly used in the design of bridge-type compliant amplifiers. The geometry parameters of each

configuration are shown in Table 2.1. Each configuration (beam) was subjected to generalized end-loads (F_{in}, P_{in}, M_{in}), resulting in end displacements (X_{out}, Y_{out}, and θ_{out}) with respect to the global coordinates X-Y-Z. By testing different geometric properties and loading conditions, the model demonstrates its versatility, accuracy, and applicability. Additionally, the parametric analysis further validates its adaptability without excessive computational costs. Since these configurations represent fundamental flexure beam behaviors, additional cases would likely yield similar results, confirming the model's reliability for practical applications.

The FEA simulations were performed in commercial software COMSOL@5.0. A general flowchart depicting the FEA simulation process with Comsol software is presented in Figure 2.3. In line with the assumptions made in the analytical model, the stages and frames were set as rigid, and no fillet was added around the sharp corner. However, it is important to avoid sharp corners in the connection area between the rigid part and the flexure, as these can cause stress singularities. In this instance, a finer mesh did not result in superior outcomes. Therefore, it may be necessary to perform a singularity check to ensure that the results converge.

2.1.2.1 FEA Verification of GLBM in Different Configurations

By incorporating the relevant parameters into the GLBM derived in Section 2.1.1, we can obtain an analytical model that governs the force-displacement characteristics of each case, subject to generalized end-loads. To comprehensively study the force-displacement characteristics, a relatively large force is applied to the beams to induce a substantial displacement.

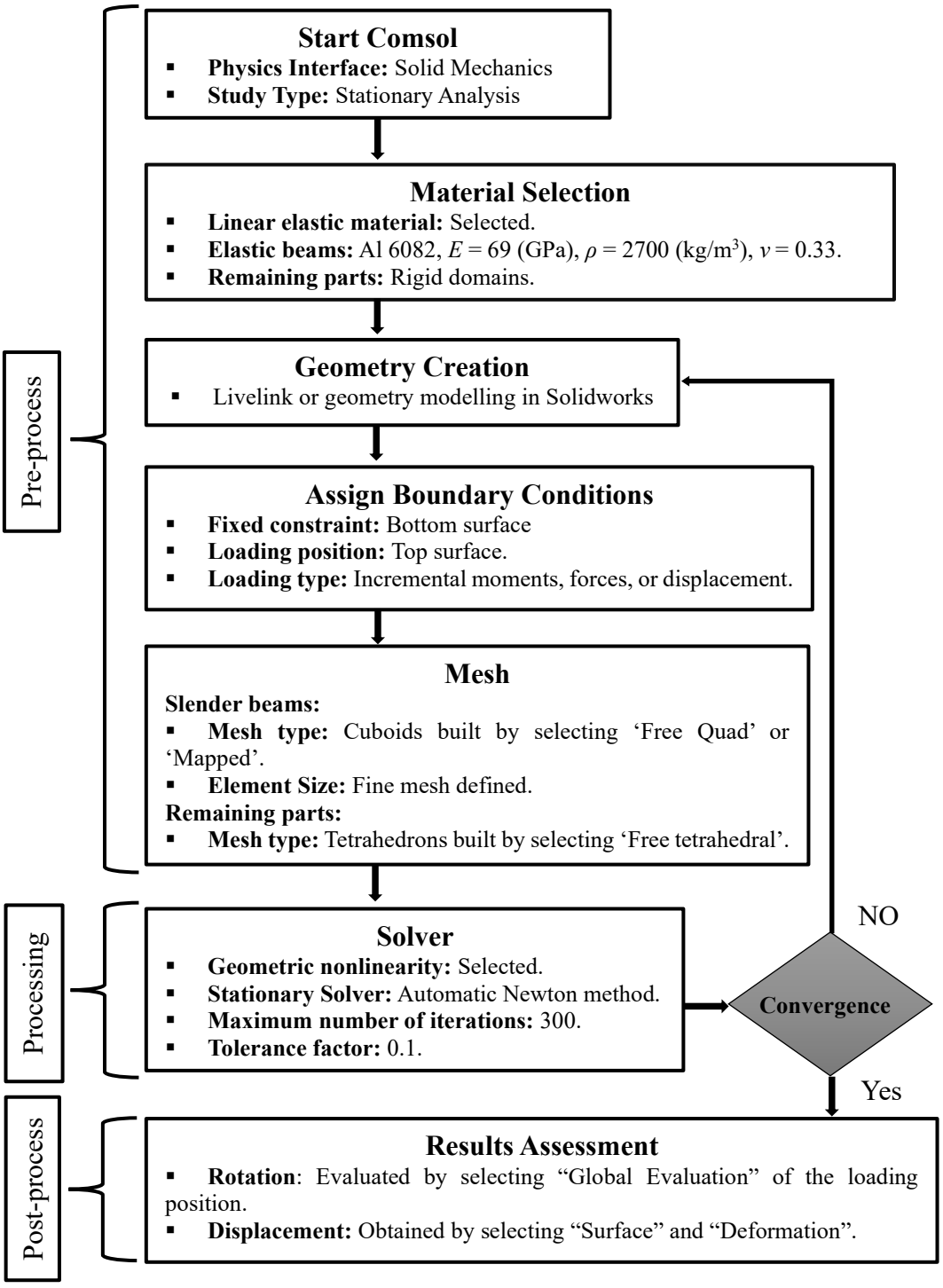


Figure 2.3 Flowchart of the process of FEA simulation based on the software Comsol.

Figure 2.4 presents a comparison between the analytical model and FEA simulation results in terms of the force-displacement relationship for the straight lumped-compliance beam. The analytical model was able to predict the resulting displacements in each direction (X_{out}, Y_{out}, and θ_{out}) with a prominent level of accuracy, as evidenced by the close agreement between the analytical and FEA results. The maximum error between the analytical and FEA results was 4.93% for the transverse displacement (Y_{out}) in Figure 2.4(b), which reached 54% of the beam length (30 mm). For the axial displacement (X_{out}) and tip rotation (θ_{out}) in Figure 2.4(a) and Figure 2.4(c), respectively, the maximum errors were 4.48% and 5.85%. Generally, a smaller displacement resulted in a better correlation between the analytical and FEA results. These findings validate the reliability of the analytical model in predicting the force-displacement behavior of the straight lumped-compliance beam.

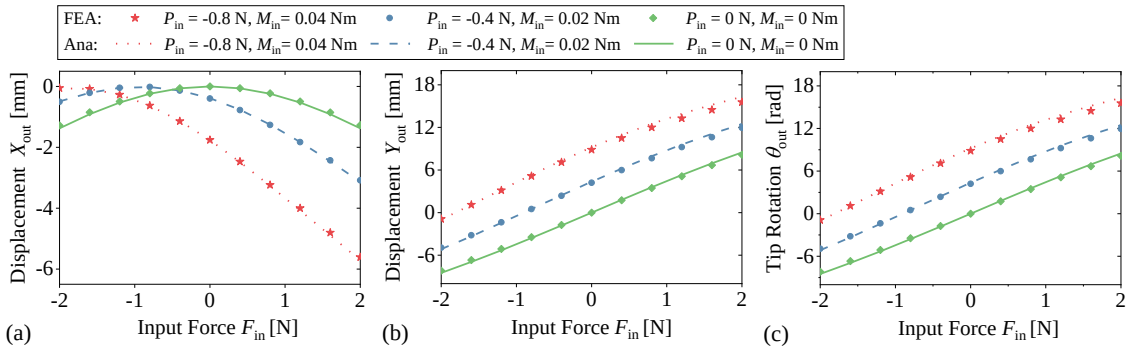


Figure 2.4 FEA verification of the lumped-compliance beam: (a) displacement in X-direction versus the input force F_{in}; (b) displacement in Y-direction versus the input force F_{in}; (c) rotation about Z-axis versus the input force F_{in}.

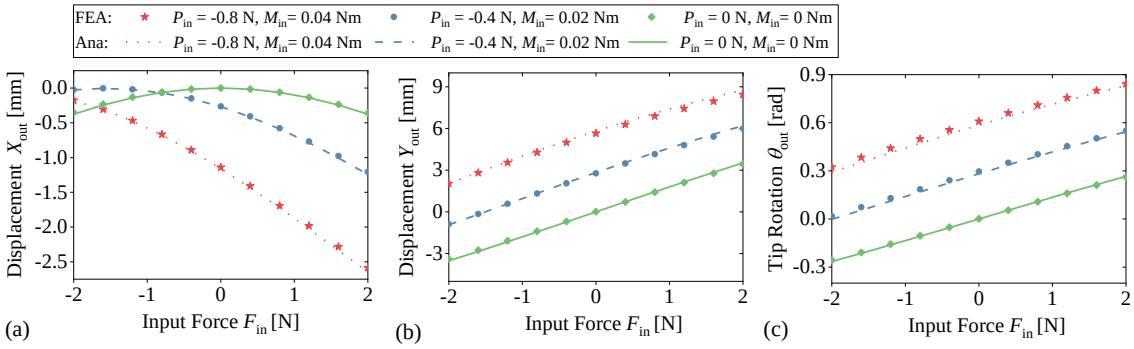


Figure 2.5 FEA verification of the distributed-compliance beam: (a) displacement in X-direction versus the input force F_{in}; (b) displacement in Y-direction versus the input force F_{in}; (c) rotation about Z-axis versus the input force F_{in}.

The results of the distributed-compliance beam are plotted in Figure 2.5 where the error is below 4.71 % for the tip rotation. When the axial displacement reaches 2.4 mm (beam length 20 mm), it produces a maximum error of 2.27% between the FEA and analytical results as shown in Figure 2.5(c). A force combination of F_{in} = 2 N, P_{in} = − 0.8 N, M_{in} = 0.04 Nm produces a transverse displacement (Y_{out}) of 8.43 mm with a maximum error of 3.77 %, which is illustrated in Figure 2.5(b).

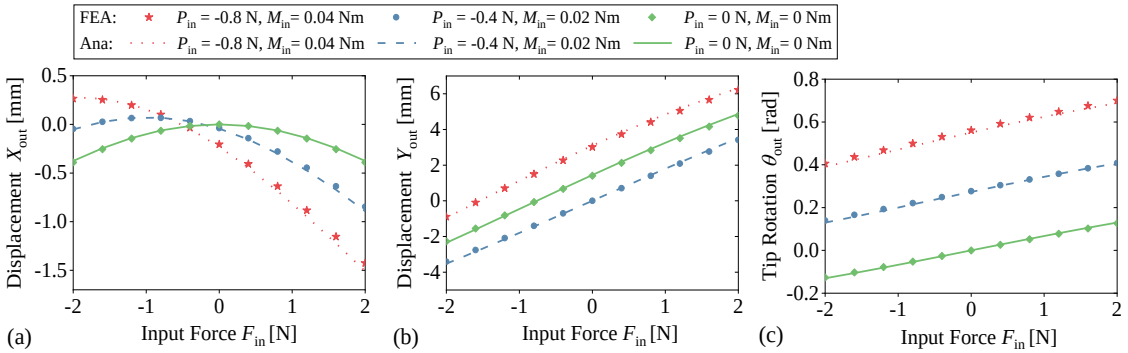


Figure 2.6 FEA verification of the inverted beam: (a) displacement in X-direction versus the input force F_{in}; (b) displacement in Y-direction versus the input force F_{in}; (c) rotation about Z-axis versus the input force F_{in}.

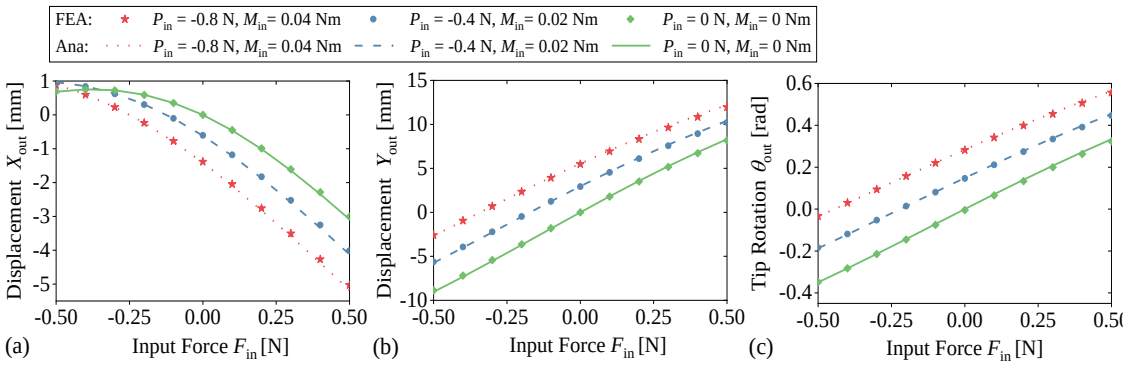


Figure 2.7 FEA verification of the inclined beam: (a) displacement in X-direction versus the input force Fin; (b) displacement in Y-direction versus the input force Fin; (c) rotation about Z-axis versus the input force Fin.

The comparison between the analytical and FEA results of case 3 (inverted beam) is plotted in Figure 2.6. The maximum error that occurs in the tip rotation is 3.12 % while the maximum error for the transverse displacement (Figure 2.6(b)) and axial displacement (Figure 2.6(a)) is 4.69 % and 2.64 %, respectively. Figure 2.7 presents the comparison of the results for case 4 (inclined beam). While the beam yields 16.82 mm in the transverse

direction (Y_{out}), it has a maximum error of 4.98 %. The maximum error between the analytical results and FEA results, in this case, is 4.28% (for θ_{out}) and 5.75% (for X_{out}).

Figure 2.8(a) displays the force-displacement characteristic of the folded beam, with a maximum error of 4.48% observed between the analytical and FEA results in terms of axial displacement. The transverse displacement and tip rotation exhibit errors of 2.75% and 5.41%, which are depicted in Figure 2.8(b) and Figure 2.8(c), respectively.

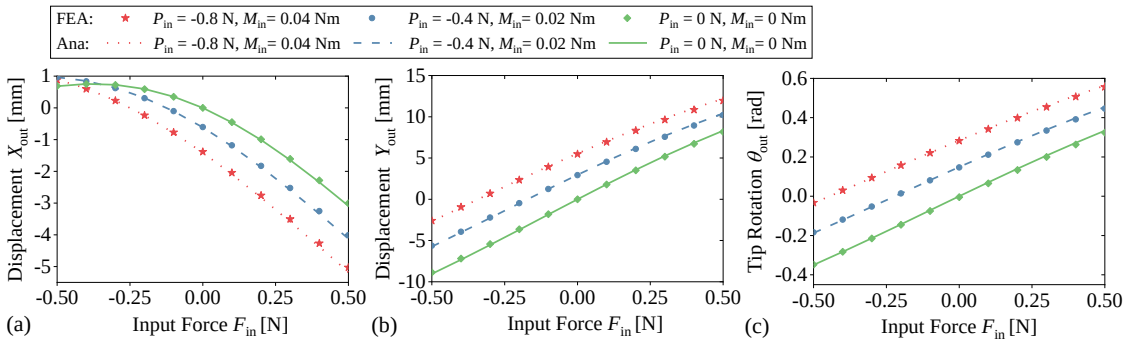


Figure 2.8 FEA verification of the folded beam: (a) displacement in X-direction versus the input force F_{in}; (b) displacement in Y-direction versus the input force F_{in}; (c) rotation about Z-axis versus the input force F_{in}.

In Section 2.1.2.1, we utilized the developed GLBM to model five representative flexure beam units. We verified the results by comparing them with those obtained from an FEA tool. Our analysis revealed that the error between the analytical results and the FEA results was in the range of 2% to 6% for a large deflection (transverse displacement over 40% of the beam length). Overall, the results suggest that the GLBM is effective in predicting the force-displacement behavior in any configuration, with reasonable accuracy as compared to the FEA simulations.

While our primary focus in this study is on accurately predicting the force-displacement relationship, we acknowledge that stress distribution analysis is also an important aspect of compliant mechanism design. Although stress is not explicitly considered in the current GLBM framework, it can be incorporated into future work by extending the model to account for material stress-strain relationships and localized stress concentrations. Given that compliant mechanisms often operate in high-strain environments, integrating stress analysis would provide further insights into structural integrity, fatigue life, and failure prediction. Future developments could enhance the GLBM by incorporating stress-based

constraints, enabling a more comprehensive design and optimization framework for compliant mechanisms.

2.1.2.2 Parametric analysis

A parametric analysis was conducted to systematically examine how geometric parameters influence the stiffness characteristics of a GLBM. By varying key parameters such as beam lengths, inclinations, and flexure angles, the analysis provides insights into the trade-offs between flexibility and rigidity, which are critical in optimizing compliant mechanism designs for specific applications.

This analysis helps designers make informed decisions when selecting beam configurations to achieve desired force-displacement behaviors, such as maximizing compliance for large deformations or enhancing stiffness for load-bearing applications. The impact of individual parameters on stiffness is assessed by generating response curves, showing how changes in beam geometry affect overall performance.

The analysis was implemented and computed in MATLAB, leveraging its numerical computation capabilities to efficiently evaluate thousands of configurations within a short processing time. MATLAB's symbolic and numerical solvers were used to derive and solve the force-displacement equations, while visualization tools were employed to plot stiffness variations across different design scenarios. This approach ensures a comprehensive understanding of parameter interactions, aiding in the refinement and optimization of compliant mechanisms.

Specifically, the geometric parameters α_1 and β_1 were chosen as variables, ranging from 0 degrees to 360 degrees with increments of 10 degrees, to investigate the changes in stiffness along the Y-direction. And the rest parameters are defined as $L_{11} = L_{12} = 10$ mm, $\gamma_1 = 0$ deg and $W_1 = 20$ mm. By applying input displacements and solving the system of equations, the stiffness was determined. Figure 2.9(a) depicts the stiffness with a neglective input displacement of 10^{-5} mm in the Y-direction. Figure 2.9(b) illustrates the stiffness for a given input displacement of $Y_{in} = 0.1$ mm, $X_{in} = 0$ and $\theta_{in} = 0$. Figure 2.9(c) illustrates the stiffness for a given input displacement of $Y_{in} = 0.2$ mm, $X_{in} = 0$ and $\theta_{in} = 0$. The input only occurs in the Y-direction, which mimics the single-leg motion of the

symmetrical traditional translational joint [168].

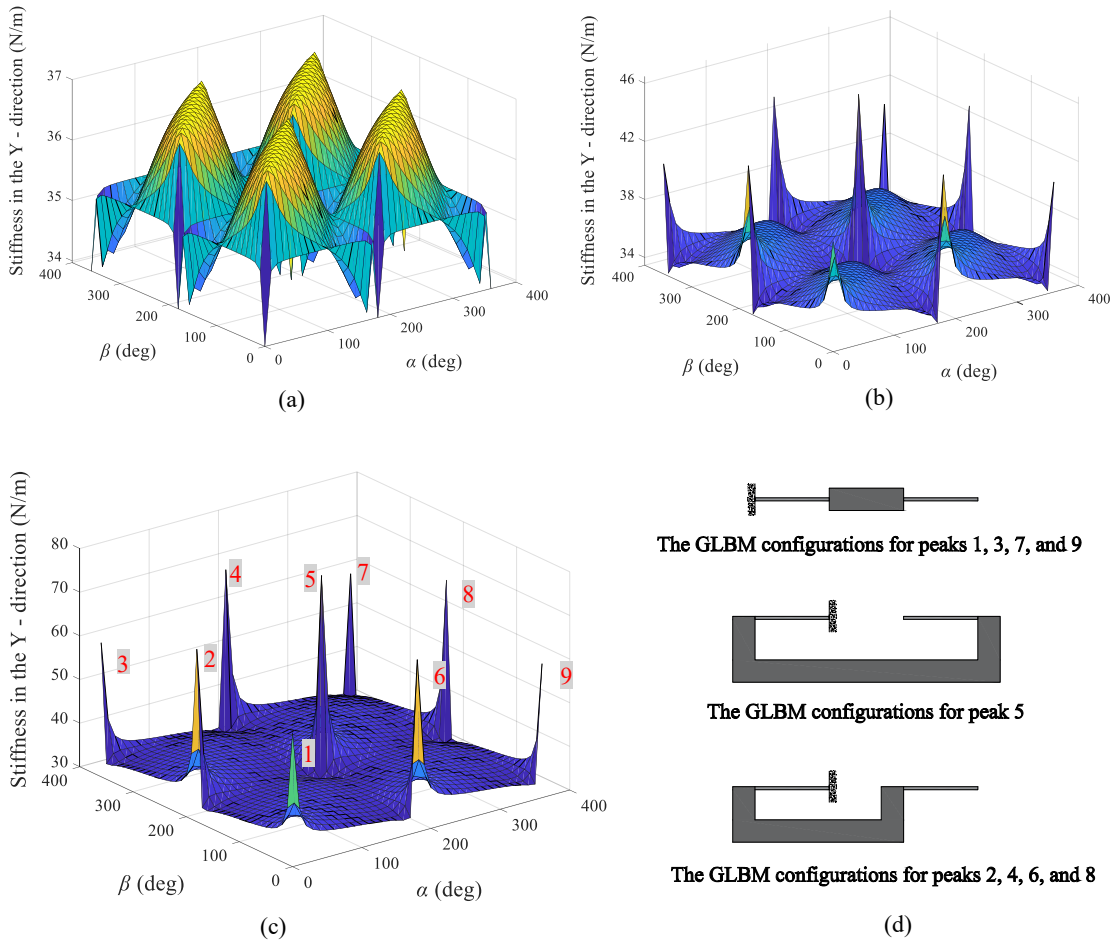


Figure 2.9 The stiffness in Y-direction with varying geometry parameters α and β: (a) instantons stiffness, the case of Y_{in} = 0 mm, X_{in} = 0 and θ_{in} = 0; (b) under the case of Y_{in} = 0.1 mm, X_{in} = 0 and θ_{in} = 0; (c) under the case of Y_{in} = 0.2 mm, X_{in} = 0 and θ_{in} = 0; (d) and the general beam configurations for each peak.

Figure 2.9(a) clearly illustrates the variation in stiffness at a small scale, ranging from 34 N/mm to 37 N/mm, when subjected to a negligible input of 10^{-3} mm in the Y-direction. However, as we increase the input displacement to 0.1 mm and 0.2 mm, the stiffness of different GLBM configurations exhibits a significant variation, ranging from 34 N/mm to 44 N/mm and from 34 N/mm to 65 N/mm, respectively.

Figure 2.9(d) presents the corresponding GLBM configurations of each peak in Figure 2.9(b) and Figure 2.9(c). Notably, the GLBM designs featuring colinear flexure beams, such as the inverted beam and the lump-compliance beam, exhibit higher stiffness

compared to the GLBM designs with non-colinear flexure beams, such as the folded beam and inclined beam. Furthermore, an interesting observation from Figure 2.9 is that the load-dependent effect is not prominent in the GLBM designs with parallel but not colinear flexure beams. This can be attributed to the minimal compression or tensile forces experienced by the flexure beams when subjected to small input displacements. In these configurations, the displacement in the X-direction and tip rotation remains zero while a displacement is applied in the Y-direction. However, it is worth noting that the GLBM model with colinear beams experiences significant tensile forces even for small displacements. The load-dependent effect is also observed by comparing Figure 2.9(a) and Figure 2.9(b). Figure 2.9(b) shows a larger value while the input displacement Y_{in} increases.

The parametric analysis in this study explores the influence of geometric variables on the kinetostatic characteristics of different GLBM configurations. This approach allows for the efficient evaluation of a large number of configurations, with each analysis requiring approximately 30 seconds of computing time in MATLAB. While this offers a significant computational advantage over traditional FEA simulations, it is important to acknowledge that the accuracy of the model remains dependent on the underlying assumptions and simplifications. Despite its efficiency, the GLBM serves as an approximate analytical tool, and FEA remains valuable for capturing complex stress distributions and validating results in detailed design stages. Nonetheless, the speed and versatility of the GLBM make it a useful tool for the parametric optimization of compliant mechanisms, facilitating rapid design iterations and performance evaluations.

2.1.3 Discussions

In this section, we provide a summary of the modeling method and discuss the potential errors associated with this method. This may lead to insights into the approach's applicability and limitations.

2.1.3.1 Summary of the Modeling Method

As depicted in Figure 2.10, the process of modeling compliant mechanisms using the GLBM entails initializing the geometry property, defining the boundary conditions,

formatting the force-displacement relationships, solving the equations, and determining if optimization is required.

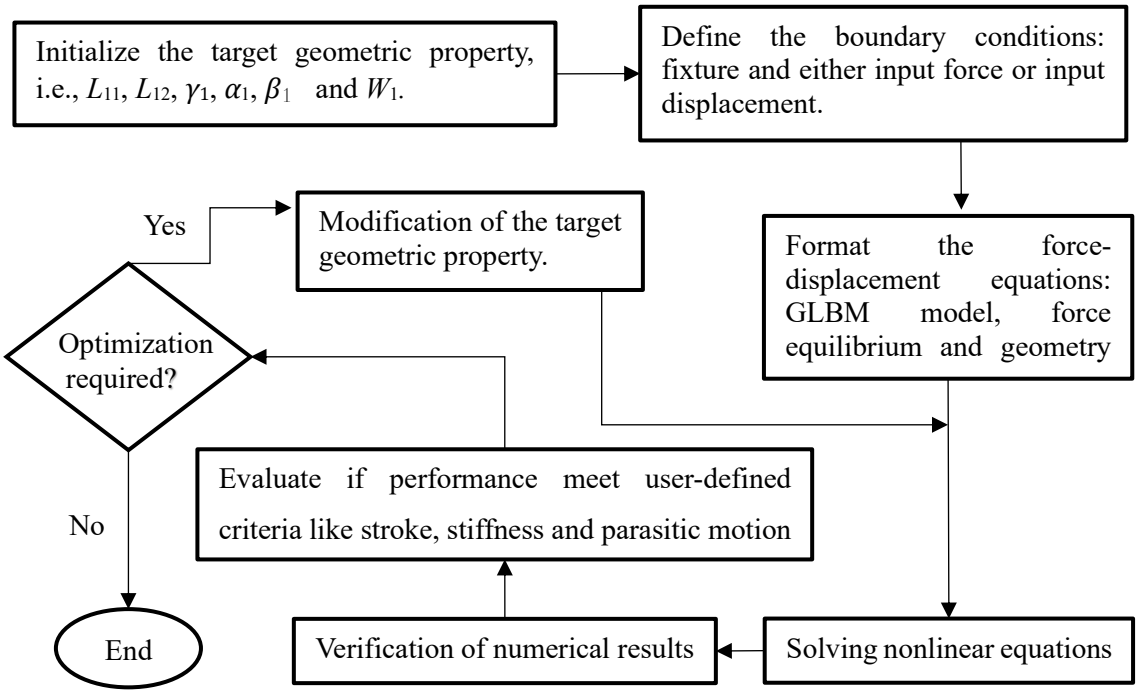


Figure 2.10 The general process of using the GLBM to model compliant mechanisms.

The geometry property of a compliant mechanism is initialized by assigning design parameters including the L_{i1}, L_{i2}, γ_i, α_i, β_i and W_i. Derivation of the force-displacement relationships of a compliant mechanism using the GLBM generally includes three components, namely the GLBM, force equilibrium, and geometry compatibility. The system equations of the force-displacement relationships can be solved numerically by providing initial guesses in mathematical software, such as Maple. Although the system of equations may appear cumbersome when dealing with complex structures that involve multiple general lumped-compliance beams, the use of the Loop function in Maple or other mathematical software allowed for a streamlined process by eliminating the need for repeating the constitutive equilibrium. This approach significantly reduced the required effort, even for complex structures.

Integrating geometry parameters into the mathematical model of a compliant mechanism enables optimization of its geometry to achieve desired performance characteristics.

Designers can vary these parameters to explore the design space and find the optimal geometry that meets the required specifications. For instance, Ref. [161] introduces several novel parameters into the bistable mechanism to better control its behavior. By adjusting the defined geometry parameters, the programmable bistable lattices can be optimized for specific targets such as a larger deformation range or higher stability. However, the optimization in [161] is done by the enumeration method, which is not efficient. In contrast, the proposed GLBM makes it possible to optimize for multiple objectives simultaneously, which is more efficient and cost-effective.

2.1.3.2 Model Error

The errors observed could be attributed to model errors and numerical errors. The model error arose from the fact that the constitutive equation relied on the mechanics of the Euler-Bernoulli beam, which disregards the shear effect. In the case of stubby beams, the model error could be significant. To address this issue, the Timoshenko beam theory, which accounts for the effect of shear strains in a beam and adds a correction term to the Euler-Bernoulli beam theory, can be used.

On the other hand, numerical errors could have resulted from the iterative numerical methods used in Maple to solve nonlinear equations. In some cases, these methods may not converge to the exact solution due to issues such as poor initial guesses. Additionally, the mesh quality (element size and shape) in the FEA tool can also contribute to numerical errors. A coarse mesh can lead to significant errors, while a fine mesh can be computationally expensive. However, a finer mesh does not necessarily guarantee better results if the solution does not converge.

2.2 3D nonlinear design of a general single-translation constraint

The chapter establishes the groundwork for the GSTC beam design, where multiple geometric parameters are integrated to achieve precise control over translational movement while constraining other degrees of freedom.

Following the model development, four representative configurations of the GSTC leaf beam undergo rigorous FEA to validate the model's accuracy and reliability. This verification step is essential for assessing the model's robustness in capturing nonlinear

spatial effects under diverse loading scenarios.

The chapter then extends into discussions on several related aspects. First, it explores additional design configurations related to the GSTC beam, highlighting the versatility and adaptability of the model for various compliant mechanism applications. Next, the potential sources of model error are addressed, providing insight into the method's limitations and conditions for optimal use.

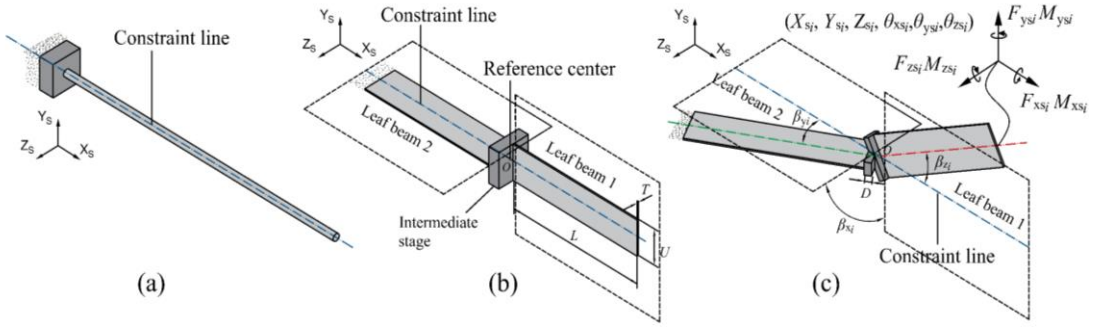


Figure 2.11 Wire beam and its equivalent: (a) a wire beam; (b) I-shape leaf beam; (c) GSTC leaf beam.

2.2.1 General single-translation constraint leaf beam design

A wire beam provides a single-translation constraint along its axial direction (shown in Figure 2.11(a)), serving as a fundamental component in the design of compliant mechanisms. From simple guiding mechanisms [7, 137, 170] to intricate compliant parallel manipulators [171, 24, 172] and spherical joints [172, 170], wire beams play a critical role. Despite their advantages in simplicity and reduced actuation, challenges arise in manufacturing when utilizing CNC mills and additive manufacturing techniques. Furthermore, wire beams struggle to withstand external loads along the beam due to their low stiffness [152].

As the demand for precision flexure systems continues to rise, especially in the realm of increasingly complex flexure-based applications, addressing these challenges becomes imperative. Recognizing this need, our previous work [152] introduced a single-translation constraint I-shape leaf beam design (Figure 2.11(b)). Subsequently, we linearly captured the kinetostatic behavior of the I-shape leaf beam and the resulting spherical joint using the compliance matrix modeling method. Building upon this foundation, we propose an enhanced approach by introducing the GSTC leaf beam,

incorporating four independent geometry parameters. This novel model facilitates the determinate synthesis of spatial force-displacement characteristics within a framework of two leaf beams based on single-translation constraint. The introduction of the GSTC leaf beam marks a significant advancement, allowing for the creation of diverse single-translation constraint leaf beam designs through the manipulation of the geometry parameters. This versatility facilitates parametric optimization to enhance performance metrics such as manufacturability, spatial efficiency, and resilience to external forces.

Figure 2.11(c) illustrates a spatial parameterized single-translation constraint leaf beam under the fixed global coordinate system Xs-Ys-Zs, comprising two leaf beams connected by an intermediate stage in series. The GSTC leaf beam is primarily characterized by four geometric parameters: angles β_{xi}, β_{yi}, β_{zi} and length D, as labeled in Figure 2.11(c). The initial axial positions of leaf beam 1 and leaf beam 2 overlap and along the Xs axis (constraint line); and the two planes that the two leaf beams lie in are initially orthogonal as well. The angle β_{xi} represents the rotation angle of leaf beam 1 about the X_S axis. The angle β_{yi} denotes the rotation angle of leaf beam 2 about the Y_S axis. The angle β_{zi} indicates the rotation angle of leaf beam 1 about the Z_S axis. The symbol D indicates the intermediate stage geometry (the length between the leaf beam 2 end and the geometry centre O). Regardless of the rotations undergone by these two beams, the constraint lines remain situated at the intersection line between the planes where the leaf beams are positioned. By adjusting these parameters, a series of single-translation constraint leaf beam modules can be obtained. The free end of the model is subjected to a general load, encompassing combined forces and moments. The symbol i corresponds to i^{th} GSTC leaf beam.

To obtain the relationship between the tip input forces (F_{xsi}, F_{ysi}, F_{zsi}, M_{xsi}, M_{ysi}, M_{zsi},) and the tip output displacements (X_{si}, Y_{si}, Z_{si}, θ_{xsi}, θ_{ysi}, θ_{zsi},) with respect to the coordinate frame X_S-Y_S-Z_S, a sequence of rotations firstly defined by three Euler angles is employed for tip rotation. The first rotation occurs about the fixed global Y-axis by an angle of θ_{ysi}, followed by a rotation about the Z-axis by an angle of $\theta_{zsi,}$ and finally, a rotation about the X-axis by an angle of θ_{xsi}. The rotation matrix, presented below, represents an extrinsic rotation [173, 174], adhering to the right-hand rule. It is important to note that throughout

this thesis, capital symbols denote dimensional parameters, while lowercase symbols denote normalized (dimensionless) ones unless specified otherwise.

$$R_{si}=\begin{bmatrix}1 & 0 & 0\\ 0 & \cos(\theta_{xsi}) & -\sin(\theta_{xsi})\\ 0 & \sin(\theta_{xsi}) & \cos(\theta_{xsi})\end{bmatrix}\begin{bmatrix}\cos(\theta_{zsi}) & -\sin(\theta_{zsi}) & 0\\ \sin(\theta_{zsi}) & \cos(\theta_{zsi}) & 0\\ 0 & 0 & 1\end{bmatrix}\begin{bmatrix}\cos(\theta_{ysi}) & 0 & \sin(\theta_{ysi})\\ 0 & 1 & 0\\ -\sin(\theta_{ysi}) & 0 & \cos(\theta_{ysi})\end{bmatrix} \tag{2.10}$$

We utilize the nonlinear SBCM reported in [119] in conjunction with the FBD method to construct the analytical model of the GSTC leaf beam. This approach is commonly utilized in solving typical mechanical problems involving three components: constitutive equations, force equilibrium, and geometry compatibility [154, 153, 155]. The constitutive equation (the SBCM) of each leaf beam under general loading conditions is elaborated in Appendix B. The force-equilibrium equations and the geometry compatibility conditions are illustrated in Appendix C.

A GSTC leaf beam comprises 12 constitutive equations, 12 force balance equations, and 6 geometry compatibility equations, collectively describing the nonlinear force-displacement characteristics of the model. When utilizing the GSTC leaf beam to synthesize a complex structure containing multiple general beams, the resulting set of equations may become voluminous. However, this issue can be readily addressed using most existing mathematical software, such as Maple, MATLAB, and Mathematica, by implementing a loop function to iteratively repeat the force-displacement equations, thereby reducing derivation time.

2.2.2 FEA verification for four representative configurations

The above proposed GSTC leaf beam can be reduced to four representative configurations (Figure 2.12) by assigning the parameters listed in Table 2.2, which are named the I-shape leaf beam [152], the specific single-translation constraint (SSTC) leaf beam, the L-shape leaf beam, and the folded leaf beam [26, 27, 175]. For instance, the SSTC leaf beam is achieved by rotating leaf beam 1 about the X_S-axis by π/2 radians (β_{xi}), about the Z_S-axis at π/6 radians (β_{zi}), and finally rotating leaf beam 2 about the Y_S-axis at π/6 radians (β_{yi}).

Table 2.2 Geometry parameters of four representative configurations derived from the GSTC leaf beam

Configuration	β_{xi} (rad)	β_{yi} (rad)	β_{zi} (rad)	D (mm)	L (mm)	T (mm)	U (mm)
I-shape leaf beam	π/2	0	0	2	50	0.5	12
SSTC leaf beam	π/2	π/6	π/6	4	50	0.5	12
L-shape leaf beam	π/2	0	π/2	4	50	0.5	12
Folded leaf beam	π/2	π/2	π/2	1	50	0.5	12

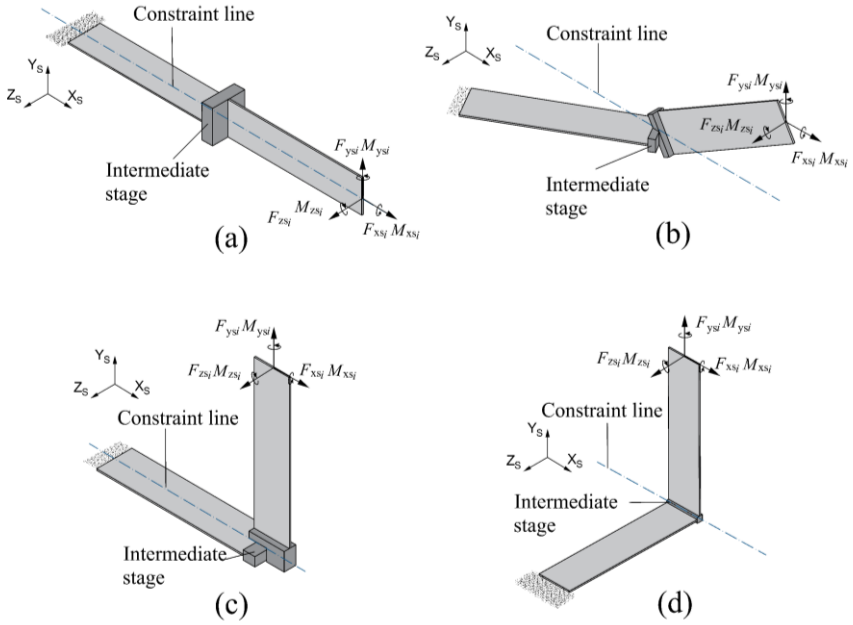


Figure 2.12 Four representative configurations in comparison: (a) I-shape leaf beam (β_{xi} = π/2; β_{yi} = 0; β_{zi} = 0); (b) SSTC leaf beam (β_{xi} = π/2; β_{yi} = π/6; β_{zi} = π/6); (c) L-shape leaf beam (β_{xi} = π/2; β_{yi} = 0; β_{zi} = π/2); (d) folded leaf beam (β_{xi} = π/2; β_{yi} = π/2; β_{zi} = π/2).

These four configurations were selected to ensure that the model's versatility and accuracy could be tested across different structural designs, verifying its ability to predict force-displacement relationships. To validate the feasibility of the GSTC leaf beam, nonlinear FEA simulations were conducted. Each design's free end was subjected to combined forces and moments, and the resulting displacement was compared with the prediction (i.e., obtained spatial kinetostatic model of the GSTC leaf beam). The simulations were executed using the commercial software COMSOL@5.0. The material properties of the leaf beam are assigned as a commonly used material in compliant mechanisms: stainless steel, with a Poisson's ratio of 0.3 and a Young's modulus of 200 GPa.

In accordance with the assumptions of the analytical model, stages and frames were treated as rigid, and no fillets were included around sharp corners to ensure compatibility with the theoretical framework. However, in FEA simulations, researchers should be cautious of potential stress singularities that may arise due to sharp corners, particularly at the interface between the rigid part and the flexure. In such cases, applying a finer mesh may not necessarily improve accuracy and can sometimes amplify localized stress values, leading to unrealistic results. To ensure result convergence, a singularity check is recommended when interpreting stress distributions. Additionally, when constructing the 3D geometry for simulation, careful attention should be given to the intermediate stage to ensure that its geometric center aligns precisely with the assumed reference point O.

The rotation sequence utilized in the FEA software is not predetermined, necessitating the determination of Euler angles with a specified rotation sequence for this study. A technique outlined in [120] leverages three mutually perpendicular beams affixed to the end effector to establish a rotation matrix, which is subsequently expressed through the deformed tip coordinates of these beams, allowing for the derivation of Euler angles. Additionally, a similar approach utilizing four points is discussed in [176] also introduced a similar method based on four points. For the present study, we opt for the method outlined in [120], due to its straightforward nature.

When verifying the GSTC leaf beam model, the selection of input forces and moments was carefully considered to ensure a comprehensive evaluation of the model's nonlinear behavior. The applied forces and moments were chosen to generate sufficient displacement in all six DOFs—three translational and three rotational—allowing for a full characterization of the beam's response under realistic loading conditions. Given the complexity of compliant mechanisms, different force combinations can lead to varied deformation patterns. The selected force inputs were designed to capture the dominant deformation modes while avoiding extreme loading scenarios that may cause unrealistic or highly localized deformations. By applying forces in both the primary translation direction and the transverse directions, along with a moment of about one axis, the study ensures that the model is assessed under practical and representative conditions.

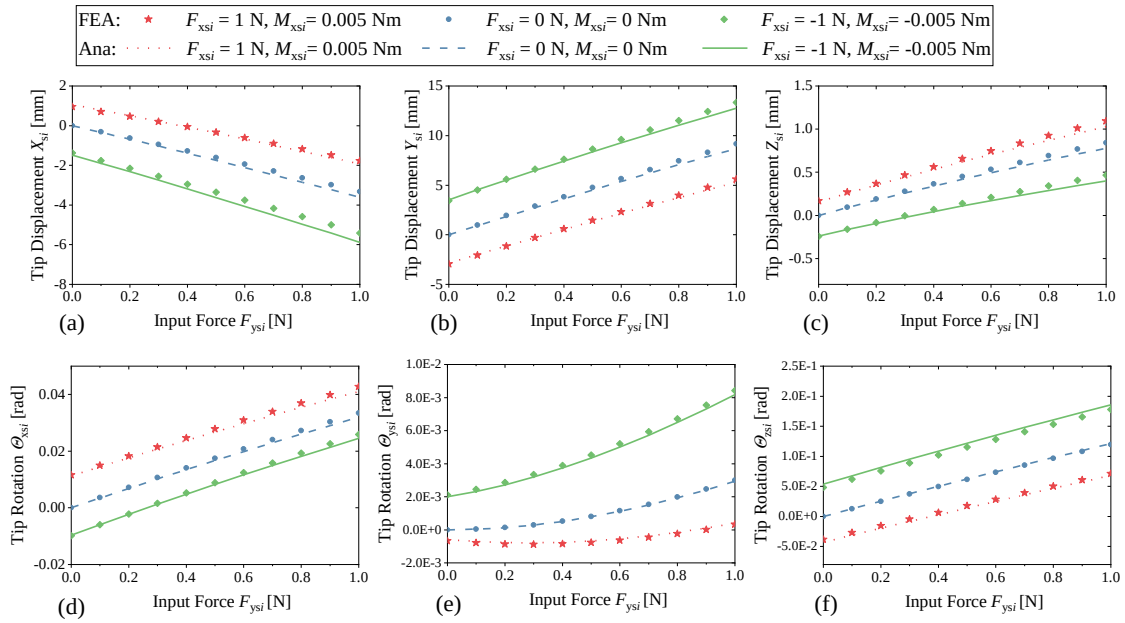


Figure 2.13 (Colour lines) The displacement comparison between the FEA and analytical results for the SSTC leaf beam, subjected to incremental forces in the Y-direction, a constant force in the X-direction and a constant moment along the X-direction: (a) the resultant displacement X_{si} ; (b) the resultant displacement Y_{si} ; (c) the resultant displacement Z_{si} ; (d) the resultant rotation θ_{xsi} ; (e) the resultant rotation θ_{ysi} ; (f) the resultant rotation θ_{zsi} ;

Figure 2.13 presents the FEA verification of the SSTC leaf beam with specified geometry parameters listed in Table 2.2. Combined forces and moments are applied to the free end of the SSTC leaf beam. The resultant displacements are compared with the results captured in the FEA. The overall comparison shows a good correlation. The results show a maximum error of 8.3% which occurs at the displacement in the X-direction (X_{si}).

Figure 2.14 illustrates a comparison of resultant displacements between FEA and analytical results, of the I-shape leaf beam. Overall, the analytical results closely correspond with the FEA outcomes. Notably, the largest deviation is observed in the resultant displacement X_{si}, with a maximum error of 6.6%. In the Y-direction, the displacement from incremental forces reaches 14 mm, exceeding 10% of the total length of the I-shape configuration, with an error of 2.8%.

Figure 2.15 depicts the results for the L-shape configuration, wherein the displacement in the X-direction constraint attains 11 mm under combined forces and moment, showing a 3.9% error compared to analytical results. Notably, the highest error emerges in the Z-direction displacement, reaching 5.8%. Moving to Figure 2.16, which displays results for

the folded configuration, the largest error manifests in the rotation about the Y-axis, at approximately 6.1%.

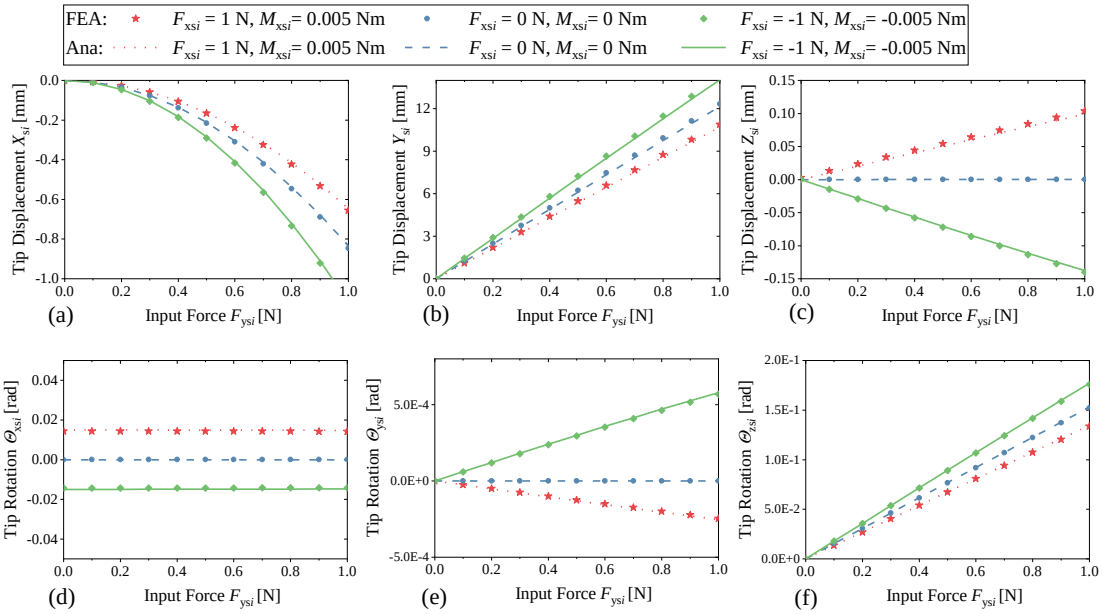


Figure 2.14 The displacement comparison between the FEA and analytical results for the I-shape leaf beam, subjected to incremental forces in the Y-direction, a constant force in the X-direction and a constant moment along the X-direction: (a) the resultant displacement X_{si}; (b) the resultant displacement Y_{si}; (c) the resultant displacement Z_{si}; (d) the resultant rotation θ_{xsi}; (e) the resultant rotation θ_{ysi}; (f) the resultant rotation θ_{zsi};

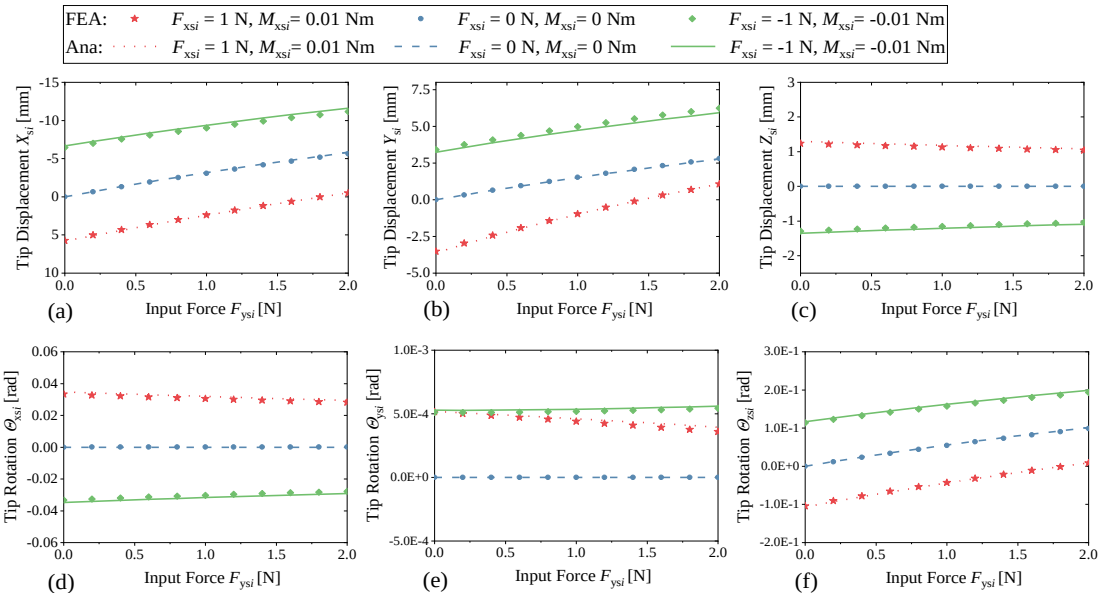


Figure 2.15 The displacement comparison between the FEA and analytical results for the L-shape leaf beam, subjected to incremental forces in the Y-direction, a constant force in the X-direction, and a constant moment along the X-direction: (a) the resultant displacement X_{si}; (b) the resultant displacement Y_{si}; (c) the resultant displacement Z_{si}; (d) the resultant rotation θ_{xsi}; (e) the resultant rotation θ_{ysi}; (f) the resultant rotation θ_{zsi}.

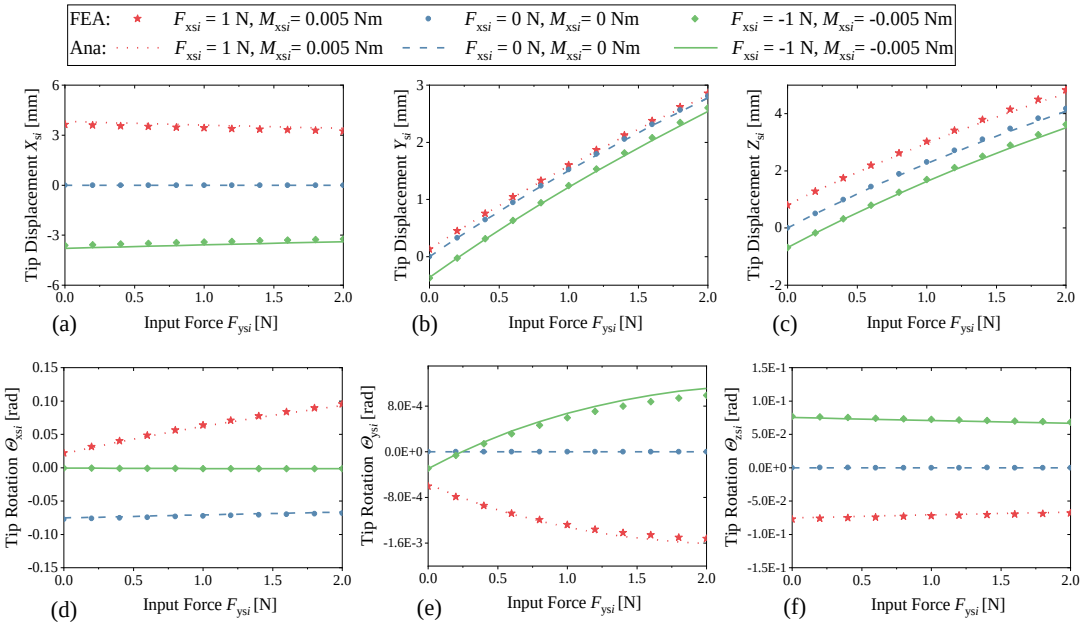


Figure 2.16 The displacement comparison between the FEA and analytical results for the folded leaf beam, subjected to incremental forces in the Y-direction, a constant force in the X-direction and a constant moment along the X-direction: (a) the resultant displacement X_{si}; (b) the resultant displacement Y_{si}; (c) the resultant displacement Z_{si}; (d) the resultant rotation θ_{xsi}; (e) the resultant rotation θ_{ysi}; (f) the resultant rotation θ_{zsi}

Based on the verification conducted using the FEA tool, it can be inferred that the analytical model of the GSTC leaf beam effectively predicts the nonlinear force-displacement characteristics of GSTC leaf beams. In comparison to employing FEA tools for determining the kinetostatic characteristics of GSTC leaf beams, the analytical model of the GSTC leaf beam offers greater efficiency. This is primarily because it allows for configuration changes through simple modification of geometric parameters, thus reducing the computational time required. In the motion range spanning 10% to 20% of the GSTC leaf beam length, the maximum error remains below 10% when compared to the results obtained from FEA. This level of accuracy suggests that the GLBM formulation effectively captures the nonlinear behavior of the GSTC leaf beam while maintaining computational efficiency. It is important to note that the largest errors tend to occur in the DoC direction, where displacements are naturally small. This is expected because, in this direction, even minor deviations in numerical calculations can lead to proportionally larger percentage errors, despite the absolute displacement being minimal.

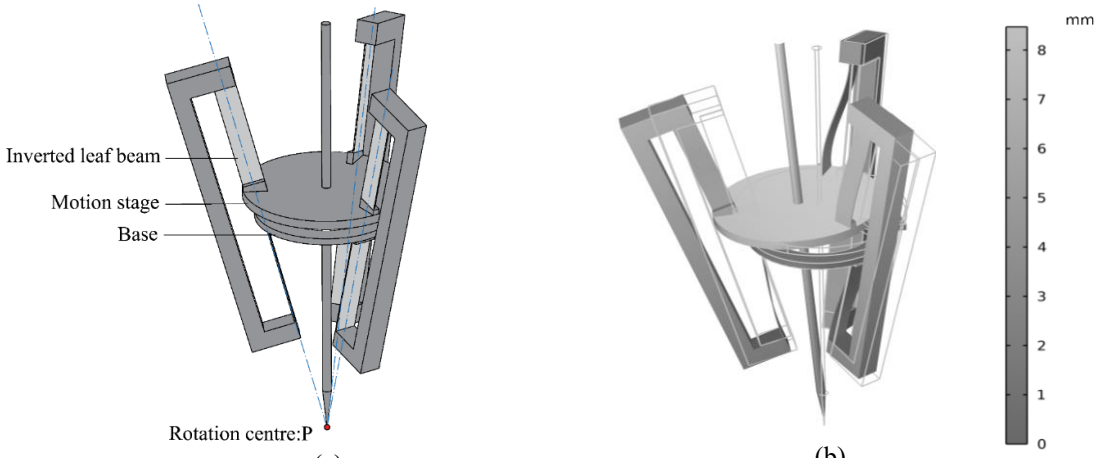


Figure 2.17 Spherical joint with inverted single-translation constraint: (a) the sketch of the geometry; (b) the deformed configuration.

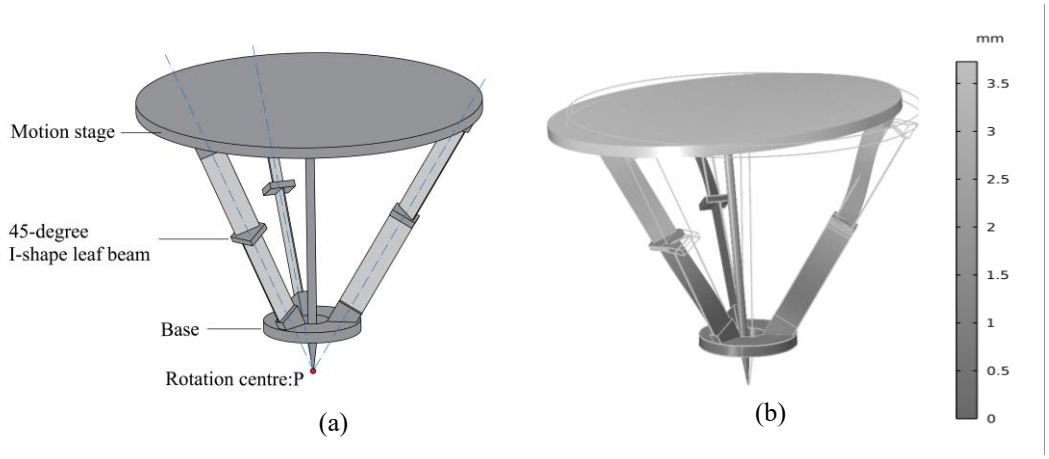


Figure 2.18 Spherical joint with 45-degree I-shape leaf beams: (a) the sketch of the geometry; (b) the deformed configuration.

2.2.3 Further discussions

2.2.3.1 Other associated designs

Interesting spherical joints can be designed using the GSTC leaf beams. In Figure 2.17(a), we observe the spherical joint featuring inverted leaf beams. This design boasts a large load-bearing capacity owing to the inherent anti-buckling property of the inverted leaf beam [177, 157]. In Figure 2.17(b), the deformed configuration of the spherical joint under a force in the Y_T-axis is illustrated. While the standard case defines $\beta_{xi} = 90$ degrees for the aforementioned spherical joint with I-shape leaf beams, other exceptions exist, as

shown in Figure 2.18 where β_{xi} equals 45 degrees. Despite this deviation, the joint still retains its spherical characteristics. However, the three embodied 45-degree I-shape leaf beams exhibit strong coupling relationships, resulting in heightened stiffness in all directions. This may pose a drawback, necessitating a higher actuation force. The deformed configuration of the spherical joint is shown in Figure 2.18(b).

2.2.3.2 Model errors

The obtained spatial kinetostatic models for the general spherical joint and the GSTC leaf beam contain source errors from the SBCM [24, 25]. On the one hand, the SBCM is based on the Euler-Bernoulli beam assumption that disregards the shear effect. In the case of stubby beams, the model error could be significant. To address this issue, the Timoshenko beam theory, which accounts for the effect of shear strains in a beam and adds a correction term to the Euler-Bernoulli beam theory, can be used. Additionally, the SBCM can introduce truncation errors due to the resulting closed-form solutions [8].

Moreover, during the FEA verification of the force-displacement characteristics of the GSTC leaf beam or the spherical joint, we observed that errors tend to be more pronounced when the resultant translation or rotations are small. This may be caused by numerical precision limitations. In FEA, the finite element method involves approximations and numerical calculations, which can introduce rounding errors. When the results are small, these errors can be significant relative to the magnitude of the result. Despite this, such inaccuracies in FEA are considered acceptable. Additionally, applying boundary conditions, including forces or displacements, which enable substantial movements in all directions simultaneously can be challenging in FEA, whereas this is more straightforward in analytical models. Understanding the above issues can help us better interpret the observed differences between the FEA and analytical models.

2.3 Summary

Chapter 2 presented two advanced parameterized nonlinear models to accurately characterize the behavior of general flexure beams: a 2D nonlinear model for general lumped-compliance beams and a 3D model for GSTC leaf beams. These models are instrumental in capturing the complex nonlinear force-displacement relationships critical

for designing precise and high-performance compliant mechanisms.

The 2D nonlinear GLBM model, was developed to overcome limitations in existing approaches. It enables accurate prediction of force-displacement characteristics for various configurations, such as folded and inverted beams. Our analysis revealed that the error between the analytical results and the FEA results was in the range of 2% to 6% for a large deflection (transverse displacement over 40% of the beam length).

The 3D nonlinear model developed for the GSTC leaf beam establishes a comprehensive spatial framework. It accurately predicts the spatial kinetostatic behavior of beams that provide a single-translation constraint along one axis while allowing five degrees of freedom in other directions. FEA validation across various beam configurations highlights its strong accuracy and adaptability. For motion ranges spanning 10% to 20% of the beam length, the maximum error remains below 10%, even under challenging configurations. Notably, the maximum error is observed in constrained directions where displacements are minimal, which aligns with expectations due to the inherent limitations of such constraints. During FEA validation, larger errors were observed when resultant translations or rotations were small, likely due to numerical precision limitations. While FEA encountered challenges in applying boundary conditions to enable simultaneous substantial movement in all directions, the analytical model effectively handled these conditions, underscoring its reliability and flexibility.

Despite their accuracy and efficiency, the proposed models have certain constraints. Both models assume elastic material behavior and do not account for plastic deformation or fatigue, which could influence long-term performance in real-world applications. Additionally, the models focus on force-displacement relationships rather than detailed stress analysis, meaning further refinements or FEA-based stress evaluation may be necessary for high-precision applications. Numerical precision issues also arise when the resultant displacements or rotations are small, affecting accuracy in low-motion scenarios. Moreover, while the models cover a broad range of beam configurations, extreme geometric nonlinearities or highly asymmetric loading conditions may require additional refinements or hybrid modeling approaches for improved accuracy.

The parameterized models introduced in this chapter provide a robust foundation for

precise and efficient modeling of flexure beams, facilitating rapid and iterative design processes. Chapter 5 will further explore the practical applications of these models in optimizing compliant amplifiers, parallel manipulators, and spherical joints. These applications will demonstrate the models' versatility and effectiveness in advancing the design and functionality of compliant mechanisms across diverse engineering domains.

CHAPTER 3

DESIGN AND NONLINEAR ANALYSIS OF NEARLY-CONSTANT AMPLIFICATION RATIO COMPLIANT MECHANISMS

In advancing compliant mechanism design, achieving a stable displacement amplification ratio across a range of input displacements is a relatively underexplored area. Chapter 3 addresses this gap by introducing an innovative over-constraint-based nearly-constant amplification ratio compliant mechanism (OCARCM), which minimizes variations in the amplification ratio, a critical factor in applications requiring consistent force and motion amplification. This chapter builds on the foundational principles and models discussed in previous chapters to establish a nonlinear framework specifically for compliant amplifiers, utilizing an over-constraint strategy to ensure enhanced stability in amplification performance.

The development of the OCARCM leverages the generic BCM method, combined with FBD analysis, to derive closed-form solutions that elucidate the nonlinear kinetostatic characteristics of this design. A comparative analysis between the OCARCM and the conventional bridge-type compliant amplifier is provided, focusing on the stability of the amplification ratio under various loading conditions. Results indicate that the OCARCM demonstrates remarkable stability, with only a 1% change in amplification ratio across the displacement range, compared to a 14% variation in the bridge-type amplifier under identical conditions. This chapter thus presents a robust modeling approach, verified through FEA with less than a 1% difference from the analytical model and experimentally validated with a maximum error of 3.4%.

3.1 The prior art of compliant mechanism-based amplifier

A compliant mechanism-based amplifier (compliant amplifier in short) can be used either as a motion amplification mechanism to increase the stroke of a device or as a motion reducer to increase the motion resolution. For example, the compliant-mechanism-based piezoelectric actuator incorporates a compliant stroke amplification mechanism to amplify the motion range since a piezoelectric actuator without an amplification mechanism can produce a stroke generally less than 0.1% of its length. Instead, the compliant amplifier can be incorporated into the piezoelectric actuator to achieve nano or even sub-nano resolution by swapping the input and output to achieve a resolution refinement.

A compliant amplifier exhibits several merits due to being a compliant mechanism, such as wear-free, zero noise, zero backlash, and vacuum compatibility [7, 8], which is essential in extensive applications, such as jet dispensing [178-180], energy harvesting [181-184], nanopositioner actuation [185-189]. Currently, three types of compliant amplifiers are being widely used, i.e., the bridge-type [179, 185, 190-194], the lever type [195-197], and their derivatives [183, 187, 198-201]. The bridge-type amplifier is mostly used due to its compact and symmetric structure [202-204].

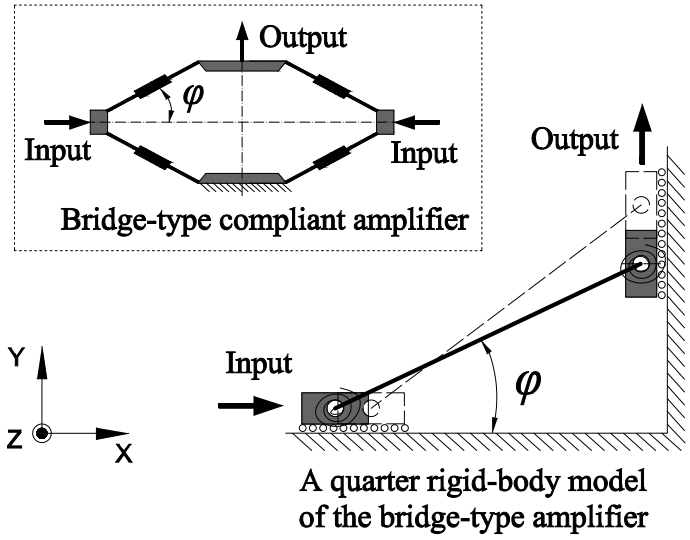


Figure 3.1 A quarter of the bridge-type compliant amplifier with a nonconstant amplification ratio.

A quarter of the bridge-type compliant amplifier can be kinematically treated as a rigid-

body double-slider mechanism (Figure 3.1), whose instantaneous amplification ratio at the current configuration can be expressed as $1/\tan\varphi$ [205]. As the input displacement in the X-direction increases, the geometry parameter φ of the bridge-type compliant amplifier will change, which leads to the change of the amplification ratio. In particular, the amplification ratio of such a mechanism exhibits a sudden increase and a gradual decrease over the range of the input displacement [164]. The change of the amplification ratio in the bridge-type amplifier remains an open issue. However, it is important to understand the potential benefits of a constant amplification ratio in a compliant amplifier before considering alleviating the changes.

The concept of a constant amplification ratio in compliant amplifiers has received limited attention in previous research, with only a few papers mentioning it. In [193], the author states that a constant amplification ratio is desirable for motion reduction in order to achieve fine position adjustments. Additionally, in [206], the authors highlight the control consideration of the variable amplification ratio for achieving high-accuracy positioning. Although the applications of a constant amplification ratio have not been extensively studied, incorporating this feature into a compliant amplifier design can provide valuable insight into predicting the output motion. A tangible application would be desired in the generation of uniform output motion resolution/precision, over the whole range of motion, in micro-/nano-positioning. In such an application, the input motion resolution is usually constant and determined by the actuator (such as PZT), then the output motion resolution is also constant if the amplification ratio is also constant, leading to uniform output motion resolution/precision over the whole range of motion.

The nonlinear modelling method based on the BCM will be used to offer a more accurate analysis of the characteristics of the compliant amplifier under large deflection. The BCM captures the geometric nonlinearities and load-stiffening effects in flexure beams [110]. Unlike the parameterized models developed in Chapter 2, which offer detailed flexibility for complex configurations, BCM provides a more streamlined approach well-suited for this application. BCM effectively models intermediate and large deflections in beams with moderate computational complexity, making it particularly valuable for compliant mechanisms that do not require the fully parameterized geometric flexibility of models

like the GLBM.

This chapter presents several main contributions:

1) The constant amplification ratio is first studied in the design of a compliant amplifier.
2) A novel over-constraint based nearly-constant amplification ratio compliant mechanism (OCARCM) is proposed, which is able to provide a nearly constant amplification ratio.
3) The nonlinear closed-form solutions of the OCARCM are derived with consideration of the effect of payloads.
4) An experiment is conducted with the consideration of payload (using a loading spring) to mimic the actuation of a compliant mechanism.

3.2 Mechanism design

Several approaches have been proposed in the literature for designing compliant mechanism-based amplifiers, each offering distinct advantages in achieving large displacement or force amplification ratios. A common strategy is the multistage design method, which enhances the amplification capability of the mechanism [207-209]. Flexure hinges are preferred over distributed-compliance beams [210-212] in order to improve the dynamic performance or load capacity of the compliant amplifier. Distributed-compliance beams are commonly used to reduce stress concentration in the compliant amplifier. A symmetrical arrangement is a commonly used method to avoid parasitic motion [2, 213, 214]. The use of serial or parallel connection of flexure modules in a compliant amplifier can lead to possible improvement of performance characteristics such as amplification ratio, parasitic motion, and load capacity [207, 215, 197, 210]. The over-constraint approach [168, 216] usually involves adding extra constraints to the compliant mechanism, such as additional beams or links, to restrict its undesired motion or performance characteristics. In this section, we employ a new over-constraint method to eliminate the amplification ratio change of a compliant amplifier maximally.

The amplification ratio of the bridge-type compliant amplifier changes with the input displacement. As shown in Figure 3.2(a), the α and β are the initial angles of the flexure beams. As the double slider mechanism at the bottom is actuated in the X-direction (the

slope of the link alters from α to α'), the amplification ratio increases. The double slider on the top is the 180-degree rotated version of the one at the bottom. When it is being actuated in the same direction as the one at the bottom, the amplification ratio decreases since the slope of the beam increases from angle β to angle β'. So, the amplification ratio of the double slider on the top is decreasing while the bottom one is increasing. If we want to constrain the amplification ratio from altering, we can simply connect the input cranks and output cranks of both double slider mechanisms, leading to an over-constraint configuration. However, the over-constrained rigid mechanism does not have any degrees of freedom, so the next step is the flexure module embodiment.

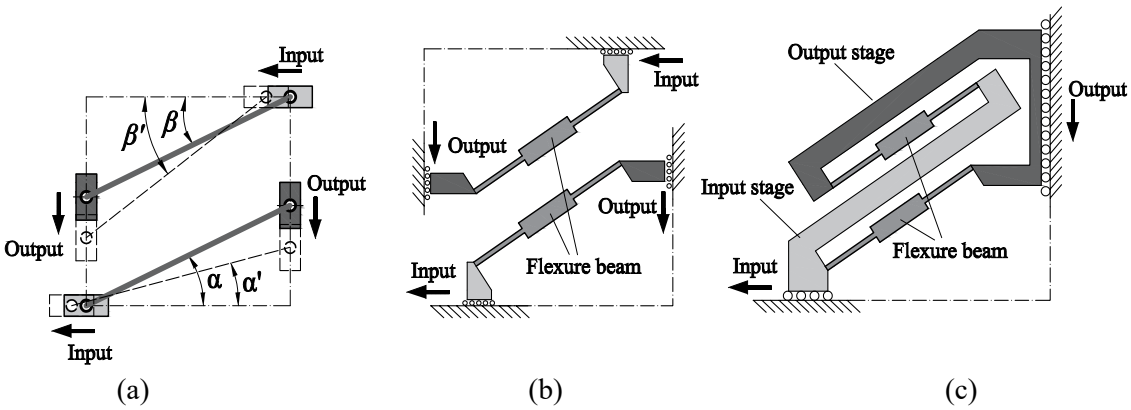


Figure 3.2 Design from traditional rigid mechanism to compliant mechanism: (a) two rotationally symmetric double slider mechanisms; (b) its compliant equivalent; (c) the over-constraint compliant mechanism.

Figure 3.2(b) shows the compliant designs of the two double slider mechanisms with parallel-arranged beams. By connecting their inputs/outputs with a rigid link, we can obtain the over-constraint compliant mechanism as shown in Figure 3.2(c). The mechanism in Figure 3.2(c) is a quarter of the bridge-type amplifier. The fully embodied amplifier, called OCARCM, is depicted in Figure 3.2(a). The OCARCM is mainly composed of two input stages, output stages, a base, and eight generic flexure beams. The OCARCM is an effective solution that not only mitigates changes in the amplification ratio but also significantly enhances the in-plane rotational stiffness of both the input and output stages compared with the bridge-type amplifier. This better-restricted rotation attributes to the formed parallelograms in the over-constraint design, which provide additional stability to the system.

The geometric parameters of the OCARCM are labeled in Figure 3.3(b), and we can notice that the geometry of the OCARCM is symmetric about the centrelines. The input force F_{IN} is assigned in the X-direction and the payload in the Y-direction is defined as F_L. It is also worth noting that only the compliant segments of the flexure beam are deformable, and the rest are rigid.

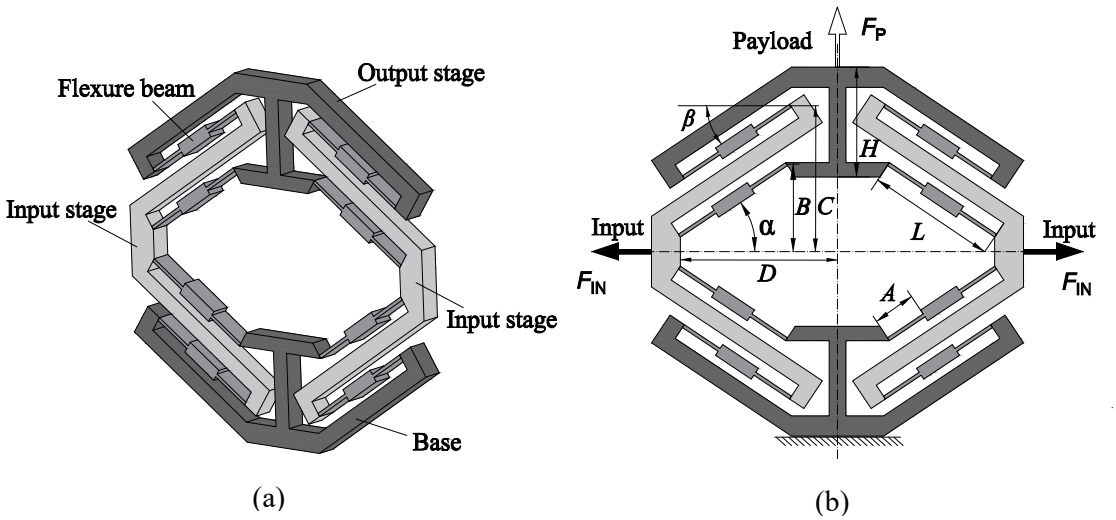


Figure 3.3 A schematic of OCARCM design with parameter labelling: (a) isometric view; (b) the front view.

3.3 Nonlinear analytical modeling and analysis

This section presents the nonlinear analytical modeling of the proposed OCARCM. The BCM for a generic flexure beam, detailed in Appendix D, was employed for modeling generalized beam flexure, allowing for accurate characterization of the proposed amplifier in conjunction with the FBD system modeling method. To assess the OCARCM's performance, a comparison with bridge-type amplifiers using the same generic flexure beam slope was conducted. Analytical results were validated against nonlinear FEA, with a maximum error of less than 3%, underscoring the model's robustness. Further analysis of the OCARCM's performance was conducted from multiple perspectives, including a study on how variations in flexure beam slope impact force-displacement characteristics and amplification ratio. This comprehensive examination highlights the influence of beam slope on the overall effectiveness of the amplifier, providing insights into optimization strategies for enhanced performance.

3.3.1 Kinetostatic analysis of the amplifier

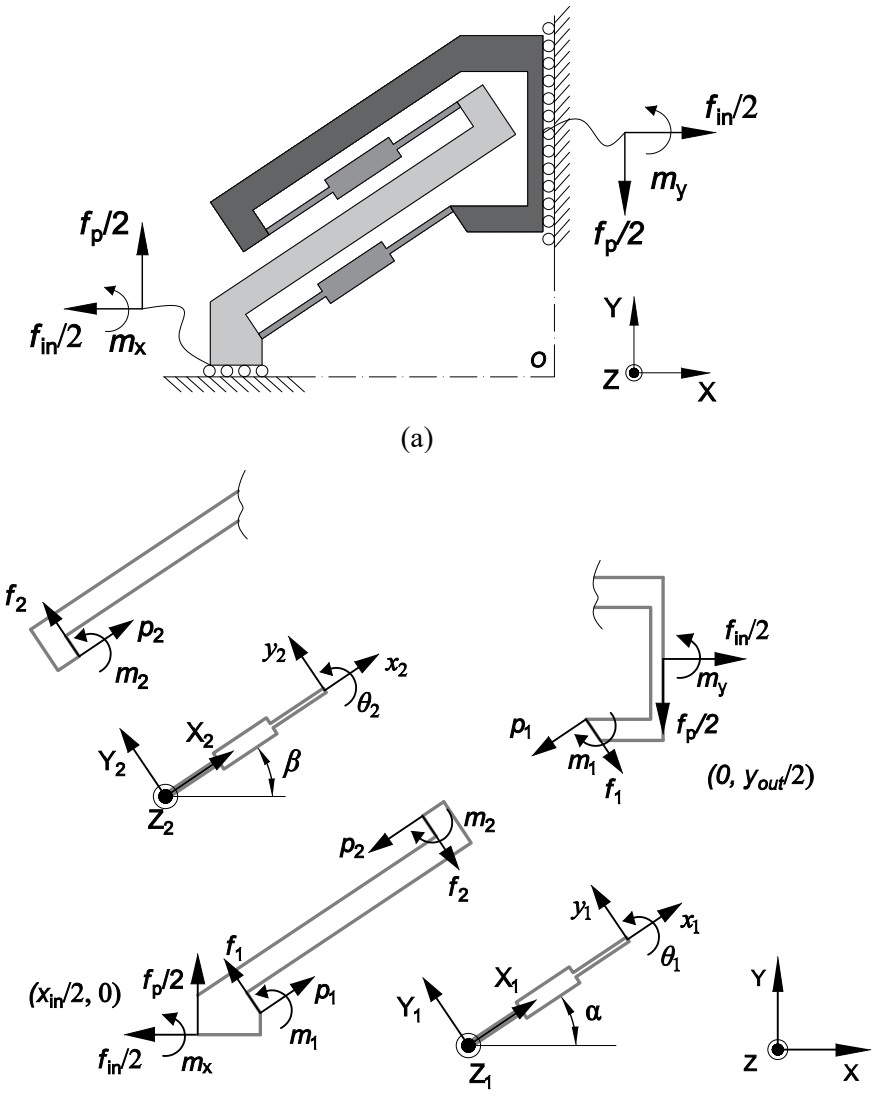


Figure 3.4 The static modelling of a quarter of the amplifier: (a) a quarter of the OCARCM; (b) the FBD of the OCARCM.

As the OCARCM is geometrically symmetrical, a quarter of the geometry is used to synthesize its kinetostatic characteristics. The FBD of a quarter of the OCARCM is presented in Figure 3.4(b), where the deformation is assumed to occur only in the flexure segments of the lumped-compliance beam, and the other parts are rigid. f_{in} and f_p labeled in Figure 3.4 are the normalised input force and the payload, respectively. m_x and m_y are the supplementary moments to maintain the zero rotation of the input stage and output

stage, respectively. Based on the constrained relations and the symmetric structure, the rotational displacement θ_i of the rigid stages in the amplifier is equal to zero. Then the constitutive equations can be simplified as:

$$\begin{cases} f_i = k_{11}^{(0)} y_i + p_i k_{11}^{(1)} y_i \\ x_i = \dfrac{p_i}{k_{33}} + g_{11}^{(0)} k_{11}^{(1)} {y_i}^2 + p_i {y_i}^2 g_{11}^{(1)} \\ m_i = p_i k_{21}^{(1)} y_i + k_{21}^{(0)} y_i \end{cases} \tag{3.1}$$

Given that the coefficient $k_{11}^{(1)}$ is equal to $-2g_{11}^{(0)}$, and $g_{11}^{(0)}$ is 400 orders of magnitude larger than $g_{11}^{(1)}$. The constitutive equation in the X-direction (Eq. (3.1)) can be further simplified by removing the third term for the practical interest.

The load-equilibrium conditions of each rigid stage can be derived from the free-body diagrams of the rigid stages shown in Figure 3.4(b). It is worth noting that the moment reference centre is the geometry centre *O* as labeled in Figure 3.4(a).

$$\begin{cases} f_{\text{in}} / 2 + f_1 \sin\alpha - f_2 \sin\beta - p_1 \cos\alpha + p_2 \cos\beta = 0 \\ -f_{\text{p}} / 2 - p_1 \sin\alpha + p_2 \sin\beta - f_1 \cos\alpha + f_2 \cos\beta = 0 \\ m_{\text{y}} - m_1 + m_2 - f_{\text{in}}(b + h/2)/2 - f_1 b \sin\alpha + f_1 \cos\alpha(d - l\cos\alpha) + p_1 b \cos\alpha \\ + p_1 \sin\alpha(d - l\cos\alpha) + f_2 \sin\beta(c - l\sin\beta) - f_2 d \cos\beta - p_2 \cos\beta(c - l\sin\beta) - p_2 d \sin\beta = 0 \end{cases} \tag{3.2}$$

$$\begin{cases} -f_{\text{in}} / 2 + f_2 \sin\beta - f_1 \sin\alpha - p_2 \cos\beta + p_1 \cos\alpha = 0 \\ f_{\text{p}} - f_2 \cos\beta + f_1 \cos\alpha - p_2 \sin\beta + p_1 \sin\alpha = 0 \\ m_{\text{x}} + m_1 - m_2 + f_l d / 2 - f_1 d \cos\alpha + f_1 \sin\alpha(b - l\sin\alpha) - p_1 \cos\alpha(b - l\sin\alpha) \\ -p_1 d \sin\alpha - f_2 c \sin\beta + f_2 \cos\beta(d - l\cos\beta) + p_2 c \cos\beta + p_2 \sin\beta(d - l\cos\beta) = 0 \end{cases} \tag{3.3}$$

The conditions of the geometric compatibility of the amplifier are given by,

$$\begin{cases} x_1 = -\dfrac{1}{2} y_{\text{out}} \cos\alpha + \dfrac{1}{2} x_{\text{in}} \cos\alpha \\ y_1 = -\dfrac{1}{2} y_{\text{out}} \cos\alpha - \dfrac{1}{2} x_{\text{in}} \sin\alpha \end{cases} \tag{3.4}$$

$$\begin{cases} x_2 = -\dfrac{1}{2} x_{\text{in}} \cos\beta + \dfrac{1}{2} y_{\text{out}} \sin\beta \\ y_2 = \dfrac{1}{2} x_{\text{in}} \sin\beta + \dfrac{1}{2} y_{\text{out}} \cos\beta \end{cases} \tag{3.5}$$

By solving the constitutive equations, load equilibrium and geometric compatibility equations simultaneously, one can obtain the displacements and amplification ratio as functions of applied forces. The analytical models for the general case of $\alpha \neq \beta$ are too complex to be presented here, which is graphically analyzed in Section 3.3.2 instead. The models for the case when the beam slope $\alpha = \beta$ are presented below.

$$\begin{cases} x_{\text{in}} = \dfrac{-3S^{1/3} f_{\text{p}} k_5 \sin\alpha\cos\alpha + 3S^{1/3} f_{\text{in}} k_5 (\cos\alpha)^2 - 48k_1 k_{33} \sin\alpha\cos\alpha + 2S^{2/3}\tan\alpha}{6k_{33}k_5 S^{1/3}} \\ y_{\text{out}} = \dfrac{-3S^{1/3} f_{\text{in}} k_5 \sin\alpha\cos\alpha - 3S^{1/3} f_{\text{p}} k_5 (\cos\alpha)^2 - 48k_1 k_{33} (\cos\alpha)^2 + 3S^{1/3} f_{\text{p}} k_5 + 2S^{2/3}}{6k_{33}k_5 S^{1/3}} \\ A_{\text{m}} = \dfrac{-3S^{1/3} f_{\text{in}} k_5 \sin\alpha\cos\alpha - 3S^{1/3} f_{\text{p}} k_5 (\cos\alpha)^2 - 48k_1 k_{33} (\cos\alpha)^2 + 3S^{1/3} f_{\text{p}} k_5 + 2S^{2/3}}{-3\sin\alpha\cos\alpha S^{1/3} f_{\text{p}} k_5 + 3S^{1/3} f_{\text{in}} k_5 (\cos\alpha)^2 - 48k_1 k_{33} \sin\alpha\cos\alpha + 2S^{2/3}\tan\alpha} \end{cases} \tag{3.6}$$

where

$$S = 6\sqrt{3}\sqrt{-27\left(\begin{array}{l} k_5^2 k_{33}\left(f_{\text{in}} + f_{\text{p}}\right)\left(f_{\text{in}} - f_{\text{p}}\right)(\cos\alpha)^2 - 2 f_{\text{in}} f_{\text{p}} k_5^2 k_{33}\cos\alpha\sin\alpha \\ - {f_{\text{in}}}^2 k_5^2 k_{33} - \dfrac{128k_1^3}{27} \end{array}\right) k_{33}^3 (\cos\alpha)^6}$$
$$+54k_5 k_{33}^2 (\cos\alpha)^3\left(f_{\text{in}}\sin\alpha + f_{\text{p}}\cos\alpha\right)$$

Furthermore, Eq. (3.6) can be simplified by dropping out some insignificant terms for an approximate calculation:

$$\begin{cases} x_{\text{in}} \approx -\dfrac{\tan\alpha\left(24(\cos\alpha)^2 k_{11}^{(0)} k_{33} - S^{2/3}\right)}{3k_{33}k_{11}^{(1)} S^{1/3}} \\ y_{\text{out}} \approx -\dfrac{24\,(\cos\alpha)^2 k_{11}^{(0)} k_{33} - S^{2/3}}{3k_{33}k_{11}^{(1)} S^{1/3}} \\ A_{\text{m}} = \dfrac{y_{\text{out}}}{x_{\text{in}}} \approx \dfrac{1}{\tan\alpha} \end{cases} \tag{3.7}$$

During the calculations for the amplification ratio (A_{m}), high-order terms are dropped without significantly affecting the accuracy of the results. The maximum error that results from dropping these high-order terms is less than 1.1%. Equation (3.7) shows that the amplification ratio can be approximated by 1/tanα (α is the initial angle). This indicates that the amplification ratio over the whole range of motion is primarily determined by the

flexure beam slope and is much less influenced by the input force and payload.

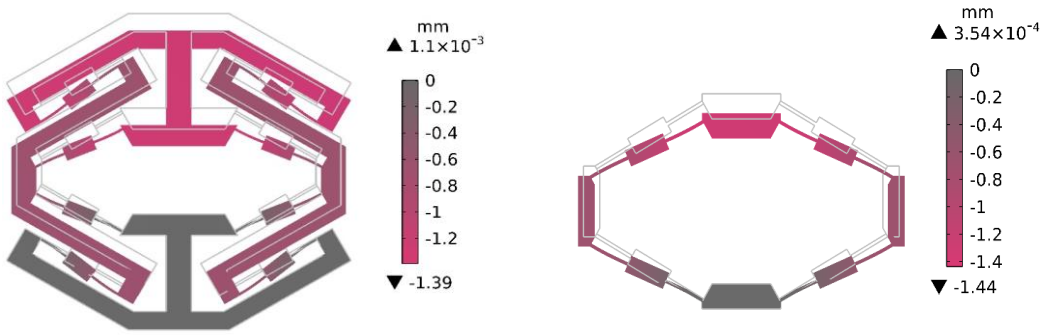
A comparison will be made between the amplification ratio characteristics of the OCARCM and those of the bridge-type compliant amplifier using the analytical model and FEA simulation. The main comparison variables are the different amplification ratios (by changing α and β), the different input and output forces, and the different beam stiffness (by changing A). The analytical model of the bridge-type compliant amplifier can be easily found by following the above derivation process.

3.3.2 Characteristics analysis with FEA verification

We conducted a comprehensive performance analysis of the OCARCM from multiple perspectives. This included a study of OCARCMs with varying flexure beam slopes to investigate how these slopes influence force-displacement characteristics and amplification ratios. Additionally, a comparative analysis between the OCARCM and bridge-type amplifiers with identical generic flexure beam slopes was performed to further evaluate performance differences. The case where the OCARCMs were assigned payload (F_L) was analyzed to examine their performance in response to the loading. Furthermore, the case where the lumped-compliance (a = 1/3) and distributed-compliance (a = 1/2) OCARCM is also considered. All the designs were modeled in COMSOL@5.0 using identical flexure beam parameters listed in Table 3.1. The simulation assumes that the stages and base set are rigid, similar to the assumptions made in analytical modeling. Nonlinear solvers were used since there are large elastic deformations. Finer hexahedra mesh was generated at the flexure beam to gain stable and accurate results. The aluminum alloy AL6061 with Young's Modulus 69 GPa and Yield Strength 276 MPa was assigned to the material. A series of incremental forces or displacements were applied to the input stages during the simulation. All the parameters were switched back to dimensional values for a more straightforward comparison.

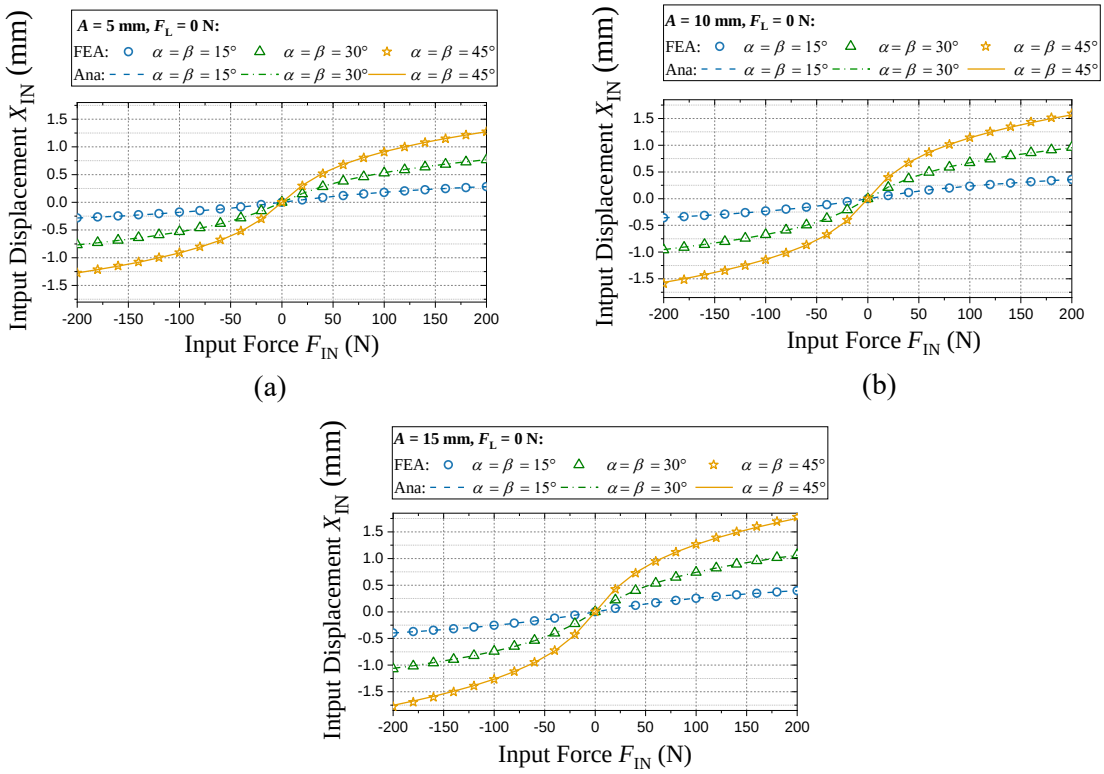
Table 3.1 Parameters for all the cases in this Section

L	*U*	*T*	*A*	
30 mm	8 mm	0.8 mm	Lumped-compliance: 5 mm and 10 mm	Distributed-compliance: 15 mm



(a) (b)

Figure 3.5 Displacement analysis: (a) the exaggerated view of the displacement plot of the OCARCM with the flexure beam slope of 30^0; (b) the deformation of the corresponding bridge-type amplifier.



(a) (b)

(c)

Figure 3.6 Force-displacement characteristics without payload (F_L = 0): (a) lumped-compliance (A = 5 mm); (b) lumped-compliance (A = 10 mm); (c) distributed-compliance (A = 15 mm).

Figure 3.5(a) plots the exaggerated results of applying 0.4 mm displacement at each input stage. The resultant displacement of the OCARCM is about 1.39 mm, while the displacement of the bridge-type amplifier is 1.44 mm. The reduced displacement of the

OCARCM reveals the over-constrained behavior occurring in the output stage.

The force-displacement relationship of both lumped-compliance and distributed-compliance OCARCMs are plotted in Figure 3.6. The plot reveals a good correlation between FEA and analytical results, where the maximum error is less than 1.0%, and it also shows that the OCARCM with a larger flexure beam slope has a larger stiffness. It can be observed in both analytical and FEA results that the force-displacement characteristic shows nonlinear characteristics, which are not encompassed by linear models.

In Figure 3.7, we compared the amplification of the lumped-compliance (A = 5 mm, A = 10 mm) and the distributed-compliance (A = 15 mm) OCARCMs to that of the lumped-compliance and distributed-compliance bridge-type amplifiers, respectively. It is worth noting that the amplification ratio is obtained based on Eq. (3.6). In the case of a zero-input displacement (x_{in}), the amplification ratio is not captured, since division by zero is mathematically undefined. In his way, the plots for the amplification ratio are not continuous lines. The plots reveal that the amplification ratio of the bridge-type compliant amplifier varies with the input displacement at a large scale while that of the OCARCM shows a nearly constant amplification ratio for both the lumped-compliance design and

the distributed-compliance design. Both FEA and analytical results show that the amplification ratio of the proposed OCARCM decreased by 1% while the bridge-type amplifier decreased by 13.9% for the design with the same flexure beam slope ($\alpha = \beta$) of 15^0. Moreover, the amplification ratio of the OCARCM is close to the simplified analytical expression ($A_m = 1/\tan\alpha$), especially when the displacement is small. The maximum error occurs in Figure 3.7(d) where the amplification ratio of the OCARCM is 1.73% smaller than the simplified results (the red dash-dot line).

It is also worth noting that there is a relatively larger nonlinearity in the amplification ratio of the design with a beam slope of 15^0 compared to the ones with 30^0 and 45^0. The nonlinear effect of load-stiffening and elastokinematic nonlinearities are associated with the axial load p. The nonlinear effects are significant for the OCARACM with a smaller beam slope as the proportional force of the input force in the axial direction imposed on each flexure beam is large. Thus, the amplification ratio of the design with a smaller beam

slope produces a larger nonlinear effect.

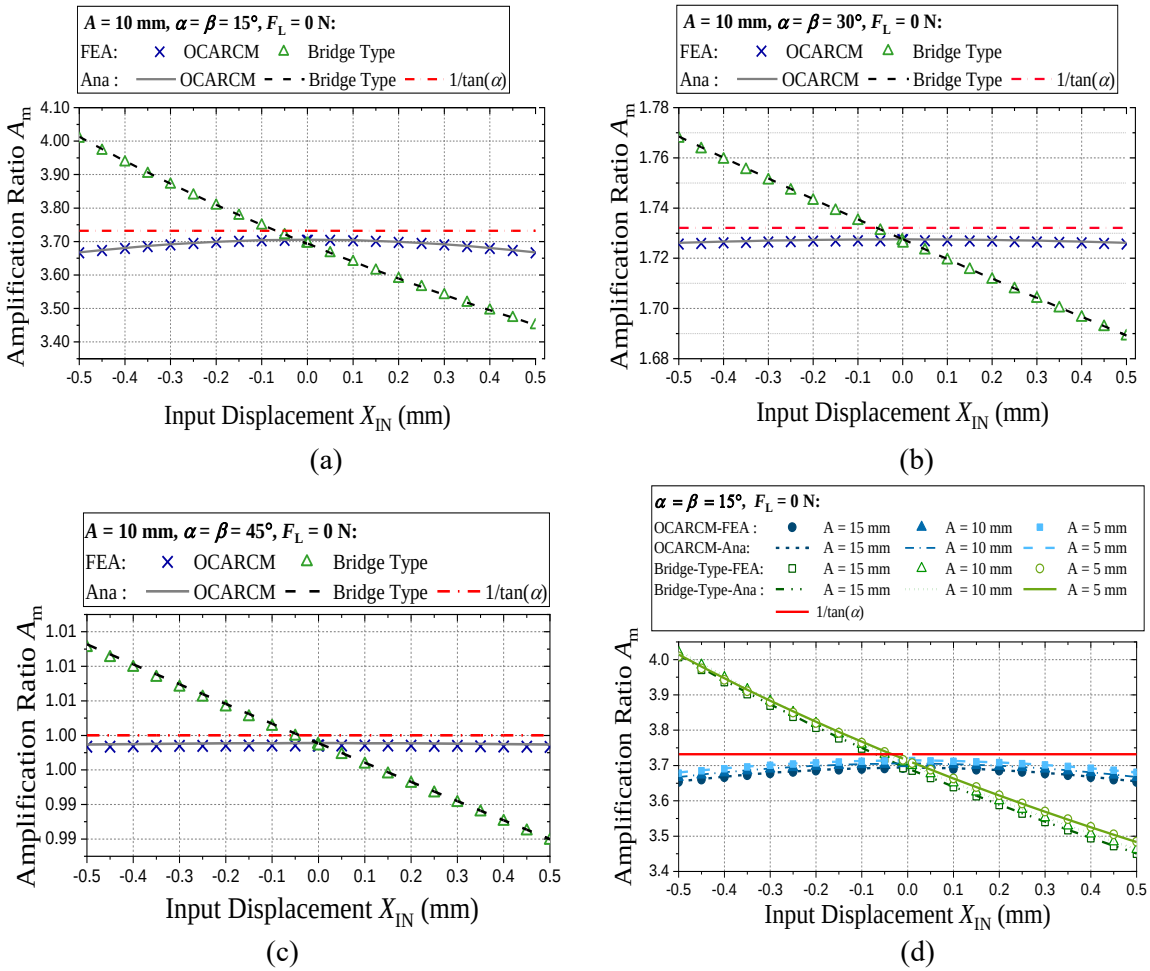


Figure 3.7 Comparison between bridge-type amplifier and OCARCM with the equal beam slope ($\alpha = \beta$): (a) lumped-compliance (A = 5 mm); (b) lumped-compliance (A = 10 mm); (c) distributed-compliance (A = 15 mm); (d) OCARCM compared with the bridge-type compliant amplifier with different compliance.

The effect of the payload (F_L) on the amplification ratio is illustrated in Figure 3.8. Figure 3.8 presents the amplification ratio of the lumped-compliance OCARCM (A = 10 mm, $\alpha = \beta = 15^0$) in response to different payloads. The results obtained from the FEA show good agreement with those obtained from the analytical results with a maximum error of 0.72%. The amplification ratio of the lumped-compliance OCARCM varies between 3.56 and 3.83 at small input as the payload changes from – 40 N to 40 N.

The amplification ratio of the bridge-type amplifier in response to the payload is graphically shown in Figure 3.8(b). The FEA results are consistent with the analytical

results. Both results indicate that the amplification ratio of the bridge-type amplifier changes at a large scale, ranging from 3.25 to 4.54. However, the variation of the amplification ratio is not only contributed by the payload but also by the character of the bridge-type amplifier itself. To demonstrate the effect of the payload on the amplification ratio, we plot the variation of the amplification ratio of the OCARCM and bridge-type amplifier in response to different payloads ranging from – 40 N to 40 N in Figure 3.8(c). The amplification ratio of the bridge-type amplifier varies within the orange region which is much larger than that of the blue region. This means the amplification ratio of the OCARCM is more robust to the applied payload. Both types of amplifiers also present the trend that the larger the payload, the greater the variation in the amplification ratio.

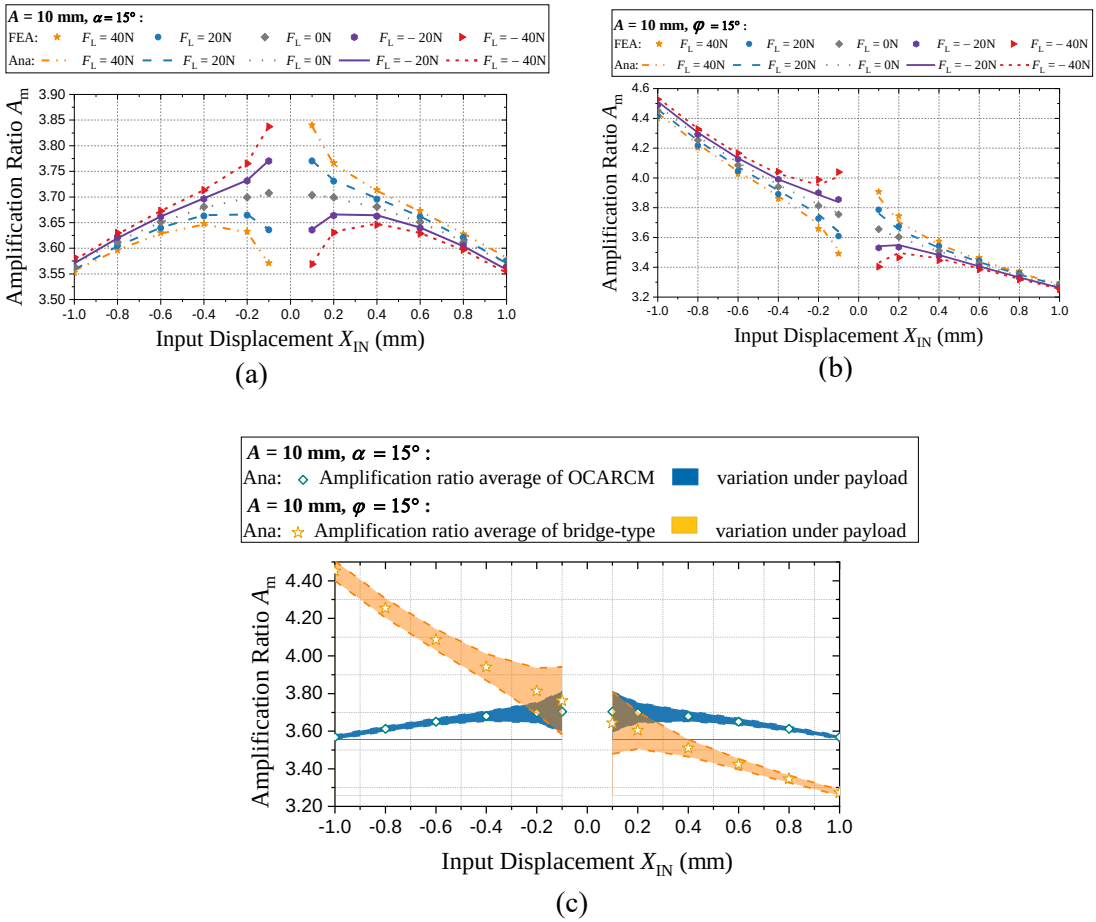


Figure 3.8 The amplification ratio under different payloads F_L: (a) the FEA results of the OCARCM compared with its analytical results; (b) the FEA results of the bridge-type compliant amplifier compared with its analytical results; (c) variation of the amplification ratio in response to the different payload F_L.

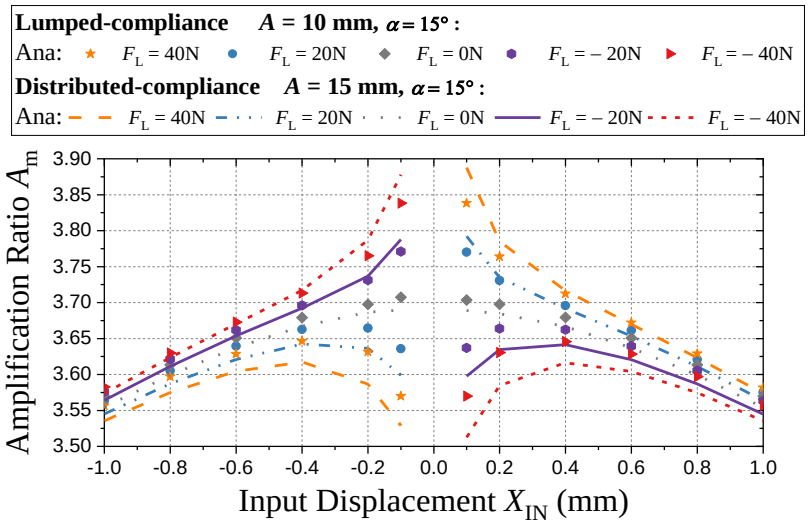


Figure 3.9 The comparison between the lumped-compliance and the distributed-compliance under different payloads F_L.

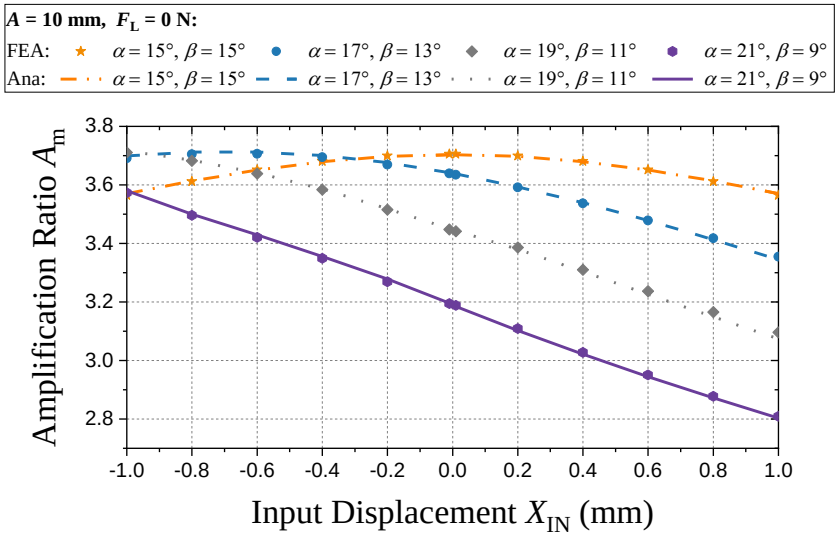


Figure 3.10 Amplification ratio of the lumped-compliance OCARCM with different beam slopes ($\alpha \neq \beta$).

The comparison between the amplification ratio of the lumped-compliance (relatively high stiffness) and the distributed-compliance (relatively high compliance) is plotted in Figure 3.9. The amplification ratio of the distributed OCARCM varies between 3.54 and 3.87, while the amplification ratio of the lumped-compliance OCARCM varies between 3.56 and 3.83 as the payload changes from – 40 N to 40 N. This indicates that the amplification ratio of the lumped-compliance OCARCM is more robust to the payload

compared with distributed-compliance OCARCM. Another pattern we can observe from the plot is that the stiffness has a slight influence on the variation scale of the amplification ratio. The difference is below 1.62% between the lumped-compliance OCARCM and the distributed-compliance OCARCM.

The influence of the different beam slopes ($\alpha \neq \beta$) on the amplification ratio is also investigated and plotted in Figure 3.10. A decrease in the amplification ratio first can be observed as the difference between the two flexure beams' slopes increases. With an increased slope difference (α minus β), the design also shows a more linear trend and a greater change in amplification ratio as the input displacement gradually increases. It tends to be preferable to design flexure beams with the same slope since they exhibit less deviation of the amplification ratio than those with different slopes.

3.4 Experiment tests

The distributed-compliance prototype was selected for experimental testing to validate the FEA and analytical results. A compliant loading spring was used as the payload to simulate the actuation typical in compliant mechanisms. The compliant loading spring was chosen as the payload to simulate real-world actuation conditions commonly found in compliant mechanism-based systems. Unlike rigid actuators or constant-force loads, compliant mechanisms often interact with other compliant structures, leading to force variations as displacement occurs. Using a compliant spring as the payload ensures that the experimental setup mimics practical scenarios where one compliant mechanism actuates another. Although such experimental studies are relatively less explored, they are gaining importance as compliant mechanisms see broader applications. The following subsections analyze and discuss the influence of the loading spring on the force-displacement characteristics and the amplification ratio of the OCARCM.

3.4.1 Fabrication of the OCARCM prototype

The prototype (Figure 3.11(b)) is monolithically manufactured using a CNC milling machine from a piece of AL7075 plate, using the same parameters listed in Table 3.1. The AL7075 material with Young's modulus of 71 GPa was selected due to its lightweight and

high-yield stress. A 1.5mm radius fillet corner is created by the milling tools. To avoid the deformation of the thin beam (0.8 mm), 3D-printed blocks are embedded to support the beams while machining. The overall dimension of this OCARCM prototype is 195 mm x 160 mm × 10 mm.

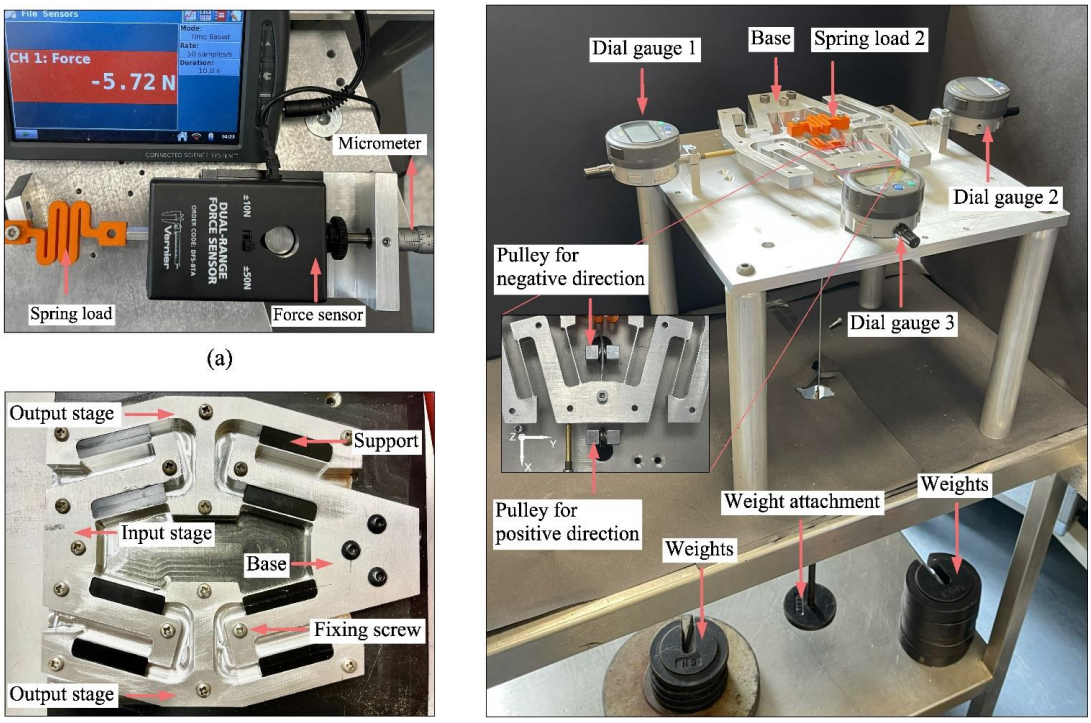


Figure 3.11 Prototype and experiment setup of the OCARCM: (a) testing of loading spring; (b) monolithically fabricated; (c) assembly.

3.4.2 Experimental setup

Loading springs were used to mimic the payload of the OCARCM, which is fabricated using 3D printing. Their stiffness was tested with a stiffness of 3.67 N/mm for loading stiffness 1 and a stiffness of 9.47 N/mm for load stiffness 2. The stiffness testing rig is shown in Figure 3.11(a). The motion range of the loading spring is designed to be 6 mm which satisfies the output displacement demand of the OCARCM. The force sensor and the micrometer are utilised to measure the reaction force and the input displacement, respectively.

Figure 3.11(c) shows the experimental setup of the OCARCM with a spring payload. In typical cases, a piezoelectric actuator is employed to achieve displacement amplification

in the amplifier. However, in this particular experiment, we opted to use a pulley system and weights as our actuators. By using the pulley system, we were able to simulate bidirectional input forces (against the PZT's unidirectional actuation), allowing us to fully characterize the properties of the OCARCM. Previously, the OCARCM was actuated by giving forces to both input stages, as illustrated in Figure 3.11. It was difficult to use a pulley system to actuate both input stages simultaneously with an even actuation force given to each input stage. Therefore, we fixed one of the input stages as the base, and the other input stage connects to the pulley system, as shown in Figure 3.11(b) and (c).

During the experiment, a pair of identical springs (loading spring 2) was installed on the top and bottom surfaces of the OCARCM to avoid the introduction of an out-of-plane payload. Dial gauges were used to measure the displacement of both the input and output stages, with a motion resolution of 0.001 mm and a spring force of 0.4-0.7 N. The OCARCM was actuated by applying a fixed force interval ranging from 0 to 200 N, and the corresponding dial gauge output displacements were recorded for each step. The experimental procedure was repeated three times to obtain an average result for each force interval.

3.4.3 Experimental results

The experiment was conducted to validate the FEA and analytical results. Figure 3.12(a), Figure 3.12(b), and Figure 3.12(c) plot the input force versus input displacement for different loading spring configurations. Both FEA and analytical results demonstrate good agreement, showing a nonlinear force-displacement pattern. However, experimental results display a more linear trend compared to FEA and analytical predictions. Figure 3.12(d) illustrates the error between experimental and analytical results, with a maximum discrepancy of 14.5%. This larger error, especially when a loading spring is used, can likely be attributed to part deformation (such as the output and input stages) that was assumed to be rigid in the analytical model. Additional factors, like minor assembly misalignments in the test rig, may also contribute. For instance, a slight misalignment between the string in the pulley system and the mechanism's centreline can cause uneven displacements between the two output stages.

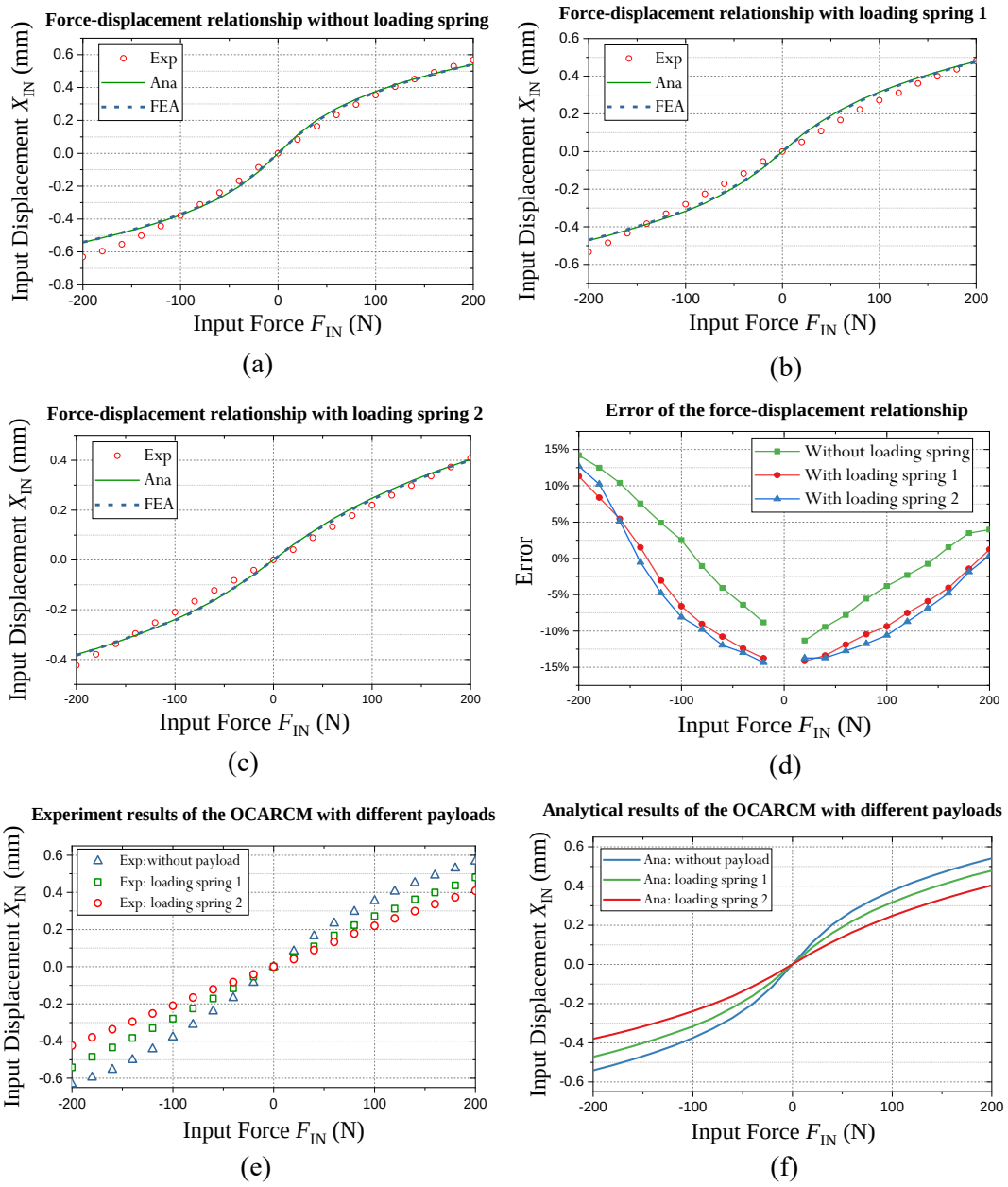


Figure 3.12 Force-displacement relationship: (a) without loading spring; (b) with loading spring 1; (c) with loading spring 2; (d) the error between experimental and analytical results; (e) integrated plots of experiment results; (f) integrated plots of analytical results.

Figure 3.12(e) and (f) compare experimental and analytical force-displacement characteristics for the OCARCM with and without a payload. These plots indicate that OCARCM stiffness increases as the stiffness of the loading spring increases, illustrating the load-dependent effect. Additionally, as loading spring stiffness increases, the force-displacement relationship tends to exhibit a more linear pattern, likely due to

deformations in components assumed rigid in the analytical model.

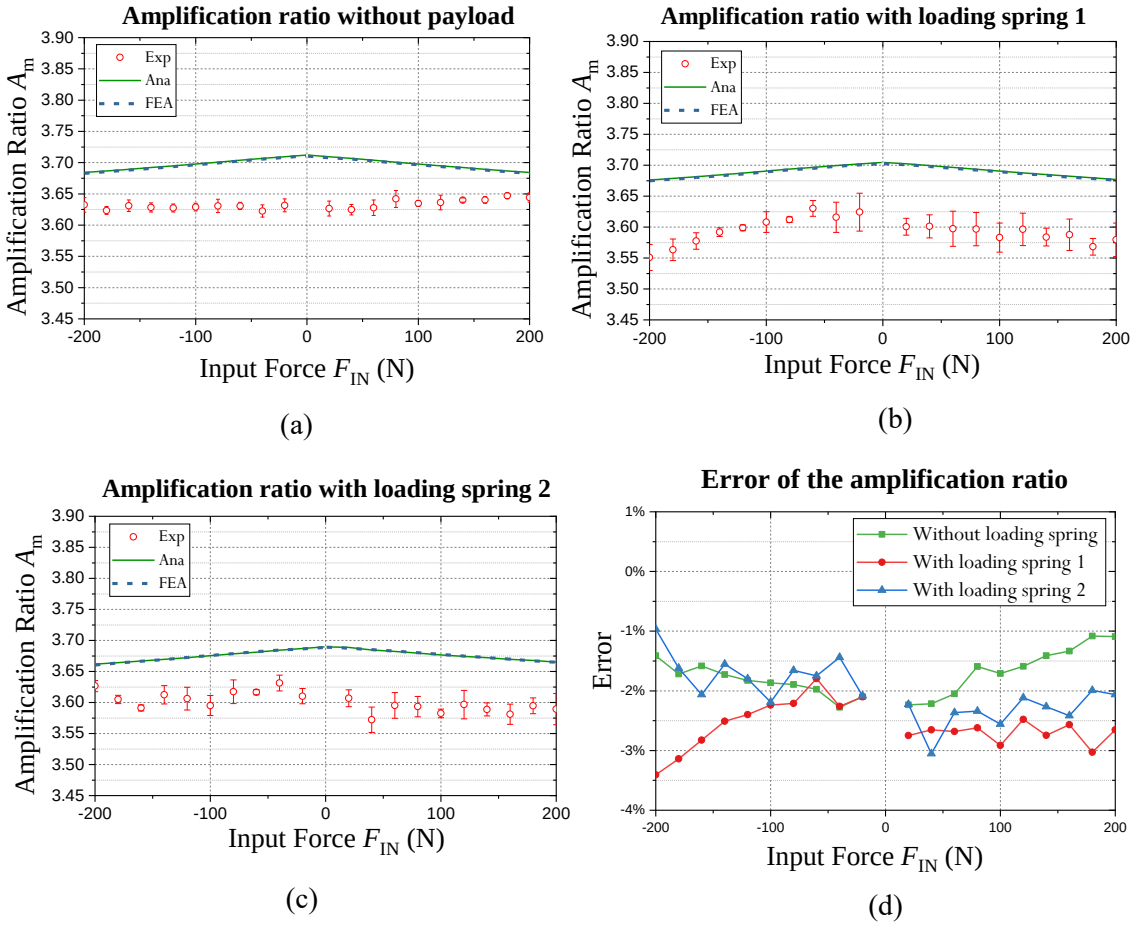


Figure 3.13 Amplification ratio of the OCARCM with different loading springs: (a) amplification ratio without payload; (b) amplification ratio with loading spring 1; (c) amplification ratio with loading spring 2; (d) Error between the experimental results and analytical results.

Next, we analyzed the influence of the loading spring on the OCARCM's amplification ratio, as shown in Figure 3.13. Experimental results show a generally constant amplification ratio with minor fluctuations, while FEA and analytical results show a slight trend of increase followed by a decrease. However, these variations are minimal, with experimental results fluctuating by less than 2.1% and FEA/analytical results by less than 0.67%. As the loading spring stiffness increases, the OCARCM amplification ratio slightly decreases. Error bars in Figure 3.13(a), Figure 3.13(b), and Figure 3.13(c) indicate the standard deviation across three experimental trials, where the standard deviation is generally lower for tests without payload compared to those with payload. This increased variation can be attributed to factors such as loading spring assembly

challenges and the limited repeatability of the 3D-printed loading spring. Figure 3.13(d) shows the error between experimental and analytical results, with a maximum fluctuation of 3.4%. The amplification ratio is primarily influenced by the flexure beam slope, meaning manufacturing inconsistencies like beam thickness or length variations have a negligible effect on amplification ratio accuracy.

3.5 Further discussions

3.5.1 Dynamic performance

A modal analysis was conducted to gain insight into the dynamic behavior of the OCARCM, with results compared to a bridge-type amplifier. Using FEA, the first four modes of both amplifiers were identified, as shown in Figure 3.14. For the OCARCM, the first mode occurs at 142.3 Hz and involves the translation of the output stage along the Y-axis, which is the desired output direction. The second mode, at 191.9 Hz, corresponds to translation along the X-axis. The third mode involves rotation of the output stage about the X-axis, and the fourth mode, at a significantly higher frequency of 1378 Hz, involves rotation about the Z-axis.

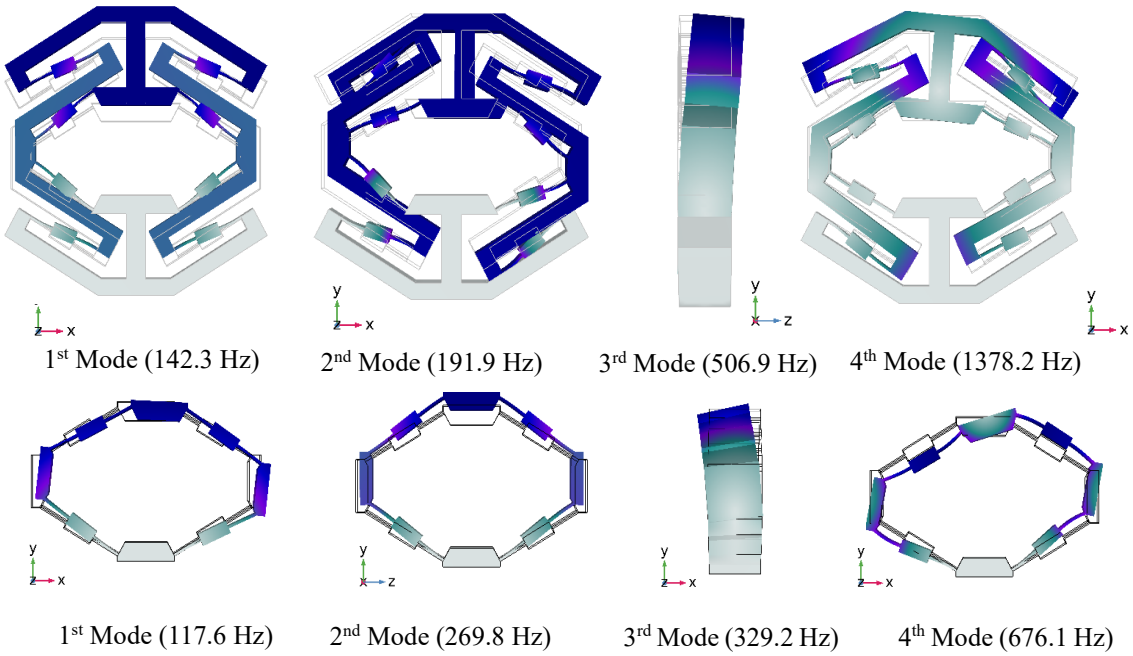


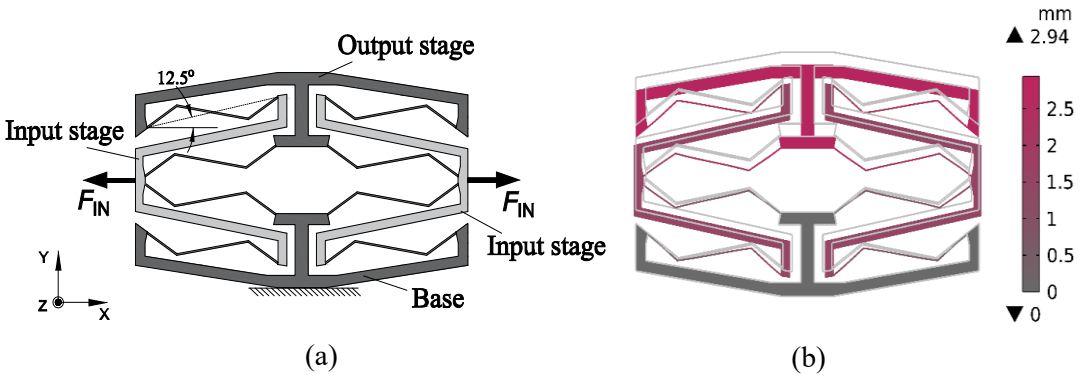
Figure 3.14 The first-four natural frequencies

In contrast, the bridge-type amplifier's first mode, occurring at 117.6 Hz, involves the undesired translation of the output stage in the X-direction. The second mode aligns with the OCARCM's first mode, translating the output stage along the Y-axis. The third and fourth modes are rotations about the X-axis and Z-axis, with natural frequencies of 329.2 Hz and 676.1 Hz, respectively.

The OCARCM's output stage is heavier than that of the bridge-type amplifier, resulting in a relatively lower first-mode natural frequency in the Y-direction compared to the bridge-type amplifier's second mode. However, other modes of the OCARCM occur at higher frequencies than their bridge-type counterparts. For instance, the fourth mode of the OCARCM, involving rotation about the Z-axis, has a natural frequency of 1378.2 Hz, which is double that of the bridge-type amplifier's fourth mode at 676.1 Hz. This difference arises because the OCARCM's design better constrains in-plane rotation due to its over-constraint design approach. Additionally, the bridge-type amplifier exhibits input stage rotation in its first mode (117.6 Hz), whereas the OCARCM's input stage rotation occurs in the fourth mode (1378.2 Hz), indicating that both the output and input stages of the OCARCM are less prone to rotational oscillations. While the OCARCM exhibits a lower first-mode natural frequency in the Y-direction, this could potentially be optimized by reducing the mass of the output stage, offering a pathway for enhanced dynamic performance.

3.5.2 Eliminating force-displacement nonlinearity

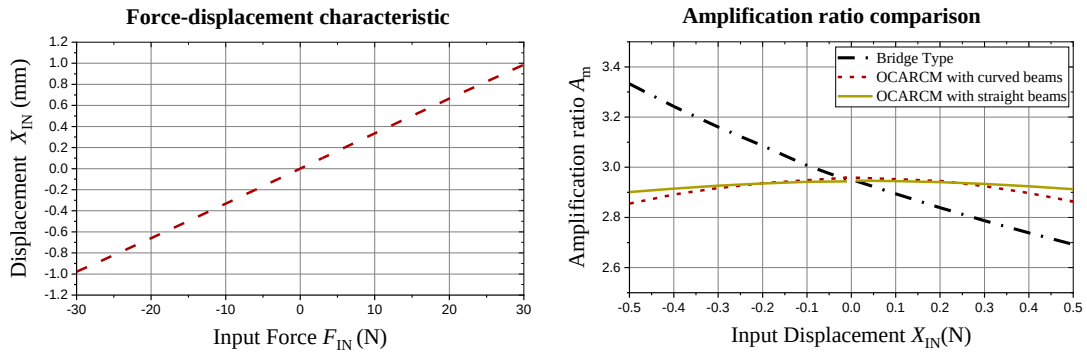
Over-constraint based design method mitigates variations in amplification ratios and increases robustness to payload variations. This may adversely lead to a nonlinear force-displacement relationship (load-stiffening effect) when using straight flexure beams as observed in Figure 3.12. This nonlinear effect is not desired for a very large range of motion and a small actuation effort [187, 217]. To eliminate the force-displacement nonlinearity, a potential solution is presented in Figure 3.15(a). Under the same topology, the straight beams were replaced by the Z-shape beams to alleviate the force-displacement nonlinearity.



(a) (b)

Figure 3.15 (a) OCARCM with Z-shape beams; (b) its deformed configuration.

The deformed configuration obtained from the FEA simulation is shown in Figure 3.15(b). The FEA shows a linear pattern between the force and displacement which is desired. We also compared the amplification ratio between the bridge-type compliant amplifier, OCARCM with straight beams, and OCARCM with Z-shape beams. The dominant factor that influences the value of the amplification ratio is the slope of the flexure beam. This also applies to OCARCM with Z-shape beams. The angle of the endpoints of the Z-shape beams is set as 12.5 degrees and corresponds to an amplification ratio of 2.95. And the angle of the straight beam in both bridge-type compliant amplifiers and the original OCARCM is set as 18.73 degrees to produce the same amplification ratio. The OCARCM with Z-shape beams shows a similar pattern as OCARCM with straight beams (previous design) but has a relatively larger variation in amplification ratio as depicted in Figure 3.16(b). And the bridge-type amplifier still shows a large variation in amplification ratio.



(a) (b)

Figure 3.16 Nonlinear FEA results: (a) force-displacement plot; (b) amplification ratio comparison.

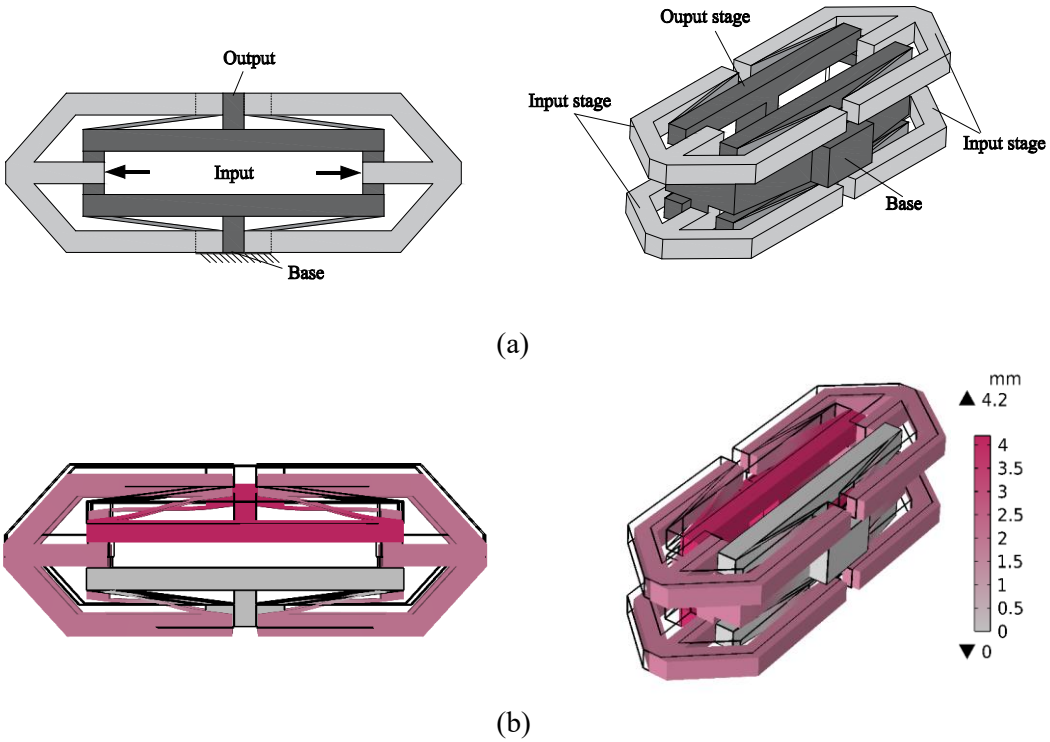


Figure 3.17 Three-layer design with reduced footprint: (a) geometry of the design; (b) deformed configuration.

3.5.3 Reducing the footprint

Compared to the bridge-type compliant amplifier, the footprint of the OCARCM increases due to the added extra flexure beams. This may bring a drawback in certain applications where space is limited. To address this issue, a multi-layer design method can be implemented [14, 218]. As presented in Figure 3.17(a), it shows a three-layer design with a reduced footprint. Figure 3.17(b) shows the deformed shape of the three-layer design. The footprint has been significantly reduced in comparison to the planar OCARCM. However, it simultaneously increases the difficulty of fabrication. The trade-off between footprint and manufacturing complexity should be taken into account during practical applications.

3.6 Summary

A compliant amplifier with a constant amplification ratio was designed to ensure uniform output motion resolution and precision. The proposed OCARCM is evaluated against a

commonly used bridge-type compliant amplifier, specifically for its ability to maintain a consistent amplification ratio with and without a payload. Using the FBD and BCM, closed-form solutions were derived to capture the nonlinearities in the force-displacement characteristics of the OCARCM. A prototype was fabricated and tested to validate these characteristics, and nonlinear FEA with large deformation enabled in COMSOL was performed to corroborate the analytical model.

The main contributions of this part of the work are as follows:

1) Constant amplification ratio: the OCARCM was designed to achieve a nearly constant amplification ratio, enabling consistent output motion resolution and precision.
2) Closed-form solutions: closed-form solutions were developed to accurately quantify the force-displacement characteristics and amplification ratio of the OCARCM, providing essential insights for design optimization.
3) FEA validation: nonlinear FEA results from Comsol show excellent agreement with the closed-form solutions, with a maximum error of only 1%, even under large deformation conditions.
4) Experimental validation: an experiment using a CNC-machined aluminum prototype demonstrated that the amplification ratio varied by less than 2.1% under loading spring conditions, with an error of under 3.4% between experimental results and FEA or analytical results within an output motion range of 1.76 mm.

The amplification ratio of the OCARCM is not perfectly constant due to the inherent nature of compliant mechanisms and the changing rate of the amplification ratio in the bridge-type amplifier. Unlike rigid mechanisms, compliant mechanisms exhibit geometric nonlinearities and load-dependent deformations, which introduce slight variations in the amplification ratio.

The OCARCM is formed by two oppositely arranged bridge-type amplifiers, which work together to balance their respective amplification variations. As the mechanism is activated, one bridge-type amplifier experiences a decreasing amplification ratio, while the other exhibits an increasing amplification ratio. However, this compensation is not perfectly symmetrical, meaning the changing rates of amplification do not fully cancel each other out. This imbalance leads to a minor fluctuation in the overall amplification

ratio.

Despite this, the OCARCM still maintains a significantly more stable amplification ratio compared to a single bridge-type amplifier, where amplification can vary by a much larger margin (e.g., 13.9%). The small deviation confirms the effectiveness of the OCARCM design in achieving a nearly constant amplification while minimizing amplification fluctuations inherent in compliant mechanisms.

CHAPTER 4

DESIGN AND NONLINEAR ANALYSIS OF A MIRROR-SYMMETRICAL XY PARALLEL MANIPULATOR

Chapter 4 focuses on the design and nonlinear analysis of a mirror-symmetrical XY compliant parallel manipulator (XY CPM) intended to address common challenges in high-precision positioning applications, including parasitic rotations, cross-axis coupling, and limited motion range. Traditional XY CPM are highly valued for applications requiring fine precision, yet they often experience undesired parasitic motions and coupling errors that can compromise overall performance. To mitigate these issues, this chapter introduces a novel mirror-symmetrical design that improves motion decoupling and enhances stiffness without increasing the mechanism's footprint.

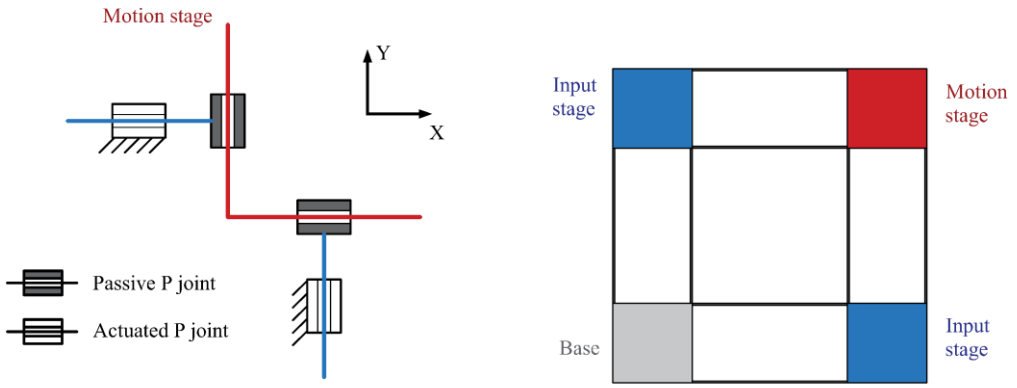
The nonlinear analysis in this chapter utilizes the BCM for slender flexure beams to predict the force-displacement behavior under varying loading conditions. While the advanced parameterized models developed in Chapter 2 provide a more comprehensive framework for general flexure beams, the choice of BCM for this study is based on two key reasons.

First, our developed model can be reduced to the BCM, meaning that the fundamental principles remain consistent, but the BCM offers a more streamlined and computationally efficient approach for this specific application. Since the mirror-symmetrical XY CPM design primarily involves slender flexure beams with well-defined boundary conditions, the BCM provides sufficient accuracy while simplifying the analytical process.

Second, the design is already fully defined, making the use of our parametric nonlinear model unnecessary, as geometry optimization is not the focus of this study. The parametric models developed in Chapter 2 are particularly valuable for exploring a broad

range of configurations and optimizing flexure beam geometries. However, in this case, the compliant parallel manipulator has a fixed and well-established structure, so applying the fully parameterized model would introduce redundancy without offering significant additional benefits.

This chapter outlines the detailed mechanism design, nonlinear modeling, FEA validation, and experimental tests conducted to ensure that the mirror-symmetrical configuration achieves minimal cross-axis coupling and enhanced motion range. The results affirm the effectiveness of this XY CPM design for applications where precision, compactness, and minimized parasitic effects are paramount, setting the stage for more refined multi-objective optimizations in future work.



(a) Rigid-body 2-PP parallel mechanism (b) 2-PP XY CPM

Figure 4.1 Exactly-constrained 2-PP mechanism

4.1 Prior art of the XY CPM

Currently, great efforts have been made to design high-precision XY CPMs with reduced parasitic rotation and large stroke to satisfy a large range of applications. In an XY CPM, the parasitic rotation refers to the in-plane rotational yaw of a rigid stage, which is inherent over the primary motion that must be suppressed by design since it cannot be compensated by control. To design a high-precision CPM, we should also consider other characteristics including: (1) a large range of motion in a compact footprint, (2) minimised cross-axis coupling error, (3) maximal actuator isolation, (4) minimum lost

motion, (5) large out-of-plane stiffness, and (6) high thermal and manufacturing insensitivities [219, 218, 220, 221].

An XY CPM can be constructed from an exactly-constrained rigid-body 2-PP mechanism which is composed of two legs. Each leg consists of two P joints (P: prismatic), one actuated P joint and one passive P joint by a serial arrangement as shown in Figure 4.1(a). We can simply replace each rigid P joint with a compliant translational joint to construct an XY CPM. As presented in Figure 4.1(b), a 2-PP XY CPM is embodied by replacing the P joint with a basic parallelogram module. From the perspective of constraints, CPMs fall into two categories: exactly-constrained and overconstrained. The representative exactly-constrained CPM is the 2-PP XY CPM presented in Figure 4.1(a), which produces a fairly large parasitic rotation. To mitigate the parasitic rotation, overconstrained designs have been well explored in the literature. For instance, an overconstrained 4-PP XY CPM with a rotationally symmetric configuration is shown in Figure 4.2(a). The method of using rotational-symmetry strategy to configure the XY CPM is firstly investigated by Awtar [153]. Such configuration makes the design very compact, and the parasitic rotation can be significantly reduced compared to the exactly-constrained design. Du et al. [222] proposed a 4-PP XY CPM as shown in Figure 4.2(b). This design uses 12 basic parallelogram modules as the constitutive mechanism which are arranged in a mirror-symmetric configuration. Such arrangement can further minimise the parasitic rotation, but magnify the footprint compared to the rotationally symmetric design. Herpe et al. [223] designed a 4-PRP XY CPM as shown in Figure 4.2(c). Each leg of the design simply has four flexure beams, forming two prismatic joints and one rotational joint (R joint). The footprint of this design is very small, but it produces a relatively large cross-axis coupling error. To eliminate the cross-axis coupling error, Hao et al. [216] further developed a completely-decoupled XY CPM using non-underconstrained compliant modules that are arranged in mirror-symmetry, with a rigid bar to connect two close-to-base rigid stages along each axis as shown in Figure 4.2(d).

In addition to the mirror-symmetry used for constraining the parasitic rotations, the connection bars act as over constraints to further alleviate the parasitic motions. However, the introduced connection bars create challenges for monolithic manufacturing and

increase the footprint in the out-of-plane direction. Although considerable advances were made in reducing the parasitic rotation, solutions for designing both compact and minimised parasitic rotation have not been fully explored. The rotationally symmetric design has a very compact structure, but it yields a relatively large parasitic rotation compared to the mirror-symmetric designs. The mirror- symmetric designs generally produce smaller parasitic rotation, but the added constraints enlarge the footprint and increase the actuation stiffness.

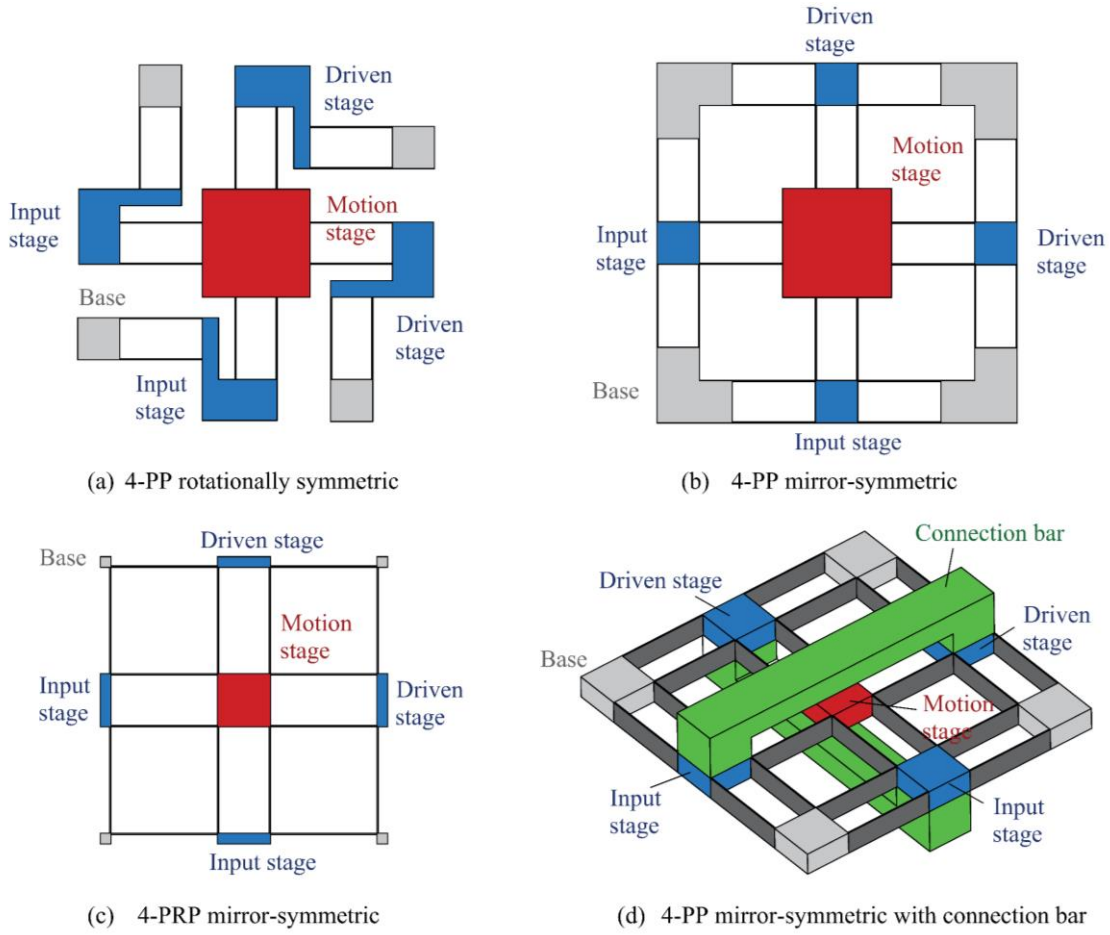


Figure 4.2 Overconstrained 4-PP CPMs

Motivated by the pros and cons of the existing XY CPMs, we proposed a methodology aiming at designing a compact XY CPM with minimised parasitic rotation without compromising other performances. The main idea of the proposed methodology is to use the mirror-symmetry to constrain the parasitic rotation of a rotationally symmetric design

without increasing the footprint based on a multi-layer design concept. The multi-layer design concept utilized in CPM has been reported in [224-226], which shows promising results in footprint reduction.

4.2 Mechanism design

4.2.1 The principle of minimising the parasitic rotation

A typical rotationally symmetrical design can consist of eight identical basic parallelogram modules as presented in Figure 4.3(a). To better illustrate the symmetry type, a black dot is used to represent the stiffness centre of a basic parallelogram module. Fixed frames and rigid stages are represented by solid lines, and the primary compliance of the basic parallelogram module is signified by a circle tangent to a short line. As shown in Figure 4.3(a), the solid lines connecting the stiffness centres are rotationally arrayed about the intersection point of the two centrelines. Such arrangement makes the design very compact, but it produces a relatively large rigid stage rotation under both a single-axis actuation and two-axis actuation.

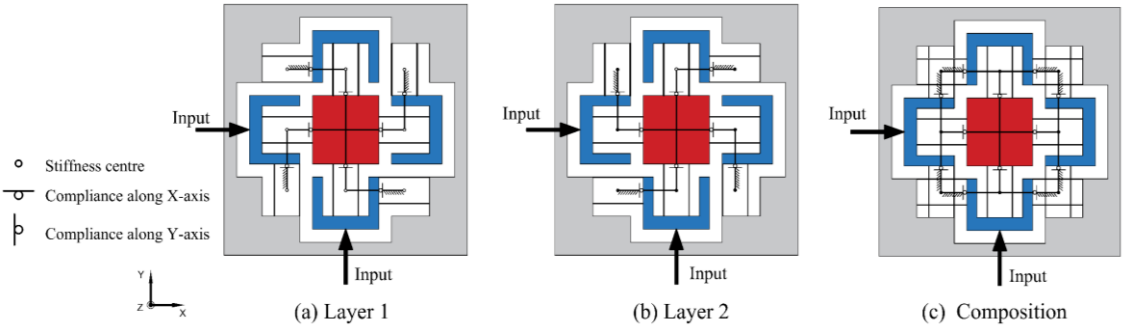


Figure 4.3 Composition of the two-layer design.

To minimise the rigid stage (including input stage and output stage) rotation, we formatted a simple solution based on the stiffness centre mirror-symmetry and multi-layer design concept. As shown in Figure 4.3, layer 2 is the 180-degree flipped version of layer 1, and they produce a pair of opposite rigid stage rotations when they have the same actuation. The rigid stage rotation can be compensated as they overlap and their rigid stages are connected, resulting in a zero rotation under a single-axis actuation (assuming that the

out-of-plane stiffness is large enough). This can also be determined by observing the solid lines connecting the stiffness centres which are mirror-symmetry as presented in Figure 4.3(c). This methodology minimizes parasitic rotation without increasing the overall footprint. Additionally, other performance characteristics, including actuator isolation and out-of-plane stiffness, benefit from the mirror-symmetric and compact design configuration, enhancing overall stability and efficiency.

4.2.2 Embodiment of the XY CPM

The constitutive flexure module of an XY CPM can be various, depending on design objectives and application types. There are always pros and cons of a constitutive flexure module. For instance, the design using basic parallelogram modules does have a good space utilization feature, but its inherited drawbacks are limited motion range and high actuation force [227, 228]. To increase the motion range and reduce the actuation force, one can use double parallelogram flexures (DPFs) to embody the design, but it introduces underconstraint in the meantime. If the underconstraint is not desired, one can employ the nested linkage flexure [229]. If robustness against buckling is preferred, the flexure mechanism proposed in [230] can be implemented to construct the XY CPM.

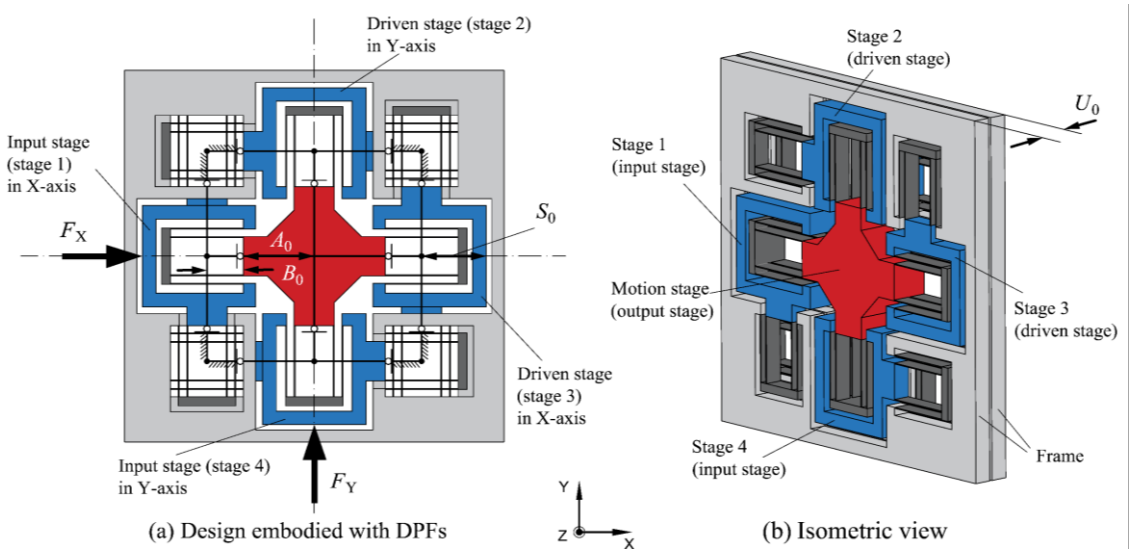


Figure 4.4 Finalized design

In this part of the work, we focus on minimising the parasitic rotation without increasing

the footprint, and in addition to that, a large motion range and a low actuation force are desired. Therefore, the DPF was selected as the constitutive flexure module due to its merits of large motion range and low actuation force required as well as compensated parasitic translation. The finalized design is depicted in Figure 4.4.

4.2.3 Nonlinear kinetostatic analytical modelling

The linear analytical modelling does not capture nonlinear stiffness characteristics and is limited to the use in a very small range of motion. To accurately model the characteristics of the proposed XY CPM, the FBD system modelling method combined with the BCM [110] was used. The BCM approach captures nonlinearities and leads to a closed-form model that can accurately estimate the kinetostatic behaviour of a generalized beam subjected to combined loads. To obtain load and displacement relationships of the proposed XY CPM, the equations associated with constitutive relationships, load-equilibrium conditions, and geometric compatibility conditions need to be solved.

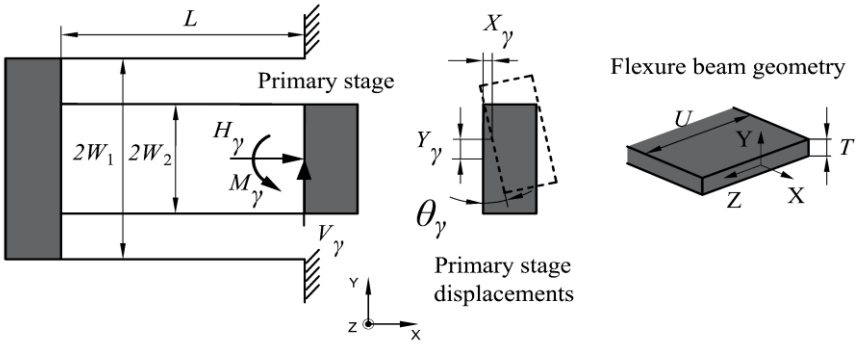


Figure 4.5 The geometry parameter and loading condition of the DPF.

The DPF modules embodied in the XY CPM are identical, one of which is depicted in Figure 4.5. The loading conditions for a DPF (number γ in the XY CPM) are represented by H_γ (axial force), V_γ (transverse force) and M_γ (moment) acting at the centre of the primary stage. The resulting displacements are represented by X_γ (displacement along X-axis), Y_γ (displacement along Y-axis) and θ_γ (rotational angle along Z-axis) with the respect to the coordinate frame attached to the undeformed configuration of the primary stage. All the length parameters and translational displacements are normalized by beam

length L, forces by EI/L^2 and moment by EI/L to reduce the complexity of equation representation. Lower-case letters are used to represent all the normalized quantities, specifically exhibited as:

$$h_\gamma = \frac{H_\gamma}{EI/L^2};\ v_\gamma = \frac{V_\gamma}{EI/L^2};\ m_\gamma = \frac{M_\gamma}{EI/L};$$
$$x_\gamma = \frac{X_\gamma}{L};\ y_\gamma = \frac{Y_\gamma}{L};\ w_{1(2)} = \frac{W_{1(2)}}{L};\ u = \frac{U}{L};\ t = \frac{T}{L}; \tag{4.1}$$

where I is the second moment of area of the flexure beam cross-section about the Z-axis, and E denotes Young's modulus of material. The other symbols are labelled in Figure 4.5. The normalized BCM of the γ^{th}-DPF can be represented as below [231]:

$$y_\gamma \approx \frac{4av_\gamma}{(2a)^2 - (eh_\gamma)^2} \tag{4.2}$$

$$x_\gamma \approx h_\gamma \left[\frac{1}{d} + \frac{y_\gamma^{\,2}}{2}\left(\frac{r}{2} - \frac{ei}{a}\right)\right] \tag{4.3}$$

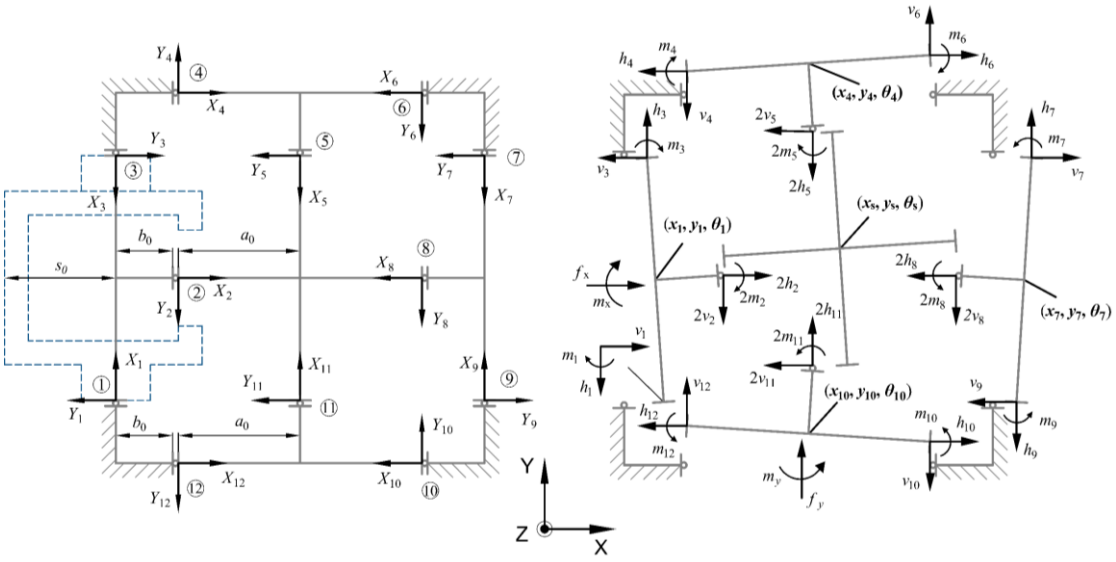
$$\theta_\gamma \approx \frac{1}{2w_1^{\,2}}\left(\frac{1}{d} + \frac{v_\gamma^{\,2}}{(2a - h_\gamma e)^2} r\right)\left[m_\gamma - \frac{v_\gamma}{(2a - h_\gamma e)}\left(1 - \frac{h_\gamma}{(2a + eh_\gamma)} + (2c - h_\gamma g)\right)\right] \tag{4.4}$$
$$+ \frac{1}{2w_2^{\,2}}\left(\frac{1}{d} + \frac{v_\gamma^{\,2}}{(2a + h_\gamma e)^2} r\right) \times \left[m_\gamma - \frac{v_\gamma}{(2a + h_\gamma e)}(2c + h_\gamma g)\right]$$

where the coefficients $a = 12$, $c = -6$, $d = 12/t^2$, $e = 1.2$, $g = -0.1$, $i = -0.6$, and $r = 1/700$. All these coefficients are non-dimensional values that characterize a uniform flexure beam. These numbers remain the same even though the dimension of the DPF changes.

In this configuration, each stage is represented by solid lines, with the DPFs denoted by a small circle tangent to a short line, indicating the primary points of compliance. Notably, deformation is restricted to the DPFs, while all other components, including the input stages (stages 1 and 4), driven stages (stages 2 and 3), motion stage, and the ground-connected frame, remain rigid. Figure 4.6(b) shows the deformed configuration of the XY CPM with actuation forces in both axes acting at the specified centres of the input stages

(Figure 4.6(b)). The FBD of each rigid stage (5 in total) is depicted in Figure 4.6(b). In each leg of the XY CPM, the two identical DPFs directly connected to the motion stage in the middle are considered to be one DPF with an out-of-plane thickness twice as much as the other DPFs connected to the ground. Therefore, as labelled in Figure 4.6(a), there are 12 DPFs, 8 connected to the ground and 4 connected to the motion stage.

As shown in Figure 4.6(b), there are overall three internal forces per DPF (12 DPFs in total) and three displacements per rigid stage (5 stages in total), leading to 51 unknowns. Correspondingly, there are 51 equations including three load-displacement relations as formulated in Eqs. (4.2), (4.3) and (4.4) of each DPF and three load-equilibrium conditions of each stage.



(a) Local coordinate frame of each flexure unit (b) Rigid body FBDs of the deformed XY CPM

Figure 4.6 Rigid body free body diagrams

The defined 5 sets of displacements as shown in Figure 4.6(b), such as $(x_1,\ y_1,\ \theta_1)$ that represent the displacements of the geometric centre point of stage 1, are measured from the global coordinates (O-XYZ). They are used to represent the tip displacements of each DPF with respect to the local coordinate labelled in Figure 4.6(a). Based on the geometry compatibility, the resultant displacements of each flexure unit are listed in the Table 4.1 below.

Table 4.1 Displacements of each DPF unit

γ	θ_γ	y_γ	x_γ
1	θ_1	$-(x_1+a_0\theta_1)$	y_1
2	$\theta_1-\theta_s$	$-(y_s-a_0\theta_s)+(y_1+b_0\theta_1)$	x_s-x_1
3	θ_1	$x_1-a_0\theta_1$	$-y_1$
4	θ_4	$y_4-a_0\theta_4$	x_4
5	$\theta_4-\theta_s$	$-(x_s-a_0\theta_s)+(x_4+b_0\theta_4)$	$-y_s+y_4$
6	θ_4	$-(y_4+a_0\theta_4)$	$-x_4$
7	θ_7	$-(x_7+a_0\theta_7)$	$-y_7$
8	$\theta_7+\theta_s$	$-(y_s+a_0\theta_s)+(y_7+b_0\theta_7)$	$-x_s+x_7$
9	θ_7	$x_7-a_0\theta_7$	y_7
10	θ_{10}	$y_{10}-a_0\theta_{10}$	$-x_{10}$
11	$\theta_{10}+\theta_s$	$-(x_s+a_0\theta_s)+(x_{10}+b_0\theta_{10})$	y_s-y_{10}
12	θ_{10}	$-(y_{10}+a_0\theta_{10})$	x_{10}

The nonlinearity of the mechanism should be captured based on the deformed configuration, but the stage rotation contributing to the force balance equation is negligible. Hence, the load-equilibrium equations of each stage can be computed as follows.

Load-equilibrium conditions of stage 1:

$$\begin{aligned} &f_x+v_1-v_3+2h_2=0 \\ &h_3-2v_2-h_1=0 \\ &m_z=m_x+m_1+2m_2+m_3+2b_0v_2-a_0(v_1+v_3)=0 \end{aligned} \tag{4.5}$$

Load-equilibrium conditions of stage 2:

$$\begin{aligned} &-2v_5+h_6-h_4=0 \\ &v_6-2-v_4=0 \\ &m_4+m_6+2m_5+2b_0v_5-a_0(v_4+v_6)=0 \end{aligned} \tag{4.6}$$

Load-equilibrium conditions of stage 3:

$$\begin{aligned} &v_7 - 2h_8 - v_9 = 0 \\ &h_7 - 2v_8 - h_9 = 0 \\ &2m_8 + m_7 + m_9 + 2b_0 v_8 - a_0\left(v_7 + v_9\right) = 0 \end{aligned} \tag{4.7}$$

Load-equilibrium conditions of stage 4:

$$\begin{aligned} &h_{10} - 2v_{11} - h_{12} = 0 \\ &f_y + v_{12} + 2h_{11} - v_{10} = 0 \\ &m_{10} + 2m_{11} + m_{12} + 2b_0 v_{11} - a_0\left(v_{10} + v_{12}\right) = 0 \end{aligned} \tag{4.8}$$

Load-equilibrium conditions of the motion stage:

$$\begin{aligned} &h_2 - v_5 - h_8 - v_{11} = 0 \\ &-v_2 + h_{11} - h_5 - v_8 = 0 \\ &m_2 + m_5 - m_8 - m_{11} + a_0(v_8 - v_2) + a_0\left(v_{11} - v_5\right) = 0 \end{aligned} \tag{4.9}$$

By solving 15 load-equilibrium conditions together with the 36 load-displacement relationships, we can obtain all 51 unknown parameters using commercial software such as MATLAB.

We can also derive the closed-form solutions for translational displacements as below:

$$\begin{aligned} x_1 &\approx \frac{128af_x}{1024a^2 - 12e^2 f_y^2} + \frac{3f_x}{8}\left[\frac{y_{10}^2}{2}\left(\frac{r}{2} - \frac{ei}{a}\right) + \frac{1}{d}\right] \\ y_1 &\approx \frac{f_y}{8}\left[\frac{x_1^2}{2}\left(\frac{r}{2} - \frac{ei}{a}\right) + \frac{1}{d}\right] \end{aligned} \tag{4.10}$$

$$\begin{aligned} x_4 &\approx \frac{f_x}{8}\left[\frac{y_{10}^2}{2}\left(\frac{r}{2} - \frac{ei}{a}\right) + \frac{1}{d}\right] \\ y_4 &\approx \frac{128af_y}{1024a^2 - 12e^2 f_x^2} - \frac{f_y}{8}\left[\frac{x_1^2}{2}\left(\frac{r}{2} - \frac{ei}{a}\right) + \frac{1}{d}\right] \end{aligned} \tag{4.11}$$

$$\begin{aligned} x_7 &\approx \frac{128af_x}{1024a^2 - 12e^2 f_y^2} - \frac{f_x}{8}\left[\frac{y_{10}^2}{2}\left(\frac{r}{2} - \frac{ei}{a}\right) + \frac{1}{d}\right] \\ y_7 &\approx \frac{f_y}{8}\left[\frac{x_1^2}{2}\left(\frac{r}{2} - \frac{ei}{a}\right) + \frac{1}{d}\right] \end{aligned} \tag{4.12}$$

$$\begin{aligned} x_{10} &\approx \frac{f_x}{8}\left[\frac{y_{10}^2}{2}\left(\frac{r}{2}-\frac{ei}{a}\right)+\frac{1}{d}\right] \\ y_{10} &\approx \frac{128af_y}{1024a^2-12e^2f_x^2}+\frac{3f_y}{8}\left[\frac{x_1^2}{2}\left(\frac{r}{2}-\frac{ei}{a}\right)+\frac{1}{d}\right] \end{aligned} \tag{4.13}$$

$$\begin{aligned} x_{\mathrm{s}} &\approx \frac{128af_x}{1024a^2-12e^2f_y^2} \\ y_{\mathrm{s}} &\approx \frac{128af_y}{1024a^2-12e^2f_x^2} \end{aligned} \tag{4.14}$$

The derivations of the above closed-form solutions require a large amount of algebraic manipulation and simplification of insignificant parameters. For example, the coefficient $r=1/700$, which contributes to the elstokinematic component of the DPF, is three orders of magnitude smaller than the coefficient $e=1.2$ and two orders of magnitude smaller than the coefficient $a=12$. Consequently, $r=1/700$ is omitted in Eq. (4.14). The expression of motion stage rotation is extremely complex by solving 51 nonlinear equations, which are presented here in specific cases:

$$\begin{cases} \theta_{\mathrm{s}} \approx \left(\dfrac{128a^2+rdf_x{}^2}{1024a^2\bar{w}^2d}\right)m_x & \text{if } f_y=m_y=0 \\ \theta_{\mathrm{s}} \approx \left(\dfrac{128a^2+rdf_y{}^2}{1024a^2\bar{w}^2d}\right)m_y & \text{if } f_x=m_x=0 \end{cases} \tag{4.15}$$

where $\bar{w}=2w_1^2w_2^2/\left(w_1^2+w_2^2\right)$. Subsequently, the normalized performance expressions of the XY CPM can be defined in Table 4.2.

Table 4.2 Performance expressions of the XY CPM

Performance	**Expression**
Stiffness in X-direction	$\partial f_x/\partial x_{\mathrm{s}}$
Cross-axis coupling error in X-direction	$x_{\mathrm{s}}-x_{\mathrm{s}}\mid_{(f_y=0)}$
Lost motion in X-direction	$x_{\mathrm{s}}-x_1$

Actuator isolation index for stage 1	$y_1 - s_0\theta_1$
Motion stage rotation θ_s in Z-direction	$\left(\frac{128a^2 + rdf_x{}^2}{1024a^2\bar{w}^2d}\right)m_x \quad if\ f_y = m_y = 0$ $\left(\frac{128a^2 + rdf_y{}^2}{1024a^2\bar{w}^2d}\right)m_y \quad if\ f_x = m_x = 0$

Before proceeding to FEA verifications, some observations can be made from the obtained closed-form expressions.

1) As we can see from Eq. (4.14), there is no elastokinematic term contributing to the primary motion that is absorbed by the four stages (stages 1, 2, 3, 4). The elastokinematic effect generated is about the quadratic function of the displacement in the other direction, illustrated in Eq. (4.10).
2) We can conclude from Eq. (4.15) that the motion stage yaw is equal to zero in respect to single-axis force actuation.

4.3 FEA verifications

A case study with specified geometrical and material parameters listed below (Table 4.3) was performed in commercial software COMSOL@5.0. Similar to the assumptions made in the analytical modelling, the stages and frames are set to be rigid. Finer hexahedra mesh was generated at the flexure beams to gain stable and accurate results. The aluminium alloy AL6061 with Young's Modulus 69 GPa and Yield Strength 276 MPa is assigned to the material. The nonlinearity solver is used in FEA since there are large elastic deformations in the DPF. The simulation scenario was conducted by applying a series of forces to the centre of stage 1 and stage 4. All the parameters are switched back to dimensional values for a more straightforward comparison.

Table 4.3 Geometry parameters

L	U	T	S_0	U_0	A_0	B_0	W_1	W_2
40 mm	10 mm	0.8 mm	38.1 mm	22 mm	38.6 mm	20 mm	14.2 mm	8.4 mm

Figure 4.7 plots the results of applying 244 N at stage 1 in the X-direction. The resultant

displacement in the X-axis is depicted in Figure 4.7(a), which is about 5.19 mm. The corresponding stress distribution obtained from FEA is presented in Figure 4.7(b), where the maximum stress reaches the yield point (276 MPa) under the specified actuation force. This gives us a glimpse of the physical behaviour of the design and thereby reduces the fatigue risk in the experiment. It is also worth noting that the six DPF units (red painted) contributing to the X-direction displacement in each axis are in mirror-symmetry.

The performance characteristics of the XY CPM, as defined in Table 4.2, are obtained in FEA. The FEA results are compared with the results from theoretical calculation to gain more insights and understanding of the characteristics of the XY CPM.

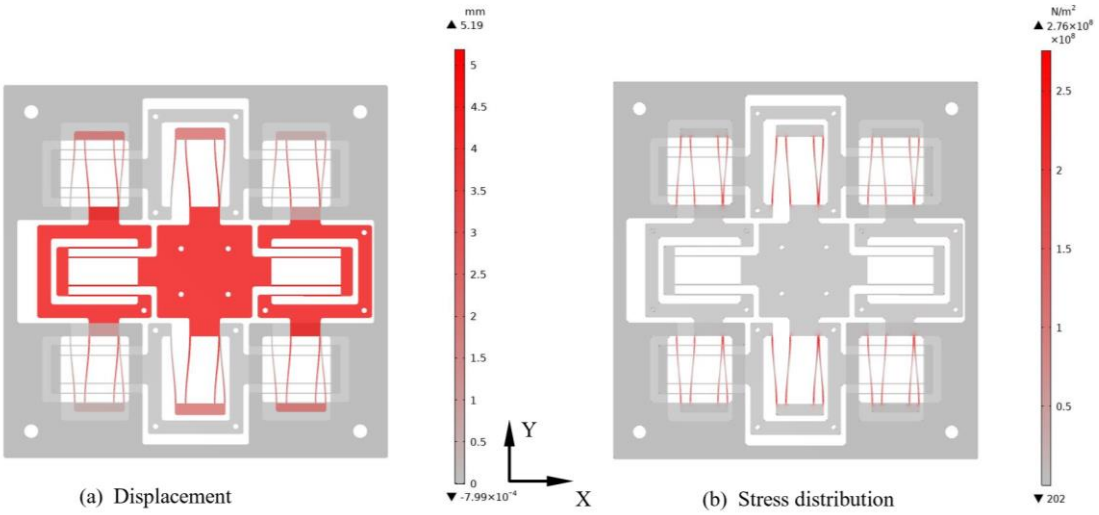
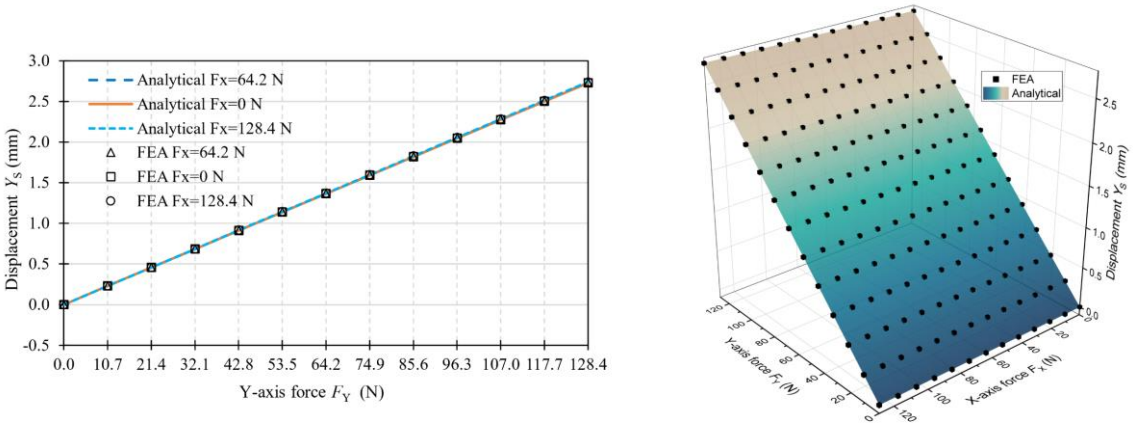


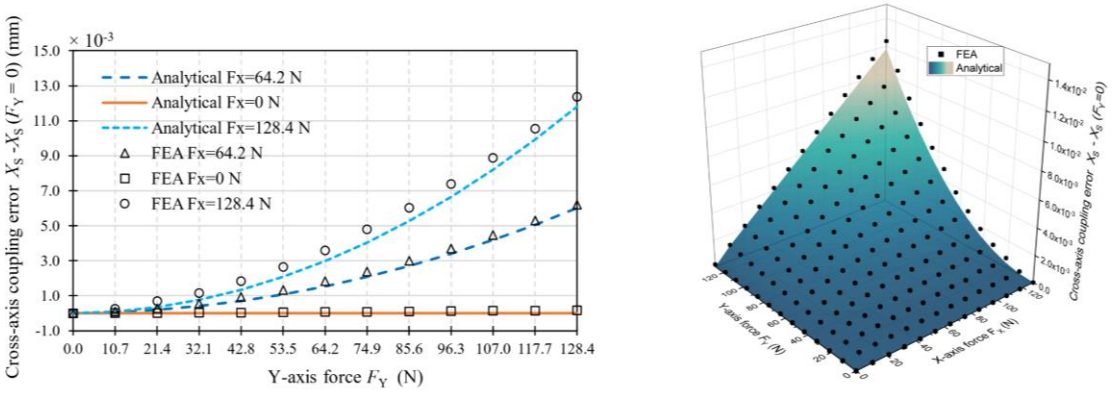
Figure 4.7 Motion range before yielding

The primary motion of the motion stage under two-axis actuation is shown in Figure 4.8. The analytical results are consistent with the FEA results with the maximum error of 1% over a specified working/motion range (2.4 mm × 2.4 mm). The specified motion range is adopted throughout the analysis in this work, which is about half of the maximum working motion (5.19 mm) to assume a safety factor of 2. Furthermore, the primary stiffness of the FEA results is about 47.4 N/mm as indicated in Figure 4.8(a). To comprehensively monitor the performance of the two-axis actuation condition, a surface is plotted as displayed in Figure 4.8(b). Over the range of the applied forces, the maximum drop of the primary stiffness is less than 0.54%, which is barely discernible.



(a) 2D chart with specific input forces in X-direction (b) 3D plot of two-axis actuations

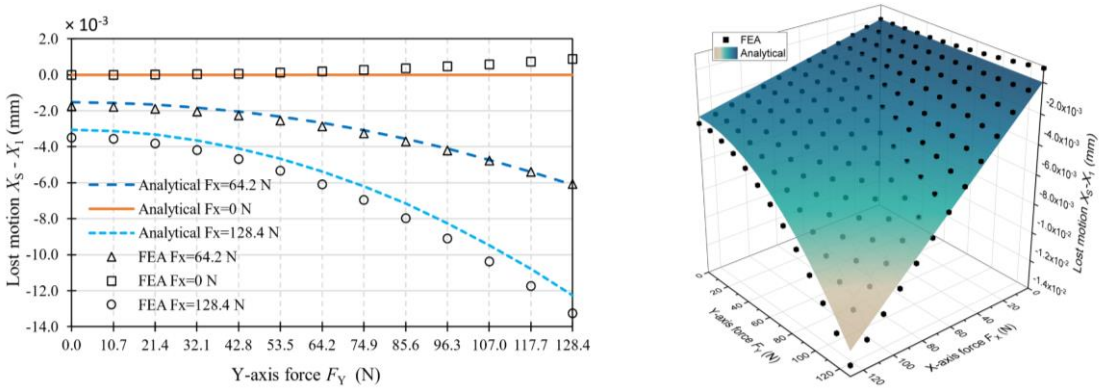
Figure 4.8 Primary motion of the XY CPM.



(a) 2D chart with specific input forces in X-direction (b) 3D plot of two-axis actuations

Figure 4.9 Cross-axis coupling error in X-direction.

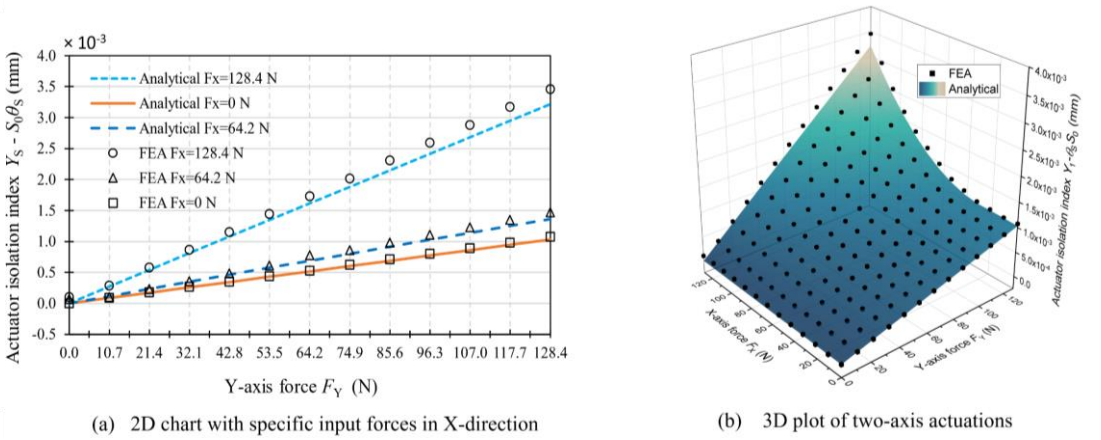
Figure 4.9 captures the cross-axis coupling error of both analytical and FEA results. The plots show that the analytical results coincide with the FEA results. The maximal cross-axis coupling error is about 0.51 % of the primary motion, which means the highest force acting in the Y-axis produces a displacement of 0.012 mm in the X direction, and vice versa. Another fact that can be observed is that the cross-axis coupling error varies nonlinearly with the actuation force as shown in Figure 4.9(a). A higher actuation force in one direction generally produces a greater cross-axis coupling error in the other direction.



(a) 2D chart with specific input forces in X-direction (b) 3D plot of two-axis actuations

Figure 4.10 Lost motion along X-direction.

A similar plot is obtained based on the closed-form solutions and FEA results of the lost motion in the X-direction as depicted in Figure 4.10. The closed-form solutions agree with the FEA results with an error less than 6.5 %. The maximum lost motion generated is close to 0.0132 mm in the X direction which is about 0.55 % of its primary motion. The lost motion represented by $x_s - x_1$ (using Eq. (4.14) and Eq. (4.10)) in the X direction is about the quadratic function of the displacement in the other direction, which also indicates that the lost motion changes nonlinearly with the force applied in the Y-axis as displayed in Figure 4.10(a).



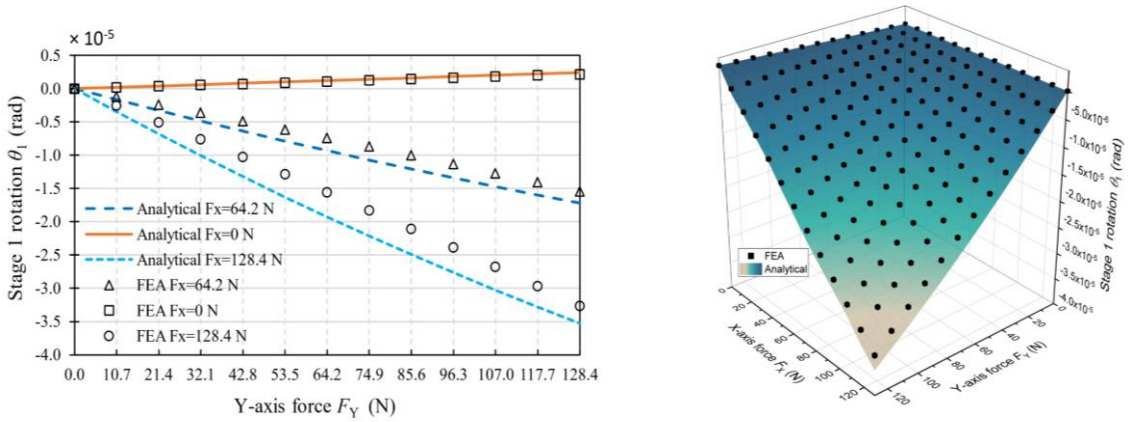
(a) 2D chart with specific input forces in X-direction (b) 3D plot of two-axis actuations

Figure 4.11 Actuator isolation index of the XY CPM.

An ideal actuator isolation refers to a zero-actuator isolation index (Table 4.2). It is evident in Figure 4.11 that the actuator isolation index is below 0.14% of the specified

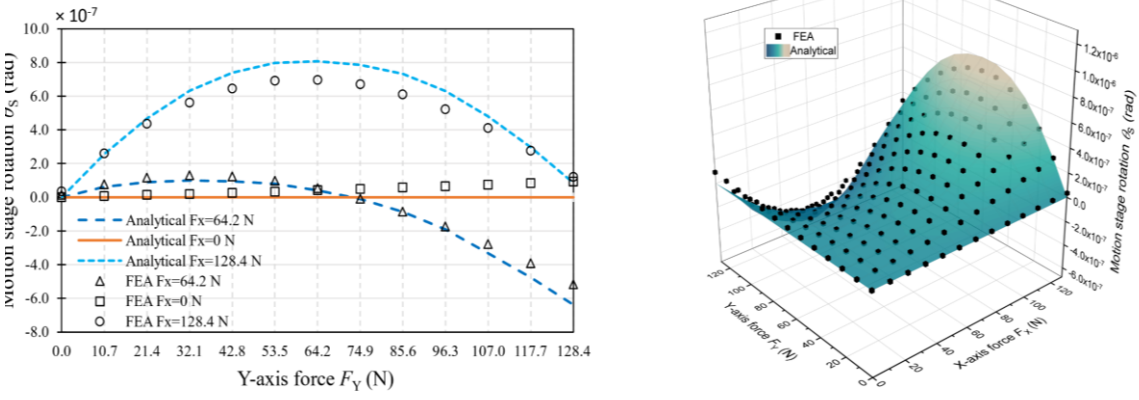
motion range (2.4 mm) and the analytical results are in good agreement with the FEA results both shown in the 2D plot and surface plot, as presented in Figure 4.11.

The rotation of input stages (stages 1 and 4) contributes to the actuator isolation index which should be minimised. The rotation of stage 1 is depicted in Figure 4.12. Both the FEA and analytical results show the maximal stage rotation is less than 36 μrad. It is worth noting that under the actuation force F_Y only, stage 1 (along the X-axis) generates a small rotation which is up to 2.43 μrad.



(a) 2D chart with specific input forces in X-direction (b) 3D plot of two-axis actuations

Figure 4.12 Stage 1 rotation.



(a) 2D chart with specific input forces in X-direction (b) 3D plot of two-axis actuations

Figure 4.13 Motion stage rotation.

The rotational angle of the motion stage is elaborated in Figure 4.13. The maximal difference between the analytical and FEA results is about 9.9%. The possible cause of

such a relatively large difference might be the inaccuracy of the FEA model in dealing with small rotations. One possible cause of this discrepancy is the numerical sensitivity of FEA when dealing with very small angular displacements. The maximum motion stage rotation recorded analytically is only 0.8 μrad, which is an extremely small value. In FEA simulations, when rotational displacements are at the micro-radian scale, round-off errors, mesh discretization effects, and solver tolerances can introduce inaccuracies in capturing these minimal deformations. This can lead to deviations from the analytical predictions, particularly in cases where the displacement magnitudes are close to the solver's numerical precision limits.

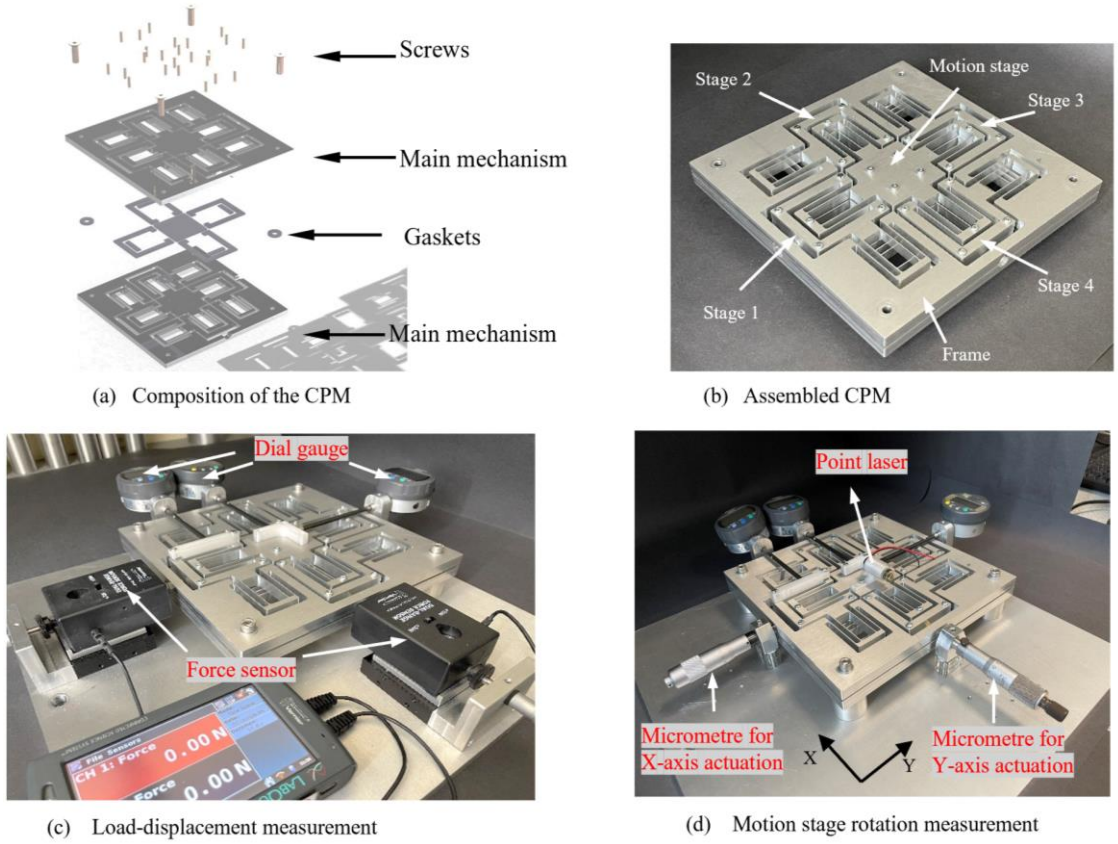
Despite this discrepancy, it is important to note that the flat region in the workspace, where stage rotation is nearly zero, shows better agreement between the analytical and FEA results. This suggests that the error is more significant when dealing with extremely small rotations, reinforcing the idea that numerical sensitivity in both models plays a role in the observed differences. Future refinements, such as higher-precision meshing strategies in FEA or adjustments to solver tolerances, could help mitigate these discrepancies.

4.4 Experimental tests

4.4.1 Fabrication of the XY CPM

The two-layer design is constructed from two monolithically fabricated mechanisms, as depicted in Figure 4.14. Each layer is machined from a single AL6061 aluminum plate using a CNC milling machine, adhering to the specifications detailed in Sec. 4.2.3. AL6061 was selected for its combination of lightweight and high yield strength, enhancing both durability and performance. The milling process incorporates filleted corners with a 1.5 mm radius. The absence of fillets in the analytical model and FEA ensures simplified mathematical formulations and a direct comparison between the two methods without additional geometric complexities. However, in the physical prototype, fillets were added to reduce stress concentrations, enhance fatigue resistance, and meet CNC manufacturing constraints. Sharp corners can lead to localized stress buildup and

premature failure, whereas a 1.5 mm fillet radius helps distribute stress more evenly, improving durability. While fillets slightly alter local stiffness, their impact on overall force-displacement behavior is minimal, ensuring the prototype remains functionally equivalent to the analytical and FEA models while being more practical and reliable for real-world applications. The two layers are assembled with a bolted overlap, separated by 2 mm gaskets to ensure alignment and functionality. The final assembled XY CPM measures 220 mm × 220 mm × 22 mm, matching the dimensions of the design used in the FEA case study.



(a) Composition of the CPM (b) Assembled CPM

(c) Load-displacement measurement (d) Motion stage rotation measurement

Figure 4.14 Fabricated XY CPM and its experimental setup

4.4.2 Low-cost apparatus setup for data acquisition

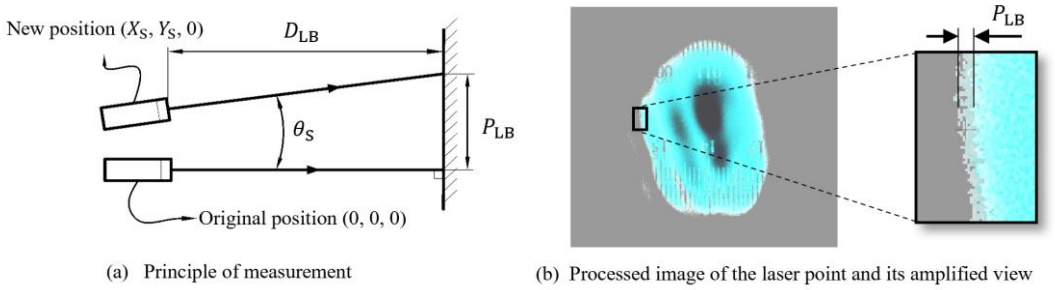
As labelled in Figure 4.14(c) and Figure 4.14(d), the testing rig is mainly composed of the following: the dial gauges (a motion resolution of 0.001 mm and a spring force of 0.4-

0.7 N) to measure the displacement of the intermediate stage and motion stage; two force sensors (a resolution of 0.01 N with measurement ranges from 0 to 50 N), used for monitoring the force reactions; two micrometres (resolution of 0.001 mm), used for actuation; and the point laser, used for measuring the stage rotation. It is noted that the actuation tip of the micrometre is rounded to provide a point contact to the input stage. This minimizes the moment introduced to the input stage under two-axis actuation, which creates the almost same loading conditions as those in the analytical model.

The principle of this low-cost stage rotation measuring method is sketched in Figure 4.15(a). As the motion stage translates and rotates, the laser fixed on the motion stage follows the same pattern moving from the original position to a new position. The translational displacement of the laser point pasted onto the wall is captured using an HD camera as shown in Figure 4.15(b). The width (P_{LB}) of the grey stripe in the middle represents the displacement caused by two adjacent actuation forces. If the motion stage displacement Y_S is much smaller than D_{LB} (the distance between the point laser and the wall), the stage rotation can be calculated as:

$$\theta_S \approx \arctan\left(\frac{P_{LB} - Y_S}{D_{LB}}\right) \tag{4.16}$$

A similar method can also be used to measure the input stage rotation.



(a) Principle of measurement (b) Processed image of the laser point and its amplified view

Figure 4.15 Stage rotation measurement

4.4.3 Experiment procedures

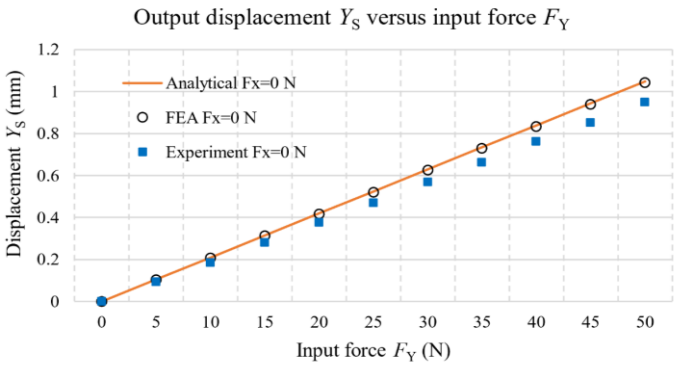
To ensure accurate and repeatable measurements, the experimental apparatus was initially calibrated. This process involved zeroing the force sensor and dial gauge, applying a small

preloading force of 0.02 N to eliminate any gap between the actuator and input stage. The XY CPM was then actuated in fixed force increments from 0 to 50 N, with corresponding displacements recorded from the dial gauge at each interval. After capturing the force-displacement relationship across the 50 N range, the force sensor was removed. To study the XY CPM further, a micrometer was used to actuate the input stage directly, with a controlled incremental input displacement of 0.2 mm, from 0 mm to 2.4 mm. Each experimental procedure was repeated three times to calculate an average result, ensuring consistency and reliability.

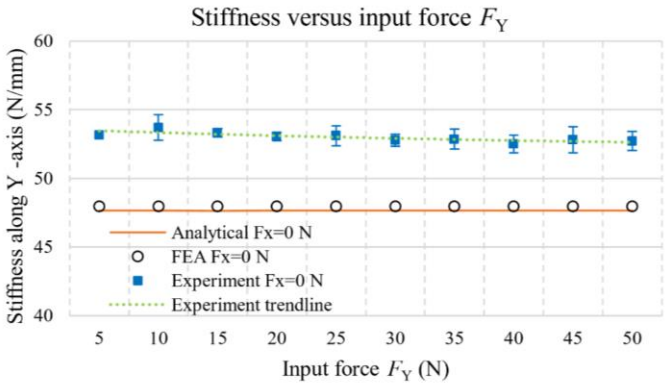
4.4.4 Experimental results

The experiment was conducted to validate the FEA and analytical results. Figure 4.16 illustrates the load-displacement relationship and the correlation between stiffness and input force of the XY CPM along the Y-axis. The load-displacement relationship appears nearly linear, with strong agreement across FEA, analytical, and experimental models, as shown in Figure 4.16(a). The stiffness-to-input force comparison among the three models is depicted in Figure 4.16(b), where error bars represent the standard deviation over three independent trials. The experimental results are presented as the mean of these trials, highlighting consistency across repetitions.

Both analytical and FEA results indicate a nearly constant stiffness, while experimental stiffness shows minor fluctuations, accompanied by a slight decreasing trend, likely due to assembly imperfections. Furthermore, the experimentally observed stiffness is slightly higher than that predicted by FEA and analytical models. This discrepancy, with a maximum observed error of 10.03%, can be attributed to fabrication differences, particularly the rounded corners in the prototype, which were not considered in the idealized sharp-cornered FEA and analytical models. These rounded edges introduce localized stiffness variations, resulting in a slightly stiffer response in the physical prototype. Despite this difference, the overall stiffness trend remains consistent across all three methods, validating the effectiveness of the analytical and numerical models in predicting the compliant mechanism's behavior.



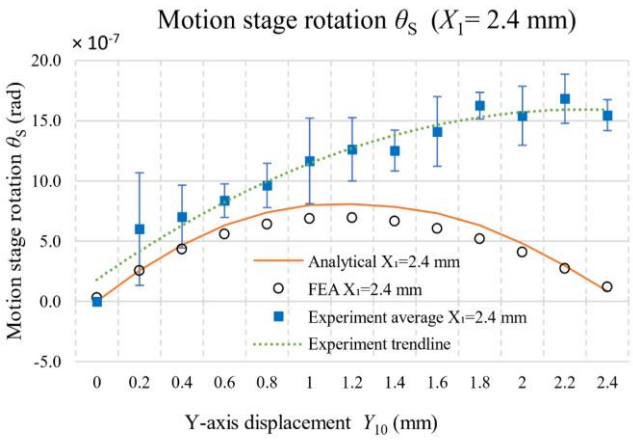
(a) Load-displacement relationship



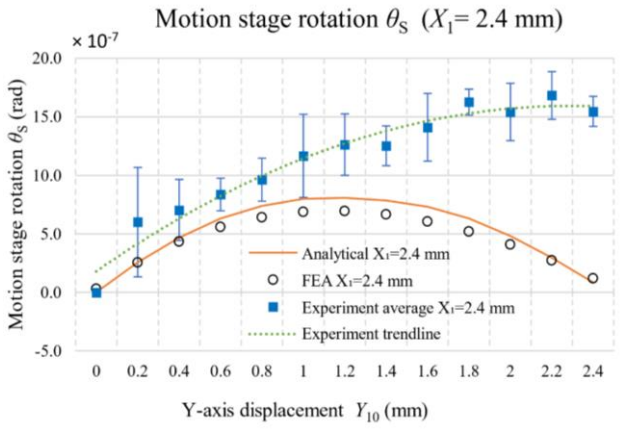
(b) Stiffness versus input force

Figure 4.16 Load-displacement relationship and stiffness in Y-axis

The stage rotation graphs for the motion stage and stage 1 under two-axis actuation are plotted in Figure 4.17. The FEA results and analytical results are well matched as provided in Sec. 4.3. It can be read from the analytical and FEA results in Figure 4.13 that when two equal forces are applied in the X-axis and Y-axis, respectively, the motion stage rotation is close to zero, and it increases as the difference between the two actuation forces enlarges. The experimental result fluctuates as the input displacement increases, mainly due to fabrication errors and experimental errors. The fabrication errors could come from the angular misalignment of the flexure beams that should be parallel to each other. The experimental error may arise from the pixelated image after zooming in. The pixelated images may cause errors when measuring the distance P_{LB}.



(a) Motion stage rotation



(a) Motion stage rotation

Figure 4.17 Motion stage rotation and input stage 1 rotation

However, similar to the FEA and analytical results, the experimental rotation angle curve in the second half also tends to decrease as shown in Figure 4.17(a). The maximum motion stage rotation recorded by the experiment is 1.68 μrad for two-axis actuations within the motion range of 2.4 mm × 2.4 mm and that of the stage 1 rotation (Figure 4.17(b)) is 52.9 μrad. The experimental rotations are much larger than the theoretical results (FEA/analytical), since the introduced fillets are not in mirror symmetry with regard to beams. Other performance characteristics like the cross-axis coupling error and lost motion are too small to be accurately captured by the adopted dial gauge (a motion resolution of 0.001 mm), so the corresponding results were not recorded in the experiment.

4.4.5 Further discussions

4.4.5.1 Dynamic considerations

The dynamic response of the proposed XY CPM, using the same parameters as defined in Sec. 4.2.3, is analysed in the commercial software COMSOL. The first six resonance frequencies are listed in Table 4.4 and their corresponding modal shapes are depicted in Figure 4.18. The first-two natural frequency occurs at 48.6 Hz, which is the corresponding simultaneous vibrations along the X-axis and Y-axis. The third mode is the motion stage rotation along the Z-axis and the fourth mode corresponds to the rotation of the secondary stage of the DPF. The fifth and sixth modes represent the translational motion of the secondary stage along the X-axis and Y-axis, respectively.

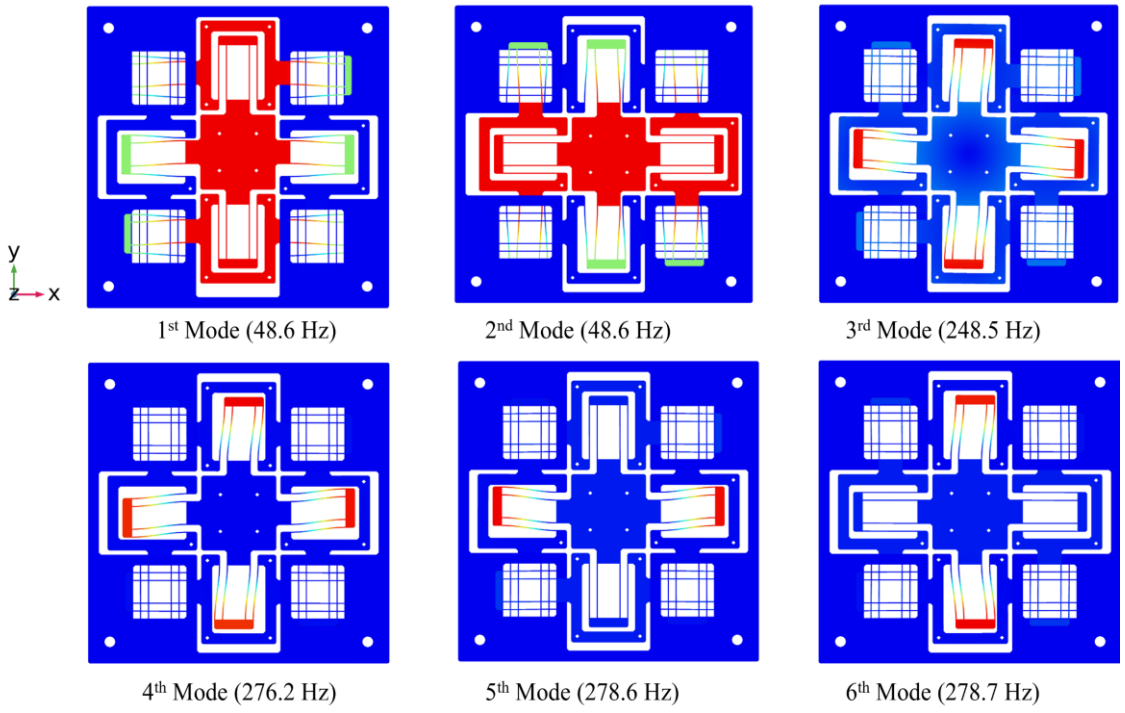


Figure 4.18 The first six modal shapes

Table 4.4 First six resonant modes

Mode	1	2	3	4	5	6
Resonance Frequency (Hz)	48.6	48.6	248.5	276.2	278.6	278.7

The DPF used as the constitutive mechanism increases the motion range and reduces the cross-axis coupling error of the XY CPM, but the introduced secondary stage/mass worsens the dynamic performance of the design. It is well-known that the resonance frequency can be raised by reducing the mass or increasing the stiffness. Specifically, we can increase the number of beams to raise the stiffness or use a high-order controller to achieve a high bandwidth [232].

4.4.5.2 Out-of-plane stiffness

A high out-of-plane stiffness is insensitive to out-of-plane vibrations and is capable of carrying a large payload without causing large parasitic motion in Z-direction. Using the FEA, the out-of-plane stiffness of the XY CPM is analysed by applying a series of forces in Z-axis (F_Z) on the motion stage with a specific actuation force on the input stage.

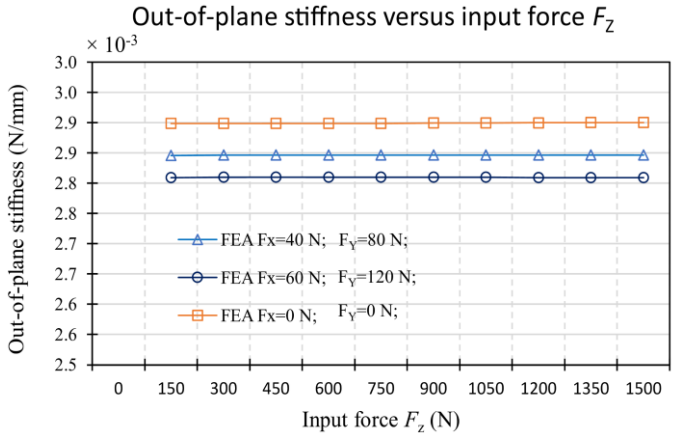


Figure 4.19 Out-of-plane stiffness versus applied force F_Z under specific actuation forces

As presented in Figure 4.19, the out-of-plane stiffness varies with different actuation forces, and it is nearly constant over different Z-axis forces. The minimum out-of-plane stiffness is close to 2800 N/mm, which means that the parasitic motion in Z-axis is below 0.5 mm with a 140 kg payload.

4.4.5.3 Three-layer design

The proposed two-layer design was considered as a mirror-symmetric configuration based on the assumption of large out-of-plane stiffness. If the out-of-plane stiffness is not

robust, the two-layer design introduces certain out-of-plane parasitic motion under an in-plane actuation. To perfectly eliminate the out-of-plane motion, a three-layer design can be facilitated, as shown in Figure 4.20. Two identical layers with a half thickness of the manipulator in the middle are set up at the top and bottom layers. Based on such an arrangement, the out-of-plane motion is eliminated under any in-plane forces. The FEA results show that the maximum motion stage rotation and cross-axis coupling error of the three-layer design is 1.9 μrad and 0.36% within the motion range of 2.4 mm × 2.4 mm. Besides, the out-of-plane stiffness is about 1603 N/mm which is smaller than that of the two-layer design.

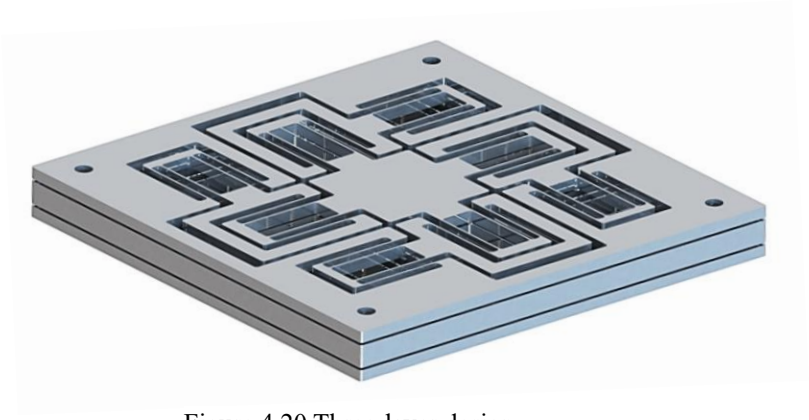


Figure 4.20 Three-layer design

4.4.5.4 Performance comparison

The performance characteristics of several representative prior XY CPMs are listed below in Table 4.5 to compare with the proposed design in this work. To provide a more precise and comprehensive comparison, Table 4.5 includes two specific proposed two-layer designs (design 1 and design 2). Design 1 uses the same parameters as defined in Sec. 4.3, and design 2 uses the same parameters as defined in [233] (i.e., a design with the same out-of-plane beam thickness (total thickness for two layers) and in-plane dimensions of Awtar's design [153]).

Table 4.5 Performance characteristics compared with existing design (ANA= Analytical results; Exp = Experimental results; the comprehensive analysis for the proposed design 2 can be accessed in [233])

Out-of-plane stiffness (N/mm)	1st resonance frequency (Hz)	Cross coupling (% of primary	Maximum input stage rotation (μrad)		Maximum motion stage rotation (μrad)		In-plane motion stiffness (N/mm)	Working range (mm)	Size (mm)	
2800 (FEA)	48.60 (FEA)	1.21 % (Ana)	0 (Ana)	Single-axis actuation (stage	0 (Ana)	Single-axis actuation (stage	47.4 (FEA)	5.19×5.19 (FEA)	220×220×22 without actuator	**Proposed two-layer Design 1 using the same parameters in Sec. 4.3**
			59.67 (Ana)	Two-axis actuations	2.24 (Ana)	Two-axis actuations				
2257 (FEA)	28.54 (FEA)	1.20% (Ana)	0 (Ana)	Single-axis actuation (stage 1, F_Y=0)	0 (Ana)	Single-axis actuation (stage 1, F_Y=0)	15.8 (FEA)	5×5 (FEA)	300×300×27 without actuator	**Proposed two-layer design 2 using the same parameters as defined in [233]**
			28.2 (Ana)	Two-axis actuations	6.1 (Ana)	Two-axis actuations				
1109 (FEA)	28. 97(FEA)	1.00% (Ana)	120 μrad (FEA)	Single-axis actuation (stage 1, F_Y=0)	0.02 μrad (FEA)	Single-axis actuation (stage 1, F_Y=0)	15.8 (FEA)	5×5 (FEA)	. 300×300×25 without actuator	**Design by Awtar in [153]**
			200 (Ana)	Two-axis actuations	15 (Ana)	Two-axis actuations				
N/A	340 (Exp)	1.50% (Exp)	N/A		4.80 (Exp)	Single- axis actuation	1626 (Exp)	0.41×0.41 (Exp)	269×269×22 with actuator	**Design by Lai et al. [234]**
					N/A	Two-axis actuations				
N/A	N/A	1.70% (FEA)	N/A	Single- axis actuation	N/A	Single- axis actuation	15.60 (FEA)	1.50×1.50(FEA)	300×300×40 with actuator	**Design by Liu et al. [235]**
			40 (FEA)	Two-axis actuations	8 (FEA)	Two-axis actuations				
N/A	320.10 (Exp)	0.65% (Exp)	N/A		13.50 (Exp)	Single- axis actuation	N/A	0.12×0.12 (Exp)	150×150×20 with actuator	**Design by Lee et al.[236]**
					N/A	Two-axis actuations				

From a direct comparison between our design (design 2) and Awtar's design [153] in Table 4.5, we can observe that our design method can minimise the parasitic rotations of input

and output stages much better than Awtar's design and can improve the out-of-plane stiffness twice better than Awtar's design when rendering other characteristics nearly the same as Awtars' design. Compared with other existing designs, our design method proposed in this work can produce a much larger motion range and better-constrained rotations, along with a very compact configuration. The small cross-axis coupling error of the proposed design also testifies the desired decoupling characteristic.

4.5 Summary

A compact XY CPM with minimised parasitic rotations has been proposed based on the mirror-symmetry and multi-layer design concept. The analytical/closed-form kinetostatic models have been obtained using BCM combined with the FBD method, which can accurately predict the performance characteristic of the proposed XY CPM. The proposed design has been simulated using the FEA method to analyse its static and dynamic performances. Furthermore, a prototype has been fabricated and tested in a measurement system to validate several performances of the design.

Compared with the emerging XY CPMs, the proposed mirror-symmetric XY CPM mainly has a smaller stage rotation and a compact structure. Other performances including cross-axis coupling, lost motion, and actuator isolation are also competitive. Through the analytical/closed-form solutions, FEA nonlinear simulations, and experimental results, one can conclude that the fabricated prototype has the following characteristics:

1) large working range up to 5.19 mm × 5.19 mm;
2) the maximum motion stage rotation is 2.24 μrad within the aforementioned motion range and that of the input stage rotation is 59.67 μrad;
3) small cross-axis coupling error less than 1.21%;
4) robust actuator isolation with a maximum actuator isolation index of 0.69% of primary motion;
5) approximately lost motion less than 1.35% of primary motion; and
6) large out-of-plane stiffness of 2800 N/mm.

In the future, we will theoretically and experimentally analyse the dynamic performance

of the XY CPM to facilitate an advanced control. The sensitivity to thermal effect needs to be investigated to minimise the adverse consequences on the positioning system since thermal expansion could cause precision issues on the XY CPM. Also, the three-layer design requires further comprehensive analysis.

CHAPTER 5

APPLICATIONS OF THE PARAMETERIZED NONLINEAR MODELS IN DESIGNING COMPLIANT MECHANISMS

In Chapter 5, we apply the parameterized nonlinear models developed in Chapter 2 to practical compliant mechanism designs. By leveraging the GLBM and the GSTC leaf beam model, this chapter illustrates the models' versatility and precision in analyzing and optimizing complex compliant systems, including revolute joints, bistable mechanisms, and spherical joints. Each section covers the design, analysis, and verification processes, offering a comprehensive approach to validating and refining these mechanisms through analytical models, FEA, and experimental setups.

Section 5.1 explores the design and nonlinear modeling of 2D compliant mechanisms. This section focuses on two cases—revolute joints and bistable mechanisms—demonstrating the application of the GLBM in achieving precise force-displacement predictions. Detailed FEA verifications and experimental validations provide insights into the model's accuracy and practical adaptability. For instance, the revolute joint, designed with inverted beams to withstand large forces, is analyzed using the GLBM's system of nonlinear equations, showing a high correlation with FEA results. In parallel, a bistable mechanism is designed to exhibit specific snap-through behavior under axial forces, providing essential insights into stress distribution and stability for practical applications.

Section 5.2 transitions to 3D designs, focusing on the modeling and analysis of a general spherical joint using the GSTC leaf beam. This section develops a nonlinear model for force-displacement and centre drift characteristics of spherical joints, an area crucial for mechanisms requiring constrained, multi-directional movement. Various leaf beam configurations, including SSTC, I-shape, L-shape, and folded designs, are explored,

offering a comparative analysis of centre drift and rotation control. FEA simulations validate the model's predictive accuracy, while experimental studies demonstrate the impact of design parameters on performance.

5.1 2D Design and nonlinear modelling of revolute joint and bistable mechanisms

In this Section, the proposed GLBM was used to synthesize two different cases, namely, the revolute joint and the bistable mechanism. To analyze the force-displacement characteristics of each compliant mechanism, we need to format a system of equations consisting of the GLBM, force equilibrium, and geometry compatibility. The system equations are solved in Maple using *Fsolve* function and the obtained results are further verified by the FEA tool using Comsol. The process of the FEA simulation generally follows the same process presented in Figure 2.3.

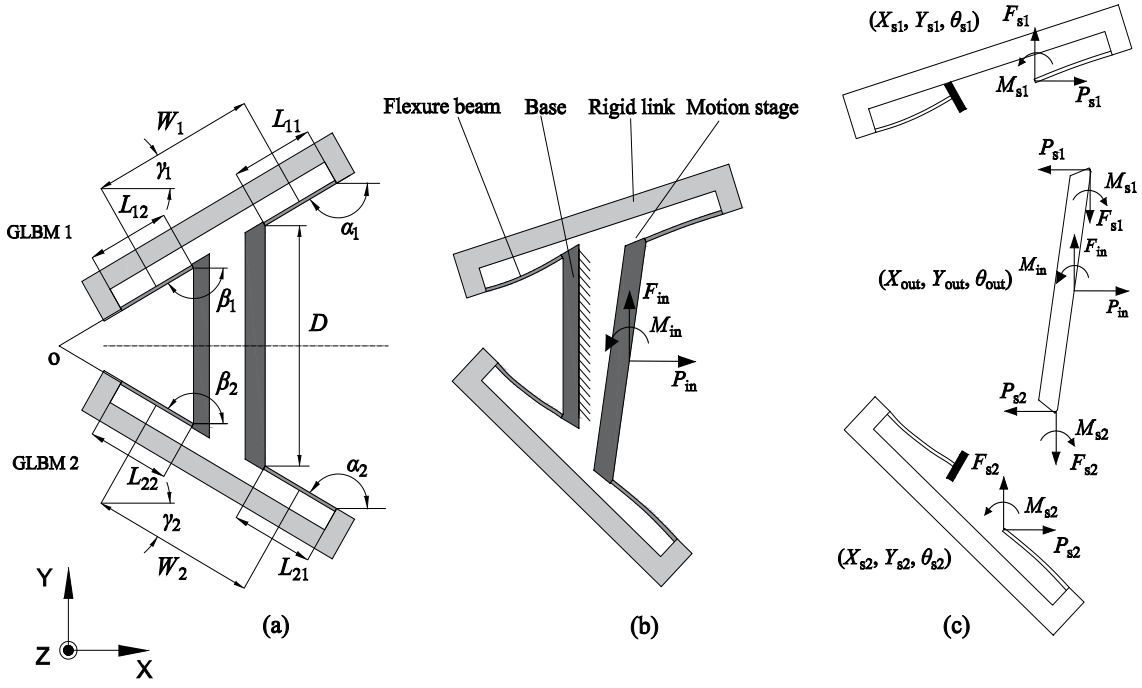


Figure 5.1 Revolute joint with inverted beams: (a) geometry; (b) deformed configuration; (c) FBD of the joint

5.1.1 Case I - revolute joint with two identical inverted beams

Figure 5.1 illustrates the revolute joint design using an inverted beam with specific geometry parameters, which are listed in Table 5.1. By simply changing the value of these parameters, we can quickly model a translational joint as shown in Figure 5.2 [237]. This allows for quick and efficient design iterations, reducing development time. In this case study, the revolute joint is being utilized as the subject of analysis.

The revolute joint with inverted beams is typically capable of withstanding a large compression force. In this case, the flexure beam only suffers tensile force which avoids buckling [237]. To derive the force balance equation, we will begin by analyzing the FBD, along with the GLBM and geometry compatibility. By combining these mechanics, we can obtain a system of equations that govern the force-displacement characteristics of the revolute joint.

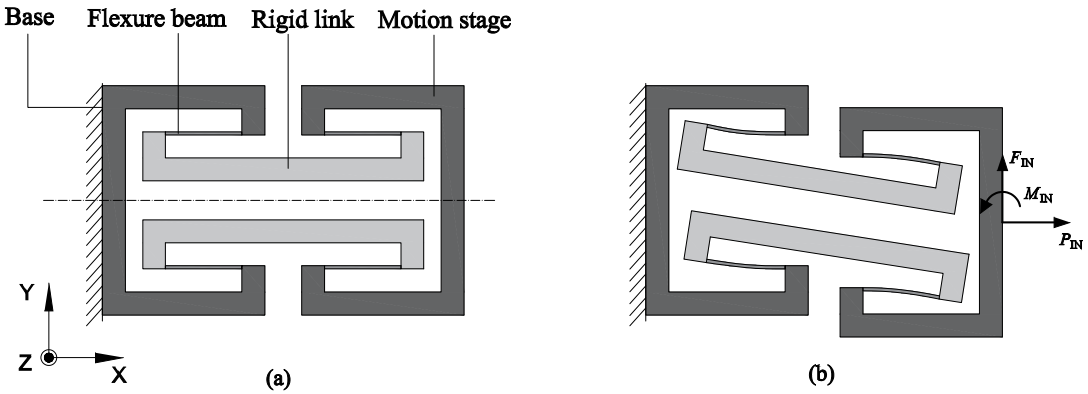


Figure 5.2 Translational joint derived from the revolute joint [65]: (a) geometric composition; (b) deformed configuration.

Table 5.1 The geometric parameters of the revolute joint

GLBM 1	α_1 (deg)	β_1 (deg)	γ_1 (deg)	W_1 (mm)	L_{11} (mm)	L_{12} (mm)	T_1 (mm)	U_1 (mm)
	−150	210	30	40	20	20	0.4	4
GLBM 2	α_2 (deg)	β_2 (deg)	γ_2 (deg)	W_2 (mm)	L_{21} (mm)	L_{22} (mm)	T_2 (mm)	U_2 (mm)
	150	−210	−30	40	20	20	0.4	4

Figure 5.1(a) and (b) illustrate the geometry and the deformed configuration under given end forces, respectively. We then substituted the corresponding geometry parameters as

shown in Table 5.1, into the GLBM to extract the constitutive equations of the inverted beams. It is important to note that each of the inverted beams has its own GLBM, as derived previously. With the constitutive equation in hand, we then continued with the force equilibrium analysis and geometry compatibility to gain a deeper understanding of the revolute joint.

Based on the FBD (Figure 5.1(c)), we can obtain the force equilibrium:

$$F_{\text{in}} = F_{\text{s1}} + F_{\text{s2}} \tag{5.1}$$

$$P_{\text{in}} = P_{\text{s1}} + P_{\text{s2}}$$

$$M_{\text{in}} = M_{\text{s1}} + M_{\text{s2}} - P_{\text{s2}} \cdot \cos\left(\theta_{\text{out}}\right) \cdot D/2 - F_{\text{s2}} \cdot \sin\left(\theta_{\text{out}}\right) \cdot D/2 + P_{\text{s1}} \cdot \cos\left(\theta_{\text{out}}\right) \cdot D/2$$

$$+F_{\text{s1}} \cdot \sin\left(\theta_{\text{out}}\right) \cdot D/2$$

where D = 50 mm is the length of the motion stage.

The geometry compatibility conditions for the revolute joint are shown below:

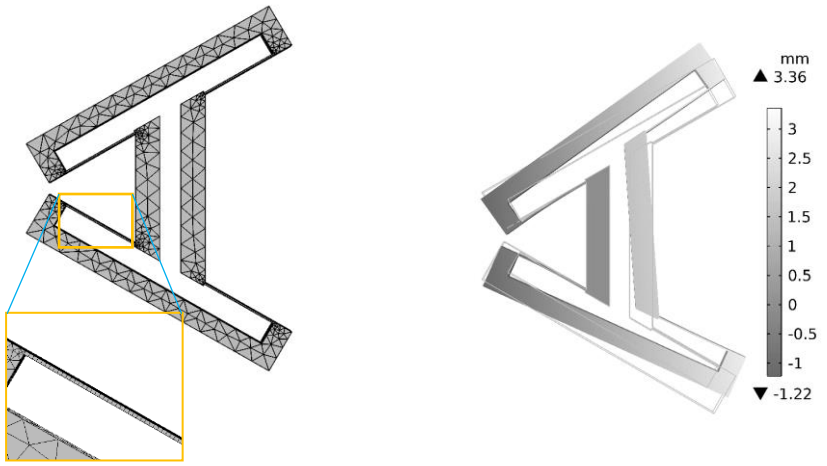
$$X_{\text{s1}} = X_{\text{out}} + \sin\left(\theta_{\text{out}}\right) \cdot D/2;\ X_{\text{s2}} = X_{\text{out}} - \sin\left(\theta_{\text{out}}\right) \cdot D/2; \tag{5.2}$$

$$Y_{\text{s1}} = Y_{\text{out}} + (1 - \cos\left(\theta_{\text{out}}\right) \cdot D/2);$$

$$Y_{\text{s2}} = Y_{\text{out}} - (1 - \cos\left(\theta_{\text{out}}\right) \cdot D/2);\ \theta_{\text{s1}} = \theta_{\text{out}};\ \theta_{\text{s2}} = \theta_{\text{out}}$$

To gain insight into the force-displacement characteristics of the revolute joint, a system of nonlinear equations was developed. Among them, 30 equations were governed by two GLBMs responsible for describing the force-displacement characteristics, and constitutive conditions of the resulting compliant mechanism. The remaining 9 equations comprised three force-equilibrium equations and 6 geometry compatibility equations. This analytical model was then used to validate our findings with the FEA tool, Comsol. By comparing the results obtained from both the analytical model and the FEA tool, we were able to obtain a more comprehensive understanding of the force-displacement behavior of the revolute joint. This approach allowed us to verify the accuracy of our model and identify any discrepancies or limitations that may exist in the analytical or computational methods used. Incremental input forces including F_{in}, P_{in}, and M_{in} are applied to the input stages with 10 steps. Calculation of the 10 steps together takes about

3-5 seconds using the Loop function in Maple, while the calculation using the FEA method takes about 80-85 seconds.



(a) (b)

Figure 5.3 FEA simulation in Comsol: (a) mesh type for the rigid bodies and flexure beams; (b) displacement plot of the revolute joint in Comsol.

Figure 5.3 depicts the mesh type and deformed configuration of the revolute joint in the FEA simulation. In Figure 5.3 (a), the rigid parts utilize default tetrahedral elements, while the flexure parts employ cuboid elements. This combination optimizes the element count, achieving a balance between computing time and accuracy without compromising the results. The displacement plot in Figure 5.3(b) illustrates the outcome of applying an input force of 0.8 N in the Y-direction. As a result, the motion stage undergoes a significant displacement of 2.11 mm along the Y-direction.

Figure 5.4 illustrates a comparison between the analytical results and the FEA simulation of the output displacement of the motion stage. The comparison shows good agreement between the two methods. Specifically, Figure 5.4(a) presents the results of the motion stage rotation (θ_{out}), with a maximum error between the analytical results and FEA simulation of 4.1%. Figure 5.4(b) plots the out displacement in the X-direction of the revolute joint under incremental input forces, demonstrating a nonlinear characteristic with a maximum error of 4.3%. Finally, Figure 5.4(c) depicts the output displacement in the Y-direction, with an error between the analytical results and FEA results of less than 2.0%. Overall, these results indicate the accuracy and reliability of both analytical and

FEA methods in analyzing the behavior of the revolute joint.

Table 5.2 The geometry parameters of the bistable mechanism

GLBM 1	α_1 (deg)	β_1 (deg)	γ_1 (deg)	W_1 (mm)	L_{11} (mm)	L_{12} (mm)	T_1 (mm)	U_1 (mm)
	−25.68	42.18	12.53	18.69	20	25	0.4	4
GLBM 2	α_2 (deg)	β_2 (deg)	γ_2 (deg)	W_2 (mm)	L_{21} (mm)	L_{22} (mm)	T_2 (mm)	U_2 (mm)
	11	11	13.65	22.42	15	15	0.4	4

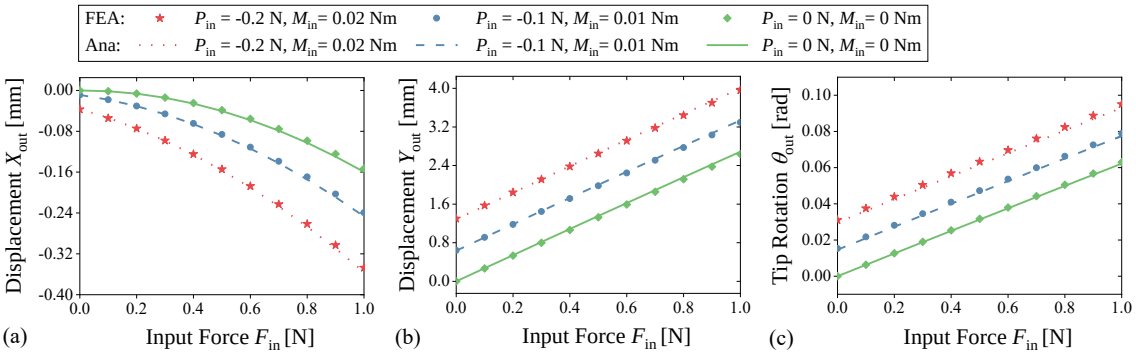


Figure 5.4 FEA verification of the revolute joint with inverted beam: (a) displacement in X-direction versus the input force F_{in}; (b) displacement in Y-direction versus the input force F_{in}; (c) rotation about Z-axis versus the input force F_{in}.

5.1.2 Case II - bistable mechanism using two types of GLBMs

A novel bistable mechanism with triangle shape flexure [238] in which torsion reinforces structures are used to increase the out-of-plane stiffness as depicted in Figure 5.5. It is mainly composed of a folded beam (GLBM 1) and an inclined beam (GLBM 2), shuttle and base. The folded beam is used to increase the torsional stiffness of the shuttle along the X-axis. To prevent self-retraction, the inclined beam is used to increase the strain energy stored in the second stable position and also to prevent the model from getting a higher buckling mode compared to the distributed-compliance beam. Figure 5.5(b) displays the labeled geometry parameters of the bistable mechanism.

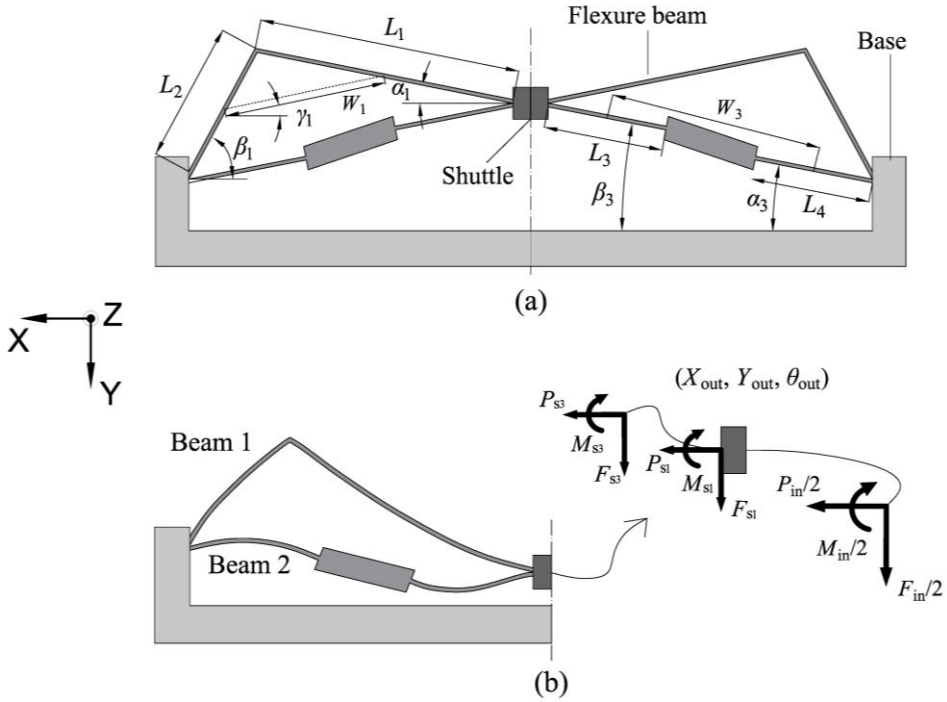


Figure 5.5 Bistable mechanism with increased out-of-plane stiffness: (a) geometry parameters; (b) deformed configuration and the FBD of the shuttle.

To model this bistable mechanism, it is necessary to establish the constitutive, force equilibrium, and geometry compatibility conditions. This process is identical to the one presented in case one. Section 5.1.2 provides the derivation of the constitutive equation for each GLBM. Meanwhile, the force equilibrium can be obtained by the given FBD in Figure 5.5(b), which is shown below.

$$F_{\text{in}}/2 = -(F_{\text{s1}} + F_{\text{s2}});\ P_{\text{in}}/2 = -(P_{\text{s1}} + P_{\text{s2}});\ M_{\text{in}}/2 = M_{\text{s1}} + M_{\text{s2}} - (F_{\text{s1}} + F_{\text{s2}}) \cdot D/2 \qquad (5.3)$$

where D = 10 mm is the length of the shuttle.

The geometry compatibility conditions for the bistable mechanism are shown below:

$$X_{\text{s1}} = 0;\ X_{\text{s2}} = 0;\ Y_{\text{s1}} = -Y_{\text{out}};\ Y_{\text{s2}} = -Y_{\text{out}};\ \theta_{\text{s1}} = 0;\ \theta_{\text{s2}} = 0 \qquad (5.4)$$

The force-displacement characteristic of the bistable mechanism now can be obtained by solving the system of nonlinear equations derived above. The shuttle is subjected to incremental displacement to activate its bistable mechanism, which is also simulated in the FEA analysis.

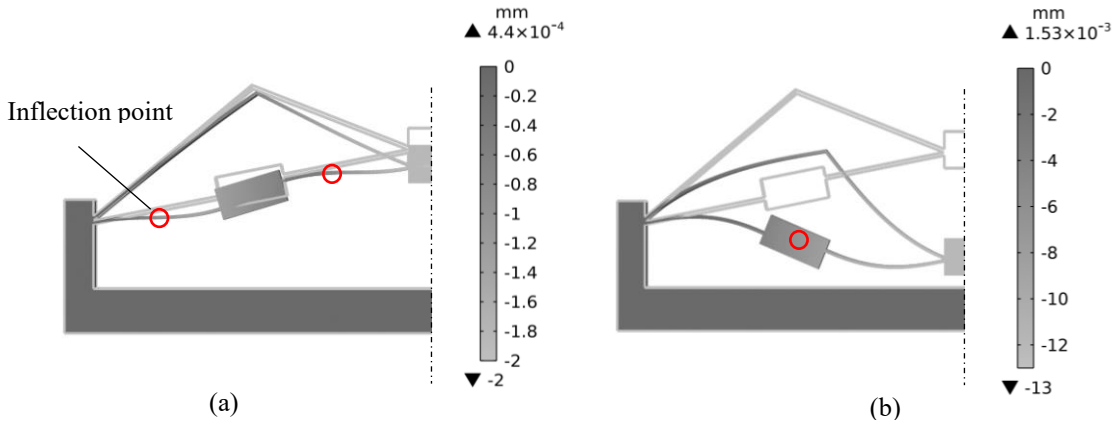


Figure 5.6 Inflection points simulated in Comsol with one inflection point vanishing during snap-through: (a) bending with two inflection points; (b) the second bistable position with only one inflection point.

The bistable mechanism's FEA simulation was conducted using Comsol, following a process similar to that presented in Figure 2.3. It's noted that achieving convergence for the solution requires setting an appropriate iteration number, especially when dealing with significant nonlinear deformations. For this study, the maximum iteration number was set to 200 (default is 25). During the simulation, a critical buckling force was determined, causing the beam to buckle into a bending mode [70]. The shape taken by the buckled mechanism is defined by the number of inflection points.

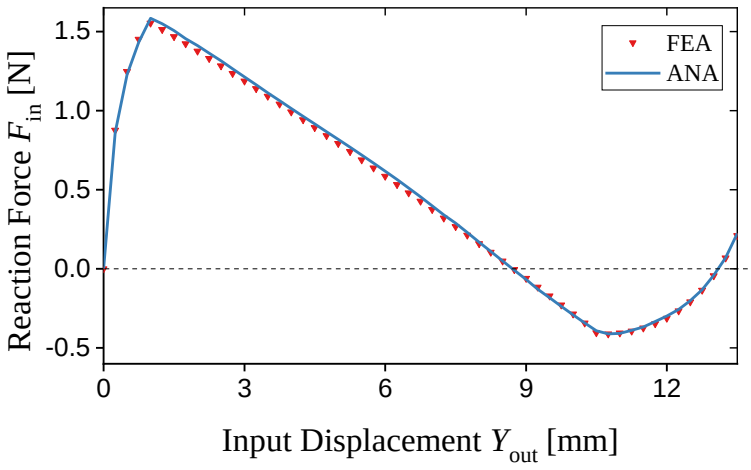


Figure 5.7 FEA verification of the behavior of the bistable mechanism

Figure 5.6(a) visually illustrates the deformed shape of the bistable mechanism, which exhibits two inflection points before the snap-through position. However, after passing

this snap-through position, the mechanism moves towards its second stable position. Figure 5.6(b) shows the deformed shape with only one inflection point.

Figure 5.7 depicts a comparison of the analytical and FEA results, revealing good agreement between the two. The maximum absolute error in the reaction force is found to be below 0.035 N, validating the accuracy of the developed model in precisely modeling bistable mechanisms with both large deflections and high axial forces.

5.1.3 Experimental validation of the revolute joint

In this section, we conducted an experimental test to validate both the FEA and analytical results of the revolute joint, as shown in Figure 5.8. To ensure a robust experiment setup, we fabricated a prototype with specific parameters outlined in Table 5.3. The flexure beams were made from copper, and all other components were 3D printed by Ultimaker S3 using Polylactic Acid (PLA) as material. We employed an auxiliary positioning frame depicted in Figure 5.8(b) to achieve precise assembly of the revolute joint to the 3D printed parts. The flexure beams were securely fixed to the rigid parts using super glue.

Table 5.3 The geometric parameters of the fabricated revolute joint prototype

GLBM 1	α_1 (deg)	β_1 (deg)	γ_1 (deg)	W_1 (mm)	L_{11} (mm)	L_{12} (mm)	T_1 (mm)	U_1 (mm)
	−150	210	30	52	20	20	0.3	10
GLBM 2	α_2 (deg)	β_2 (deg)	γ_2 (deg)	W_2 (mm)	L_{21} (mm)	L_{22} (mm)	T_2 (mm)	U_2 (mm)
	150	−210	−30	52	20	20	0.3	10

5.1.3.1 Experimental Setup of the Revolute Joint

Figure 5.8(a) illustrates the experimental setup used to evaluate the force-displacement characteristics of the revolute joint under different loading conditions. The setup comprises five key components: a micrometer, a force sensor, a linear guide, the fabricated prototype, and a pulley system. The micrometer enabled us to precisely control and apply prescribed input displacements, while the force sensor, sitting on a linear guide, measured the reaction force from the motion stage. We utilized a pulley system to apply 100-gram and 200-gram weights acting payloads (P_{in}) to the motion stage in addition to the exerted input force from the micrometer. Figure 5.8(c) showcases the deformed

configuration of the revolute joint with a 200-gram payload. To ensure the reliability of our results, each experimental procedure was repeated three times, and the average of the experiment results was calculated for plot and comparison.

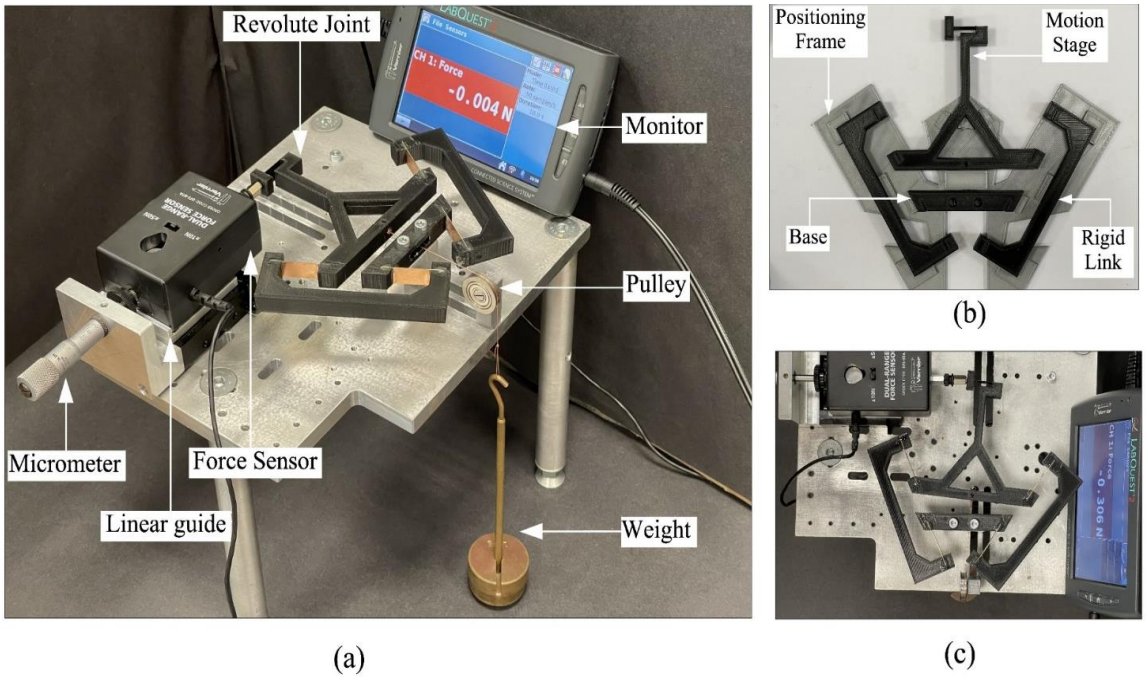


Figure 5.8 Experimental setup and the prototype of the revolute joint: (a) Experimental setup; (b) 3D-printed positioning frame, motion stage, rigid link, and base; (c) its deformed configuration.

5.1.3.2 Experimental Results

The experiment was carried out successfully to validate both the FEA and analytical results. Figure 5.9 shows the tip force-displacement characteristics of the revolute joint under different payloads. As expected, the experimental results align closely with both the FEA and analytical results, demonstrating a maximum error of 5.6%. Notably, the revolute joint displays a load-dependent effect, where an increase in payload leads to a reduction in the rotational stiffness of the joint. This phenomenon, attributed to the combined effects of geometric nonlinearity and material elasticity, highlights the importance of accurately accounting for load variations in the design and optimization processes.

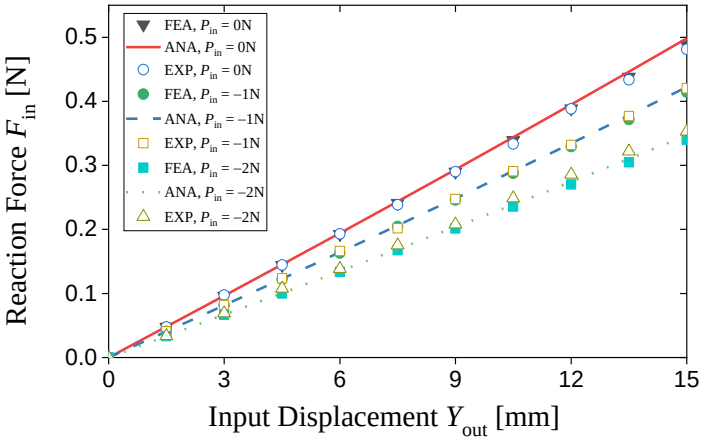


Figure 5.9 Tip force-displacement characteristics under different payload.

5.1.4 Experimental validation of the bistable mechanism

In this section, we conducted experiments on a new bistable mechanism as shown in Figure 5.10. To create a cost-effective experimental setup, we fabricated a monolithic 3D-printed prototype (Figure 5.10(b)) and assembled it on the testing apparatus. The prototype was printed using the Ultimaker S3, with a layer height of 0.1 mm. PLA was used as the material, with a Young's modulus of 3.3 GPa and a yield strength of 52.5 MPa. The experiment was carried out within the yield strength which is first simulated in the Comsol. The new bistable mechanism comprises two identical bistable mechanisms. The two compositional bistable mechanisms are arranged in parallel to reduce the stage rotation while achieving prescribed translational displacement. The specific geometry parameters of each GLBM used in the mechanism are outlined in Table 5.4.

Table 5.4 The geometry parameters of the fabricated bistable mechanism

GLBM 1	α_1 (deg)	β_1 (deg)	γ_1 (deg)	W_1 (mm)	L_{11} (mm)	L_{12} (mm)	T_1 (mm)	U_1 (mm)
	−19.17	40.83	10.93	28	32.32	32.32	0.4	8
GLBM 2	α_2 (deg)	β_2 (deg)	γ_2 (deg)	W_2 (mm)	L_{21} (mm)	L_{22} (mm)	T_2 (mm)	U_2 (mm)
	10	10	11.59	36.01	20	20	0.4	8

5.1.4.1 Experimental Setup

The assembly of the experimental setup primarily involves four components: the

micrometer, force sensor, linear guide, and fabricated prototype, as depicted in Figure 5.10(a). To accurately measure the retraction force of the bistable mechanism, we affixed a powerful magnet to the shuttle of the mechanism. This magnet ensures a firm attachment between the shuttle and the probe of the force sensor. Figure 5.10(c) illustrates the new bistable mechanism at its second stable position. To ensure reliable results, each experimental procedure was repeated three times, and the average of the experiment results was calculated for plot and comparison. Additionally, we calculated the standard deviation of these three results to assess the repeatability of the measurements.

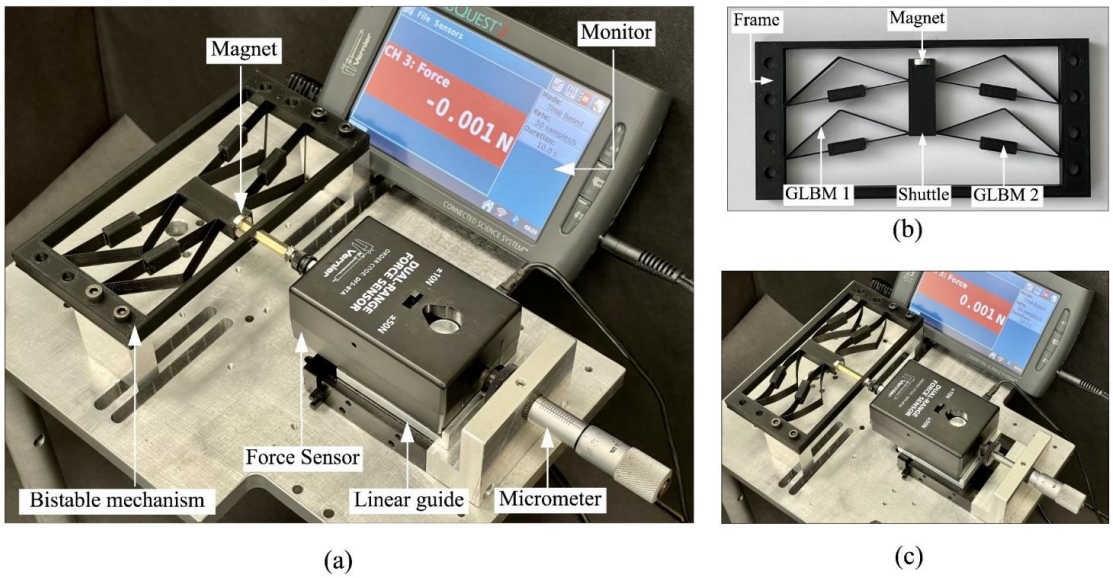


Figure 5.10 Experimental setup and the prototype of the bistable mechanism: (a) Experimental setup; (b) 3D-printed prototype; (c) Second stable position of the bistable mechanism.

5.1.4.2 Experimental Results

After conducting the experiment three times, we plotted the average reaction force along with its standard deviation in Figure 5.11. A comparison of the experimental results with both the FEA and analytical results revealed a similar pattern. Remarkably, the FEA and analytical results showed better agreement, while the experimental results deviated from both, with a maximum difference of 0.62 N. Several factors could contribute to this deviation, including potential fabrication or assembly errors and undesired elastic deformation of the parts that were assumed to be rigid during the theoretical analysis.

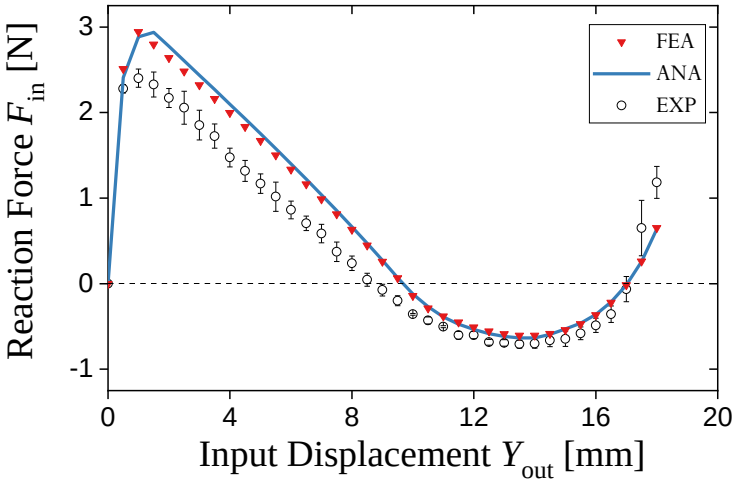


Figure 5.11 Force-displacement characteristic of the bistable mechanism.

5.2 3D Design and nonlinear modelling of the general spherical joint

In this section, our objective is to utilize the GSTC leaf beam for the design and analysis of a general spherical joint. Initially, we will develop a general nonlinear force-displacement model for the spherical joint using the GSTC leaf beam as the basis and it will be verified by the FEA simulation. Subsequently, four representative spherical joints will then undergo centre drift analysis.

5.2.1 Design of a general spherical joint based on the GSTC leaf beams

A spherical joint is formed by the intersection of three single-translation constraint wire beams [96, 8] as depicted in Figure 5.12(a). The joint can rotate about the remote centre, denoted as point P. By substituting these wire beams with three GSTC leaf beams, we can create a general spherical joint.

The general spherical joint can be reduced to several interesting designs. Figure 5.12(b) presents a spherical joint with SSTC leaf beams. Figure 5.12(c) showcases a spherical joint featuring three I-shape leaf beams, previously discussed in our work [152]. Figure 5.12(d) displays a spherical joint with folded leaf beams, documented in [26, 238]. Figure 5.12(e) exhibits a spherical joint with L-shape leaf beams, also introduced in our earlier research. While additional configurations are feasible using the GSTC leaf beam, this

work concentrates on analyzing these representative spherical joints, with a specific emphasis on centre drift analysis, a topic less previously explored.

5.2.2 Nonlinear modelling of the general spherical joint

To analyse the newly designed general spherical joint, we commence by deriving the nonlinear force-displacement characteristics of the general spherical joint. This derivation parallels previous analyses, necessitating the establishment of three fundamental components: constitutive equations, force equilibrium, and geometry compatibility.

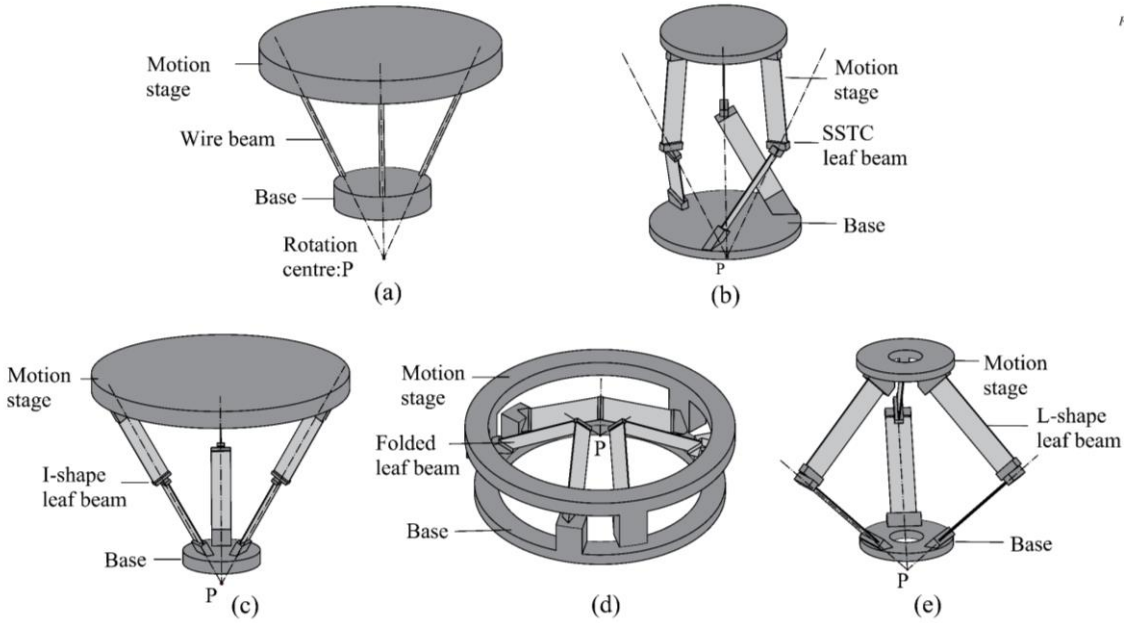


Figure 5.12 Spherical joints: (a) wire beam based spherical joint; (b) general spherical joint using SSTC leaf beams; (c) spherical joint using I-shape leaf beams; (d) spherical joint using folded leaf beams; (e) spherical joint using L-shape leaf beams. A video showcasing the design of the general spherical joint is available on YouTube: https://youtu.be/tWx_8c3q-Qw.

The spherical joint experiences general loading denoted as F_{xt}, F_{yt}, F_{zt}, M_{xt}, M_{yt}, and M_{zt}, at reference point O_t, resulting in spatial displacements denoted as X_t, Y_t, Z_t, θ_{xt}, θ_{yt}, and θ_{zt}, as depicted in Figure 5.13(a). These displacements are defined within the global coordinate system X_T-Y_T-Z_T as shown in Figure 5.13(b). Furthermore, the displacement of each GSTC leaf beam is defined in the coordinate system X_{Si}-Y_{Si}-Z_{Si} (symbol i represents the i^{th} GSTC leaf beam).

Geometry parameters γ_0, β_0, and R_0 as labeled in Figure 5.13(a) and (b), are defined as the

main variables for determining the orientation and position of the GSTC leaf beam. Specifically, γ_0 donates the GSTC leaf beam self-rotation about the X_S axis, β_0 donates the angle between the constraint line of the GSTC leaf beam and the centre line of the spherical joint, and R_0 (non-normalized) donates the distance from the geometry centre O of the GSTC leaf beam to the centre line of the spherical joint. All these parameters are defined in the global X_T-Y_T-Z_T coordinate system. It is noteworthy that the orientation of the local coordinate system for each GSTC leaf beam aligns with the global X_T-Y_T-Z_T coordinate system prior to positioning. The rotation matrix, presented below, represents an extrinsic rotation adhering to the right-hand rule.

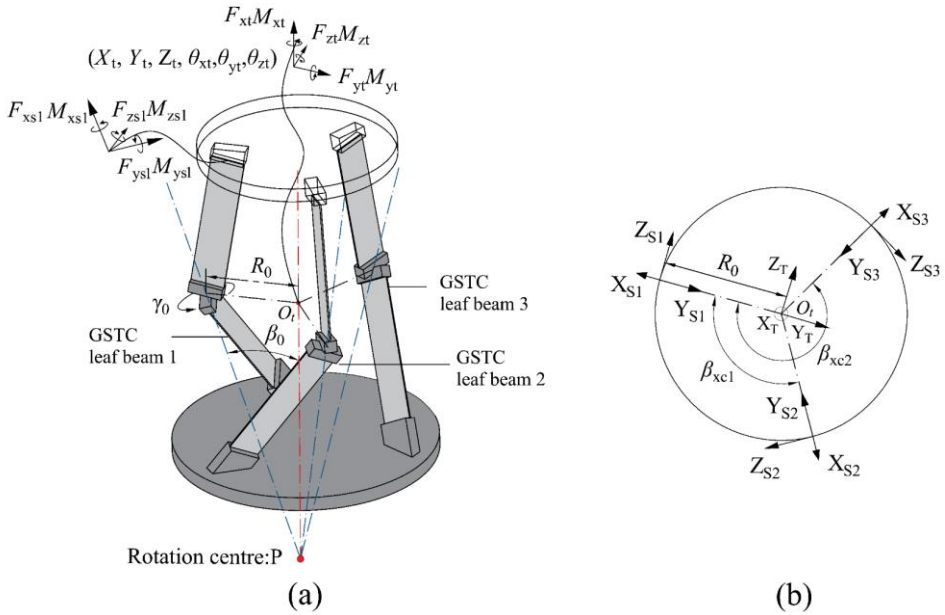


Figure 5.13 General spherical joint with GSTC leaf beams: (a) geometry labeling; (b) top view of the coordinate systems.

$$R_t = \begin{bmatrix} 1 & 0 & 0 \\ 0 & \cos(\theta_{xt}) & -\sin(\theta_{xt}) \\ 0 & \sin(\theta_{xt}) & \cos(\theta_{xt}) \end{bmatrix} \begin{bmatrix} \cos(\theta_{zt}) & -\sin(\theta_{zt}) & 0 \\ \sin(\theta_{zt}) & \cos(\theta_{zt}) & 0 \\ 0 & 0 & 1 \end{bmatrix} \begin{bmatrix} \cos(\theta_{yt}) & 0 & \sin(\theta_{yt}) \\ 0 & 1 & 0 \\ -\sin(\theta_{yt}) & 0 & \cos(\theta_{yt}) \end{bmatrix} \tag{5.5}$$

The force equilibrium of the motion stage is established based on the FBD under the deformed configuration.

$$\begin{aligned}\left[f_{xt},\ f_{yt},\ f_{zt},\ m_{xt},\ m_{yt},\ m_{zt}\right]^{T} &= D_{T1}^{T}R_{ZT}R_{XT}R_{YT}R_{XS}\left[f_{xs1},\ f_{ys1},\ f_{zs1},\ m_{xs1},\ m_{ys1},\ m_{zs1}\right]^{T} \\ &+D_{T2}^{T}R_{XC1}R_{ZT}R_{XT}R_{YT}R_{XS}\left[f_{xs2},\ f_{ys2},\ f_{zs2},\ m_{xs2},\ m_{ys2},\ m_{zs2}\right]^{T} \\ &+D_{T3}^{T}R_{XC2}R_{ZT}R_{XT}R_{YT}R_{XS}\left[f_{xs3},\ f_{ys3},\ f_{zs3},\ m_{xs3},\ m_{ys3},\ m_{zs3}\right]^{T}\end{aligned} \tag{5.6}$$

where D_{T1}, $D_{T2,}$ and D_{T3} represent 6×6 normalized translation matrices for the free ends of GSTC leaf beams 1, 2, and 3, respectively. Their general form is provided below. In addition, the transform matrices R_{YT}, R_{XT}, and R_{ZT} donate the 6×6 rotational matrices about the Y_T, $Z_{T,}$ and X_T axis, respectively. The rotation order of the GSTC leaf beam can be defined by the user. In this work, the author adopts the order used in Solidworks for convenience in constructing the 3D model. R_{XS} is the 6×6 rotation matrix which rotates about the local coordinate X_S (intrinsic rotation). R_{XC1} and R_{XC2} donate the 6×6 rotation matrix of the GSTC leaf beam 2 and 3 respectively, about the axis X_T. The centre of the moment (equilibrium position) is located at the point O_t.

$$D_{Ti}=\begin{bmatrix} & 0 & d_i(3,1) & -d_i(2,1) \\ I_{3\times3} & -d_i(3,1) & 0 & d_i(1,1) \\ & d_i(2,1) & -d_i(1,1) & 0 \\ 0_{3\times3} & & I_{3\times3} & \end{bmatrix} \tag{5.7}$$

$$d_1 = R_t(R_{zt}R_{xt}R_{yt}R_{xs}\left[\lambda_x,\ \lambda_y,\ \lambda_z\right]^{T}+\left[0,\ r_0,\ 0\right]^{T}) \tag{5.8}$$

$$d_2 = R_t(R_{xc1}R_{zt}R_{xt}R_{yt}R_{xs}\left[\lambda_x,\ \lambda_y,\ \lambda_z\right]^{T}+R_{xc1}\left[0,\ r_0,\ 0\right]^{T});$$

$$d_3 = R_t(R_{xc2}R_{zt}R_{xt}R_{yt}R_{xs}\left[\lambda_x,\ \lambda_y,\ \lambda_z\right]^{T}+R_{xc2}\left[0,\ r_0,\ 0\right]^{T});$$

$$R_{ZT}=\begin{bmatrix} R_{zt} & 0_{3\times3} \\ 0_{3\times3} & R_{zt}\end{bmatrix};\ R_{XT}=\begin{bmatrix} R_{xt} & 0_{3\times3} \\ 0_{3\times3} & R_{xt}\end{bmatrix};R_{XS}=\begin{bmatrix} R_{xs} & 0_{3\times3} \\ 0_{3\times3} & R_{xs}\end{bmatrix} \tag{5.9}$$

The transform matrices R_{yt}, $R_{xt,}$ and R_{zt} donate the 3×3 rotation matrices about the Y_T, Z_T, and X_T axis, respectively, which are used to define the orientation of the free end of the GSTC leaf beam. These three rotations contribute to the angle of β_0, which is known. R_{xs} is the 3×3 rotation matrix which rotates about the local coordinate X_S (intrinsic rotation). R_{xc1} and R_{xc2} donate the 3×3 rotation matrix about the X_T-axis of the GSTC leaf beam 2 and 3 respectively, about the axis X_T. λ_x, λ_y and λ_z donate the coordinates of the free end of the GSTC leaf beam 1 relative to the X_T-Y_T-Z_T coordinate before the rotation of angle β_0. r_0 donates the normalized R_0.

$$R_{\mathrm{yt}}=\begin{bmatrix}\cos(\beta_{\mathrm{yt}}) & 0 & \sin(\beta_{\mathrm{yt}})\\ 0 & 1 & 0\\ -\sin(\beta_{\mathrm{yt}}) & 0 & \cos(\beta_{\mathrm{yt}})\end{bmatrix};R_{\mathrm{zt}}=\begin{bmatrix}\cos(\beta_{\mathrm{zt}}) & -\sin(\beta_{\mathrm{zt}}) & 0\\ \sin(\beta_{\mathrm{zt}}) & \cos(\beta_{\mathrm{zt}}) & 0\\ 0 & 0 & 1\end{bmatrix};R_{\mathrm{xt}}=\begin{bmatrix}1 & 0 & 0\\ 0 & \cos(\beta_{\mathrm{xt}}) & -\sin(\beta_{\mathrm{xt}})\\ 0 & \sin(\beta_{\mathrm{xt}}) & \cos(\beta_{\mathrm{xt}})\end{bmatrix} \tag{5.10}$$

$$R_{\mathrm{xs}}=\begin{bmatrix}1 & 0 & 0\\ 0 & \cos(\gamma_0) & -\sin(\gamma_0)\\ 0 & \sin(\gamma_0) & \cos(\gamma_0)\end{bmatrix};\ R_{\mathrm{xc1}}=\begin{bmatrix}1 & 0 & 0\\ 0 & \cos(\beta_{\mathrm{xc1}}) & -\sin(\beta_{\mathrm{xc1}})\\ 0 & \sin(\beta_{\mathrm{xc1}}) & \cos(\beta_{\mathrm{xc1}})\end{bmatrix};\ R_{\mathrm{xc2}}=\begin{bmatrix}1 & 0 & 0\\ 0 & \cos(\beta_{\mathrm{xc2}}) & -\sin(\beta_{\mathrm{xc2}})\\ 0 & \sin(\beta_{\mathrm{xc2}}) & \cos(\beta_{\mathrm{xc2}})\end{bmatrix} \tag{5.11}$$

The geometric compatibility between the free end of each GSTC leaf beam and the motion stage can be derived as follows. It is important to note that the initial position of the force and displacement relationship of the motion stage is represented at the position of point O_{t}.

$$R_{\mathrm{zt}}R_{\mathrm{xt}}R_{\mathrm{yt}}R_{\mathrm{sx}}\left[x_{\mathrm{s1}},\ \mathrm{y}_{\mathrm{s1}},\ \mathrm{z}_{\mathrm{s1}}\right]^{\mathrm{T}}=(R_{\mathrm{t}}-I_{3\times3})(R_{\mathrm{zt}}R_{\mathrm{xt}}R_{\mathrm{yt}}R_{\mathrm{sx}}\left[\lambda_{\mathrm{x}},\ \lambda_y,\ \lambda_{\mathrm{z}}\right]^{\mathrm{T}}+\left[0,\ r_0,\ 0\right]^{\mathrm{T}})+\left[x_{\mathrm{t}},\ y_{\mathrm{t}},\ z_{\mathrm{t}}\right]^{\mathrm{T}}$$

$$R_{\mathrm{zt}}R_{\mathrm{xt}}R_{\mathrm{yt}}R_{\mathrm{sx}}\left[\theta_{\mathrm{xs1}},\ \theta_{\mathrm{ys1}},\ \theta_{\mathrm{zs1}}\right]^{\mathrm{T}}=\left[\theta_{\mathrm{xt}},\ \theta_{\mathrm{yt}},\ \theta_{\mathrm{zt}}\right]^{\mathrm{T}}; \tag{5.12}$$

$$R_{\mathrm{xc1}}R_{\mathrm{zt}}R_{\mathrm{xt}}R_{\mathrm{yt}}R_{\mathrm{sx}}\left[x_{\mathrm{s2}},\ \mathrm{y}_{\mathrm{s2}},\ \mathrm{z}_{\mathrm{s2}}\right]^{\mathrm{T}}=(R_{\mathrm{t}}-I_{3\times3})(R_{\mathrm{xc1}}R_{\mathrm{zt}}R_{\mathrm{xt}}R_{\mathrm{yt}}R_{\mathrm{sx}}\left[\lambda_{\mathrm{x}},\ \lambda_y,\ \lambda_{\mathrm{z}}\right]^{\mathrm{T}}+R_{\mathrm{xc1}}\left[0,\ r_0,\ 0\right]^{\mathrm{T}})+\left[x_{\mathrm{t}},\ y_{\mathrm{t}},\ z_{\mathrm{t}}\right]^{\mathrm{T}}$$

$$R_{\mathrm{xc1}}R_{\mathrm{z}}R_{\mathrm{x}}R_{\mathrm{y}}R_{\mathrm{sx}}\left[\theta_{\mathrm{xs2}},\ \theta_{\mathrm{ys2}},\ \theta_{\mathrm{zs2}}\right]^{\mathrm{T}}=\left[\theta_{\mathrm{xt}},\ \theta_{\mathrm{yt}},\ \theta_{\mathrm{zt}}\right]^{\mathrm{T}}; \tag{5.13}$$

$$R_{\mathrm{xc2}}R_{\mathrm{zt}}R_{\mathrm{xt}}R_{\mathrm{yt}}R_{\mathrm{sx}}\left[x_{\mathrm{s3}},\ \mathrm{y}_{\mathrm{s3}},\ \mathrm{z}_{\mathrm{s3}}\right]^{\mathrm{T}}=(R_{\mathrm{t}}-I_{3\times3})(R_{\mathrm{xc2}}R_{\mathrm{zt}}R_{\mathrm{xt}}R_{\mathrm{yt}}R_{\mathrm{sx}}\left[\lambda_{\mathrm{x}},\ \lambda_y,\ \lambda_{\mathrm{z}}\right]^{\mathrm{T}}+R_{\mathrm{xc2}}\left[0,\ r_0,\ 0\right]^{\mathrm{T}})+\left[x_{\mathrm{t}},\ y_{\mathrm{t}},\ z_{\mathrm{t}}\right]^{\mathrm{T}}$$

$$R_{\mathrm{xc2}}R_{\mathrm{zt}}R_{\mathrm{xt}}R_{\mathrm{yt}}R_{\mathrm{sx}}\left[\theta_{\mathrm{xs3}},\ \theta_{\mathrm{ys3}},\ \theta_{\mathrm{zs3}}\right]^{\mathrm{T}}=\left[\theta_{\mathrm{xt}},\ \theta_{\mathrm{yt}},\ \theta_{\mathrm{zt}}\right]^{\mathrm{T}}; \tag{5.14}$$

In total, there are 114 equations, which include 3×30 force-displacement relations of the GSTC leaf beams, 6 force-equilibrium equations, and 18 geometry compatibility equations. The system of nonlinear equations was solved by MATLAB using solver *fsolve*. The feasibility of this general spherical joint model is verified by the FEA simulation using *Comsol*. A combined force and moment is applied to the motion stage at point O_{t}. The displacement results are compared with the results obtained in *Comsol*.

5.2.3 FEA verification of the general spherical joint

This section focuses on the FEA verification of the general force-displacement model of the general spherical joint. First, the verification of the force-displacement relationship at the motion stage's reference point, O_{t} is illustrated, followed by the verification of the resultant centre drift under combined forces and moments.

5.2.3.1 Force-displacement relationship of the motion stage

The developed general force-displacement model for spherical joints was verified using nonlinear FEA simulations. Four representative spherical joints as discussed before were configured with the same initial geometry parameters $\gamma_0 = 0$, $\beta_0 = \pi/4$, and $R_0 = 50$ mm, and the rest parameters are defined in Table 2.2. The other parts are assumed to be rigid.

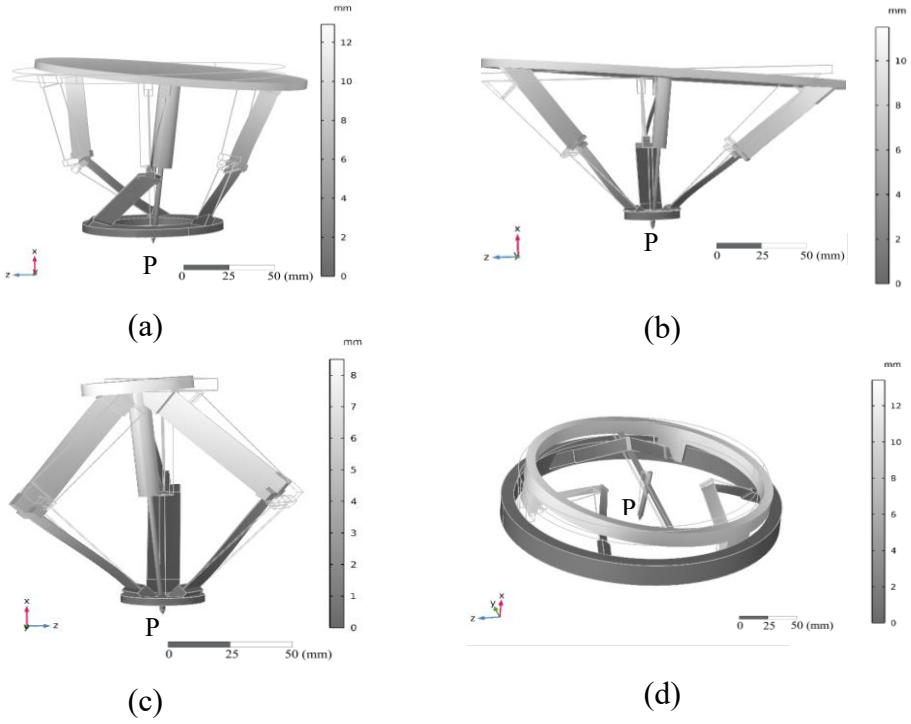


Figure 5.14 The deformed spherical joints under combined forces and moments (all obtained from FEA): (a) spherical joint with SSTC leaf beams; (b) spherical joint with I-shape leaf beams; (c) spherical joint with L-shape leaf beams; (d) spherical joint with folded leaf beams.

The deformation of each spherical joint in FEA under combined forces and moments is shown in Figure 5.14. All joints share the same structure parameters ($\gamma_0 = 0$, $\beta_0 = \pi/4$, and $R_0 = 50$ mm) as well as the same dimensions for the leaf beams. The material for the leaf beams is stainless steel, with a Poisson's ratio of 0.3 and a Young's modulus of 200 GPa, while the remaining parts are assumed to be rigid.

Figure 5.16 shows the comparison results between the analytical model and the FEA simulation for the spherical joint with SSTC leaf beams subjected to combined forces and moments. The resultant displacements show good agreement, where the maximum error

is 9.1% while the rotation along the Y-axis reaches about 0.12 radians.

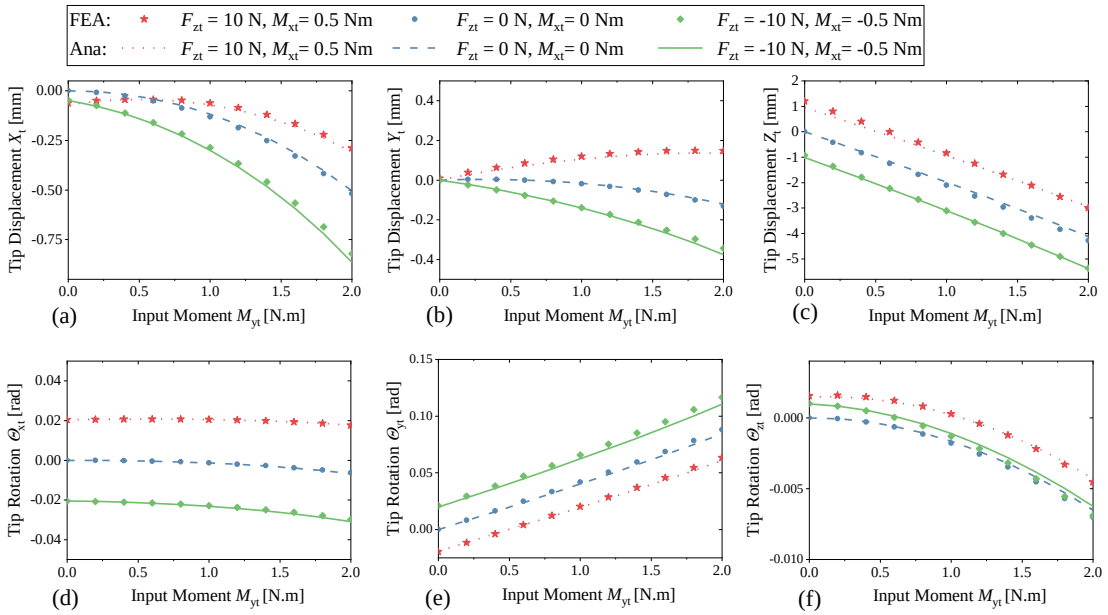


Figure 5.15 (Colour lines) The displacement comparison between the FEA and analytical results for the spherical joint with SSTC leaf beams, subjected to incremental moment along the Y-direction, a constant moment along the X-direction and a constant force in the Z-direction: (a) the resultant displacement X_t; (b) the resultant displacement Y_t; (c) the resultant displacement Z_t; (d) the resultant rotation θ_{xt}; (e) the resultant rotation θ_{yt}; (f) the resultant rotation θ_{zt};

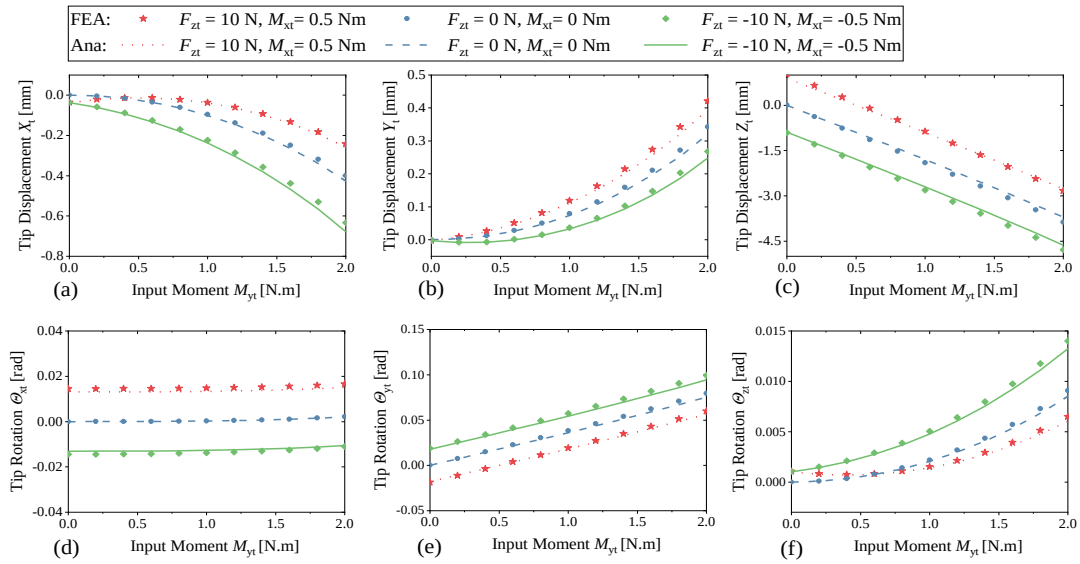


Figure 5.16 (Colour lines) The displacement comparison between the FEA and analytical results for the spherical joint with I-shape leaf beams, subjected to incremental moment along the Y-direction, a constant moment along the X-direction and a constant force in the X-direction: (a) the resultant displacement X_t; (b) the resultant displacement Y_t; (c) the resultant displacement Z_t; (d) the resultant rotation θ_{xt}; (e) the resultant rotation θ_{yt}; (f) the resultant rotation θ_{zt};

Figure 5.15 presents a comparison between analytical and FEA results for the spherical joint featuring I-shape leaf beams. The largest deviation, at 11.8%, occurs in the X-direction tip displacement of the motion stage. However, displacements in other directions exhibit a closer alignment with FEA results, with a maximum error of 6.5%.

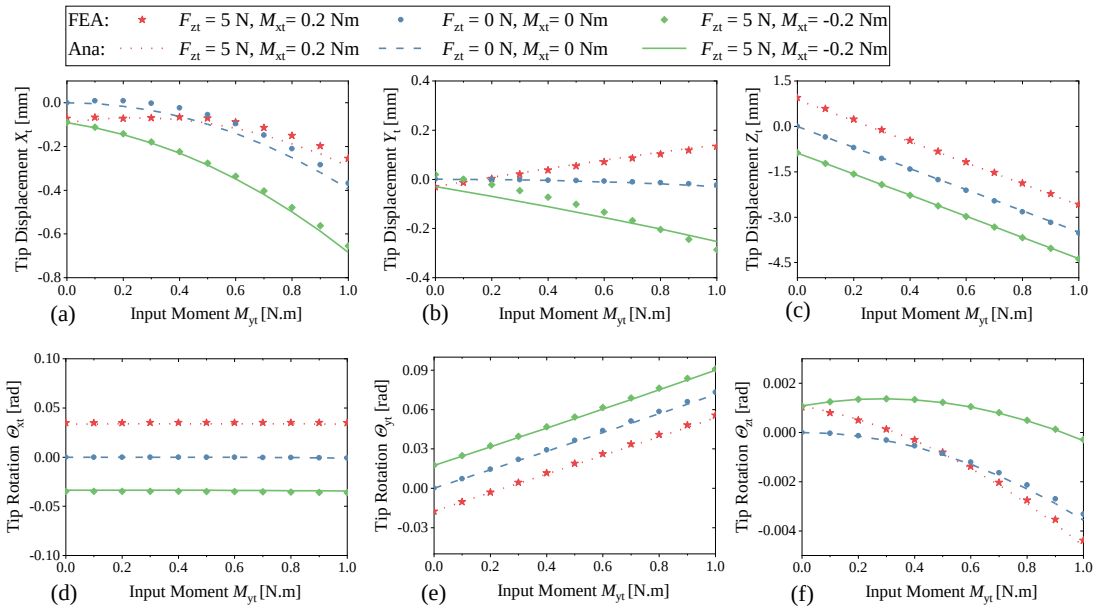


Figure 5.17 (Colour lines) The displacement comparison between the FEA and analytical results for the spherical joint with L-shape leaf beams, subjected to incremental moment along the Y-direction, a constant moment along the X-direction and a constant force in the X-direction: (a) the resultant displacement X_t; (b) the resultant displacement Y_t; (c) the resultant displacement Z_t; (d) the resultant rotation θ_{xt}; (e) the resultant rotation θ_{yt}; (f) the resultant rotation θ_{zt};

In Figure 5.17, comparing the spherical joint with L-shape leaf beams, the overall agreement between analytical and FEA results is evident. Yet, similar to Figure 5.15, the greatest deviation, 9.2%, is observed in the X-direction displacement. Figure 5.18 extends this comparison to spherical joints with folded leaf beams, showing a similar pattern of agreement to the FEA results. However, the X-direction displacement (X_t) exhibits a 9.8% difference under a 0.085 radians rotation along the Y-direction. This disparity is reasonable as X_t, constrained by design, consistently remains small.

While the developed GSTC leaf beam model accurately captures the force-displacement characteristics, it exhibits a relatively larger error when predicting displacements in constrained directions compared to those in unconstrained degrees of freedom. This discrepancy arises because displacements in constrained directions are inherently small,

making even minor numerical deviations result in a higher percentage error. Such behavior aligns with expectations, as small absolute displacements are more sensitive to numerical precision limits in both analytical modeling and FEA simulations.

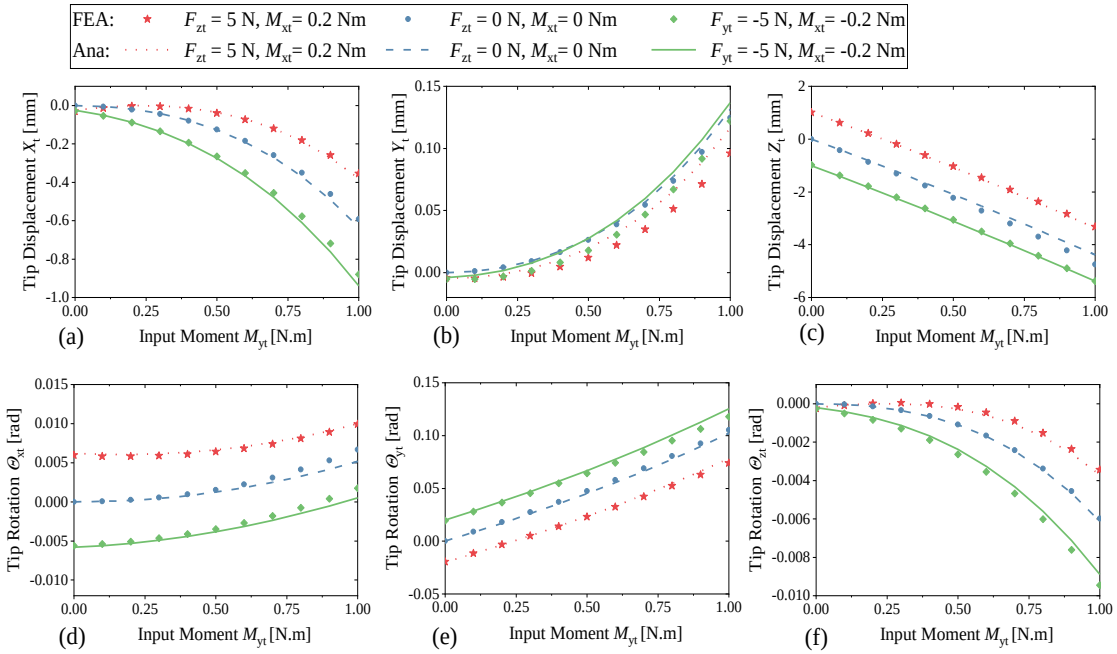


Figure 5.18 (Colour lines) The displacement comparison between the FEA and analytical results for the spherical joint with folded leaf beams, subjected to incremental moment along the Y-direction, a constant moment along the X-direction and a constant force in the X-direction: (a) the resultant displacement X_t; (b) the resultant displacement Y_t; (c) the resultant displacement Z_t; (d) the resultant rotation θ_{xt}; (e) the resultant rotation θ_{yt}; (f) the resultant rotation θ_{zt};

5.2.3.2 Centre drift verification

Centre drift, in this context, refers to any deviation from the intended rotation centre of the joint. Investigating this drift is crucial for optimizing system performance and ensuring that movements are accurate and precise. In many applications, precision and accuracy are paramount for safety. Significant centre drift in a spherical joint can result in errors in positioning or movement. Here, d_{xc}, d_{yc} and d_{zc} are used to represent the normalised centre drift in the X, Y, and Z direction, respectively, in the global coordinate X_T-Y_T-Z_T. The centre drift can be derived as below.

$$\begin{bmatrix} d_{xc} \\ d_{yc} \\ d_{zc} \end{bmatrix} = \begin{bmatrix} x_t \\ y_t \\ z_t \end{bmatrix} + (R_t - I_{3\times3}) \begin{bmatrix} \dfrac{r_0}{\tan\beta_0} \\ 0 \\ 0 \end{bmatrix} \tag{5.15}$$

To verify the accuracy of the general analytical model for predicting centre drift in spherical joints, FEA simulations were conducted. Combined forces and moments were applied to the spherical joint, and the resultant centre drifts in the X, Y, and Z directions were captured and compared.

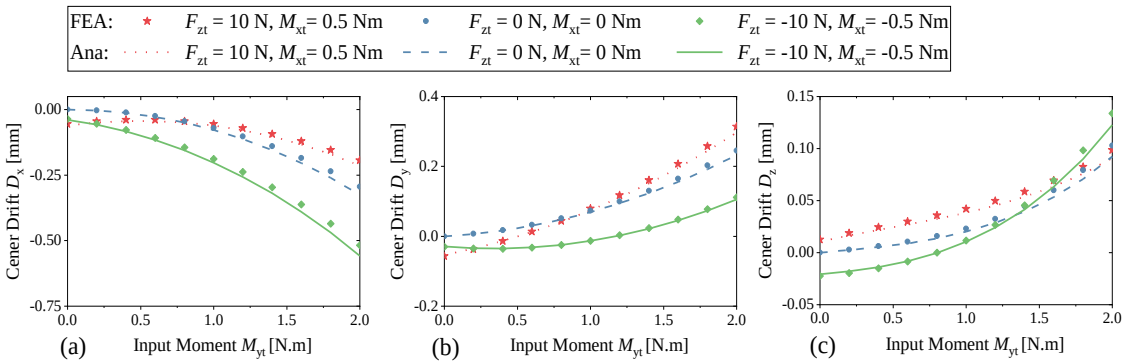


Figure 5.19 (Colour lines) The centre drift comparison between the FEA and analytical results for the spherical joint with SSTC leaf beams, subjected to incremental moment along the Y-direction, a constant moment along the X-direction and a constant force in the X-direction: (a) the resultant displacement D_{xc}; (b) the resultant displacement D_{yc}; (c) the resultant displacement D_{zc};

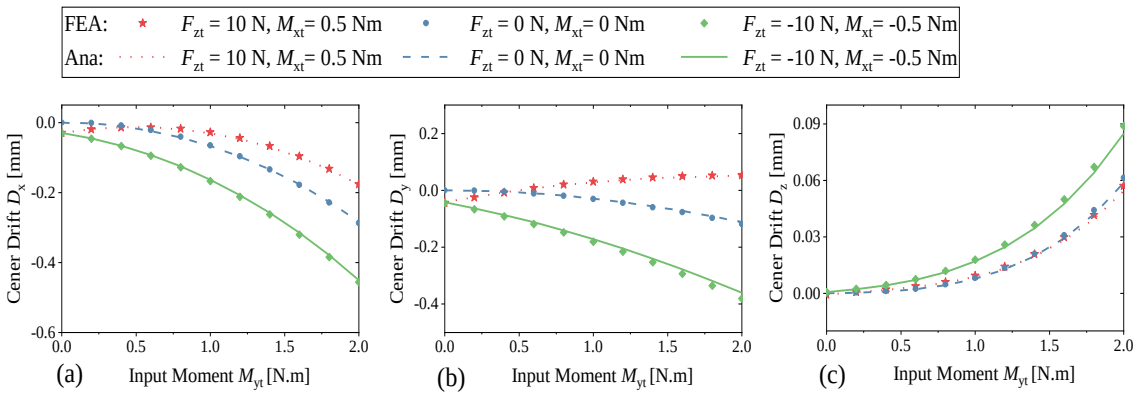


Figure 5.20 (Colour lines) The centre drift comparison between the FEA and analytical results for the spherical joint with I-shape leaf beams, subjected to incremental moment along the Y-direction, a constant moment along the X-direction and a constant force in the X-direction: (a) the resultant displacement D_{xc}; (b) the resultant displacement D_{yc}; (c) the resultant displacement D_{zc};

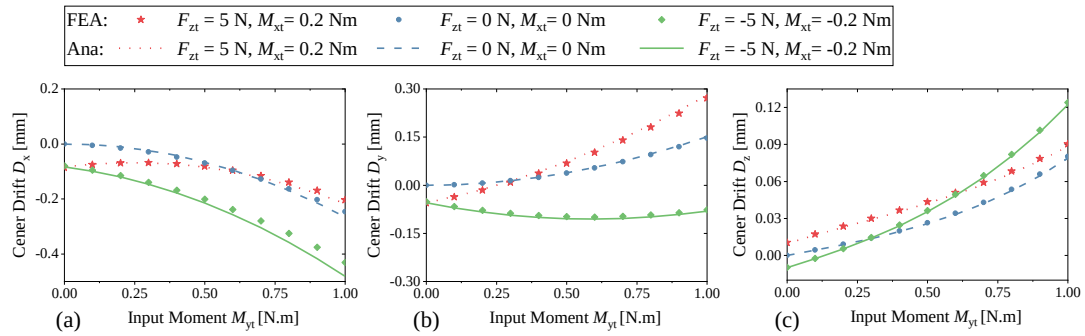


Figure 5.21 (Colour lines) The centre drift comparison between the FEA and analytical results for the spherical joint with L-shape leaf beams, subjected to incremental moment along the Y-direction, a constant moment along the X-direction and a constant force in the X-direction: (a) the resultant displacement D_{xc}; (b) the resultant displacement D_{yc}; (c) the resultant displacement D_{zc};

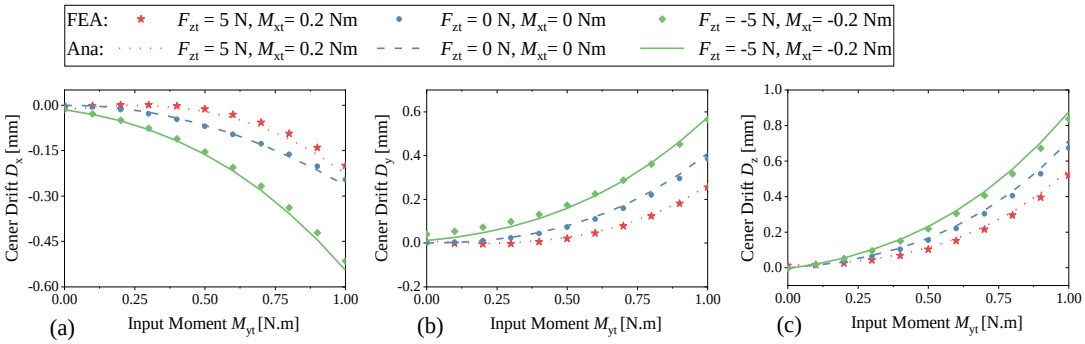


Figure 5.22 (Colour lines) The centre drift comparison between the FEA and analytical results for the spherical joint with folded leaf beams, subjected to incremental moment along the Y-direction, a constant moment along the X-direction and a constant force in the X-direction: (a) the resultant displacement $D_{xc;}$ (b) the resultant displacement D_{yc}; (c) the resultant displacement D_{zc}.

Figure 5.19 presents the FEA verification of the spherical joint with SSTC leaf beams, revealing a maximum error of approximately 8.5% between the analytical model and FEA at the centre drift in the Z-direction. The observed maximum centre drift reaches 0.56 mm in the X-direction.

Similarly, Figure 5.20 displays the verification for the spherical joint with I-shape leaf beams, where similar nonlinear patterns are evident. The comparison between analytical and FEA results shows a good correlation, with a maximum error of 7.1%. Figure 5.21 and Figure 5.22 illustrate the comparison results for spherical joints with L-shape and folded leaf beams, respectively. The error between analytical and FEA results is 9.3% for the L-shape leaf beams and 7.5% for the folded leaf beams.

Overall, the FEA verification of the centre drift demonstrates a good correlation with the analytical results, with errors consistently below 10% across all four types of spherical joints. This analysis considers centre drifts up to approximately 0.1 radians in the Y-axis, subjected to combined forces and moments.

5.2.3.3 Centre drift analysis of several specific spherical joints

This section focuses on the centre drift analysis of four representative spherical joints. To provide a comprehensive analysis, the geometric parameters γ_0, β_0, and R_0, which determine the spatial position and orientation of the GSTC leaf beam, will be considered to understand their impact on the centre drift of the spherical joints. Four representative spherical joints were configured with the initial geometry parameters $\gamma_0 = 0$, $\beta_0 = \pi/4$, and $R_0 = 50$ mm. The remaining parameters are defined in Table 2.2, except for the length of the intermediate stage D, which is consistently set to 2 mm across all spherical joints.

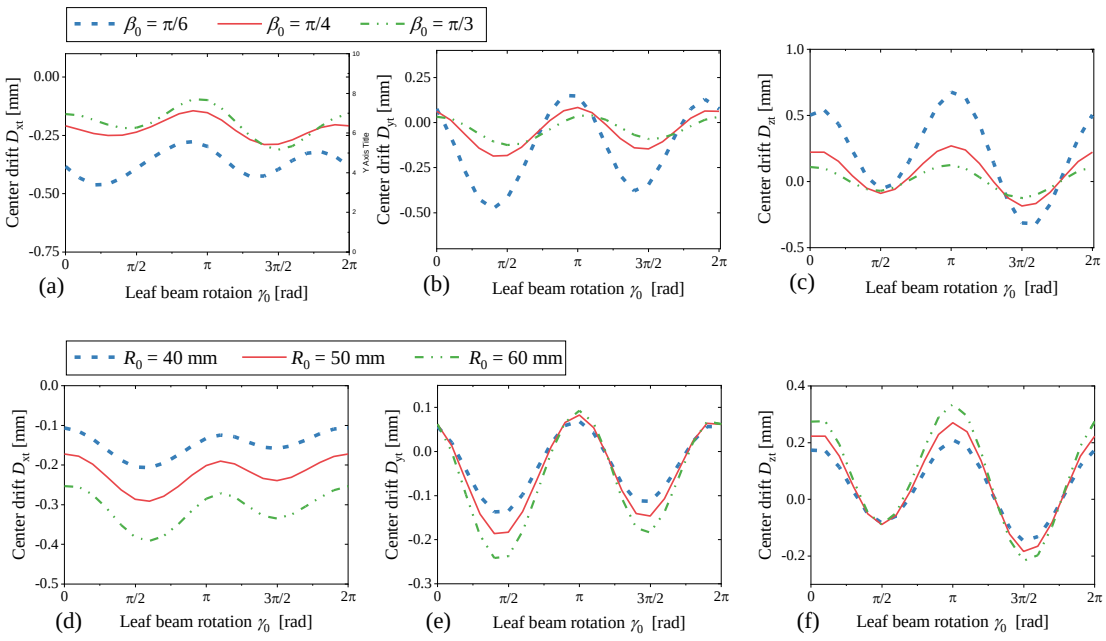


Figure 5.23 (Colour lines) The influence of geometry parameters γ_0, β_0, and R_0 on the center drift of the spherical joint with SSTC leaf beams under constant motion stage rotation ($\theta_{xt} = 0.2$ rad, $\theta_{yt} = 0.3$ rad and $\theta_{zt} = 0.5$ rad): (a), (b), and (c) illustrate the incremental changes in γ_0 and β_0 with a constant R_0 value of 50 mm; (d), (e), and (f) showcase the incremental changes in γ_0 and R_0 with a constant β_0 value of $\pi/4$;

Figure 5.23 presents the centre drift analysis of spherical joints equipped with SSTC leaf beams, subjected to constant rotations ($\theta_{xt} = 0.2$ rad, $\theta_{yt} = 0.3$ rad and $\theta_{zt} = 0.5$ rad). As

depicted in figures (a), (b), and (c), it is evident that a larger value of β_0 (ranging from π/6 to π/3) generally results in reduced centre drift. Conversely, figures (d), (e), and (f) illustrate that a larger value of R_0 (ranging from 40 mm to 60 mm) correlates with increased centre drift. Overall, the value of the centre drift in all directions fluctuates between 0 mm to 0.71 mm.

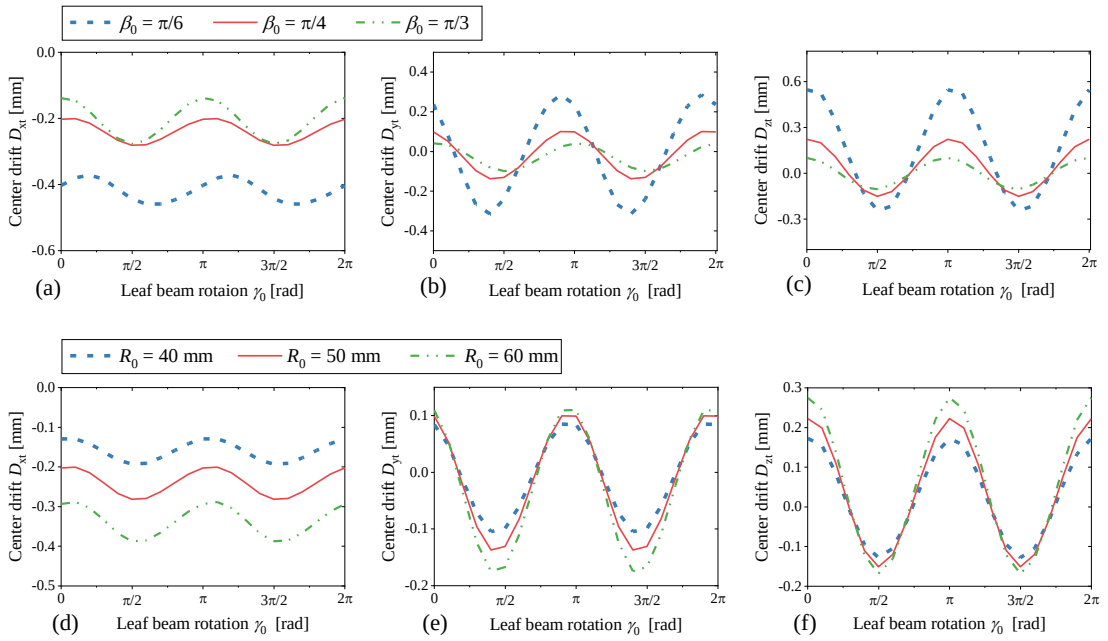


Figure 5.24 (Colour lines) The influence of geometry parameters γ_0, β_0, and R_0 on the center drift of the spherical joint with I-shape leaf beams under constant motion stage rotation ($\theta_{xt} = 0.2$ rad, $\theta_{yt} = 0.3$ rad and $\theta_{zt} = 0.5$ rad): (a), (b), and (c) illustrate the incremental changes in γ_0 and β_0 with a constant R_0 value of 50 mm; (d), (e), and (f) showcase the incremental changes in γ_0 and R_0 with a constant β_0 value of π/4;

Figure 5.24 illustrates the centre drift analysis of the spherical joint with I-shape leaf beams. It is evident from Figure 5.24(a), (b), and (c) that a larger value of β_0 (ranging from π/6 to π/3) generally produces smaller centre drift, with the peaks of the centre drift shifting as β_0 changes. Figure 5.24(d), (e), and (f) indicate that an increase in the value of R_0 corresponds to a larger centre drift. Overall, the value of the centre drift in all directions fluctuates between 0 mm to 0.55 mm.

A similar analysis is conducted for a spherical joint employing L-shape leaf beams, as demonstrated in Figure 5.25. It becomes apparent from Figure 5.25(a), (b), and (c) that, for the same range of rotation, a larger value of β_0 results in a diminished centre drift across all directions. Conversely, Figure 5.25(d), (e), and (f) indicate that an increase in

the length of R_0 genuinely corresponds to a larger centre drift. Overall, the value of the centre drift in all directions fluctuates between 0 mm to 0.61 mm.

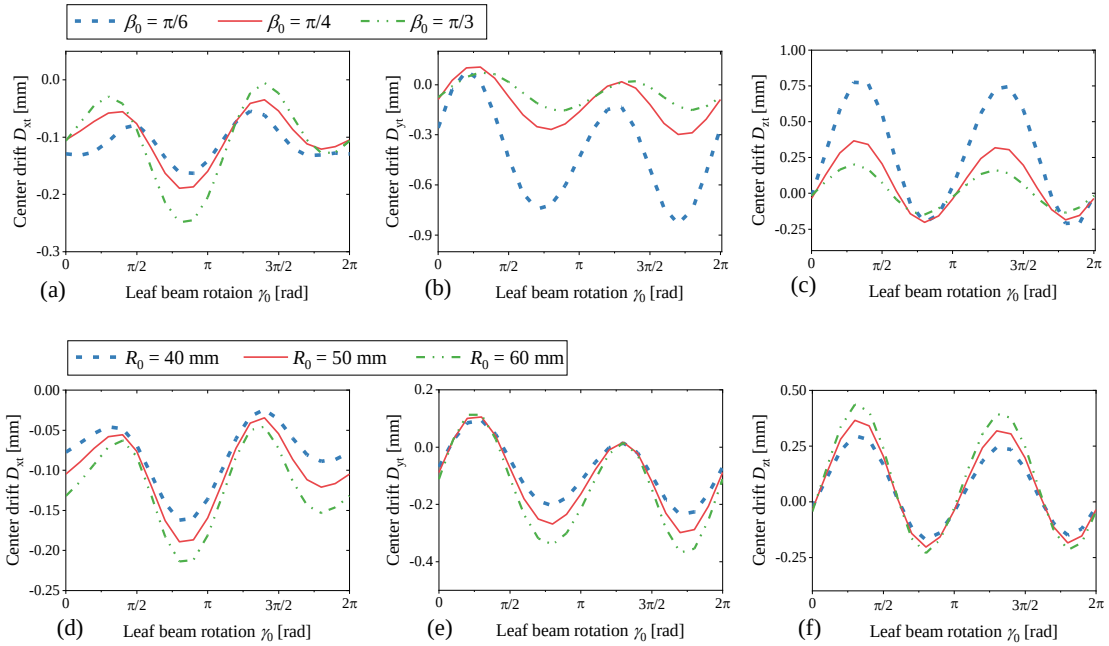


Figure 5.25 (Colour lines) The influence of geometry parameters γ_0, β_0, and R_0 on the center drift of the spherical joint with folded leaf beams under constant motion stage rotation (θ_{xt} = 0.2 rad, θ_{yt} = 0.3 rad and θ_{zt} = 0.5 rad): (a), (b), and (c) illustrate the incremental changes in γ_0 and β_0 with a constant R_0 value of 50 mm; (d), (e), and (f) showcase the incremental changes in γ_0 and R_0 with a constant β_0 value of π/4;

The centre drift for the spherical joint employing folded leaf beams is presented in Figure 5.26. Overall, it is evident that a lower value of β_0 leads to a higher centre drift in all directions. Figure 5.26(d), (e), and (f) further indicate that an increase in R_0 corresponds to a larger centre drift. Overall, the value of the centre drift in all directions fluctuates between 0 mm to 0.78 mm.

Determining the exact value of γ_0 for the spherical joint with optimal performance, characterized by minimal centre drift in all directions, poses a challenge due to potential variations in the smallest centre drift across different directions. For instance, in Figure 5.24, the designs with $\gamma_0 = 1.1\pi$ radians and 0π radians have the lowest value of centre drift in the X-direction. For the Y-direction, the designs with $\gamma_0 = 0.7\pi$ and 1.7π radians have the lowest value of centre drift. The designs with $\gamma_0 = 0.3\pi$ and 1.3π radians have the lowest value of centre drift in the Z-direction. Moreover, the activation of the spherical

joint, involving different combinations of input further influences the γ_0 value associated with the smallest centre drift. However, Table 5.5 provides a comparison of the maximum centre drift in each direction for the four spherical joints, offering insights into which design has the best performance.

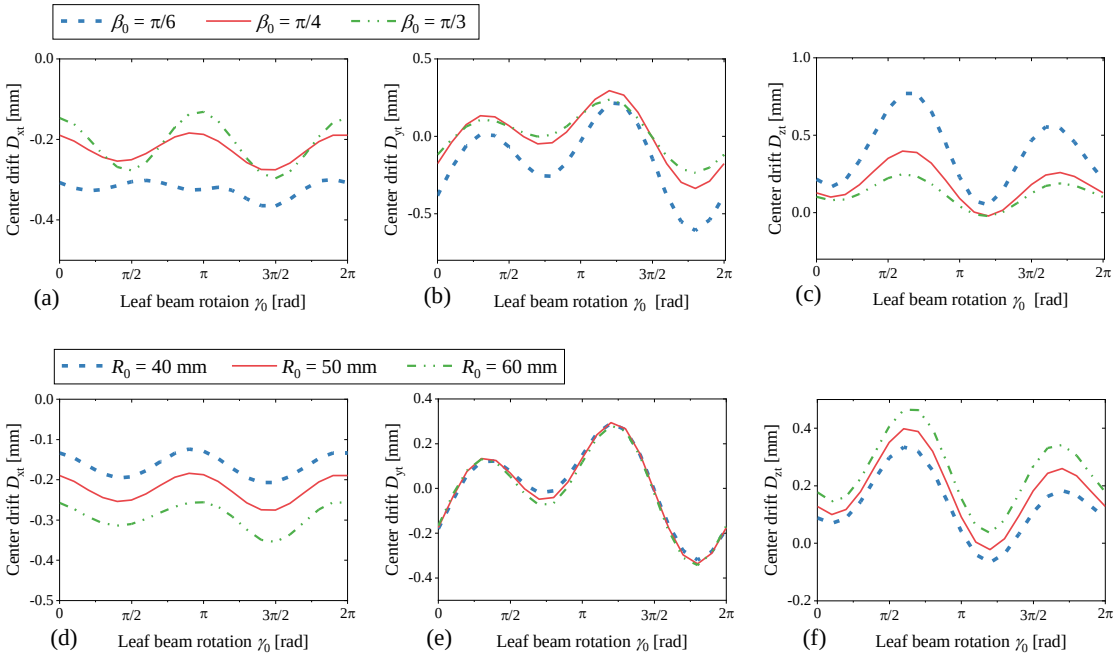


Figure 5.26 (Colour lines) The influence of geometry parameters γ_0, β_0, and R_0 on the center drift of the spherical joint with L-shape leaf beams under constant motion stage rotation (θ_{xt} = 0.2 rad, θ_{yt} = 0.3 rad and θ_{zt} = 0.5 rad): (a), (b), and (c) illustrate the incremental changes in γ_0 and β_0 with a constant R_0 value of 50 mm; (d), (e), and (f) showcase the incremental changes in γ_0 and R_0 with a constant β_0 value of π/4;

Table 5.5 Maximum centre drift comparison (γ_0 ranging from 0 to 2π and R_0 equals to 50 mm)

Spherical Joint	**Max D_x (mm)**			**Max D_y (mm)**			**Max D_z (mm)**		
	If β_0 equals to			If β_0 equals to			If β_0 equals to		
	π/6	π/4	π/3	π/6	π/4	π/3	π/6	π/4	π/3
I-shape	0.459	0.281	0.277	0.315	0.137	0.098	0.546	0.222	0.104
SSTC	0.461	0.289	0.311	0.503	0.294	0.191	0.710	0.331	0.210
L-shape	0.364	0.275	0.296	0.608	0.336	0.238	0.770	0.399	0.248
Folded	0.163	0.189	0.248	0.833	0.299	0.154	0.775	0.366	0.201

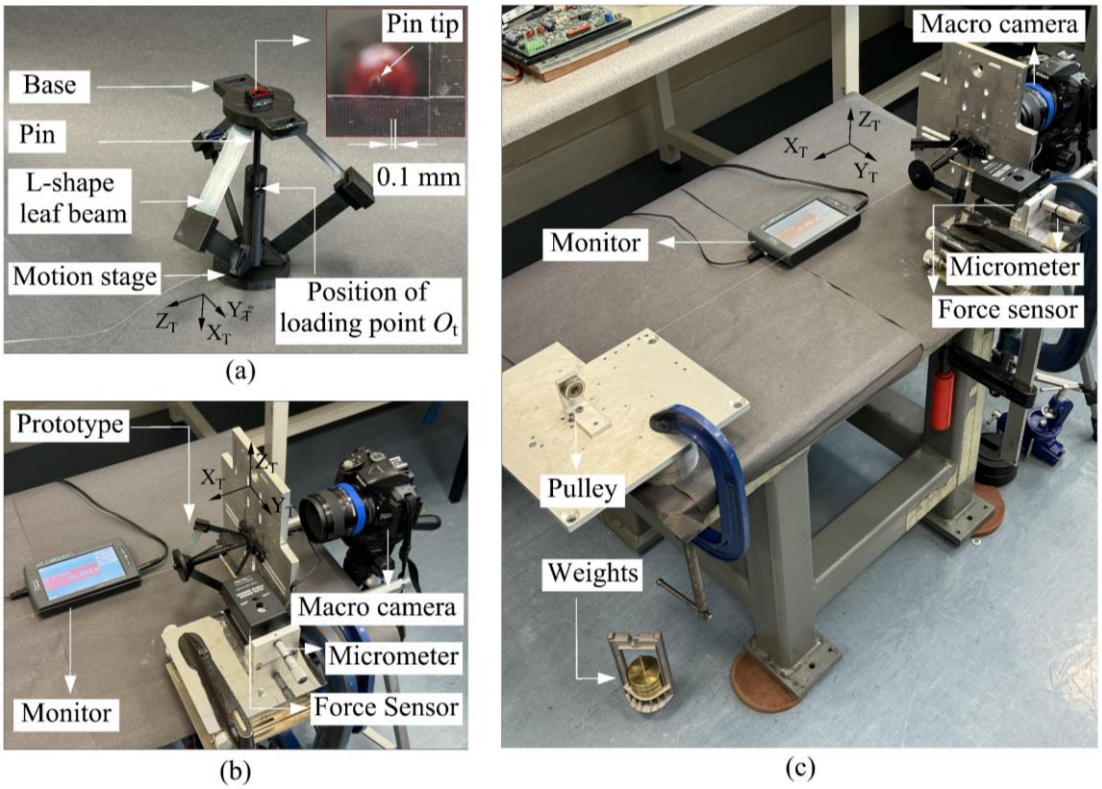


Figure 5.27 Experimental setup: (a) the spherical joint with L-shape leaf beams (pin tip is the remote centre P joint); (b) testing rig; (c) an overview of the experimental platform.

Table 5.5 summarizes the maximum centre drift of each spherical joint with γ_0 ranging from 0 to 2π radians and R_0 equal to 50 mm, under the loading conditions of $\theta_{xt} = 0.2$ rad, $\theta_{yt} = 0.3$ rad and $\theta_{zt} = 0.5$ rad. Notably, the spherical joint with folded leaf beams exhibits the lowest maximum centre drift in the X-direction, while the spherical joint with I-shape leaf beams demonstrates the lowest maximum centre drift in both the Y-direction and Z-direction. Conversely, the spherical joint with folded leaf beams yields the largest maximum centre drift, reaching 0.833 mm in the Y-direction. In contrast, the spherical joint with I-shape leaf beams achieves the lowest centre drift overall. Based on this data, it can be concluded that the spherical joint with I-shape leaf beams delivers the best performance, characterized by the smallest overall centre drift.

5.2.4 Experiment

The spherical joint with L-shape leaf beams has been selected for experimental tests,

because it has a compact and simple configuration to facilitate the fabrication and the other the specific spherical joints with I-shape leaf beams and folded leaf beams were experimentally studied in [152] and [26, 238], respectively. The study in this section will test both the force-displacement characteristics (including load-dependent effects) and the displacement-centre drift relationships. The experimental results will be compared with the analytical and FEA results.

5.2.4.1 Fabrication of the prototype

Figure 5.27(a) illustrates the fabricated prototype, which includes non-deformable components such as the motion stage, intermediate stage, and base, being all fabricated using tough PLA filament through additive manufacturing. A 3D-printed pin using tough PLA (Polylactic Acid) is affixed to the motion stage, with its colored tip serving as the remote centre of rotation for the spherical joint. A ruler with 0.1 mm resolution is placed on the base to provide a reference for the camera-based measurement of the pin tip position after each incremental displacement. The leaf beam is cut from a 0.3 mm thick stainless-steel sheet (Young's modulus: 200 GPa, Poisson's ratio: 0.33). The assembly is completed by inserting the leaf beams into the slotted non-deformable parts and bonding them with super glue. Detailed dimensions are provided in Table 5.6.

Table 5.6 The geometry parameters of the spherical joint with L-shape leaf beams

Leaf beam in spherical joint	γ_0 **(rad)**	β_0 **(rad)**	R_0 **(mm)**	D **(mm)**	L **(mm)**	T **(mm)**	U **(mm)**
L-shape	0	$\pi/4$	55	9	50	0.3	12

5.2.4.2 Experimental hardware setup

The assembly of the experimental hardware setup consists of five primary sub-systems: the micrometer, force sensor, pulley system, fabricated prototype, and a macro camera, as shown in Figure 5.27(b). The micrometer, with a resolution of 0.001 mm, is used for precise displacement actuation/input. The force sensor, with a resolution of 0.001 N and a range of 0 to 10 N, is aligned along the Y_T-direction to monitor reaction forces. The pulley system is employed to attach extra forces along the X_T-direction, simulating load-dependent effects on the spherical joint. The distance between the motion stage of the

spherical joint and the pulley is intentionally set long enough to minimize loading misalignment during actuation, as illustrated in Figure 5.27(c). The macro camera is used to capture the images of the pin tip and the ruler and enables the image-processing-based calculation of the pin tip position based on the reference ruler. By comparing these images at each incremental displacement, the movement of the pin tip (centre drift) can be measured.

5.2.4.3 Experimental results

The experimental results are compared with FEA and analytical results to validate two key aspects of the spherical joint: the force-displacement relationship of the motion stage and the resultant centre drift versus input displacement. As shown in Figure 5.28(a), the experimental results align with both the FEA and analytical results, with a maximum error of 8.9%. The graph also demonstrates the expected nonlinear load-dependent effects where a larger axial force leads to a larger line slope (i.e., a lager rotational stiffness). Figure 5.28 (b) and (c) show comparisons of the resultant centre drift under incremental input displacements. Figure 5.28(b) compares the analytical results with the FEA results, while Figure 5.28(c) compares the analytical results with the experimental results. Both figures show the same nonlinear pattern of centre drift under different axial forces where the largest axial force results in the smallest centre drift. This finding means that the undesired centre drift can be further mitigated by using axial loading on the spherical joint. It is also observed in Figure 5.28(b) and (c) that the analytical results agree better with the FEA results with a maximum error of 11.2%, and they deviate from the experimental results with a maximum error of 16.7%. Several factors could contribute to this deviation, including potential fabrication errors, assembly errors, and measurement errors, which are further elaborated below:

1) Fabrication errors primarily result from unintended elastic deformations of several parts (such as the motion stage) that were assumed to be rigid in the theoretical analysis.
2) Assembly errors may arise from the system misalignment between the pulley system and the motion stage, and the prototype inherent assembly error between

the 3D printed part and the stainless-steel leaf beam.

3) Measurement errors can occur due to the use of a 0.1 mm resolution ruler for marking the position of the pin tip, which may not provide sufficient precision.

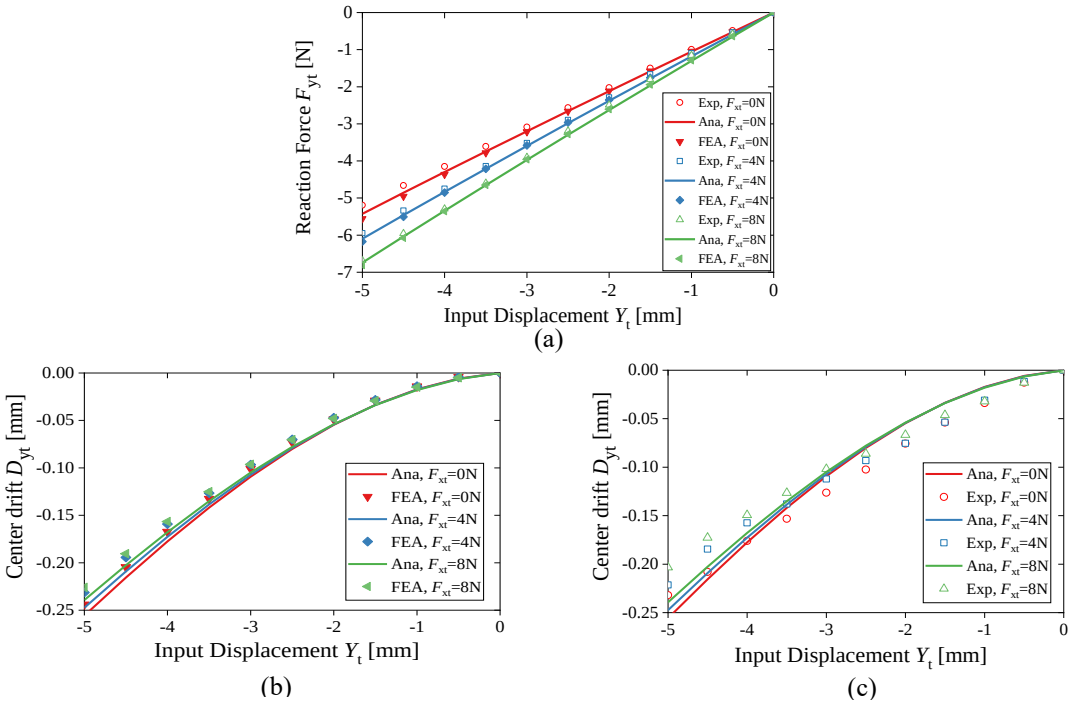


Figure 5.28 (Colour lines) Comparison of experimental, FEA, and analytical results: (a) force-displacement relationship of the motion stage; (b) centre drift analysis by comparing analytical and FEA results; (c) centre drift analysis by comparing analytical and experimental results.

From Figure 5.28(b) and (c), we observe that the experimental centre drift is approximately 22 times smaller than the displacement of the actuation point on the motion stage (reference point O_t as defined in Figure 5.13) when the input displacement reaches 5 mm. Conversely, when the input displacement is around 1 mm, the experimental centre drift is about 55 times smaller than the input displacement. This quantitatively demonstrates the nonlinear pattern of the centre drift: as the input displacement increases, the centre drift increases exponentially. Note the spherical joint with the L-shape leaf beams can be further optimized to minimize the centre drift. The experiment intended to verify the accuracy of the proposed model, and therefore the parameters of this prototype were selected to ease fabrication and experimental measurement.

5.2.4.4 Demonstrated application and other prototypes

The proposed spherical joint is a versatile element with broad applications in fields such as compliant parallel robots and minimally invasive surgery. Figure 5.29 demonstrates an example application of the spherical joint with L-shape leaf beams, in a minimally invasive surgical procedure.

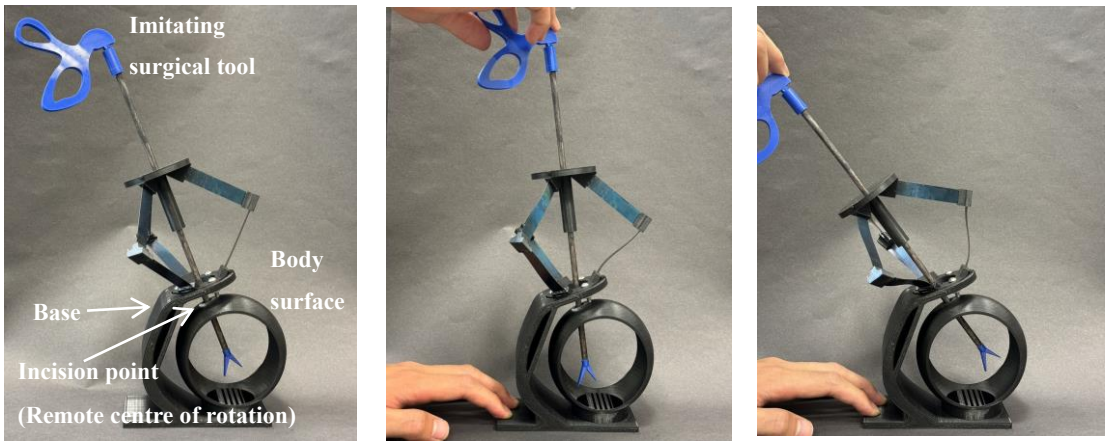


Figure 5.29 Demonstration of the spherical joint (with L-shape leaf beams) in the application of minimally invasive surgery: (a) the configuration as fabricated; (b) rotation about one direction; (c) rotation about another direction.

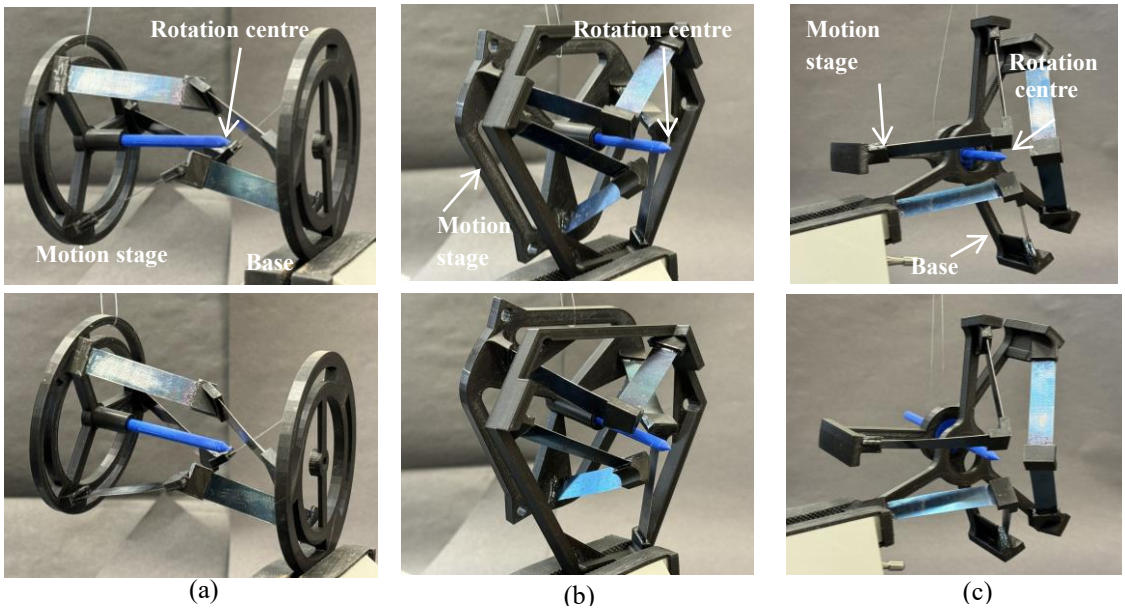


Figure 5.30 Other fabricated prototypes: (a) the spherical joint with SSTC leaf beams; (b) the spherical joint with L-shape leaf beams; (c) the spherical joint with folded leaf beams.

Several other prototypes, showcased in Figure 5.30, have been fabricated using a similar method to further explore the potential of the proposed general spherical joint. These prototypes have demonstrated promising results, achieving the goals of material conservation and simplified fabrication. Moreover, the designs can be made more compact, making them ideal for use in confined spaces, such as those encountered in surgical or robotic applications.

5.3 Summary

Chapter 5 explores the application of parameterized nonlinear models in the design and analysis of compliant mechanisms, focusing on the 2D GLBM and the GSTC leaf beam model. These models are applied to two major case studies: compliant revolute joints and bistable mechanisms in 2D, and a general spherical joint in 3D. The chapter demonstrates how these models facilitate precise force-displacement predictions, account for load-dependent effects, and analyze center drift behavior, making them valuable tools for compliant mechanism optimization.

For the revolute joint and bistable mechanism, the GLBM enables accurate force-displacement predictions by solving a system of equations incorporating force equilibrium and geometric compatibility. The analytical results are validated through FEA simulations and experimental testing, showing strong agreement while also highlighting minor discrepancies due to fabrication tolerances and assembly misalignments. These validations confirm the model's reliability and practical applicability in compliant joint and bistable mechanism design.

The 3D GSTC model is applied to the design of a general spherical joint, showcasing its capability to capture complex spatial motion under combined forces and moments. The study highlights how the model accurately predicts center drift and load-dependent behaviors, essential for high-precision applications. FEA simulations and experimental results validate the model’s predictions, confirming its effectiveness in nonlinear spatial modeling.

Overall, this chapter demonstrates that parameterized nonlinear models offer an efficient

and accurate approach to analyzing and optimizing compliant mechanisms. The ability to predict nonlinear behaviors, optimize geometric configurations, and validate results against FEA and experiments underscores their potential for engineering applications ranging from precision robotics to flexible structures. Future work could extend these models to consider stress analysis and advanced material behaviors, further enhancing their predictive capabilities.

CHAPTER 6

CONCLUSIONS

6.1 Contributions

This thesis advances the field of compliant mechanisms by developing parameterized nonlinear models for flexure beams, conducting comprehensive validations, and exploring innovative designs. The main contributions are summarized below:

1) Development of the 2d general lumped-compliance beam model (GLBM):

The GLBM provides a versatile 2D nonlinear analytical model for lumped-compliance beams, incorporating six key geometric parameters to address a range of configurations such as folded, inverted, and inclined beams. This model enables efficient force-displacement prediction and facilitates rapid design iterations. Validated through FEA with less than a 6% error and tested under experimental setups, the GLBM offers high accuracy in capturing nonlinear characteristics critical for high-precision applications.

2) Creation of the 3d nonlinear model for general single-translation constraint (GSTC) leaf beam:

The GSTC leaf beam model is developed as a 3D nonlinear framework, enabling flexible and precise control of constrained motion in mechanisms with single-translation constraints while allowing five degrees of freedom. The model was validated through comprehensive FEA and innovative low-cost experimental setups, confirming its robustness across configurations like I-shape, L-shape, and folded beams, especially in applications involving compliant spherical joints.

3) Design of over-constraint-based nearly-constant amplification ratio compliant mechanisms (OCARCM):

The OCARCM introduces a novel approach for maintaining a stable displacement

amplification ratio, leveraging an over-constraint design to minimize amplification variability. By applying the BCM, combined with FBD analysis, the model effectively captures nonlinear kinetostatics and achieves a consistent amplification ratio with a maximum variation of only 1%. Validated through FEA and experimental testing, this design outperformed conventional bridge-type amplifiers with a variation as high as 14%.

4) Development of a mirror-symmetrical XY compliant parallel manipulator (XY CPM):

This novel XY CPM design addresses challenges in precision applications by minimizing parasitic rotations and cross-axis coupling while maintaining a compact footprint. The BCM was employed to achieve an efficient analysis of force-displacement behavior under complex loading. Experimental validation showed strong alignment with FEA results, confirming the XY CPM's effectiveness in multi-directional decoupling and stiffness optimization.

5) Comprehensive FEA and experimental validations:

Each model and mechanism were rigorously verified through FEA and low-cost, high-precision experiments, underscoring the models' predictive accuracy and reliability in real-world conditions. The experimental setups provided invaluable insights into design parameters and ensured model applicability across different configurations.

6.2 Conclusions

The thesis begins by providing a comprehensive introduction to compliant mechanisms, highlighting their fundamental principles and advantages in precision engineering applications. It delves into the basic building blocks of compliant mechanisms, including flexure beams and flexure hinges, which serve as the core components enabling elastic deformation for motion. The discussion then transitions to the nonlinear modeling techniques essential for understanding and predicting the force-displacement behavior of these mechanisms under realistic operational conditions. Additionally, the thesis explores advanced design methodologies, emphasizing approaches such as topology optimization, kinematics-based methods, and modular building-block frameworks, which are critical for addressing the challenges associated with the complexity and performance constraints

of compliant mechanisms.

The thesis then identifies the limitations of existing nonlinear modeling techniques and the performance constraints of widely-used compliant mechanisms such as CPMs and compliant amplifiers. To address these challenges, parameterized nonlinear models were developed to extend traditional modeling methods, enabling precise predictions of force-displacement behavior even under large deformations. By incorporating parameterized variables, these models provide adaptable and efficient solutions for mechanisms with complex geometries and diverse operational requirements.

In addition to advancing modeling techniques, the research applied these frameworks to the design of innovative compliant mechanisms. For instance, the OCARCM was developed to address the instability of amplification ratios in compliant amplifiers, while a mirror-symmetrical XY CPM was designed to mitigate parasitic motions and cross-axis coupling, enhancing precision and reliability. These novel designs demonstrated significant performance improvements, validating the utility of parameterized nonlinear models in practical applications.

Furthermore, the thesis explored the application of the developed models to complex systems, including revolute joints, bistable mechanisms, and general spherical joints. These studies showcased the versatility of the parameterized frameworks in addressing real-world engineering challenges, enabling iterative optimization for high-performance designs.

Comprehensive FEA and experimental validation underpinned the entire research, confirming the accuracy of the developed models and the efficacy of the proposed designs. The experimental setups were both cost-effective and innovative, ensuring the reliability of the results while demonstrating their practical utility.

In conclusion, this thesis not only bridges the gap between modeling and design in compliant mechanisms but also sets a foundation for future research by providing robust, adaptable, and efficient modeling tools. These contributions advance the state-of-the-art in compliant mechanisms, paving the way for their broader adoption and enhanced performance in precision engineering applications. The methodologies and insights

presented herein will serve as a valuable resource for researchers and practitioners striving to push the boundaries of compliant mechanism design and application.

6.3 Future work

Building upon the contributions of this PhD thesis, several directions for future work are proposed to expand the scope, refine the methodologies, and enhance the real-world impact of the research. These avenues include theoretical advancements, experimental validation, integration with cutting-edge technologies, and industrial applications. The proposed future work is summarized as follows:

1) Integration of digital twin technology

Parameterized nonlinear modeling techniques can be expanded to facilitate the development of digital twins for compliant mechanisms by serving as the core analytical engine for real-time simulations and performance predictions. These models can be enhanced to support real-time data acquisition from sensors embedded in physical mechanisms, enabling bi-directional communication between the physical and virtual systems. By incorporating advanced numerical simulations and multi-physics modeling, the digital twin can dynamically update predictions of force-displacement behavior and monitor critical parameters like strain, stress, and parasitic motion under varying operational conditions.

2) Improved experimental validation techniques

Improving experimental validation techniques is critical for advancing the reliability and applicability of parameterized nonlinear models for compliant mechanisms. Future work should focus on the development of innovative, cost-effective experimental setups that enhance measurement precision and facilitate comprehensive model validation across diverse operational conditions. High-resolution sensing technologies, such as optical encoders and laser displacement sensors, should be incorporated to capture fine-scale deflections and rotations with minimal noise.

3) Multi-objective optimization for complex design requirements

Future research should focus on developing advanced multi-objective optimization

frameworks tailored for compliant mechanism design. These frameworks must balance competing performance criteria, such as stiffness, precision and motion range, while accommodating complex geometries and nonlinear behaviors. Advanced computational algorithms, such as evolutionary optimization, genetic algorithms, and machine learning-driven approaches, can be leveraged to efficiently explore vast design spaces and identify optimal solutions. Incorporating parameterized nonlinear modeling into the optimization process enables designers to integrate detailed geometric and material constraints, ensuring designs meet both functional and operational requirements.

4) Real-world applications of the developed compliant mechanisms

Expanding the application of novel compliant mechanisms, such as compliant parallel manipulators (CPMs), spherical joints, over-constraint-based nearly constant amplification ratio mechanisms (OCARCMs), and bistable mechanisms, to real-world systems presents significant opportunities. For CPMs, future efforts should focus on integrating these mechanisms into high-precision robotics and micro-positioning systems, addressing challenges such as dynamic performance and enhanced load-handling capabilities. Spherical joints, with their multi-directional compliance, can be adapted for aerospace and biomedical applications, where precise orientation control is crucial. The OCARCM, with its nearly constant amplification ratio, offers immense potential for adaptive optics and vibration isolation systems, where consistent force and motion amplification are essential. Lastly, bistable mechanisms could be implemented in energy-efficient switches or deployable structures, leveraging their snap-through characteristics for reliable actuation. Establishing robust design-to-application workflows, supported by advanced simulation and experimental validation, will facilitate the seamless transition of these innovative mechanisms into diverse industrial and technological domains.

REFERENCES

[1] Jovanova, J., Nastevska, A., Frecker, M., and Aguirre, M. E., 2018, Analysis of a functionally graded compliant mechanism surgical grasper, *2018 International Conference on Reconfigurable Mechanisms and Robots (ReMAR)*, pp. 1-8. https://doi.org/10.1109/REMAR.2018.8449868

[2] Schmitt, P., and Hoffmann, M., 2020, Engineering a Compliant Mechanical Amplifier for MEMS Sensor Applications, *Journal of Microelectromechanical Systems,* 29 (2), pp. 214-227. https://doi.org/10.1109/jmems.2020.2965260

[3] Instrumente, P. 2024. *Nanometer Precision: Nanopositioners, Piezo Stages, Nanopositioning Stages* 2024 [cited Nov 14 2024]. Available from https://www.pi-usa.us/en/products/piezo-flexure-nanopositioners/nanopositioning-stage-basics-achieving-nanometer-precision.

[4] Markl, X. 2024. *The Flexure Revolution, Compliant Mechanisms applied to Watchmaking* 2017 [cited Nov 14 2024]. Available from https://monochrome-watches.com/technical-perspective-flexure-revolution-compliant-mechanisms-applied-watchmaking/.

[5] Zirbel, S. A., Lang, R. J., Thomson, M. W., Sigel, D. A., Walkemeyer, P. E., Trease, B. P., Magleby, S. P., and Howell, L. L., 2013, Accommodating thickness in origami-based deployable arrays, *Journal of Mechanical Design,* 135 (11), pp. 111005. https://doi.org/10.1115/1.4025372

[6] Heng, W., Solomon, S., and Gao, W., 2022, Flexible Electronics and Devices as Human–Machine Interfaces for Medical Robotics, *Advanced Materials,* 34 (16), pp. 2107902. https://doi.org/10.1002/adma.202107902

[7] Howell, L. L., 2013, Compliant mechanisms, In *21st century kinematics*, pp. 189-216. Springer. https://doi.org/10.1007/978-1-4471-4510-3_7

[8] Lobontiu, N., 2002, *Compliant mechanisms: design of flexure hinges*, CRC press. https://doi.org/10.1201/9781420040272

[9] Silberschmidt, V., 2020, *Mechanics of materials in modern manufacturing methods and processing techniques*, Elsevier.

[10] Iqbal, S., Lai, Y., Shakoor, R. I., Raffi, M., and Bazaz, S. A., 2021, Design, analysis, and experimental investigation of micro-displacement amplification compliant mechanism for micro-transducers, *Rev Sci Instrum,* 92 (10), pp. 105007. https://doi.org/10.1063/5.0061820

[11] Dearden, J., Grames, C., Jensen, B. D., Magleby, S. P., and Howell, L. L., 2017, Inverted L-Arm Gripper Compliant Mechanism, *Journal of Medical Devices,* 11 (3). https://doi.org/10.1115/1.4036336

[12] Kuo, C. H., Dai, J. S., and Dasgupta, P., 2012, Kinematic design considerations for minimally invasive surgical robots: an overview, *Int J Med Robot,* 8 (2), pp. 127-45. https://doi.org/10.1002/rcs.453

[13] Lee, H.-J., Woo, S., Park, J., Jeong, J.-H., Kim, M., Ryu, J., Gweon, D.-G., and Choi, Y.-M., 2018, Compact compliant parallel XY nano-positioning stage with high dynamic performance, small crosstalk, and small yaw motion, *Microsystem Technologies,* 24 (6), pp. 2653-2662. https://doi.org/10.1007/s00542-017-3626-z

[14] Zhu, J., Hao, G., Li, S., and Kong, X., 2022, A Compact Mirror-Symmetrical XY Compliant Parallel Manipulator for Minimizing Parasitic Rotations, *Journal of Mechanical Design,* 144 (7). https://doi.org/10.1115/1.4053818

[15] Polit, S., and Dong, J. 2010. Design of a High-Bandwidth XY Nanopositioning Stage for High-Throughput Micro/Nano Manufacturing. https://doi.org/10.1115/IMECE2010-37794

[16] Thalmann, E. F. G. 2020. Flexure pivot oscillators for mechanical watches.

[17] Thalmann, E., Gubler, Q., and Henein, S. J. M., 2022, Gravity-Compensation Design Approaches for Flexure-Pivot Time Bases, 10 (7), pp. 580. https://doi.org/10.3390/machines10070580

[18] Fowler, R. M., Howell, L. L., and Magleby, S. P., 2011, Compliant space mechanisms: a new frontier for compliant mechanisms, *Mech. Sci.,* 2 (2), pp. 205-215. 10.5194/ms-2-205-2011

[19] Liang, H., Hao, G., and Olszewski, O. Z., 2021, A review on vibration-based piezoelectric energy harvesting from the aspect of compliant mechanisms, *Sensors and Actuators A: Physical,* 331. 10.1016/j.sna.2021.112743

[20] Li, Y., and Yan, P., 2023, A compliant mechanism based piezoelectric beam energy harvester with multi-mode frequency up conversion, *Energy Reports,* 10, pp. 932-940. https://doi.org/10.1016/j.egyr.2023.07.044

[21] Dan, W., Zhang, J., Jiangzhen, G., and Rui, F. J. C. J. o. A., 2019, A closed-form nonlinear model for spatial Timoshenko beam flexure hinge with circular cross-section, 32 (11), pp. 2526-2537. https://doi.org/10.1016/j.cja.2019.01.025

[22] Jia, M., Jia, R. P., and Yu, J. J., 2015, A Compliance-Based Parameterization Approach for Type Synthesis of Flexure Mechanisms, *Journal of Mechanisms and Robotics,* 7 (3). https://doi.org/10.1115/1.4028932

[23] Hao, G., and Li, H. J. P. o. t. I. o. M. E., Part C: Journal of Mechanical Engineering Science, 2015, Conceptual designs of multi-degree of freedom compliant parallel manipulators composed of wire-beam based compliant mechanisms, 229 (3), pp. 538-555. https://doi.org/10.1177/0954406214535925

[24] Hao, G., and Kong, X. J. M. S., 2016, A structure design method for compliant parallel manipulators with actuation isolation, *Mechanical*

Sciences, 7, pp. 247-253. https://doi.org/10.5194/ms-7-247-2016

[25] Smith, S. T., 2000, *Flexures: elements of elastic mechanisms*, Crc Press.

[26] Naves, M., Aarts, R. G. K. M., and Brouwer, D. M., 2019, Large stroke high off-axis stiffness three degree of freedom spherical flexure joint, *Precision Engineering,* 56, pp. 422-431. https://doi.org/10.1016/j.precisioneng.2019.01.011

[27] Schellekens, P., Rosielle, N., Vermeulen, H., Vermeulen, M., Wetzels, S., and Pril, W. J. C. A., 1998, Design for precision: current status and trends, 47 (2), pp. 557-586. https://doi.org/10.1016/S0007-8506(07)63243-0

[28] Kargar, S. M., Parmiggiani, A., Baggetta, M., Ottonello, E., Hao, G., and Berselli, G., 2024, Optimization of a tetrahedron compliant spherical joint via computer-aided engineering tools, *The International Journal of Advanced Manufacturing Technology,* 132 (3-4), pp. 1151-1162. https://doi.org/10.1007/s00170-024-13314-3

[29] Rommers, J., van der Wijk, V., and Herder, J. L., 2021, A new type of spherical flexure joint based on tetrahedron elements, *Precision Engineering,* 71, pp. 130-140. https://doi.org/10.1016/j.precisioneng.2021.03.002

[30] Bilancia, P., and Berselli, G., 2021, An Overview of Procedures and Tools for Designing Nonstandard Beam-Based Compliant Mechanisms, *Computer-Aided Design,* 134. https://doi.org/10.1016/j.cad.2021.103001

[31] Cucuzza, R., Rosso, M. M., and Marano, G. C., 2021, Optimal preliminary design of variable section beams criterion, *SN Applied Sciences,* 3 (8), pp. 745. https://doi.org/10.1007/s42452-021-04702-5

[32] Le Chau, N., Tran, N. T., and Dao, T.-P., 2022, A New Compliant Joint with Thin-Wall Structure, 47 (12), pp. 15633-15646. https://doi.org/10.1007/s42452-021-04702-5

[33] Lee, D.-C., 2022, MODELING FOR ORTHO-PLANAR FLEXURE BASED COMPLIANT MECHANISM, *International Journal of Science Academic Research,* 03 (07), pp. 4152-4156.

[34] Parvari Rad, F., Vertechy, R., Berselli, G., and Parenti-Castelli, V., 2018, Design and stiffness evaluation of a compliant joint with parallel Architecture Realizing an Approximately Spherical motion, *Actuators*, (2) pp. 20. https://doi.org/10.3390/act7020020

[35] Lezgy-Nazargah, M. J. M. o. A. M., and Structures, 2022, A finite element model for static analysis of curved thin-walled beams based on the concept of equivalent layered composite cross section, 29 (7), pp. 1020-1033. https://doi.org/10.1080/15376494.2020.1804649

[36] Kalpathy Venkiteswaran, V., and Su, H.-J., 2017, Pseudo-rigid-body models of initially-curved and straight beams for designing compliant mechanisms, *International Design Engineering Technical Conferences and Computers*

and Information in Engineering Conference, pp. V05AT08A006. https://doi.org/10.1115/DETC2017-67431

[37] Chen, G., Ma, F., Hao, G., and Zhu, W., 2019, Modeling Large Deflections of Initially Curved Beams in Compliant Mechanisms Using Chained Beam Constraint Model, *Journal of Mechanisms and Robotics,* 11 (1). https://doi.org/10.1115/1.4041585

[38] Hosseini, S. F., Moetakef-Imani, B., Hadidi-Moud, S., and Hassani, B., 2018, Pre-bent shape design of full free-form curved beams using isogeometric method and semi-analytical sensitivity analysis, *Structural and Multidisciplinary Optimization,* 58 (6), pp. 2621-2633. https://doi.org/10.1007/s00158-018-2041-0

[39] Wu, Y., and Zhou, Z., 2002, Design calculations for flexure hinges, *Review of Scientific Instruments,* 73 (8), pp. 3101-3106. https://doi.org/10.1063/1.1494855

[40] Lobontiu, N., Garcia, E., and Canfield, S., 2003, Torsional stiffness of several variable rectangular cross-section flexure hinges for macro-scale and MEMS applications, *Smart Materials and Structures,* 13 (1), pp. 12. https://doi.org/10.1088/0964-1726/13/1/002

[41] Smith, S. T., Badami, V. G., Dale, J. S., and Xu, Y., 1997, Elliptical flexure hinges, *Review of Scientific Instruments,* 68 (3), pp. 1474-1483. https://doi.org/10.1063/1.1147635

[42] Chen, G., Shao, X., and Huang, X., 2008, A new generalized model for elliptical arc flexure hinges, *Review of scientific instruments,* 79 (9). https://doi.org/10.1063/1.2976756

[43] Lobontiu, N., Paine, J. S., Garcia, E., and Goldfarb, M., 2001, Corner-filleted flexure hinges, *J. Mech. Des.,* 123 (3), pp. 346-352. https://doi.org/10.1115/1.1372190

[44] Harfensteller, F., Henning, S., Zentner, L., and Husung, S., 2022, Modeling of corner-filleted flexure hinges under various loads, *Mechanism Machine Theory*

175, pp. 104937. https://doi.org/10.1016/j.mechmachtheory.2022.104937

[45] Lobontiu, N., Garcia, E., Hardau, M., and Bal, N., 2004, Stiffness characterization of corner-filleted flexure hinges, *Review of Scientific Instruments,* 75 (11), pp. 4896-4905. https://doi.org/10.1063/1.1806999

[46] Qiu, L., Yue, X., Xie, Z. J. M., and Theory, M., 2019, Design and analysis of Multicavity Flexure Hinge (MCFH) based on three-dimensional continuum topology optimization, 139, pp. 21-33. https://doi.org/10.1016/j.mechmachtheory.2019.04.004

[47] Zhang, X., and Zhu, B., 2018, Topology Optimization of Flexure Hinges, In *Topology Optimization of Compliant Mechanisms*, pp. 25-80. edited by Zhang and Zhu. Singapore: Springer Singaporehttps://doi.org/10.1007/978-

981-13-0432-3_2

[48] Zhu, B., Zhang, X., Liu, M., Chen, Q., and Li, H., 2019, Topological and Shape Optimization of Flexure Hinges for Designing Compliant Mechanisms Using the Level Set Method, *Chinese Journal of Mechanical Engineering,* 32 (1). 10.1186/s10033-019-0332-z

[49] Yao, G., Liu, P., Lu, S., and Yan, P., 2022, Design and Analysis of Additive Manufactured Flexure Hinge with Large Stroke and High Accuracy, *International Journal of Precision Engineering and Manufacturing,* 23 (7), pp. 753-761. https://doi.org/10.1007/s12541-022-00657-8

[50] Berselli, G., Piccinini, M., and Vassura, G., 2011, Comparative evaluation of the selective compliance in elastic joints for robotic structures, *2011 IEEE International Conference on Robotics and Automation*, pp. 4626-4631. https://doi.org/10.1109/ICRA.2011.5980201

[51] Linß, S., Erbe, T., Theska, R., and Zentner, L., 2011, The influence of asymmetric flexure hinges on the axis of rotation,

[52] Zhang, Z., and Hu, H., 2009, Comparison of single-notch circular flexure hinge rotational stiffness equations with fea results and derivation of empirical formulations, *2009 International Joint Conference on Computational Sciences and Optimization*, pp. 286-288.

[53] Zhang, L., Liu, M., Hong, L., Li, C., and Zhou, Z., 2022, Design and Optimization of an FBG Accelerometer Based on Single-Notch Circular Flexure Hinge for Medium-Frequency Vibration Measurement, *IEEE Sensors Journal,* 22 (21), pp. 20303-20311. 10.1109/JSEN.2022.3207780

[54] Wang, Y., Zhang, L., Meng, L., Lu, H., and Ma, Y. J. S., 2024, Theoretical Modeling and Experimental Verification of Elliptical Hyperbolic Hybrid Flexure Hinges, 16 (3), pp. 345.

[55] Dai, J. S., and Cannella, F., 2007, Stiffness Characteristics of Carton Folds for Packaging, *Journal of Mechanical Design,* 130 (2). https://doi.org/10.1115/1.2813785

[56] Yong, Y. K., Lu, T.-F., and Handley, D. C. J. P. e., 2008, Review of circular flexure hinge design equations and derivation of empirical formulations, 32 (2), pp. 63-70. https://doi.org/10.1016/j.precisioneng.2007.05.002

[57] Gopal, V., Bharanidaran, R., Stevewake, M. A., and Jayakanthan, N., 2024, Design and Analysis of Asymmetric Circular Flexure Hinges using Micro Gripper for Compliant Mechanism, In *Advances in Additive Manufacturing Technologies*, pp. 202-207. CRC Press

[58] Kong, J., Huang, Z., Xian, X., Wang, Y., and Yu, P., 2020, Generalized model for conic-V-shaped flexure hinges, *Science Progress,* 103 (4), pp. 0036850420981211. https://doi.org/10.1177/0036850420981211

[59] Nguyen, T. T.-V., Le, H.-D., Hsu, H.-C., Nguyen, C.-N., and Chiang, C.-C., 2024, A medium-high frequency FBG accelerometer based on a V-shaped

flexible hinge, *Measurement,* 224, pp. 113865. https://doi.org/10.1016/j.measurement.2023.113865

[60] Pei, X., Yu, J., Zong, G., Bi, S., Su, H. J. M., and Theory, M., 2009, The modeling of cartwheel flexural hinges, 44 (10), pp. 1900-1909. https://doi.org/10.1016/j.mechmachtheory.2009.04.006

[61] Mauser, K., and Hasse, A., 2020, How to prestress compliant mechanisms for a targeted stiffness adjustment, *Smart Materials and Structures,* 29 (8), pp. 085021. 10.1088/1361-665X/ab9237

[62] Goldfarb, M., and Speich, J. E., 2000, The development of a split-tube flexure, *ASME International Mechanical Engineering Congress and Exposition*, pp. 861-866. https://doi.org/10.1115/IMECE2000-2386

[63] Goldfarb, M., and Speich, J. E., 1999, A well-behaved revolute flexure joint for compliant mechanism design, *ASME. J. Mech. Des,* 121(3): 424–429. https://doi.org/10.1115/1.2829478

[64] Yang, J., and Yan, P., 2024, Generalized model and performance analysis of elliptical-fillet cross-sectional flexure hinges, *Proceedings of the Institution of Mechanical Engineers, Part C: Journal of Mechanical Engineering Science,* 238 (5), pp. 1355-1365. https://doi.org/10.1177/09544062231182282

[65] Li, L., Zhang, D., Qu, H., and Wang, Y., 2022, Generalized model and configuration design of multiple-axis flexure hinges, *Mechanism and Machine Theory,* 169, pp. 104677. https://doi.org/10.1016/j.mechmachtheory.2021.104677

[66] Lobontiu, N., and Garcia, E., 2003, Two-axis flexure hinges with axially-collocated and symmetric notches, *Computers & Structures,* 81 (13), pp. 1329-1341. https://doi.org/10.1016/S0045-7949(03)00056-7

[67] Wei, H., Tian, Y., Zhao, Y., Ling, M., and Shirinzadeh, B., 2023, Two-axis flexure hinges with variable elliptical transverse cross-sections, *Mechanism and Machine Theory,* 181, pp. 105183. https://doi.org/10.1016/j.mechmachtheory.2022.105183

[68] Parvari Rad, F., Vertechy, R., Berselli, G., and Parenti-Castelli, V., 2016, Analytical compliance analysis and finite element verification of spherical flexure hinges for spatial compliant mechanisms, *Mechanism and Machine Theory,* 101, pp. 168-180. https://doi.org/10.1016/j.mechmachtheory.2016.01.010

[69] Huang, H., and Li, J., 2021, *Piezoelectric Actuators: Principles, Design, Experiments and Applications*, BoD–Books on Demand.

[70] Awtar, S., Slocum, A. H., and Sevincer, E., 2007, Characteristics of Beam-Based Flexure Modules, *Journal of Mechanical Design,* 129 (6), pp. 625-639. https://doi.org/10.1115/1.2717231

[71] Craig Jr, R. R., and Taleff, E. M., 2020, *Mechanics of materials*, John Wiley

& Sons.

[72] Lewis, G., Monasa, F., and Structures, 1981, Large deflections of cantilever beams of nonlinear materials, *Computers & Structures,* 14 (5-6), pp. 357-360. https://doi.org/10.1016/0045-7949(81)90054-7

[73] Henning, S., and Zentner, L., 2021, Analysis of planar compliant mechanisms based on non-linear analytical modeling including shear and lateral contraction, *Mechanism and Machine Theory,* 164. https://doi.org/10.1016/j.mechmachtheory.2021.104397

[74] Odhner, L. U., and Dollar, A. M., 2012, The Smooth Curvature Model: An Efficient Representation of Euler–Bernoulli Flexures as Robot Joints, *IEEE Transactions on Robotics,* 28 (4), pp. 761-772. https://doi.org/10.1109/TRO.2012.2193232

[75] Liu, T., Hao, G., Zhu, J., Kuresangsai, P., Abdelaziz, S., and Wehrle, E., 2024, Modeling compliant bistable mechanisms: An energy method based on the high-order smooth curvature model, *International Journal of Mechanical Sciences,* 275, pp. 109315. https://doi.org/10.1016/j.ijmecsci.2024.109315

[76] Bai, R., Li, B., and Chen, G., 2024, Nonlinear closed-form model for beam flexures subject to large axial loads, *Applied Mathematical Modelling,* 130, pp. 676-692. https://doi.org/10.1016/j.apm.2024.03.018

[77] Chen, G., and Ma, F., 2015, Kinetostatic Modeling of Fully Compliant Bistable Mechanisms Using Timoshenko Beam Constraint Model, *Journal of Mechanical Design,* 137 (2). 10.1115/1.4029024

[78] Ling, M., Yuan, L., and Zhang, X., 2024, Geometrically nonlinear analysis of compliant mechanisms using a dynamic beam constraint model (DBCM), *Mechanism and Machine Theory,* 191, pp. 105489. https://doi.org/10.1016/j.mechmachtheory.2023.105489

[79] Li, R., and Yang, Z., 2022, Modeling the nonlinear deflection of elliptical-arc-fillet leaf springs, *Mechanism and Machine Theory,* 176. https://doi.org/10.1016/j.mechmachtheory.2022.105037

[80] Li, R., Yang, Z., Chen, G., and Wu, B., 2021, Analytical solutions for nonlinear deflections of corner-fillet leaf-springs, *Mechanism and Machine Theory,* 157. https://doi.org/10.1016/j.mechmachtheory.2020.104182

[81] Sen, S., and Awtar, S., 2014, Nonlinear Strain Energy Formulation of a Generalized Bisymmetric Spatial Beam for Flexure Mechanism Analysis, *J Mech Des N Y,* 136 (2), pp. 0210021-2100213. https://doi.org/10.1115/1.4025705

[82] Yu, Y.-Q., and Zhang, N., 2019, Dynamic modeling and performance of compliant mechanisms with inflection beams, *Mechanism and Machine Theory,* 134, pp. 455-475. https://doi.org/10.1016/j.mechmachtheory.2019.01.010

[83] Jin, M., Zhu, B., Mo, J., Yang, Z., Zhang, X., and Howell, L. L., 2020, A CPRBM-based method for large-deflection analysis of contact-aided compliant mechanisms considering beam-to-beam contacts, *Mechanism and Machine Theory,* 145. https://doi.org/10.1016/j.mechmachtheory.2019.103700

[84] Yu, Y.-Q., Feng, Z.-L., and Xu, Q.-P., 2012, A pseudo-rigid-body 2R model of flexural beam in compliant mechanisms, *Mechanism and Machine Theory,* 55, pp. 18-33. https://doi.org/10.1016/j.mechmachtheory.2012.04.005

[85] Su, H.-J., 2009, A Pseudorigid-Body 3R Model for Determining Large Deflection of Cantilever Beams Subject to Tip Loads, *Journal of Mechanisms and Robotics,* 1 (2). https://doi.org/10.1115/1.3046148

[86] Yu, Y.-Q., Li, Q., and Xu, Q.-P., 2017, Pseudo-rigid-body dynamic modeling and analysis of compliant mechanisms, *Proceedings of the Institution of Mechanical Engineers, Part C: Journal of Mechanical Engineering Science,* 232 (9), pp. 1665-1678. https://doi.org/10.1177/0954406217707547

[87] Zhang, A., and Chen, G., 2013, A Comprehensive Elliptic Integral Solution to the Large Deflection Problems of Thin Beams in Compliant Mechanisms, *Journal of Mechanisms and Robotics,* 5 (2). https://doi.org/10.1115/1.4023558

[88] Iwatsuki, N., and Kosaki, T., 2015, Large deformation analysis and synthesis of elastic closed-loop mechanism made of a certain spring wire described by free curves, *Chinese Journal of Mechanical Engineering,* 28 (4), pp. 756-762. https://doi.org/10.3901/cjme.2015.0506.067

[89] Howell, L. L., and Midha, A., 1995, Parametric Deflection Approximations for End-Loaded, Large-Deflection Beams in Compliant Mechanisms, *Journal of Mechanical Design,* 117 (1), pp. 156-165. https://doi.org/10.1115/1.2826101

[90] Howell, L. L., Midha, A., and Norton, T. W., 1996, Evaluation of Equivalent Spring Stiffness for Use in a Pseudo-Rigid-Body Model of Large-Deflection Compliant Mechanisms, *Journal of Mechanical Design,* 118 (1), pp. 126-131. https://doi.org/10.1115/1.2826843

[91] Chen, G., Xiong, B., and Huang, X., 2011, Finding the optimal characteristic parameters for 3R pseudo-rigid-body model using an improved particle swarm optimizer, *Precision Engineering,* 35 (3), pp. 505-511. 10.1016/j.precisioneng.2011.02.006

[92] Yu, Y.-Q., and Zhu, S.-K., 2017, 5R pseudo-rigid-body model for inflection beams in compliant mechanisms, *Mechanism and Machine Theory,* 116, pp. 501-512. https://doi.org/10.1016/j.mechmachtheory.2017.06.016

[93] Pauly, J., and Midha, A., 2006, Pseudo-Rigid-Body Model Chain Algorithm: Part 2 — Equivalent Representations for Combined Load Boundary Conditions, *ASME 2006 International Design Engineering Technical*

Conferences and Computers and Information in Engineering Conference, pp. 183-190. 10.1115/detc2006-99463

[94] Pauly, J., and Midha, A., 2006, Pseudo-Rigid-Body Model Chain Algorithm: Part 1 — Introduction and Concept Development, *ASME 2006 International Design Engineering Technical Conferences and Computers and Information in Engineering Conference*, pp. 173-181. https://doi.org/10.1115/DETC2006-99460

[95] Awtar, S., and Sen, S., 2010, A Generalized Constraint Model for Two-Dimensional Beam Flexures: Nonlinear Load-Displacement Formulation, *Journal of Mechanical Design,* 132 (8), pp. 081008. https://doi.org/10.1115/1.4002005

[96] Hao, G., and Kong, X., 2013, A normalization-based approach to the mobility analysis of spatial compliant multi-beam modules, *Mechanism and Machine Theory,* 59, pp. 1-19. https://doi.org/10.1016/j.mechmachtheory.2012.08.013

[97] Sen, S., and Awtar, S., 2013, A Closed-Form Nonlinear Model for the Constraint Characteristics of Symmetric Spatial Beams, *Journal of Mechanical Design,* 135 (3). https://doi.org/10.1115/1.4023157

[98] Radgolchin, M., and Moeenfard, H., 2017, A constraint model for beam flexure modules with an intermediate semi-rigid element, *International Journal of Mechanical Sciences,* 122, pp. 167-183. https://doi.org/10.1016/j.ijmecsci.2016.10.011

[99] Ma, F., and Chen, G., 2017, Bi-BCM: A Closed-Form Solution for Fixed-Guided Beams in Compliant Mechanisms, *Journal of Mechanisms and Robotics,* 9 (1). https://doi.org/10.1115/1.4035084

[100] Bilancia, P., Baggetta, M., Hao, G., and Berselli, G., 2021, A variable section beams based Bi-BCM formulation for the kinetostatic analysis of cross-axis flexural pivots, *International Journal of Mechanical Sciences,* 205. https://doi.org/10.1016/j.ijmecsci.2021.106587

[101] Cammarata, A., Lacagnina, M., and Sequenzia, G., 2018, Alternative elliptic integral solution to the beam deflection equations for the design of compliant mechanisms, *International Journal on Interactive Design and Manufacturing (IJIDeM),* 13 (2), pp. 499-505. https://doi.org/10.1007/s12008-018-0512-6

[102] Howell, L. L., and Leonard, J. N., 1997, Optimal loading conditions for non-linear deflections, *International Journal of Non-Linear Mechanics,* 32 (3), pp. 505-514. https://doi.org/10.1016/S0020-7462(96)00069-8

[103] Lyon, S. M., Howell, L. L., and Roach, G. M., 2000, Modeling Flexible Segments With Force and Moment End Loads via the Pseudo-Rigid-Body Model, *ASME 2000 International Mechanical Engineering Congress and Exposition*, pp. 883-890. https://doi.org/10.1115/imece2000-2390

[104] Kimball, C., and Tsai, L.-W., 2002, Modeling of Flexural Beams Subjected to Arbitrary End Loads, *Journal of Mechanical Design,* 124 (2), pp. 223-235. https://doi.org/10.1115/1.1455031

[105] Ma, F., and Chen, G., 2016, Modeling Large Planar Deflections of Flexible Beams in Compliant Mechanisms Using Chained Beam-Constraint-Model1, *Journal of Mechanisms and Robotics,* 8 (2). https://doi.org/10.1115/1.4031028

[106] Kontoudis, G. P., Liarokapis, M., Vamvoudakis, K. G., and Furukawa, T., 2019, An Adaptive Actuation Mechanism for Anthropomorphic Robot Hands, *Front Robot AI,* 6, pp. 47. https://doi.org/10.3389/frobt.2019.00047

[107] Kuresangsai, P., Cole, M. O. T., and Hao, G., 2022, Grasp Stability and Design Analysis of a Flexure-jointed Gripper Mechanism via Efficient Energy-based Modeling, *IEEE Robotics and Automation Letters*, pp. 1-8. https://doi.org/10.1109/lra.2022.3220152

[108] Liarokapis, M. V., and Dollar, A., 2016, Post-contact, in-hand object motion compensation with adaptive hands, 15 (2), pp. 456-467. https://doi.org/10.1109/TASE.2016.2622001

[109] Awtar, S., Slocum, A. H., and Sevincer, E., 2006, Characteristics of Beam-Based Flexure Modules, *Journal of Mechanical Design,* 129 (6), pp. 625-639. https://doi.org/10.1115/1.2717231

[110] Awtar, S., and Sen, S., 2010, A Generalized Constraint Model for Two-Dimensional Beam Flexures: Nonlinear Strain Energy Formulation, *Journal of Mechanical Design,* 132 (8), pp. 081009. https://doi.org/10.1115/1.4002006

[111] Howell, L. L., and Midha, A., 1994, A Method for the Design of Compliant Mechanisms With Small-Length Flexural Pivots, *Journal of Mechanical Design,* 116 (1), pp. 280-290. https://doi.org/10.1115/1.2919359

[112] Ma, F., and Chen, G., 2014, Chained Beam-Constraint-Model (CBCM): a powerful tool for modeling large and complicated deflections of flexible beams in compliant mechanisms, *International Design Engineering Technical Conferences and Computers and Information in Engineering Conference*, pp. V05AT08A027. https://doi.org/10.1115/DETC2014-34140

[113] Jin, M., Yang, Z., Ynchausti, C., Zhu, B., Zhang, X., and Howell, L. L., 2020, Large-Deflection Analysis of General Beams in Contact-Aided Compliant Mechanisms Using Chained Pseudo-Rigid-Body Model, *Journal of Mechanisms and Robotics,* 12 (3). https://doi.org/10.1115/1.4045425

[114] Rasmussen, N. O., Wittwer, J. W., Todd, R. H., Howell, L. L., and Magleby, S. P., 2006, A 3d pseudo-rigid-body model for large spatial deflections of rectangular cantilever beams, *International Design Engineering Technical Conferences and Computers and Information in Engineering Conference*, pp. 191-198. https://doi.org/10.1115/DETC2006-99465

[115] Chase Jr, R. P., Todd, R. H., Howell, L. L., and Magleby, S., 2011, A 3-D chain algorithm with pseudo-rigid-body model elements, *Mechanics Based Design of Structures and Machines,* 39 (1), pp. 142-156. https://doi.org/10.1080/15397734.2011.541783

[116] Chimento, J., Lusk, C., and Alqasimi, A., 2014, A 3-D pseudo-rigid body model for rectangular cantilever beams with an arbitrary force end-load, *International Design Engineering Technical Conferences and Computers and Information in Engineering Conference*, pp. V05AT08A029. https://doi.org/10.1115/DETC2014-34292

[117] Nijenhuis, M., Meijaard, J. P., Mariappan, D., Herder, J. L., Brouwer, D. M., and Awtar, S., 2017, An Analytical Formulation for the Lateral Support Stiffness of a Spatial Flexure Strip, *Journal of Mechanical Design,* 139 (5). https://doi.org/10.1115/1.4035861

[118] Nijenhuis, M., Meijaard, J. P., and Brouwer, D. M., 2020, A spatial closed-form nonlinear stiffness model for sheet flexures based on a mixed variational principle including third-order effects, *Precision Engineering,* 66, pp. 429-444. https://doi.org/10.1016/j.precisioneng.2020.08.003

[119] Bai, R., Chen, G., and Awtar, S., 2021, Closed-form solution for nonlinear spatial deflections of strip flexures of large aspect ratio considering second order load-stiffening, *Mechanism and Machine Theory,* 161. https://doi.org/10.1016/j.mechmachtheory.2021.104324

[120] Bai, R., Awtar, S., and Chen, G., 2019, A closed-form model for nonlinear spatial deflections of rectangular beams in intermediate range, *International Journal of Mechanical Sciences,* 160, pp. 229-240. https://doi.org/10.1016/j.ijmecsci.2019.06.042

[121] Bai, R., Yang, N., Li, B., and Chen, G., 2024, Nonlinear strain energy formulation of spatially deflected strip flexures, *Mechanism and Machine Theory,* 195. https://doi.org/10.1016/j.mechmachtheory.2024.105594

[122] Hao, G., Kong, X., and Reuben, R. L., 2011, A nonlinear analysis of spatial compliant parallel modules: Multi-beam modules, *Mechanism and Machine Theory,* 46 (5), pp. 680-706. https://doi.org/10.1016/j.mechmachtheory.2010.12.007

[123] Eschenauer , H. A., and Olhoff , N., 2001, Topology optimization of continuum structures: A review, *Applied Mechanics Reviews,* 54 (4), pp. 331-390. 10.1115/1.1388075

[124] Zhu, B., Zhang, X., Zhang, H., Liang, J., Zang, H., Li, H., and Wang, R., 2020, Design of compliant mechanisms using continuum topology optimization: A review, *Mechanism and Machine Theory,* 143, pp. 103622. https://doi.org/10.1016/j.mechmachtheory.2019.103622

[125] Zhou, H., 2010, Topology Optimization of Compliant Mechanisms Using Hybrid Discretization Model, *Journal of Mechanical Design,* 132 (11). https://doi.org/10.1115/1.4002663

[126] Lu, K.-J., and Kota, S., 2005, Topology and Dimensional Synthesis of Compliant Mechanisms Using Discrete Optimization, *Journal of Mechanical Design,* 128 (5), pp. 1080-1091. https://doi.org/10.1115/1.2216729

[127] Frecker, M., Kikuchi, N., and Kota, S., 1999, Topology optimization of compliant mechanisms with multiple outputs, *Structural optimization,* 17 (4), pp. 269-278. https://doi.org/10.1007/BF01207003

[128] Luo, Z., Chen, L., Yang, J., Zhang, Y., and Abdel-Malek, K., 2005, Compliant mechanism design using multi-objective topology optimization scheme of continuum structures, *Structural and Multidisciplinary Optimization,* 30 (2), pp. 142-154. https://doi.org/10.1007/s00158-004-0512-y

[129] Sigmund, O., 1997, On the Design of Compliant Mechanisms Using Topology Optimization*, *Mechanics of Structures and Machines,* 25 (4), pp. 493-524. https://doi.org/10.1080/08905459708945415

[130] Kumar, P., Sauer, R. A., and Saxena, A., 2021, On topology optimization of large deformation contact-aided shape morphing compliant mechanisms, *Mechanism and Machine Theory,* 156, pp. 104135. https://doi.org/10.1016/j.mechmachtheory.2020.104135

[131] Ansola, R., Veguería, E., Canales, J., and Tárrago, J. A., 2007, A simple evolutionary topology optimization procedure for compliant mechanism design, *Finite Elements in Analysis and Design,* 44 (1), pp. 53-62. https://doi.org/10.1016/j.finel.2007.09.002

[132] Li, Y., Huang, X., Xie, Y. M., and Zhou, S. W., 2014, Evolutionary topology optimization of hinge-free compliant mechanisms, *International Journal of Mechanical Sciences,* 86, pp. 69-75. https://doi.org/10.1016/j.ijmecsci.2013.10.013

[133] Emmendoerfer, H., Fancello, E. A., and Silva, E. C. N., 2020, Stress-constrained level set topology optimization for compliant mechanisms, *Computer Methods in Applied Mechanics and Engineering,* 362, pp. 112777. https://doi.org/10.1016/j.cma.2019.112777

[134] van Dijk, N. P., Yoon, G. H., van Keulen, F., and Langelaar, M., 2010, A level-set based topology optimization using the element connectivity parameterization method, *Structural and Multidisciplinary Optimization,* 42 (2), pp. 269-282. https://doi.org/10.1007/s00158-010-0485-y

[135] Midha, A., Howell, L. L., and Norton, T. W., 2000, Limit positions of compliant mechanisms using the pseudo-rigid-body model concept, *Mechanism and Machine Theory,* 35 (1), pp. 99-115. https://doi.org/10.1016/S0094-114X(98)00093-7

[136] Bapat, S. G., Midha, A., and Koli, A. B., 2014, On a Generalized Approach for Design of Compliant Mechanisms Using the Pseudo-Rigid-Body Model Concept, *ASME 2014 International Mechanical Engineering Congress and*

Exposition, V014T06A001, https://doi.org/10.1115/imece2014-38788

[137] Liu, P., and Yan, P. J. M. S., 2017, A modified pseudo-rigid-body modeling approach for compliant mechanisms with fixed-guided beam flexures, *Mechanical Sciences,* 8 (2), pp. 359-368. https://doi.org/10.5194/ms-8-359-2017

[138] Bagivalu Prasanna, P., Bapat, S. G., Midha, A., and Lodagala, V., 2020, A Methodology for Determining Static Mode Shapes of a Compliant Mechanism Using the Pseudo-Rigid-Body Model Concept and the Degrees-Of-Freedom Analysis, *Journal of Mechanisms and Robotics,* 12 (2). https://doi.org/10.1115/1.4045971

[139] Hopkins, J. B., and Culpepper, M. L., 2010, Synthesis of multi-degree of freedom, parallel flexure system concepts via Freedom and Constraint Topology (FACT) – Part I: Principles, *Precision Engineering,* 34 (2), pp. 259-270. https://doi.org/10.1016/j.precisioneng.2009.06.008

[140] Hopkins, J. B., and Culpepper, M. L., 2010, Synthesis of multi-degree of freedom, parallel flexure system concepts via freedom and constraint topology (FACT). Part II: Practice, *Precision Engineering,* 34 (2), pp. 271-278. https://doi.org/10.1016/j.precisioneng.2009.06.007

[141] Hao, G., Yu, J., and Liu, Y. 2018. Compliance Synthesis of a Class of Planar Compliant Parallelogram Mechanisms Using the Position Space Concept. https://doi.org/10.1109/remar.2018.8449882

[142] Li, H., and Hao, G., 2018, Position-Space-Based Design of a Symmetric Spatial Translational Compliant Mechanism for Micro-/Nano-Manipulation, *Micromachines (Basel),* 9 (4). https://doi.org/10.3390/mi9040189

[143] Li, H., Hao, G., and Kavanagh, R. C., 2016, Position-Space-Based Compliant Mechanism Reconfiguration Approach and Its Application in the Reduction of Parasitic Motion, *Journal of Mechanical Design,* 138 (9). https://doi.org/10.1115/1.4033988

[144] Su, H.-J., Dorozhkin, D. V., and Vance, J. M., 2009, A Screw Theory Approach for the Conceptual Design of Flexible Joints for Compliant Mechanisms, *Journal of Mechanisms and Robotics,* 1 (4). https://doi.org/10.1115/1.3211024

[145] Qiu, C., and Dai, J. S., 2021, *Analysis and synthesis of compliant parallel mechanisms--screw theory approach*, 1st edition 2021. ed, *Springer Tracts in Advanced Robotics, 139*, Springer International Publishing. Cham. https://doi.org/10.1007/978-3-030-48313-5

[146] Su, H.-J., Dorozhkin, D. V., and Vance, J. M., 2009, A Screw Theory Approach for the Type Synthesis of Compliant Mechanisms With Flexures, *ASME 2009 International Design Engineering Technical Conferences and Computers and Information in Engineering Conference*, pp. 151-161. https://doi.org/10.1115/detc2009-86684

[147] Hoetmer, K., Herder, J. L., and Kim, C. J., 2009, A Building Block Approach for the Design of Statically Balanced Compliant Mechanisms, *ASME 2009 International Design Engineering Technical Conferences and Computers and Information in Engineering Conference*, pp. 313-323. https://doi.org/10.1115/detc2009-87451

[148] Kim, C. J., Moon, Y.-M., and Kota, S., 2008, A Building Block Approach to the Conceptual Synthesis of Compliant Mechanisms Utilizing Compliance and Stiffness Ellipsoids, *Journal of Mechanical Design,* 130 (2). https://doi.org/10.1115/1.2821387

[149] Krishnan, G., Kim, C., and Kota, S., 2012, Building block method: a bottom-up modular synthesis methodology for distributed compliant mechanisms, *Mech. Sci.,* 3 (1), pp. 15-23. https://doi.org/10.5194/ms-3-15-2012

[150] Blad, T. W. A., van Ostayen, R. A. J., and Tolou, N., 2021, A method for tuning the stiffness of building blocks for statically balanced compliant ortho-planar mechanisms, *Mechanism and Machine Theory,* 162. 10.1016/j.mechmachtheory.2021.104333

[151] Gallego, J. A., and Herder, J., 2009, Synthesis Methods in Compliant Mechanisms: An Overview, *ASME 2009 International Design Engineering Technical Conferences and Computers and Information in Engineering Conference*, pp. 193-214. https://doi.org/10.1115/detc2009-86845

[152] Hao, G., He, X., Zhu, J., and Li, H., 2024, Design and Analysis of Leaf Beam Single-Translation Constraint Compliant Modules and the Resulting Spherical Joints, *Journal of Mechanical Design,* 146 (8). https://doi.org/10.1115/1.4064415

[153] Awtar, S., 2003, *Synthesis and Analysis of Parallel Kinematic XY Flexure Mechanisms*, *PhD diss., Massachusetts Institute of Technology*. Cambridge, MA.

[154] Den Hartog, J. P., 1987, *Advanced strength of materials*, Courier Corporation.

[155] Archer, R. R., Crandall, S. H., Dahl, N. C., and Lardner, T. J. J., 1959, *An introduction to the mechanics of solids*. McGraw-Hill, New York.

[156] Rommers, J., and Herder, J., 2019, Design of a Folded Leaf Spring with high support stiffness at large displacements using the Inverse Finite Element Method, *Advances in Mechanism and Machine Science: Proceedings of the 15th IFToMM World Congress on Mechanism and Machine Science 15*, pp. 2109-2118.

[157] Masters, N. D., and Howell, L. L., 2003, A self-retracting fully compliant bistable micromechanism, *Journal of Microelectromechanical Systems,* 12 (3), pp. 273-280. https://doi.org/10.1109/jmems.2003.811751

[158] Wu, K., and Hao, G., 2020, Design and nonlinear modeling of a novel planar

compliant parallelogram mechanism with general tensural-compresural beams, *Mechanism and Machine Theory,* 152. https://doi.org/10.1016/j.mechmachtheory.2020.103950

[159] Kong, K., Chen, G., and Hao, G., 2019, Kinetostatic Modeling and Optimization of a Novel Horizontal-Displacement Compliant Mechanism, *Journal of Mechanisms and Robotics,* 11 (6). 10.1115/1.4044334

[160] Chen, G., Wu, H., Li, B., and Wang, M. Y., 2021, Fully compliant bistable mechanisms with enhanced pitch stiffness, *Mechanical Systems and Signal Processing,* 161. https://doi.org/10.1016/j.ymssp.2021.107926

[161] Liu, T., and Hao, G., 2022, Design of Deployable Structures by Using Bistable Compliant Mechanisms, *Micromachines (Basel),* 13 (5). 10.3390/mi13050651

[162] Han, Q., Jin, K., Chen, G., and Shao, X., 2017, A novel fully compliant tensural-compresural bistable mechanism, *Sensors and Actuators A: Physical,* 268, pp. 72-82. 10.1016/j.sna.2017.10.012

[163] Ling, M., Cao, J., Zeng, M., Lin, J., Inman, D. J. J. S. M., and Structures, 2016, Enhanced mathematical modeling of the displacement amplification ratio for piezoelectric compliant mechanisms, 25 (7), pp. 075022.

[164] Choi, K.-B., Lee, J. J., Kim, G. H., Lim, H. J., and Kwon, S. G., 2018, Amplification ratio analysis of a bridge-type mechanical amplification mechanism based on a fully compliant model, *Mechanism and Machine Theory,* 121, pp. 355-372. https://doi.org/10.1016/j.mechmachtheory.2017.11.002

[165] Luharuka, R., and Hesketh, P. J., 2007, Design of fully compliant, in-plane rotary, bistable micromechanisms for MEMS applications, *Sensors and Actuators A: Physical,* 134 (1), pp. 231-238. 10.1016/j.sna.2006.04.030

[166] Han, Q., Huang, X., and Shao, X., 2017, Nonlinear kinetostatic modeling of double-tensural fully-compliant bistable mechanisms, *International Journal of Non-Linear Mechanics,* 93, pp. 41-46. 10.1016/j.ijnonlinmec.2017.04.020

[167] Dunning, A. G., Tolou, N., Pluimers, P. P., Kluit, L. F., and Herder, J. L., 2012, Bistable Compliant Mechanisms: Corrected Finite Element Modeling for Stiffness Tuning and Preloading Incorporation, *Journal of Mechanical Design,* 134 (8). 10.1115/1.4006961

[168] Hao, G., He, X., and Awtar, S., 2019, Design and analytical model of a compact flexure mechanism for translational motion, *Mechanism and Machine Theory,* 142. https://doi.org/10.1016/j.mechmachtheory.2019.103593

[169] Naves, M., Brouwer, D. M., and Aarts, R. G. K. M., 2017, Building Block-Based Spatial Topology Synthesis Method for Large-Stroke Flexure Hinges, *Journal of Mechanisms and Robotics,* 9 (4).

https://doi.org/10.1115/1.4036223

[170] Soemers, H. M., 2010, *Design principles for precision mechanisms*, University of Twente.

[171] Dan, W., and Rui, F., 2016, Design and nonlinear analysis of a 6-DOF compliant parallel manipulator with spatial beam flexure hinges, *Precision Engineering,* 45, pp. 365-373. https://doi.org/10.1016/j.precisioneng.2016.03.013

[172] Howell, L. L., Magleby, S. P., and Olsen, B. M., 2013, *Handbook of Compliant Mechanisms*, Wiley. New York. 10.1002/9781118516485

[173] Slabaugh, G. G., 1999, Computing Euler angles from a rotation matrix, *Retrieved on August 6,* 6 (2000), pp. 39-63.

[174] Morawiec, A., 2003, *Orientations and rotations*, Springer.

[175] Zhu, J., and Hao, G., 2023, Modelling of a general lumped-compliance beam for compliant mechanisms, *International Journal of Mechanical Sciences*. https://doi.org/10.1016/j.ijmecsci.2023.108779

[176] Li, S., and Hao, G., 2022, Design and nonlinear spatial analysis of compliant anti-buckling universal joints, *International Journal of Mechanical Sciences,* 219. https://doi.org/10.1016/j.ijmecsci.2022.107111

[177] Hao, G., and Zhu, J., 2019, Design of a Monolithic Double-Slider Based Compliant Gripper with Large Displacement and Anti-Buckling Ability, *Micromachines (Basel),* 10 (10). https://doi.org/10.3390/mi10100665

[178] Hamedi, M., Salimi, P., and Vismeh, M., 2012, Simulation and experimental investigation of a novel electrostatic microgripper system, *Microelectronic Engineering,* 98, pp. 467-471. https://doi.org/10.1016/j.mee.2012.07.096

[179] Deng, G., Wang, N., Zhou, C., and Li, J., 2018, A Simplified Analysis Method for the Piezo Jet Dispenser with a Diamond Amplifier, *Sensors (Basel),* 18 (7), pp. 2115. https://doi.org/10.3390/s18072115

[180] Zhou, S., and Yan, P., 2023, Design and Analysis of a Hybrid Displacement Amplifier Supporting a High-Performance Piezo Jet Dispenser, 14 (2), pp. 322. https://doi.org/10.3390/mi14020322

[181] Qian, F., Xu, T.-B., and Zuo, L., 2019, Piezoelectric energy harvesting from human walking using a two-stage amplification mechanism, *Energy,* 189. https://doi.org/10.1016/j.energy.2019.116140

[182] Abdelnaby, M. A., and Arafa, M., 2016, Energy harvesting using a flextensional compliant mechanism, *Journal of Intelligent Material Systems and Structures,* 27 (19), pp. 2707-2718. https://doi.org/10.1177/1045389x16641220

[183] Elsisy, M. M., Arafa, M. H., Saleh, C. A., and Anis, Y. H., 2021, Modeling of a Symmetric Five-Bar Displacement Amplification Compliant Mechanism for Energy Harvesting, *Sensors (Basel),* 21 (4), pp. 1095.

https://doi.org/10.3390/s21041095

[184] Chen, X., and Li, Y., 2022, Design, modeling and testing of a vibration absorption device with energy harvesting based on force amplifier and piezoelectric stack, *Energy Conversion and Management,* 255. https://doi.org/10.1016/j.enconman.2022.115305

[185] Wu, H., Lai, L., Zhang, L., and Zhu, L., 2022, A novel compliant XY micro-positioning stage using bridge-type displacement amplifier embedded with Scott-Russell mechanism, *Precision Engineering,* 73, pp. 284-295. https://doi.org/10.1016/j.precisioneng.2021.09.014

[186] Hao, G., and Kong, X., 2012, A Novel Large-Range XY Compliant Parallel Manipulator With Enhanced Out-of-Plane Stiffness, *Journal of Mechanical Design,* 134 (6). https://doi.org/10.1115/1.4006653

[187] Bazaei, A., Ettefagh, M. H., and Chen, Z., 2021, Displacement amplification and differential actuation in piezo driven nanopositioners, *Mechanical Systems and Signal Processing,* 151, pp. 107356. https://doi.org/10.1016/j.ymssp.2020.107356

[188] Xi, X., Clancy, T., Wu, X., Sun, Y., and Liu, X., 2016, A MEMSXY-stage integrating compliant mechanism for nanopositioning at sub-nanometer resolution, *Journal of Micromechanics and Microengineering,* 26 (2), pp. 025014. https://doi.org/10.1088/0960-1317/26/2/025014

[189] Wang, F., Huo, Z., Liang, C., Shi, B., Tian, Y., Zhao, X., and Zhang, D., 2019, A Novel Actuator-Internal Micro/Nano Positioning Stage With an Arch-Shape Bridge-Type Amplifier, *IEEE Transactions on Industrial Electronics,* 66 (12), pp. 9161-9172. https://doi.org/10.1109/tie.2018.2885716

[190] Chen, J., Zhang, C., Xu, M., Zi, Y., and Zhang, X., 2015, Rhombic micro-displacement amplifier for piezoelectric actuator and its linear and hybrid model, *Mechanical Systems and Signal Processing,* 50-51, pp. 580-593. https://doi.org/10.1016/j.ymssp.2014.05.047

[191] Kim, J. H., Kim, S. H., and Kwak, Y. K., 2004, Development and optimization of 3-D bridge-type hinge mechanisms, *Sensors and Actuators A: Physical,* 116 (3), pp. 530-538. https://doi.org/10.1016/j.sna.2004.05.027

[192] Liu, P., and Yan, P., 2016, A new model analysis approach for bridge-type amplifiers supporting nano-stage design, *Mechanism and Machine Theory,* 99, pp. 176-188. 10.1016/j.mechmachtheory.2016.01.005

[193] Slusher, R. B., and Westminster, C. 1999. MOTION REDUCING FLEXURE STRUCTURE. U.S.Patent 5,969,892, Ball Aerospace & Technologies Corp., Broomfield, Colo.

[194] Ling, M., Wang, J., Wu, M., Cao, L., and Fu, B., 2021, Design and modeling of an improved bridge-type compliant mechanism with its application for hydraulic piezo-valves, 324, pp. 112687.

https://doi.org/10.1016/j.sna.2021.112687

[195] Shen, X., Zhang, L., and Qiu, D., 2021, A lever-bridge combined compliant mechanism for translation amplification, *Precision Engineering,* 67, pp. 383-392. https://doi.org/10.1016/j.precisioneng.2020.10.010

[196] Qian, J., and Yan, P., 2019, Design and analysis of a compliant micro-gripper with LBL type displacement amplifier, *2019 IEEE International Conference on Manipulation, Manufacturing and Measurement on the Nanoscale (3M-NANO)*, pp. 112-117. https://doi.org/10.1109/3m-nano46308.2019.8947391

[197] Chen, G., Ma, Y., and Li, J., 2016, A tensural displacement amplifier employing elliptic-arc flexure hinges, *Sensors and Actuators A: Physical,* 247, pp. 307-315. https://doi.org/10.1016/j.sna.2016.05.015

[198] Ouyang, P. R., Zhang, W. J., and Gupta, M. M., 2008, A New Compliant Mechanical Amplifier Based on a Symmetric Five-Bar Topology, *Journal of Mechanical Design,* 130 (10). https://doi.org/10.1115/1.2965600

[199] Zhu, J., and Hao, G., 2020, Design and test of a compact compliant gripper using the Scott–Russell mechanism, *Archives of Civil and Mechanical Engineering,* 20 (3). https://doi.org/10.1007/s43452-020-00085-3

[200] Li, H., Guo, F., Wang, Y., Wang, Z., Li, C., Ling, M., and Hao, G., 2022, Design and modeling of a compact compliant stroke amplification mechanism with completely distributed compliance for ground-mounted actuators, *Mechanism and Machine Theory,* 167, pp. 104566. https://doi.org/10.1016/j.mechmachtheory.2021.104566

[201] Ling, M., Zhang, C., and Chen, L., 2022, Optimized design of a compact multi-stage displacement amplification mechanism with enhanced efficiency, *Precision Engineering,* 77, pp. 77-89. https://doi.org/10.1016/j.precisioneng.2022.05.012

[202] Prabhu, P., Muralidhara, Veeresha, R. K., and Venugopal, T. R., 2021, Design, fabrication, and testing of flexurally amplified piezo actuator, *Materials Today: Proceedings,* 46, pp. 9490-9497. https://doi.org/10.1016/j.matpr.2020.03.502

[203] Xu, Q., and Li, Y., 2011, Analytical modeling, optimization and testing of a compound bridge-type compliant displacement amplifier, *Mechanism and Machine Theory,* 46 (2), pp. 183-200. https://doi.org/10.1016/j.mechmachtheory.2010.09.007

[204] Chen, W., Kong, C., Lu, Q., Liang, Y., Luo, L., and Wei, H., 2022, Nonlinear analysis, optimization, and testing of the bridge-type compliant displacement amplification mechanism with a single input force for microgrippers, *Precision Engineering,* 73, pp. 166-182. https://doi.org/10.1016/j.precisioneng.2021.09.001

[205] Ma, H.-W., Yao, S.-M., Wang, L.-Q., and Zhong, Z., 2006, Analysis of the

displacement amplification ratio of bridge-type flexure hinge, *Sensors and Actuators A: Physical,* 132 (2), pp. 730-736. https://doi.org/10.1016/j.sna.2005.12.028

[206] Hricko, J., and Havlík, Š., 2020, Compliant Mechanisms for Motion/Force Amplifiers for Robotics, In *Advances in Service and Industrial Robotics: In Advances in Service and Industrial Robotics: Proceedings of the 28th International Conference on Robotics in Alpe-Adria-Danube Region (RAAD 2019)* pp. 26-33. Springer International Publishing.https://doi.org/10.1007/978-3-030-19648-6_4

[207] Ling, M., Cao, J., Jiang, Z., and Lin, J., 2016, Theoretical modeling of attenuated displacement amplification for multistage compliant mechanism and its application, *Sensors and Actuators A: Physical,* 249, pp. 15-22. https://doi.org/10.1016/j.sna.2016.08.011

[208] Yang, Z., and Zu, J., 2014, High-efficiency compressive-mode energy harvester enhanced by a multi-stage force amplification mechanism, *Energy Conversion and Management,* 88, pp. 829-833. https://doi.org/10.1016/j.enconman.2014.09.026

[209] Wen, S., and Xu, Q., 2019, Design of a Novel Piezoelectric Energy Harvester Based on Integrated Multistage Force Amplification Frame, *IEEE/ASME Transactions on Mechatronics,* 24 (3), pp. 1228-1237. https://doi.org/10.1109/tmech.2019.2906999

[210] Lai, L.-J., and Zhu, Z.-N., 2017, Design, modeling and testing of a novel flexure-based displacement amplification mechanism, *Sensors and Actuators A: Physical,* 266, pp. 122-129. 10.1016/j.sna.2017.09.010

[211] Dong, W., Chen, F., Gao, F., Yang, M., Sun, L., Du, Z., Tang, J., and Zhang, D., 2018, Development and analysis of a bridge-lever-type displacement amplifier based on hybrid flexure hinges, *Precision Engineering,* 54, pp. 171-181. https://doi.org/10.1016/j.precisioneng.2018.04.017

[212] Ding, Y., and Lai, L. J., 2019, Design and analysis of a displacement amplifier with high load capacity by combining bridge-type and Scott-Russell mechanisms, *Rev Sci Instrum,* 90 (6), pp. 065102. https://doi.org/10.1063/1.5091672

[213] Dang, M. P., Le, H. G., Le Chau, N., and Dao, T.-P., 2019, A multi-objective optimization design for a new linear compliant mechanism, *Optimization and Engineering,* 21 (2), pp. 673-705. https://doi.org/10.1007/s11081-019-09469-8

[214] Wang, Q., Wei, J., Long, Y., and Tan, J., 2022, Topology optimization design of compliant amplification mechanisms with low parasitic displacement, *Journal of Micromechanics and Microengineering,* 33 (2). https://doi.org/10.1088/1361-6439/aca4dc

[215] Liu, M., Zhang, X., and Fatikow, S., 2016, Design and analysis of a high-accuracy flexure hinge, *Rev Sci Instrum,* 87 (5), pp. 055106.

https://doi.org/10.1063/1.4948924

[216] Hao, G., and Yu, J., 2016, Design, modelling and analysis of a completely-decoupled XY compliant parallel manipulator, *Mechanism and Machine Theory,* 102, pp. 179-195. https://doi.org/10.1016/j.mechmachtheory.2016.04.006

[217] Juuti, J., Kordás, K., Lonnakko, R., Moilanen, V. P., and Leppävuori, S., 2005, Mechanically amplified large displacement piezoelectric actuators, *Sensors and Actuators A: Physical,* 120 (1), pp. 225-231. 10.1016/j.sna.2004.11.016

[218] Hao, G., 2014, A 2-legged XY parallel flexure motion stage with minimised parasitic rotation, *Proceedings of the Institution of Mechanical Engineers, Part C: Journal of Mechanical Engineering Science,* 228 (17), pp. 3156-3169. 10.1177/0954406214526865

[219] Awtar, S., and Parmar, G., 2013, Design of a Large Range XY Nanopositioning System, *Journal of Mechanisms and Robotics,* 5 (2), pp. 021008. https://doi.org/10.1115/1.4023874

[220] Pinskier, J., and Shirinzadeh, B., 2019, Topology optimization of leaf flexures to maximize in-plane to out-of-plane compliance ratio, *Precision Engineering,* 55, pp. 397-407. https://doi.org/10.1016/j.precisioneng.2018.10.008

[221] Polit, S., and Dong, J., 2011, Development of a High-Bandwidth XY Nanopositioning Stage for High-Rate Micro-/Nanomanufacturing, *IEEE/ASME Transactions on Mechatronics,* 16 (4), pp. 724-733. 10.1109/TMECH.2010.2052107

[222] Du, Y., Li, T., Jiang, Y., and Wang, H., 2016, Design and analysis of a 2-degree-of-freedom flexure-based micro-motion stage, *Advances in Mechanical Engineering,* 8 (3), pp. 1-13. https://doi.org/10.1177/1687814016638301

[223] Herpe, X., Walker, R., Dunnigan, M., and Kong, X., 2018, On a simplified nonlinear analytical model for the characterisation and design optimisation of a compliant XY micro-motion stage, *Robotics and Computer-Integrated Manufacturing,* 49, pp. 66-76. 10.1016/j.rcim.2017.05.012

[224] Xu, Q., 2014, Design and Development of a Compact Flexure-Based XY Precision Positioning System With Centimeter Range, *IEEE Transactions on Industrial Electronics,* 61 (2), pp. 893-903. https://doi.org/10.1109/TIE.2013.2257139

[225] Zhang, H., Wu, Z., and Xu, Q., 2020, Design of a New XY Flexure Micropositioning Stage With a Large Hollow Platform, *Actuators,* 9 (3), pp. 65. https://doi.org/10.3390/act9030065

[226] Roy, N. K., and Cullinan, M. A., 2018, Design and characterization of a two-axis, flexure-based nanopositioning stage with 50 mm travel and reduced

higher order modes, *Precision Engineering,* 53, pp. 236-247. https://doi.org/10.1016/j.precisioneng.2018.04.007

[227] Smith, S. T., 2003, *Foundations of ultra-precision mechanism design*, Vol. 2, CRC Press. New York.

[228] Hao, G., and Hand, R. B., 2016, Design and static testing of a compact distributed-compliance gripper based on flexure motion, *Archives of Civil and Mechanical Engineering,* 16 (4), pp. 708-716. https://doi.org/10.1016/j.acme.2016.04.011

[229] Panas, R. M., and Hopkins, J. B., 2015, Eliminating Underconstraint in Double Parallelogram Flexure Mechanisms, *Journal of Mechanical Design,* 137 (9), pp. 092301. https://doi.org/10.1115/1.4030773

[230] Hao, G., He, X., and Awtar, S., 2019, Design and analytical model of a compact flexure mechanism for translational motion, *Mechanism and Machine Theory,* 142, pp. 103593. https://doi.org/10.1016/j.mechmachtheory.2019.103593

[231] Awtar, S., and Slocum, A. H., 2006, Constraint-Based Design of Parallel Kinematic XY Flexure Mechanisms, *Journal of Mechanical Design,* 129 (8), pp. 816-830. https://doi.org/10.1115/1.2735342

[232] Hao, G., and Li, H., 2015, Design of 3-legged XYZ compliant parallel manipulators with minimised parasitic rotations, *Robotica,* 33 (4), pp. 787-806. https://doi.org/10.1017/S0263574714000575

[233] Zhu, J., Hao, G., Li, S., Yu, S., and Kong, X., 2021, A Mirror-Symmetrical XY Compliant Parallel Manipulator With Improved Performances Without Increasing the Footprint, *ASME 2021 International Design Engineering Technical Conferences and Computers and Information in Engineering Conference*, Virtual, Online., DETC2021-69032. https://doi.org/10.1115/detc2021-69032

[234] Lai, L. J., Gu, G. Y., and Zhu, L. M., 2012, Design and control of a decoupled two degree of freedom translational parallel micro-positioning stage, *Review of Scientific Instruments,* 83 (4), pp. 045105. 10.1063/1.3700182

[235] Liu, Z., Zhang, Z., and Yan, P., 2018, A self-adjusting stiffness center design for large stroke compliant XY nanomanipulators, *Mechanical Sciences,* 9 (1), pp. 41-50. 10.5194/ms-9-41-2018

[236] Lee, H., Woo, S., Park, J., Jeong, J., Kim, M., Ryu, J., Gweon, D., and Choi, Y., 2017, Compact compliant parallel XY nano-positioning stage with high dynamic performance, small crosstalk, and small yaw motion, *Microsystem Technologies,* 24 (6), pp. 2653-2662. 10.1007/s00542-017-3626-z

[237] Hao, G., Yu, J., and Liu, Y., 2018, Compliance synthesis of a class of planar compliant parallelogram mechanisms using the position space concept, *2018 International Conference on Reconfigurable Mechanisms and Robots*

(ReMAR), pp. 1-10.

[238] Rommers, J., Naves, M., Brouwer, D. M., and Herder, J. L., 2021, A Flexure-Based Linear Guide With Torsion Reinforcement Structures, *Journal of Mechanisms and Robotics,* 14 (3). https://doi.org/10.1115/1.4052971

APPENDIX

A

FORCE-DISPLACEMENT CHARACTERISTIC OF A SLENDER FLEXURE BEAM

As shown in Figure A.1, the loading conditions for a single flexure beam are represented by F_{i1} (axial force), P_{i1} (transverse force), and M_{i1} (moment) acting at the tip of the beam. The resulting displacements are represented by X_{i1} (displacement along X-axis), Y_{i1} (displacement along Y-axis), and θ_{i1} (rotational angle along Z-axis) with respect to the local coordinate frame. The closed-form solution of the force-displacement characteristic for this flexure beam is represented below [95]:

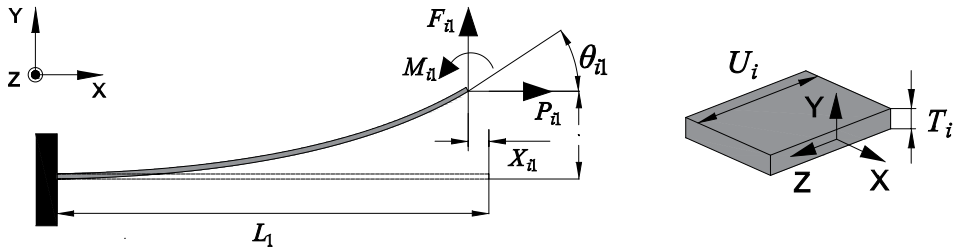


Figure A.1 Simple slender beam with generalized end load

$$\begin{bmatrix} F_{i1}L_{i1}^2/EI \\ M_{i1}L_{i1}^2/EI \end{bmatrix} = \begin{bmatrix} 12 & -6 \\ -6 & 4 \end{bmatrix} \begin{bmatrix} Y_{i1}/L_{i1} \\ \theta_{i1} \end{bmatrix} + P_{i1}L_{i1}^2/EI \begin{bmatrix} 1.2 & -0.1 \\ -0.1 & 2/15 \end{bmatrix} \begin{bmatrix} Y_{i1}/L_{i1} \\ \theta_{i1} \end{bmatrix}$$

$$\frac{X_{i1}}{L_{i1}} = ((T_i/L_{i1}^2)^2/12)\cdot(P_{i1}L_{i1}^2/EI) + 0.5\begin{bmatrix} Y_{i1}/L_{i1} & \theta_{i1} \end{bmatrix} \begin{bmatrix} 1.2 & -0.1 \\ -0.1 & 2/15 \end{bmatrix} \begin{bmatrix} Y_{i1}/L_{i1} \\ \theta_{i1} \end{bmatrix}$$

$$+(P_{i1}L_{i1}^2/EI)\begin{bmatrix} Y_{i1}/L_{i1} & \theta_{i1} \end{bmatrix} \begin{bmatrix} 1/700 & -1/1400 \\ -1/1400 & 11/6300 \end{bmatrix} \begin{bmatrix} Y_{i1}/L_{i1} \\ \theta_{i1} \end{bmatrix} \quad \text{(A.1)}$$

APPENDIX

B

THE NONLINEAR SPATIAL BEAM CONSTRAINT MODEL OF A FLEXURE BEAM

Each of the leaf beams is kinetostatically modelled using the nonlinear spatial beam constraint model (SBCM) as reported in [120]. This modelling approach is capable of accurately capturing the nonlinear effects such as load-stiffening and elastokinematic nonlinearities over the intermediate deflection range defined as 0.1 of the beam length. It provides closed-form solutions for the force-displacement characteristics at the tip of the flexure beam under a general loading condition. Below is an example of leaf beam 1 subjected to such a condition (Figure B.1), followed by the closed-form solution for SBCM of flexure beam 1.

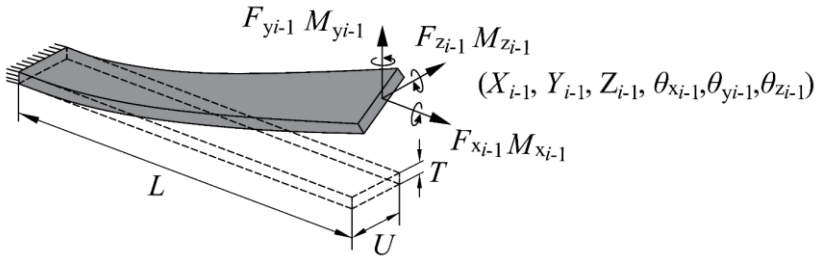


Figure B.1 Description of flexure beam 1 subjected to a general loading condition and its resulting displacements

$$\begin{bmatrix} f_{yi-1} \\ m_{zi-1} \\ m_{xi-1} \end{bmatrix} = H_1 \begin{bmatrix} y_{i-1} \\ \theta_{zi-1} \\ \theta_{xi-1} \end{bmatrix} + \left(f_{xi-1}H_2 + f_{zi-1}H_3 + m_{yi-1}H_4 \right) \begin{bmatrix} y_{i-1} \\ \theta_{zi-1} \\ \theta_{xi-1} \end{bmatrix}$$

$$+ \left(f_{xi-1}^2 H_5 + f_{zi-1}^2 H_6 + f_{zi\text{-}1} m_{yi-1} H_7 + m_{yi-1}^2 H_8 \right) \begin{bmatrix} y_{i-1} \\ \theta_{zi-1} \\ \theta_{xi-1} \end{bmatrix} \tag{B.1}$$

$$z_{i-1} = f_{zi-1}\left(\frac{r}{3}+\frac{1}{\kappa k_s}\right)-\frac{m_{yi-1}r}{2}+\begin{bmatrix} f_{zi-1} & m_{yi-1} & f_{xi-1}\end{bmatrix}C_1\begin{bmatrix} f_{zi-1}\\ m_{yi-1}\\ f_{xi-1}\end{bmatrix}$$

$$-\begin{bmatrix} y_{i-1} & \theta_{zi-1} & \theta_{xi-1}\end{bmatrix}(H_3/2)\begin{bmatrix} y_{i-1}\\ \theta_{zi-1}\\ \theta_{xi-1}\end{bmatrix} \tag{B.2}$$

$$-\begin{bmatrix} y_{i-1} & \theta_{zi-1} & \theta_{xi-1}\end{bmatrix}\left(f_{zi-1}H_6+m_{yi-1}H_7/2+f_{xi-1}f_{zi-1}C_2+f_{xi-1}m_{yi-1}C_3\right)\begin{bmatrix} y_{i-1}\\ \theta_{zi-1}\\ \theta_{xi-1}\end{bmatrix}$$

$$\theta_{yi} = -\frac{f_{zi-1}r}{2}+m_{yi-1}r+\begin{bmatrix} f_{zi-1} & m_{yi-1} & f_{xi-1}\end{bmatrix}C_4\begin{bmatrix} f_{zi-1}\\ m_{yi-1}\\ f_{xi-1}\end{bmatrix} \tag{B.3}$$

$$-\begin{bmatrix} y_{i-1} & \theta_{zi-1} & \theta_{xi-1}\end{bmatrix}(H_4/2+H_9)\begin{bmatrix} y_{i-1}\\ \theta_{zi-1}\\ \theta_{xi-1}\end{bmatrix}$$

$$-\begin{bmatrix} y_{i-1} & \theta_{zi-1} & \theta_{xi-1}\end{bmatrix}\left(f_{zi-1}H_7/2+m_{yi-1}H_8+f_{xi-1}f_{zi-1}C_5+f_{xi-1}m_{yi-1}C_6\right)\begin{bmatrix} y_{i-1}\\ \theta_{zi-1}\\ \theta_{xi-1}\end{bmatrix}$$

$$z_{i-1} = \frac{f_{xi-1}}{k_a}-\begin{bmatrix} y_{i-1} & \theta_{zi-1} & \theta_{xi-1}\end{bmatrix}(H_2/2+f_{xi-1}H_5)\begin{bmatrix} y_{i-1}\\ \theta_{zi-1}\\ \theta_{xi-1}\end{bmatrix} \tag{B.4}$$

where $f_{xi\text{-}1}$, $f_{yi\text{-}1}$, $f_{zi\text{-}1}$, $m_{xi\text{-}1}$, $m_{yi\text{-}1}$ and $m_{zi\text{-}1}$ donate the forces and moments of the tip flexure beam 1, and the resultant displacements are $x_{i\text{-}1}$, $y_{i\text{-}1}$, $z_{i\text{-}1}$, $\theta_{xi\text{-}1}$, $\theta_{yi\text{-}1}$ and $\theta_{zi\text{-}1}$ as shown in Figure A1. A similar labelling pattern applies to flexure beam 2. i donate the i^{th} *GSTC* leaf beam; I_y denotes the cross-section moment of inertia about the y_i-axis, which is expressed as $I_y = TU^3/12$; $\kappa = 10(1+\nu)/(12+11\nu)$; $k_a = UTL^2/I_z$; $k_t = GJ/(EI_z)$; $k_s = GUTL2/(EI_z)$; $r = I_z/I_y$.

The coefficients H_1 through H_9, C_1 through C_5, and J are formulated as Eqs. (B.5) through (B.7), respectively.

$$H_1=\begin{bmatrix} 12 & -6 & 0\\ -6 & 4 & 0\\ 0 & 0 & k_t\end{bmatrix};H_2=\begin{bmatrix} 1.2 & -0.1 & 0\\ -0.1 & 2/15 & 0\\ 0 & 0 & 0\end{bmatrix};H_3=\begin{bmatrix} 0 & 0 & 0\\ 0 & 0 & -1/6\\ 0 & -1/6 & 0\end{bmatrix};H_4=\begin{bmatrix} 0 & 0 & -1\\ 0 & 0 & 1\\ -1 & 0 & 0\end{bmatrix}; \tag{B.5}$$

$$H_5=\begin{bmatrix} -1/700 & 1/1400 & 0\\ 1/1400 & -11/6300 & 0\\ 0 & 0 & 0\end{bmatrix};H_6=\frac{1}{k_t}\begin{bmatrix} -3/35 & 1/105 & 0\\ 1/105 & -13/1260 & 0\\ 0 & 0 & -1/180\end{bmatrix};$$

$$H_7=\frac{1}{k_t}\begin{bmatrix} 1/5 & -1/30 & 0\\ -1/30 & 1/15 & 0\\ 0 & 0 & 0\end{bmatrix};H_8=\frac{1}{k_t}\begin{bmatrix} -1/5 & 1/10 & 0\\ 1/10 & -2/15 & 0\\ 0 & 0 & 0\end{bmatrix};H_9==\begin{bmatrix} 0 & 0 & 0\\ 0 & 0 & 0\\ 0 & 1 & 0\end{bmatrix};$$

$$C_1=\begin{bmatrix} 0 & 0 & -\frac{r^2}{15} \\ 0 & 0 & \frac{5r^2}{48} \\ -\frac{r^2}{15} & \frac{5r^2}{48} & 0 \end{bmatrix};C_2=\begin{bmatrix} \frac{415r+14}{12600k_t} & -\frac{245r+6}{50400k_t} & 0 \\ -\frac{245r+6}{50400k_t} & \frac{235r+8}{12600k_t} & 0 \\ 0 & 0 & 0 \end{bmatrix};C_3=\begin{bmatrix} -\frac{40r+1}{700k_t} & \frac{30r+1}{600k_t} & 0 \\ \frac{30r+1}{600k_t} & -\frac{410r+33}{50400k_t} & 0 \\ 0 & 0 & 0 \end{bmatrix}; \quad \text{(B.6)}$$

$$C_4=\begin{bmatrix} 0 & 0 & \frac{5r^2}{48k_t} \\ 0 & 0 & -\frac{r^2}{6} \\ \frac{5r^2}{48k_t} & -\frac{r^2}{6} & 0 \end{bmatrix};C_5=\begin{bmatrix} -\frac{35r+1}{700k_t} & \frac{403r+7}{4200k_t} & 0 \\ \frac{403r+7}{4200k_t} & -\frac{835r+103}{25200k_t} & 0 \\ 0 & 0 & 0 \end{bmatrix};C_6=\begin{bmatrix} \frac{4r+1}{350k_t} & -\frac{190r+3}{2100k_t} & 0 \\ -\frac{190r+3}{2100k_t} & \frac{175r+22}{6300k_t} & 0 \\ 0 & 0 & 0 \end{bmatrix};$$

$$J=\frac{2\cdot T^3\cdot U^3}{7\cdot T^2+7\cdot U^2}\cdot\left(\frac{1.167\cdot\eta^5+29.49\cdot\eta^4+30.9\cdot\eta^3+100.9\cdot\eta^2+30.38\cdot\eta+29.41}{\eta^5+25.91\cdot\eta^4+41.58\cdot\eta^3+90.43\cdot\eta^2+41.74\cdot\eta+25.21}\right); \quad \text{(B.7)}$$

APPENDIX

C

FORCE-EQUILIBRIUM EQUATIONS AND GEOMETRY COMPATIBILITY CONDITIONS OF THE GSTC LEAF BEAM

This appendix presents the force-equilibrium equations and geometry compatibility conditions for the GSTC leaf beam. The force-equilibrium equations are derived based on the free-body diagram (FBD) in the deformed configuration, mainly accounting for the contributions of the axial load to the bending moment. The geometry-compatibility conditions are kinematic relationships that adheres to the geometric constraints defined in this work, which are also derived under the deformed condition.

$$\left[f_{xi-2},\, f_{yi-2},\, f_{zi-2},\, m_{xi-2},\, m_{xi-2},\, m_{xi-2} \right]^{\mathrm{T}} = D_{Si}^{\mathrm{T}} R_{SYi} R_{Si} R_{SYi}^{\mathrm{T}} R_{SZi} R_{SXi} \left[f_{xi-1},\, f_{yi-1},\, f_{zi-1},\, m_{xi-1},\, m_{xi-1},\, m_{xi-1} \right]^{\mathrm{T}};$$

$$\left[f_{xsi},\, f_{ysi},\, f_{zsi},\, m_{xsi},\, m_{ysi},\, m_{zsi} \right]^{\mathrm{T}} = R_{SYi} R_{Si} R_{SYi}^{\mathrm{T}} R_{SZi} R_{SXi} \left[f_{xi-1},\, f_{yi-1},\, f_{zi-1},\, m_{xi-1},\, m_{xi-1},\, m_{xi-1} \right]^{\mathrm{T}}; \quad \text{(C.1)}$$

where $f_{Xi\text{-}1}$, $f_{yi\text{-}1}$, $f_{Zi\text{-}1}$, $m_{Xi\text{-}1}$, $m_{yi\text{-}1}$ and $m_{Zi\text{-}1}$ donate the forces and moments of the tip of leaf beam 1, and the resultant displacements are $x_{i\text{-}1}$, $y_{i\text{-}1}$, $z_{i\text{-}1}$, $\theta_{xi\text{-}1}$, $\theta_{yi\text{-}1}$ and $\theta_{zi\text{-}1}$. A similar labelling pattern applies to leaf beam 2. The matrix D_{Si} donates a 6×6 normalised translational matrix for the tip of the GSTC leaf beam module, as provided below. R_{Si} donates rotational matrix for the tip GSTC leaf beam. When multiplied by the force represented in the global coordinate system, it yields the moments created by the forces in the deformed configuration. All forces and moments are expressed with respect to the global coordinate system X_S-Y_S-Z_S, achieved by multiplying the transformation matrices, namely R_{SXi}, R_{SYi} and R_{SZi}.

$$R_{Si}=\begin{bmatrix} R_{si} & 0_{3\times3} \\ 0_{3\times3} & R_{si} \end{bmatrix};\ R_{SYi}=\begin{bmatrix} R_{yi} & 0_{3\times3} \\ 0_{3\times3} & R_{yi} \end{bmatrix};\ R_{SZi}=\begin{bmatrix} R_{zi} & 0_{3\times3} \\ 0_{3\times3} & R_{zi} \end{bmatrix};\ R_{SXi}=\begin{bmatrix} R_{xi} & 0_{3\times3} \\ 0_{3\times3} & R_{xi} \end{bmatrix}; \tag{C.2}$$

$$R_{xi}=\begin{bmatrix} 1 & 0 & 0 \\ 0 & \cos(\beta_{xi}) & -\sin(\beta_{xi}) \\ 0 & \sin(\beta_{xi}) & \cos(\beta_{xi}) \end{bmatrix};R_{yi}=\begin{bmatrix} \cos(\beta_{yi}) & 0 & \sin(\beta_{yi}) \\ 0 & 1 & 0 \\ -\sin(\beta_{yi}) & 0 & \cos(\beta_{yi}) \end{bmatrix};R_{zi}=\begin{bmatrix} \cos(\beta_{zi}) & -\sin(\beta_{zi}) & 0 \\ \sin(\beta_{zi}) & \cos(\beta_{zi}) & 0 \\ 0 & 0 & 1 \end{bmatrix};$$

$$D_{Si}=\begin{bmatrix} & 0 & A^*(3,1) & -A^*(2,1) \\ I_{3\times3} & -A^*(3,1) & 0 & A^*(1,1) \\ & A^*(2,1) & -A^*(1,1) & 0 \\ 0_{3\times3} & & I_{3\times3} & \end{bmatrix}; \tag{C.3}$$

where $I_{3\times3}$ donates a 3×3 identity matrix, while $0_{3\times3}$ donates a zero matrix. A^* donates a 3×3 matrix which represents the deformed position of the tip of the GSTC leaf beam with respect to the global coordinate X_S-Y_S-Z_S. The expression is presented below.

$$A^*=R_{yi}R_{si}\left[\cos\beta_{yi}(\cos\beta_{zi}l+\cos\beta_{yi}d),\ \sin\beta_{zi}(d+l),\ \cos\beta_{zi}\sin\beta_{yi}(d+l)\right]^{\mathrm{T}}$$
$$+R_{yi}R_{si}R_{yi}^{\mathrm{T}}R_{zi}R_{xi}\left[x_{i-1},\ y_{i-1},\ z_{i-1}\right]^{\mathrm{T}}; \tag{C.4}$$

The geometry compatibility for the GSTC leaf beam is derived based on its deformed configuration, as detailed below.

$$\left[x_{si},\ y_{si},\ z_{si}\right]^{\mathrm{T}}=R_{yi}\left[x_{i-2},\ y_{i-2},\ z_{i-2}\right]^{\mathrm{T}}+R_{yi}R_{si}R_{yi}^{\mathrm{T}}R_{zi}R_{xi}\left[x_{i-1},\ y_{i-1},\ z_{i-1}\right]^{\mathrm{T}}$$
$$+R_{yi}(R_{si}(\left[\cos\beta_{yi}(\cos\beta_{zi}l+\cos\beta_{yi}d),\ \sin\beta_{zi}(d+l),\ \cos\beta_{zi}\sin\beta_{yi}(d+l)\right]^{\mathrm{T}}-I_{3\times1})); \tag{C.5}$$

$$\left[\theta_{xsi},\ \theta_{ysi},\ \theta_{zsi}\right]^{\mathrm{T}}=R_{yi}\left[\theta_{xi-2},\ \theta_{yi-2},\ \theta_{zi-2}\right]^{\mathrm{T}}+R_{yi}R_{si}R_{yi}^{\mathrm{T}}R_{zi}R_{xi}\left[\theta_{xi-1},\ \theta_{yi-1},\ \theta_{zi-1}\right]^{\mathrm{T}}; \tag{C.6}$$

where R_{si} donates the 3×3 rotational matrix for the tip GSTC leaf beam. R_{xi}, R_{yi} and R_{zi} donate the 3×3 rotational matrices about the X-axis, Y-axis and Z-axis, respectively.

APPENDIX

D

FORCE-DISPLACEMENT CHARACTERISTIC OF A GENERIC FLEXURE BEAM

Linear analytical modeling fails to capture nonlinear stiffness characteristics and can only be applied over a relatively small range of motion. In this section, the BCM [95] was used for a generalized beam flexure, serving to accurately model the characteristics of the proposed amplifier when combing with the FBD system modelling method. The BCM approach captures nonlinearities and leads to a closed-form model that can accurately estimate the kinetostatic behavior of a generalized beam subjected to combined loads. It is necessary to solve equations associated with constitutive relationships, load-equilibrium conditions, and geometric compatibility conditions to obtain the load and displacement relationships of the proposed amplifier.

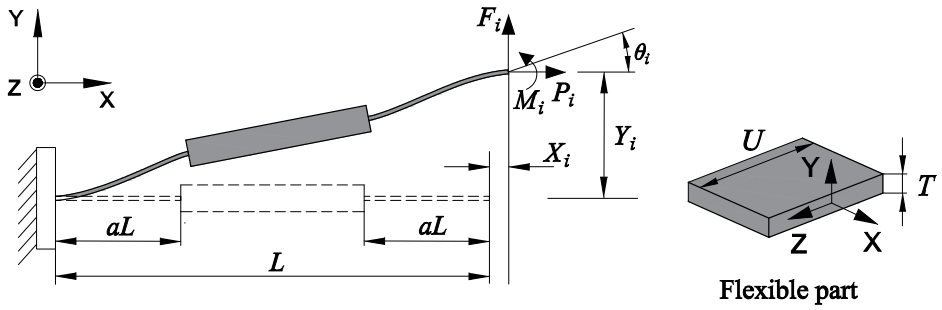


Figure D.1 Loading condition and geometry parameters of the generic flexure beam (the middle part considered to be rigid, with a thickness much larger than T); Under the condition of a = 1/2, the generic beam corresponds to a uniform thickness beam, i.e., distributed-compliance beam.

The generic flexure beams embodied in the amplifier are identical, one of which, in its deformed configuration, is shown in Figure D.1. The loading conditions for a single flexure beam are represented by F_i (axial force), P_i (transverse force), and M_i

(moment) acting at the tip of the beam. The resulting displacements are represented by X_i (displacement along X-axis), Y_i (displacement along Y-axis), θ_i and (rotational angle along Z-axis) with the respect to the local coordinate frame. To simplify the equation representation, all length parameters and translational displacements are normalized by beam length L, forces by EI/L^2, and moments by EI/L. Each of the normalized quantities is indicated in lowercase, specifically:

$$f_i = \frac{F_i}{EI/L^2},\ p_i = \frac{P_i}{EI/L^2},\ m_i = \frac{M_i}{EI/L},\ x_i = \frac{X_i}{L},\ y_i = \frac{Y_i}{L},\ u = \frac{U}{L},\ t = \frac{T}{L} \tag{D.1}$$

where I is the second moment of area of the generic flexure beam cross-section about the Z-axis, and E denotes Young's modulus of the material. The constitutive equations of each flexure beam are represented below [109]:

$$\begin{bmatrix} f_i \\ m_i \end{bmatrix} = \begin{bmatrix} k_{11}^{(0)} & k_{12}^{(0)} \\ k_{21}^{(0)} & k_{22}^{(0)} \end{bmatrix} \begin{bmatrix} y_i \\ \theta_i \end{bmatrix} + p_i \begin{bmatrix} k_{11}^{(1)} & k_{12}^{(1)} \\ k_{21}^{(1)} & k_{22}^{(1)} \end{bmatrix} \begin{bmatrix} y_i \\ \theta_i \end{bmatrix} \tag{D.2}$$

$$x_i = \frac{p_i}{k_{33}} + \begin{bmatrix} y_i & \theta_i \end{bmatrix} \begin{bmatrix} g_{11}^{(0)} & g_{12}^{(0)} \\ g_{13}^{(0)} & g_{14}^{(0)} \end{bmatrix} \begin{bmatrix} y_i \\ \theta_i \end{bmatrix} + p_i \begin{bmatrix} y_i & \theta_i \end{bmatrix} \begin{bmatrix} g_{11}^{(1)} & g_{12}^{(1)} \\ g_{13}^{(1)} & g_{14}^{(1)} \end{bmatrix} \begin{bmatrix} y_i \\ \theta_i \end{bmatrix} \tag{D.3}$$

where the coefficients k and g are non-dimensional values that characterize the stiffness of a double-notch flexure beam, and they have been provided in [109]. It is also worth noting that coefficients/entries associated with the symbols, k and g, are the functions of a (Figure D.1) In the case of a = 1/2, the generic beam corresponds to a distributed-compliance beam.